Accuracy of the Transverse Emittance Measurements of the CERN Large Hadron Collider

Thèse présentée à la Faculté des Sciences de Base
Institut de Physique de l'Energie et des Particules
Section de Physique

pour l'obtention du grade de Docteur ès Sciences

par

Federico Roncarolo

Ingénieur-nucléaire

Politecnico di Milano, Italie

Lausanne
2005

CERN-THESIS-2005-082
//2005

Abstract

High energy accelerators and storage rings are designed to collide charged particle beams and study their collision products. The production rate of the collision products has to be maximized in order to reduce the statistical uncertainty of the produced events.
Monitoring the transverse distribution of the accelerated species allows to measure and optimize the beam transverse emittance, which directly affects the secondary particles production rate. The beam transverse emittance is measured by a class of diagnostics, the *transverse profile monitors,* designed to observe the particles transverse distributions.
This thesis work aims at determining the accuracy of two classes of profile monitors presently installed in the CERN accelerators and foreseen for the Large Hadron Collider (LHC): wire scanners and residual gas monitors.
The explanation of the linear dynamics that characterize the particles transverse motion in an accelerator is followed by the description of the principles of operation of the studied monitors. In addition, numerical simulations predict the effect of limited resolution and excessive noise.
The particles transverse distributions are parameterized with a Gaussian density distribution and the approximation procedures are studied.
Two types of wire scanners are used in the Super Proton Synchrotron (SPS), based on a linear and rotational displacement of the wire respectively. The systematic differences between the wire scanner monitors have been measured with several beam conditions and vary from below $1\,\%$ to about $35\,\%$ of the absolute beam normalized emittance. The reasons of such discrepancies are discussed. The statistical fluctuations of the wire scanner monitors, expressing their repeatability, resulted to be below $3\,\%$ of the absolute emittance. In terms of beam size, the repeatability is about $11\,\mu m$ for the linear wire scanners and varies from 39 to $58\,\mu m$ for the rotational.
Comparative measurements between the SPS wire scanners and the Ionization Profile Monitor (IPM) underline the IPM limitations when used to measure beam transverse distributions with Gaussian widths smaller than $500\,\mu m$. In terms of beam size, the maximum discrepancy between the two classes of instruments decreased from $250\,\mu m$ to $150\,\mu m$ after the IPM hardware optimization. The wire scanner monitors, installed in all the LHC pre-accelerators, have been utilized to characterize the beam transverse emittance during acceleration from $1.4\,GeV$ to $450\,GeV$. For the first time, this kind of measurements were carried out systematically for the different beam types that will be employed first for the LHC commissioning phase and later for its operation as a collider.

Résumé

Les accélérateurs de faisceaux à haute énergie associés à des anneaux de stockage sont conçus afin d'étudier les produits dérivés créés lors de la collision de ces faisceaux de particules chargés. Le taux de génération de particules doit être optimisé dans le but de réduire l'incertitude statistique des événements ainsi produits.
L'observation de la distribution transversale des espèces accélérées permet de mesurer et d'optimiser l'emittance transversale du faisceau, laquelle affecte directement le taux de production des particules secondaires.
L'emittance transversale du faisceau est mesurée par le biais d'un moniteur de profil, un outil de diagnostique conçu pour observer la distribution transversale des particules.
L'objectif de cette thèse est de déterminer la précision de deux types différents de moniteurs de profils: un scanneur à fil et un moniteur de profil à ionisation (IPM). Les deux sont actuellement installés au CERN et leur utilisation est prévue sur le grand collisionneur de hadrons (LHC).
Afin de mieux comprendre l'utilisation faite de ces moniteurs, la première partie de cette thèse présente une introduction à la dynamique linéaire qui caractérise le mouvement transversal des particules dans un accélérateur. Une description des principes de fonctionnement des deux moniteurs est donnée par la suite. Une série des simulations numériques est également présentée afin de quantifier les effets d'une faible résolution du moniteur et de l'excès de bruit de fond sur la précision de la mesure.
La dernière partie de cette thèse présente une description des principes appliqués dans l'étude des moniteurs et les conclusions obtenues.
Les distributions transversales des particules sont paramétrées en utilisant une distribution de densité Gaussienne. Les procédures d'approximation sont également étudiées.
Deux types différents de scanneur à fil sont utilisés dans le Super Proton Synchrotron (SPS), leur différence provenant du mouvement du fil, soit linéaire, soit circulaire.
Les différences systématiques entre les résultats obtenus avec les différents scanneurs à fil ont été mesurées pour des conditions de faisceaux divers et varient du $1\,\%$ jusqu'à $35\,\%$ de la valeur absolue de l'emittance normalisée du faisceau. L'origine de ces différences est également discutée ici. Les fluctuations statistiques des moniteurs à scanneur à fil, du point de vue de la répétitivité, est inférieure à $3\,\%$ de l'emittance absolue. Par rapport à la taille du faisceau, la répétitivité est approximativement de $11\,\mu m$ pour les scanneurs linéaires et varie entre 39 et $58\,\mu m$ pour les circulaires.
Les mesures comparatives entre les scanneurs à fil du SPS et le moniteur IPM montrent les limitations de l'IPM pour la mesure de profils d'une largeur Gaussienne inférieure à $500\,\mu m$. Suite à la conséquente optimisation du hardware de l'IPM, la différence entre les mesures de la taille du faisceau obtenues par les deux types dŠinstruments se réduit de 250 à $150\,\mu m$.
Les moniteurs de scanneur à fil installés dans tous les pré-accelerateurs du LHC ont été utilisés pour caractériser l'emittance transversale du faisceau pendant l'accélération de 1.4 GeV jusqu'à 450 GeV. C'est la première fois que ces mesures ont été réalisées systématiquement pour les différents types de faisceaux qui seront utilisés d'abord pour la phase de mise au point du LHC et par la suite pendant son opération comme collisionneur.

Acknowledgements

This work could be carried out thanks to the support of the Ecole Polytechnique Fédérale de Lausanne (EPFL) in collaboration with CERN. I would like to thank Prof. Jean-Pierre Perroud for his supervision at EPFL and for the fruitful discussions we had during the thesis work and the redaction of this report. I am grateful also to Prof. Aurelio Bay for his constant support.
I am sincerely thankful to Dr. Bernd Dehning. His wise supervision of my work was crucial from the beginning to the end of my work, from the proposition of the thesis subject to the very stimulating time spent in the SPS control room and to the remarkable amount of time he spent in reviewing this report. Not only did I learn a lot from him about beam instrumentation and accelerator physics, but he also enriched my professional experience with his clever way of facing the different aspects of our work. Also, I very much appreciated his behavior with the colleagues, fundamental for a successful team work.
I am also very much obliged to several members of the CERN AB-BDI Group. First of all I would like to acknowledge Jan Koopman and Gianfranco Ferioli. Indeed, I profited a lot from their competence about the monitors I studied. They made much easier for me the accomplishment of many aspects of my work. In addition, I would like to thank Dr. Claude Fischer for the kind collaboration we had in studying the Ionization Profile Monitor.
I would like to express a particular acknowledgment to Enrico Bravin, not only for his friendship, but also for sharing with me his remarkable knowledge about physics, electronics, statistics and ... of course sailing. Many thanks also to Dr. Hermann Schmickler, who always supported my work and encouraged me to attend several training courses and accelerator schools.
I spent most of the experimental part of my thesis work in the SPS control room and I would like to thank all the members of the AB-OP and AB-ABP groups, who were always very kindly disposed to help me in the accelerator setup for our measurements. In particular I would like to acknowledge Dr. Gianluigi Arduini who dedicated much time in explaining to me several aspects of accelerator physics and always encouraged me to study the emittance monitors accuracy. Some important results of this thesis could have been obtained due to his collaboration and his expertise. I am also grateful to Dr. Jorg Wenninger for his help in making me understand the SPS setting up, in performing the betatron function measurements and for the always prompt answers to my frequent questions.
Thanks to Madeleine Catin and Erika Luthi, always so kind and professional when I had any need from them.
In 2003 I had the privilege to spend few months at the Fermi National Laboratory, in Chicago, in order to study the accuracy of the Tevatron flying wire monitors. I believe that it was a great opportunity to enrich my personal and professional experience and I am really thankful to Dr. Jean Slaughter, Dr. Stephen Pordes and Dr. Alberto Marchionni for how they quickly introduced me to such a new environment.

Non posso terminare senza ringraziare i miei genitori, le persone a cui piu' di tutti voglio dedicare questo lavoro. Grazie per tutto quello che mi avete insegnato, per il vostro appoggio, per il vostro affetto.

Contents

Glossary

ACRONYMS AND ACCELERATOR PHYSICS DEFINITIONS

BCT Beam Current Transformer. It consists of a high precision DC current transformer (DCCT) which detects the DC component of the stored beam. The magnetic field induced by the moving charges in the ferrite core of the monitor provides an absolute measurement of the average beam current.

BPM Beam Position Monitor. The type used at CERN is based on the measurement of the image current induced by the beam on two (or four) electrodes placed around it. The combination of the electrodes voltages allows to retrieve the beam position.

Bucket Area in longitudinal phase space within which the accelerator radio frequency (RF) system forces the particles to stay, thanks to longitudinal focusing forces.

Bunch Ensemble of particles captured within one RF bucket.

Bunch Length Amplitude of the bunch of particles in the longitudinal plane (direction of movement of the particles). It is usually given in the time coordinate, as $1\,\sigma$ of the Gaussian function which parameterizes the bunch in the time domain.

Bunch Spacing Time separation between consecutive bunches.

Batch Train of bunches, characterized by the number of bunches and by the bunch spacing in time.

- **PS batch** Train of N bunches injected in the SPS in one PS-to-SPS transfer. N=72 for the LHC nominal beam (see Section 1.2).
- **SPS batch** Trains of M PS batches injected into the LHC in one SPS-to-LHC transfer. M=3 or M=4 for the present designed injection schemes.

Cycle (or filling cycle) Term used to indicate the time necessary to fill the accelerator with the desired particles and bring them to the energy required for the transfer in another accelerator or their storage in the same ring (for storage rings), the extraction to expiremental areas (for fixed target operation) or the collision (for colliders). A cycle is normally at least subdivided in an injection and an acceleration periods.

Crossing angle Relative angle between the two colliding beams directions at the interaction points.

LHC Large Hadron Collider, future CERN accelerator designed to accelerate and collide two proton beams in a first phase and two heavy ion beams in a second.

PS Proton Synchrotron, one of the CERN accelerators.

PSB Protron Synchrotron Booster, one of the CERN accelerators.

TOTEM Total Cross Section, Elastic Scattering and Diffraction Dissociation, one of the physics experiments at LHC. The **TOTEM BEAM** is the beam accelerated for this experiment, characterized by low intensity bunches spaced by $525\,ns$ (see Section 1.2).

CONCEPTS QUALIFYING INSTRUMENTS AND MEASUREMENTS

(derived from [1, 2, 3])

Accuracy Closeness of the agreement between the result of a measurement and the true value of the measurand

Precision Qualitative term often used in the context of repeatability and reproducibility. It has not to be used in the place of accuracy.

Repeatability Closeness of the agreement between the results of successive measurements of the same measurand carried out under the same conditions (same measurement procedure, same measuring instrument). It can be seen as a repetition of the results over a short period of time.

Reproducibility Closeness of the agreement between the results of successive measurements of the same measurand carried out under conditions which have been restored after a change.

Resolution The smallest increment of the measurand which can be discerned by the measurement device.

Uncertainty Qualitative parameter, associated with the result of a measurement, that characterizes the dispersion of the values that could be reasonably attributed to the measurand.

Chapter 1

Introduction

CERN is the European Organization for Nuclear Research, one of the world most influential particle physics center. Founded in 1954, the laboratory was one of Europe's first joint ventures, and has become a shining example of international collaboration. From the original 12 signatories of the CERN convention, membership has grown to the present 20 Member States.
CERN's history is bound up with the construction of large accelerators: the Synchro-Cyclotron (SC, 1957) and the Proton Synchrotron (PS, 1959) were followed by the Intersecting Storage Rings (ISR, 1971), the Proton Synchrotron Booster (PSB, 1972) and the Super Proton Synchrotron (SPS, 1976).
From 1981 the SPS was operated as proton-antiproton collider. In 1983 it allowed the discovery of the W-bosons and the Z-boson, the carriers of the weak nuclear force, thus confirming the theory of electro-weak interactions and unifying the weak and electromagnetic forces.
The Large Electron-Positron storage ring (LEP) was completed in 1989 and was installed in a tunnel of $27\,km$ circumference, located between 80 and 150 m underground. It was operated between 1989 and 2001 and lead to the experimental verification of several elements of the Standard Model, such as the Z and W bosons mass accurate determination.
The Large Hadron Collider (LHC) is under construction, and will be installed in the LEP tunnel, which has been completely emptied after the LEP definitive shut down.
The LHC will be the first storage ring in which quarks and gluons collide in the TeV energy range and represents the next step in high energy physics research. As CERN's first accelerators were catalysts for European collaboration, the LHC will set a precedent for a worldwide collaboration in physics research.

The particles production of a collider is characterized by the accelerated species of particles, by their energy and by their availability. As it will be discussed in Chapter 2, the particle production rate can be expressed as $\dot{n} = \sigma \cdot \mathscr{L}$, where σ is the interaction cross section and the *Luminosity* $\mathscr{L}$ depends on the colliding particles distribution. In particular $\mathscr{L}$ is inversely proportional to the width of transverse distribution at the colliding point. Such width varies at different locations and normally it cannot be measured at the colliding points. However, it can be associated with the beam *transverse emittance* that is invariant. Measuring the transverse distribution in a location in the ring allows to determine the beam emittance and consequently the beam size at the interaction point. Therefore the luminosity can be derived and the collider performance established.

The next chapter will explain the accelerator physics principles, focusing on the transverse beam dynamics. The equation of motion in the transverse plane and the representation of the particles distribution in phase space, will lead to the definitions of beam size and transverse emittance.
In Chapter 3 we will first give an overview of the various methods for monitoring the beam transverse distribution and then explain in details the ones studied in this work. The motivations leading to the choice of such intruments and the measurement requirements for the CERN SPS and LHC will

be also discussed in that chapter. In addition, we will present a way to measure experimentally the amplitude of the betatron function, necessary, together with the beam size, to determine the transverse beam emittance. A section is devoted to study the effects of the monitors limited resolution and the presence of noise, by simulating the different dependencies.
Chapter 4 gives the hardware specifications of the studied monitors.
Chapter 5 discusses the emittance increase induced by the operation of wire scanner monitors. Chapter 6 describes the electromagnetic coupling, observed for the first time, between the wires of the scanners and the proton beam in the SPS. A description of the phenomenon is followed by the modifications applied to avoid the damage of the monitors.
Chapter 7 presents the methods for acquiring and analyzing the emittance measurements. The procedures used to characterize the particles transverse distribution with a Gaussian function are described. The Gaussian fit confidence level is considered as the parameter attesting the parametrization quality.
Chapter 8 contains the experimental results of this work, that yield the monitors accuracy, repeatability and resolution. The last part of the chapter presents the outcome of measurements campaigns dedicated to track the transverse emittance of different beam types in the LHC pre-accelerators.

1.1 LHC and Injectors Chain

LHC will be accommodated in the 27 km tunnel previously used for LEP. Four experimental areas will be equipped for observing the proton beams collisions. Two of them will consist of general purpose detectors, ATLAS [4] and CMS [5]. The other two will be: a detector dedicated also to heavy ions, ALICE [6], and a detector specialized in the physics of the B-meson, LHC-B [7]. The locations of the four areas around the ring are depicted in Fig. 1.1. In addition, the experimental setup named TOTEM [8] will investigate the p-p total cross section, elastic scattering and diffraction processes.

LHC will be supplied with protons by the injector chain illustrated in Fig. 1.2. The protons are generated by a *Duoplasmatron source* from which they are extracted with a kinetic energy of $100\,keV$ and injected in the *Linac*. The linac consists of a beam transport line of about $80\,m$ along which the particles are accelerated to $50\,MeV$ and grouped in buckets which can last from 20 to $150\,\mu s$ by mean of radio frequency cavities.
The protons are then injected in the *Proton Synchrotron Booster (PSB)*, a $157\,m$ circumference complex capable of accelerating high intensity beams up to $1.4\,GeV$ and composed of a stack of four separate rings with a common magnetic and radio frequency system.
From the PSB the particles are transferred to the *Proton Synchrotron (PS)*, a $628\,m$ circumference ring, where they are accelerated to $26\,GeV$.
Up to this point the accelerators complex is installed at ground level. A beam transport line connects the PS to the *Super Proton Synchrotron (SPS)*, which has a circumference of $6.9\,km$ and lays at about $50\,m$ underground. In the SPS the beam energy increases from 26 to $450\,GeV$.
The particles beams will be injected from the SPS to the LHC via two different transfer lines in order to establish two circulating beams in opposite directions. These two transfer lines provide the connection between the SPS tunnel and the LHC plane which lays between 80 and $150\,m$ underground.

1.2 Beams for LHC commissioning and operation

LHC will be the first CERN accelerator based on superconductive magnets. Undesired effects could cause large losses of protons, with a consequent energy deposition onto the superconductive coils of the magnets. This scenario is potentially very dangerous with respect to the magnets integrity and loss of superconductivity, and can require long down-time of the accelerator for their recovery or repair.

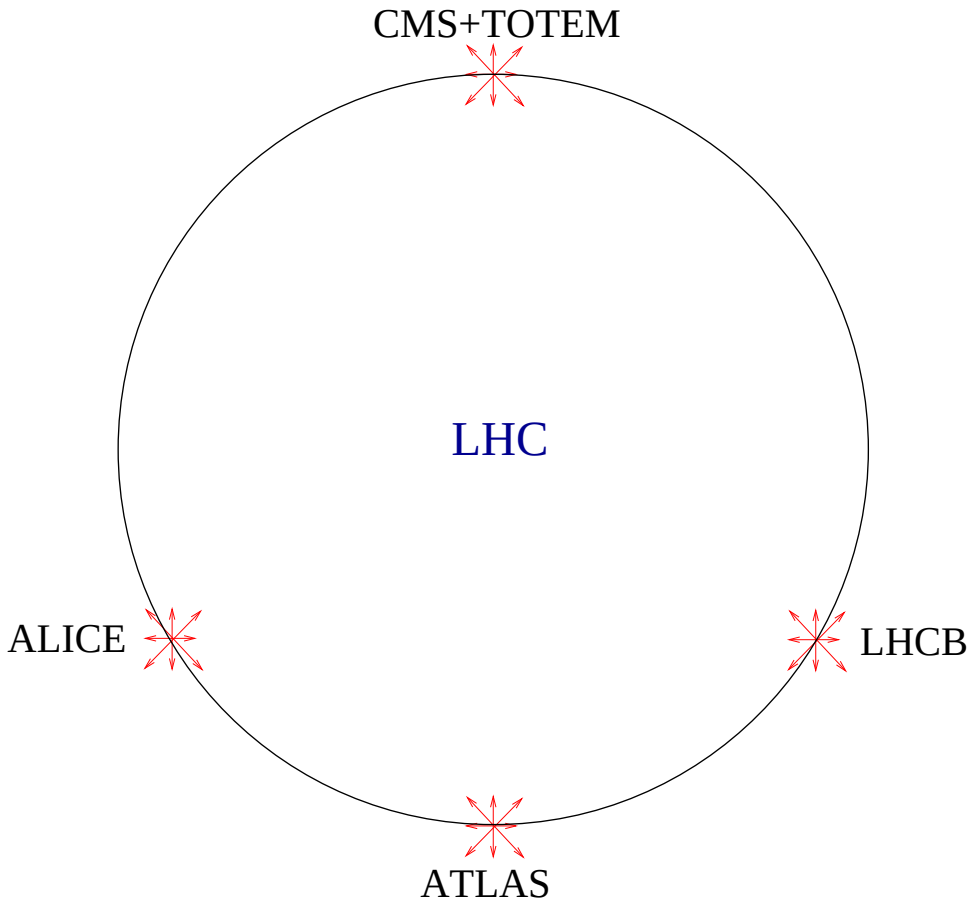

Figure 1.1: Location of the five experimental zones around the LHC ring.

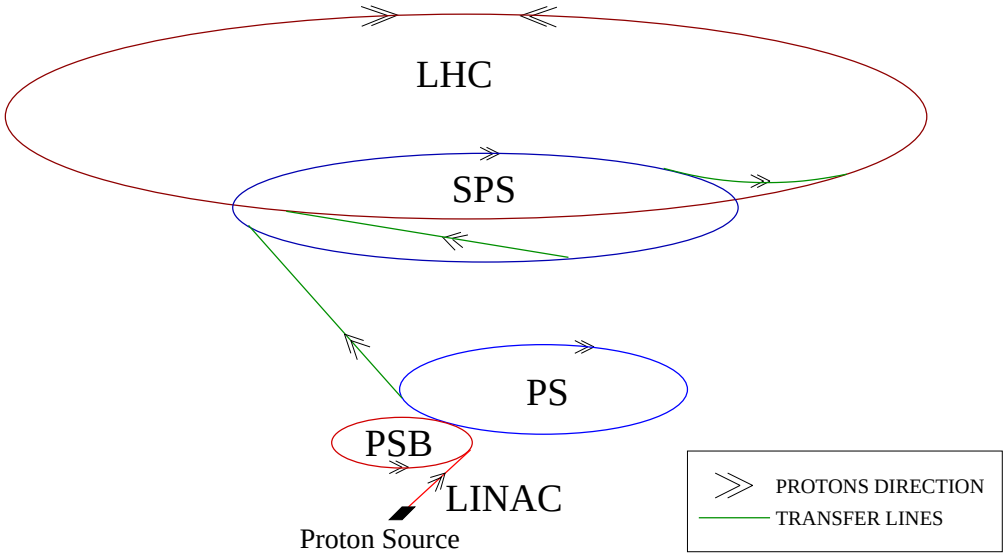

Figure 1.2: The LHC ring with the pre-accelerators chain.

Table 1.1: Different beam types accelerated in the SPS during the various phases of the LHC operation.

Name	I_b $[10^{10}\,p]$	N_b †	$\epsilon_{h,v}$ μm	Δ_{t_b} $[ns]$	LHC Phase
Pilot bunch	0.5	1	< 1	$\backslash$	Pilot
75 ns Beam	4	$1 - 4 \times 24$	2.5	75	Commissioning, early physics
25 ns Low Int	3	$1 - 4 \times 72$	2.5	25	Intermediate, early physics
TOTEM Beam	3	$1 - 4 \times 4$	< 1	525	Commissioning, zero crossing angle physics
Nominal Beam	11	$1 - 4 \times 72$	3.5	25	Nominal
Ultimate Beam	17	$1 - 4 \times 72$	3.5	25	Ultimate

† N_b = number of bunches. Except for the pilot bunch, the number of bunches are given as number of injected PS batches times the number of bunches per batch.

To minimize the losses, different *beam types* have been designed to accomplish the various phases of LHC operation. Here we specify them as done in the *LHC Design Report* [9, 10]: pilot beam, commissioning beam, intermediate beam, nominal beam and ultimate beam.
The *pilot* beam consists of a single bunch with $5 \cdot 10^9$ protons. It corresponds to the maximum number of charges which can be lost on a single superconductive magnet without causing a quench[1] [11].
The *commissioning* beam is designed for maximum luminosity with a limited beam current and small transverse dimensions. This allows some margins concerning the magnets quenches and the mechanical apertures.
The *intermediate* beam is adapted for high accuracy beam measurements with a reduced beam power (i.e. reduced beam intensity).
The *nominal* beam is conceived to reach the design luminosity with some operational margins for future enhancements in terms of beam intensity and collision performances.
The *ultimate* beam consists of the nominal number of bunches, with the nominal beam parameters, but with the ultimate number of particles per bunch (about $50\,\%$ higher than the nominal). This kind of beam is supposed to provide the largest luminosity and has no operational margins.
The first four beam types have been already set-up and measured in the pre-accelerators chain as discussed in Chapter 8, even though the different beams role and specification is still under discussion.
Table 1.1 summarizes the most significant features of the beams which have been accelerated until now in the SPS (the ultimate beam has not been accelerated yet). The last two columns indicate the probable role according to the LHC Design Report definitions and additional comments about their utilization.
The table also reports about the *TOTEM beam* parameters, a very low intensity beam designed to have collisions with zero crossing angle. This is reached with a bunch spacing larger than the 25 or $75\,ns$ used for the other beam types. With a larger distance between consecutive bunches, they interact very weakly with the colliding bunches of the other beam (*beam-beam effects*), and the crossing angle can be made very small. Due to the low intensity, it can be used as commissioning beam. It has been very much exploited during this thesis work to cross-calibrate different instruments, because its low emittance allows to study the monitors resolution and repeatability.

[1] A quench is the event during which the material crosses its critical temperature and looses the superconductive properties

1.3 LHC cycle in the SPS

Most of the work presented in this report is related to the protons transverse distribution measured during their injection and acceleration in the SPS. Fig. 1.3 shows the proton intensity in the SPS during the injection of four batches from the PS and the beam momentum evolution during the $21.6\,s$ cycle.
One PS batch is injected every $3.6\,s$. After the injection of the fourth batch the energy starts to increase until the top energy at $18.5\,s$. The cycle will be repeated twelve times for filling each of the two LHC rings.
The filling procedure will alternate three and four batches injections according to the sequence $334\,334\,334\,333$ for a total of 39 PS batches, each composed of 72 bunches. Hence, each LHC beam will be composed of 2808 bunches and it will take about 4.3 minutes to fill one ring.
Each PS batch is composed of 72 bunches spaced of $\Delta t_b = 25\,ns$ (nominal beam). We define the

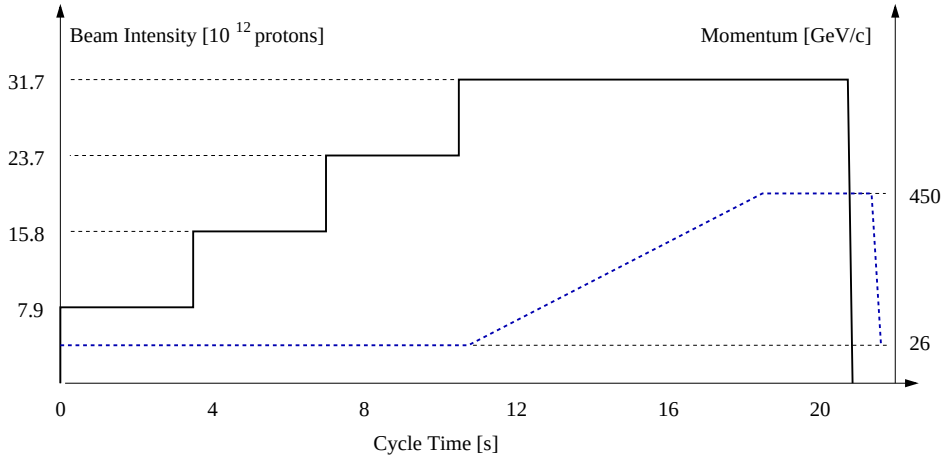

Figure 1.3: Schematic diagram of the beam intensity and momentum during the $21.6\,s$ cycle of the LHC beam in the SPS.

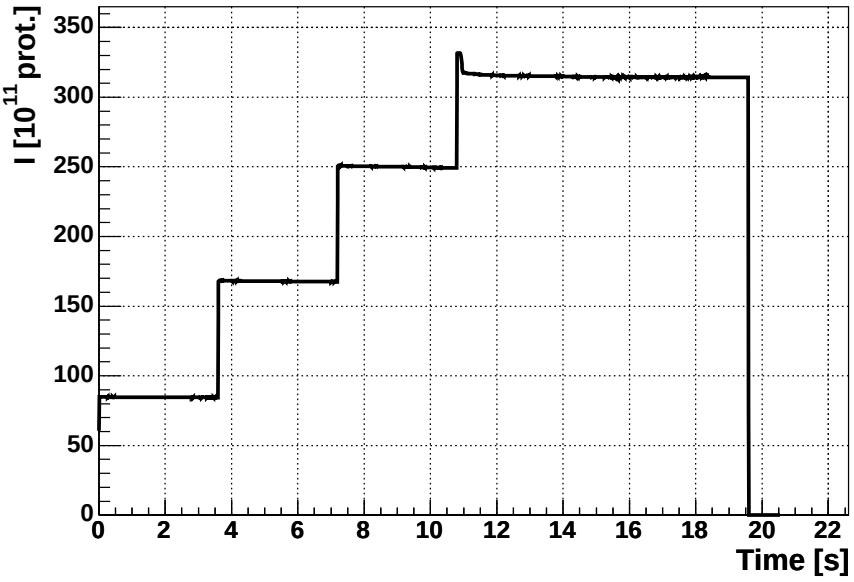

Figure 1.4: Signal of four batches injected in the SPS, as measured by a Beam Current Transformer monitor. In this case the beam was dumped before the end of the magnetic cycle.

bunch length as the standard deviation of the Gaussian distribution in the longitudinal plane. The bunch length τ_b is about $1\,ns$ at injection and decreases to about $0.38\,ns$ during acceleration.
The duration of one batch can be estimated as

$$t_B = (N_{bunches} - 1) * \Delta t_b + \tau_b \tag{1.1}$$

by summing the bunch spacings and half the bunch length of the first and last bunch. The four injections are synchronized in such a way to have $225\,ns$ between two batches. Hence the duration of four batches results about $7.1\,\mu s$.
Fig. 1.4 shows the measured intensity signal of four PS batches in the SPS as measured by a Beam Current Transformer (BCT). The signal is averaged over a period of $200\,ms$. Therefore, the measurement time resolution is not sufficient to distinguish single bunches.
The intensity drop after the injection of the fourth batch takes place at the beginning of the energy increase process. At this stage the strength of several elements of the accelerator is varied, with a consequent excitation of transverse and longitudinal beam oscillations which induce particles losses.

Chapter 2

Accelerator Physics Principles

This chapter introduces the concepts of beam guidance in an accelerator, presenting the main features of bending and focusing magnets. This is sufficient to develop the equations characterizing a linear approximation for the motion of the charged particles about the reference beam orbit.
From the beam linear dynamics in the transverse plane, it is possible to derive the beam transverse size and formulate the concept of transverse emittance. The description of the influence of the transverse emittance variation on the collision efficiency is followed by an overview of Coulomb scattering effects with respect to the beam emittance preservation.

2.1 Basics of a particle accelerator

This section gives an overview of the principles of operation of particle accelerators. Some general concepts can be applied to any accelerator design, but the description is intended to introduce circular accelerators.
The theoretical conception of an accelerator starts assuming a constant energy and a stable beam trajectory. The machine elements are chosen in such a way that the particles are guided along the ideal (reference) path, accelerated to the desired energy and strongly focused at the locations designed for collision.
The following definitions refer to the coordinate system shown in Fig. 2.1 in which the longitudinal direction *s* is defined as the one following the beam reference path, while *x* and *y* define the transverse plane (orthogonal to the particle trajectory) and describe the particle deviations from the reference path. Locally, the design trajectory (reference orbit) has a curvature radius ρ.
Such coordinate system moves following the reference path along sections which can be straight as well as curved and is therefore a curvilinear coordinate system. The trajectory of the reference particle is the one for which $x = 0$ and $y = 0$ for all s.
The scope of the accelerator design is the arrangement of the beam line elements with the aim of guiding the beam particles along the reference path and accelerate it to a desired energy. In practice it is not possible to keep all the particles on the same trajectory, the beam is populated by a number of particles performing small amplitude oscillations around the reference orbit.
The principal elements of particle accelerators are those that provide the beam guidance and focusing system. This is achieved by applying electromagnetic forces to the charged particles. Such forces are intended to accelerate, bend and direct the particles on the design trajectory, or to hold them close to it.
Lorentz law describes the force acting on a particle of charge e travelling in an electromagnetic field:

$$\overrightarrow{F} = e(\overrightarrow{E} + \overrightarrow{v} \times \overrightarrow{B}) \tag{2.1}$$

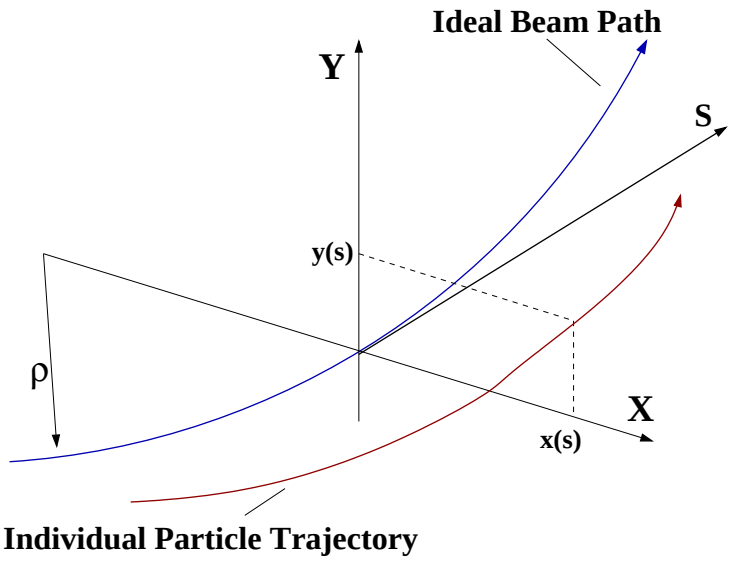

Figure 2.1: Coordinate system

where $\overrightarrow{E}$ and $\overrightarrow{B}$ are the electric and magnetic fields, and $\overrightarrow{v}$ the particle's velocity.
Longitudinal electric fields are used to accelerate the particles, while the transverse bending and focusing are guaranteed by transverse magnetic fields.
The most important kind of magnets used in accelerators to create the guiding fields are the dipole and quadrupole magnets. By design the magnetic field has a null component in the s direction, therefore it can be expressed as:

$$\begin{aligned} \overrightarrow{B} &= B_x \overrightarrow{i} + B_y \overrightarrow{j} \\ B_x &= B_x(0,0) + \frac{\partial B_x}{\partial x}x + \frac{\partial B_x}{\partial y}y \\ B_y &= B_y(0,0) + \frac{\partial B_y}{\partial x}x + \frac{\partial B_y}{\partial y}y \end{aligned} \tag{2.2}$$

where $\overrightarrow{i}$ and $\overrightarrow{j}$ are the unit vectors defining the transverse plane and the field components have been expanded to the first order terms.
Dipole magnets provide a constant field B_y in the magnet gap. The instantaneous radius of curvature ρ for a particle with momentum p, travelling in the horizontal plane, comes from the equilibrium between the centrifugal and the centripetal Lorentz forces:

$$\rho = \frac{p}{eB_y} \tag{2.3}$$

Fig. 2.2 shows the cross section of a quadrupole magnet and the force applied to a particle passing at different locations in the magnet. A particle passing through the center of the quadrupole does not experience any force, the particle bending rises linearly with the distance from the center. Maxwell equation $\overrightarrow{\nabla} \times \overrightarrow{B} = 0$ always imposes

$$\frac{\partial B_x}{\partial y} = \frac{\partial B_y}{\partial x} \tag{2.4}$$

and due to the field pattern the Lorentz force is always focusing in one coordinate and defocusing in the other. Consequently quadrupoles with opposite polarities, alternated in an accelerator system, provide focusing in the two transverse directions. The most common structure consists in

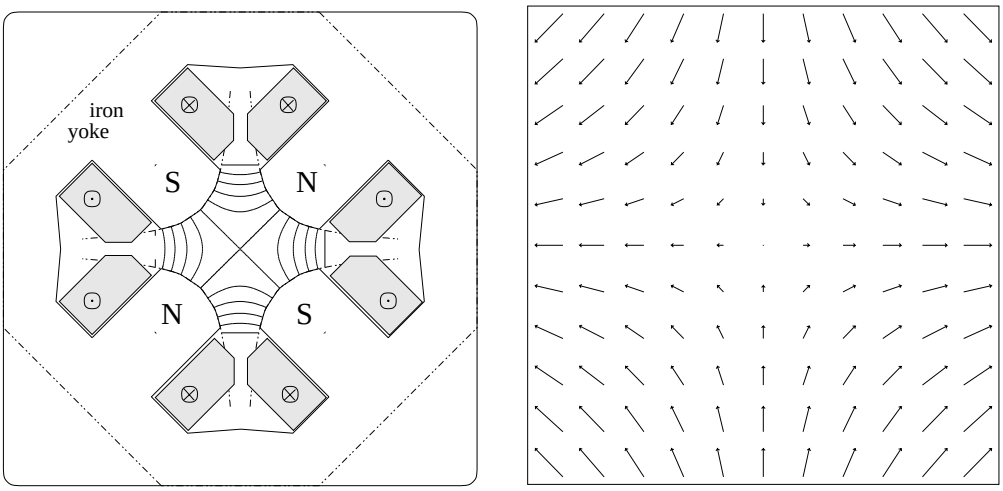

Figure 2.2: Cross section of a quadrupole magnet with indicated the magnetic field lines and Lorentz forces in vectorial representation. The force felt by a particle is increasing with the distance from the magnet center.

the repetition of identical units called FODO cells. Each cell contains a horizontal focusing (F) quadrupole, a drift space (O), a horizontal defocusing (D) quadrupole and another drift space. The dipole magnets designed for the bending are inserted in between the quadrupoles.
Since they use quadrupoles, FODO cells are also defined as *strong focusing* structures: the restoring forces are as high as possible, but the magnetic elements cannot focus in the two planes at the same time. However simple considerations, involving geometrical optics, guarantee that if the drift spaces between quadrupoles are small compared to the magnets focal lengths, each FODO cell produces a net focusing in both planes.
Higher order multipole magnets are also normally included in FODO cells. They are intended to correct beam perturbations which can be characterized only going beyond the approximation of transverse linear motion, that will be treated in the next section. Higher order field multipoles will not be considered in this thesis.

2.2 Transverse linear motion

This section describes the transverse motion of the accelerated charged particles in a first order (linear) approximation. An additional assumption is the absence of coupling of the two transverse planes: the motion in the horizontal plane is not affected by the one in the vertical. A complete treatment of the subject is covered in [12].
As aforementioned, the accelerator magnetic elements are designed to guide and focus the beam along the reference circular orbit. However, particles which at the time t_0 have non zero transverse coordinates (x_0, y_0) and slopes (x'_0, y'_0) start to perform oscillations in the horizontal (bending) and vertical planes around the reference orbit. Such oscillations are called *Betatron Oscillations* for historical reasons and depend on the magnetic fields applied in the ring.
The equation of motion derives from Lorentz law and reads:

$$\frac{d\overrightarrow{p}}{dt} = e\overrightarrow{v} \times \overrightarrow{B} \tag{2.5}$$

The motion is referred to the coordinate system of Fig. 2.1. The magnetic field $\overrightarrow{B}$ can be defined and expanded as in Eq. (2.2) with horizontal (B_x) and vertical (B_y) components, while as a first

approximation the field component along the curvilinear coordinate s is null.
Developing the vector product of Eq. (2.5), leads to the expression of the motion in the two transverse directions:

$$x'' + \left[\frac{1}{\rho^2(s)} + \frac{1}{(B\rho)}\frac{\partial B_y(s)}{\partial x}\right] x = 0 \tag{2.6}$$

$$y'' - \frac{1}{(B\rho)}\frac{\partial B_y(s)}{\partial x} y = 0 \tag{2.7}$$

$(B\rho)$ is equal to the ratio of momentum to charge p/e and is called *magnetic rigidity*. The two equations differ for the term $1/\rho^2(s)$ which is related to the centripetal force in the radial direction.
The gradient terms result equal due to the curl condition of Eq. (2.4) and its meaning can be explained as follows.
Considering a particle passing through a magnetic field with gradient $B' = \partial B_y/\partial x$ over a distance Δs, the slope of the particle's trajectory (in a circular machine with radius ρ) $x' = dx/ds$ changes by an amount such that:

$$\frac{\Delta x'}{\Delta s} = -\frac{B'(s)}{B\rho} x. \tag{2.8}$$

In fact, with the limit $\Delta s \to 0$, the previous equation becomes a second order differential equation:

$$x'' + \frac{B'(s)}{B\rho} x = 0. \tag{2.9}$$

which perfectly reproduces the equation of motion in the vertical direction and the one in the horizontal direction without the centripetal term.
The gradient term depends on the momentum and is also defined as the *normalized quadrupole strength*

$$k(s) = \frac{1}{(B\rho)}\frac{\partial B_y(s)}{\partial x} = \frac{e}{p}\frac{\partial B_y(s)}{\partial x}. \tag{2.10}$$

Eq. (2.6) and Eq. (2.7) can both be written according to the form:

$$x'' + K(s)x = 0 \tag{2.11}$$

$$y'' + K(s)y = 0 \tag{2.12}$$

in which $K(s) = 1/\rho^2(s) + k(s)$ and $K(s) = -k(s)$ respectively. The following considerations will apply to both directions.
The obtained second order differential equation resembles the one of a harmonic oscillator, with the only difference of having the "spring constant" K that depends on the variable s. Within each component of the accelerator, K can be considered constant, and therefore the harmonic oscillator solutions can be used to describe the particle motion through each single component. The solutions can be divided in three cases which depend on the value of K. For $K = 0$ the evolution of $x(s)$ and $x'(s)$ along an element of length L can be written in matrix formalism

$$\begin{bmatrix} x(s) \\ x'(s) \end{bmatrix}_f = \begin{bmatrix} 1 & L \\ 0 & 1 \end{bmatrix} \begin{bmatrix} x(s) \\ x'(s) \end{bmatrix}_i \tag{2.13}$$

and reflects a passage of the particle through a drift space of length L. For $K > 0$

$$\begin{bmatrix} x(s) \\ x'(s) \end{bmatrix}_f = \begin{bmatrix} \cos(\sqrt{K}L) & \frac{1}{\sqrt{K}}\sin(\sqrt{K}L) \\ -\sqrt{K}\sin(\sqrt{K}L) & \cos(\sqrt{K}L) \end{bmatrix} \begin{bmatrix} x(s) \\ x'(s) \end{bmatrix}_i \tag{2.14}$$

while for $K < 0$ the solution is

$$\begin{bmatrix} x(s) \\ x'(s) \end{bmatrix}_f = \begin{bmatrix} \cosh(\sqrt{|K|}L) & \frac{1}{\sqrt{K}}\sinh(\sqrt{|K|}L) \\ \sqrt{|K|}\sinh(\sqrt{|K|}L) & \cosh(\sqrt{|K|}L) \end{bmatrix} \begin{bmatrix} x(s) \\ x'(s) \end{bmatrix}_i \tag{2.15}$$

Every accelerator component has its characteristic matrix M_j and the transport of a particle through N elements is described by a matrix $M = M_N \cdot M_{N-1} \cdot \ldots M_1$. When M represents the transport along one accelerator turn, M^n describes the particle motion after n revolutions. For a stable motion of a particle with initial conditions x_0 and x'_0 the quantity

$$M^n \begin{bmatrix} x_0 \\ x'_0 \end{bmatrix} \tag{2.16}$$

must remain finite for an arbitrary large value of n.
It can be proved, by calculating the matrix eigenvalues, that the stability condition results

$$-2 < \mathrm{Trace(M)} < 2. \tag{2.17}$$

Considering a FODO cell, the elements of M, depending of the values of $K(s)$, reflect the bending and focusing strengths and the stability criteria requires

$$\left| \frac{d}{2f} \right| \leq 1 \tag{2.18}$$

where d is the distance between a focusing and a defocusing magnet, both with focal length f.
A more rigorous solution of the equation of motion can be deduced observing that Eq. (2.11) has the form of Hill's equation which has been extensively studied during the nineteenth century. For K everywhere a positive constant the solution would become the one of a harmonic oscillator which can now be expressed as

$$x = A\cos(\Psi(s) + \Psi_0) \tag{2.19}$$

with $\Psi(s) = \sqrt{K}s$ and A, Ψ_0 the constants of integration.
For all circular accelerators, the function $K(s)$ is periodic,

$$K(s + C) = K(s). \tag{2.20}$$

The period C can coincide with the accelerator circumference, but normally it corresponds to the distance between two FODO cells. The general solution of the equation is

$$x(s) = Aw(s)\cos(\Psi(s) + \Psi_0) \tag{2.21}$$

A and Ψ_0 being the two constants of integration that depend on the initial conditions, and $w(s)$ a periodic function with periodicity C. The motion has a spatially varying amplitude, and a phase which does not change linearly with s.
By substituting the general solution Eq. (2.21) in Eq. (2.11), we get (see Appendix A.1.1):

$$\begin{aligned} &[w"(s)w(s)\Psi'^2(s) + K(s)w(s)]\cos(\Psi(s) + \Psi_0) + \\ &\quad -[2w'(s)\Psi'(w) + w(s)\Psi"(s)]\sin(\Psi(s) + \Psi_0) \;\; = \;\; 0 \end{aligned} \tag{2.22}$$

$w(s)$ and $\Psi(s)$ must not vary with Ψ_0, in order to be independent from a particular motion. To accomplish this condition, the sine and cosine coefficients have to individually vanish. By multiplying the sine coefficient by $w(s)$ and equal it to zero, follows:

$$2w(s)w'(s)\Psi'(w) + w^2(s)\Psi"(s) = [w^2(s)\Psi'(s)]' = 0 \tag{2.23}$$

which can be written as

$$\frac{\partial\Psi(s)}{\partial s} = \Psi' = \frac{k}{w^2(s)} \tag{2.24}$$

Here, k is a constant of integration.
Eq. (2.21) can also be written as

$$x(s) = w(s)(A_1\cos\Psi + A_2\sin\Psi) \tag{2.25}$$

which results in

$$x'(s) = \left(A_1 w' + \frac{A_2 k}{w}\right)\cos\Psi + \left(A_2 w' - \frac{A_1 k}{w}\right)\sin\Psi. \tag{2.26}$$

The constants A_1 and A_2 can be determined by imposing some initial conditions x_0 and x_0',

$$A_1 = \frac{x_0}{w} \tag{2.27}$$

$$A_2 = \frac{x_0' w - x_0 w'}{k}. \tag{2.28}$$

Recalling that $w(s)$ is periodic with period C, the transport from s_0 to $s_0 + C$ is

$$\begin{bmatrix} x(s_0+C) \\ x'(s_0+C) \end{bmatrix} \begin{bmatrix} \cos\Delta\Psi_C - \frac{ww'}{k}\sin\Delta\Psi_C & \frac{w^2}{k}\sin\Delta\Psi_C \\ -\frac{1+(ww'/k)^2}{w^2/k}\sin\Delta\Psi_C & \cos\Delta\Psi_C + \frac{ww'}{k}\sin\Delta\Psi_C \end{bmatrix} \begin{bmatrix} x(s_0) \\ x'(s_0) \end{bmatrix} \tag{2.29}$$

in which

$$\Delta\Psi_C = \Psi(s) - \Psi_0 = \Psi(s_0 \to s_0 + C) = \int_{s_0}^{s_0+C} \frac{k\,ds}{w^2(s)} \tag{2.30}$$

is the phase advance along one period C.
In the matrix above, the function $w^2(s)$ and its derivative, scale with the constant of integration k. A new set of variables is commonly defined:

$$\beta(s) \equiv \frac{w^2(s)}{k} \tag{2.31}$$

$$\alpha(s) \equiv -\frac{1}{2}\frac{d\beta(s)}{ds} \tag{2.32}$$

$$\gamma(s) \equiv \frac{1+\alpha^2(s)}{\beta(s)}. \tag{2.33}$$

α, β and γ are called *Courant-Snyder parameters*. With this new parametrization Eq. (2.29) yields

$$\begin{bmatrix} x(s_0+C) \\ x'(s_0+C) \end{bmatrix} = \begin{bmatrix} \cos\Delta\Psi_C + \alpha\sin\Delta\Psi_C & \beta\sin\Delta\Psi_C \\ -\gamma\sin\Delta\Psi_C & \cos\Delta\Psi_C - \alpha\sin\Delta\Psi_C \end{bmatrix} \begin{bmatrix} x(s_0) \\ x'(s_0) \end{bmatrix} \tag{2.34}$$

with the one turn phase advance equal to

$$\Delta\Psi_C = \int_{s_0}^{s_0+C} \frac{d\overline{s}}{\beta(\overline{s})} + \Psi_0, \tag{2.35}$$

Referring to the new variables the general solution of the equation of motion is written as

$$x(s) = A\sqrt{\beta(s)}\cos[\Psi(s) + \Psi_0], \tag{2.36}$$

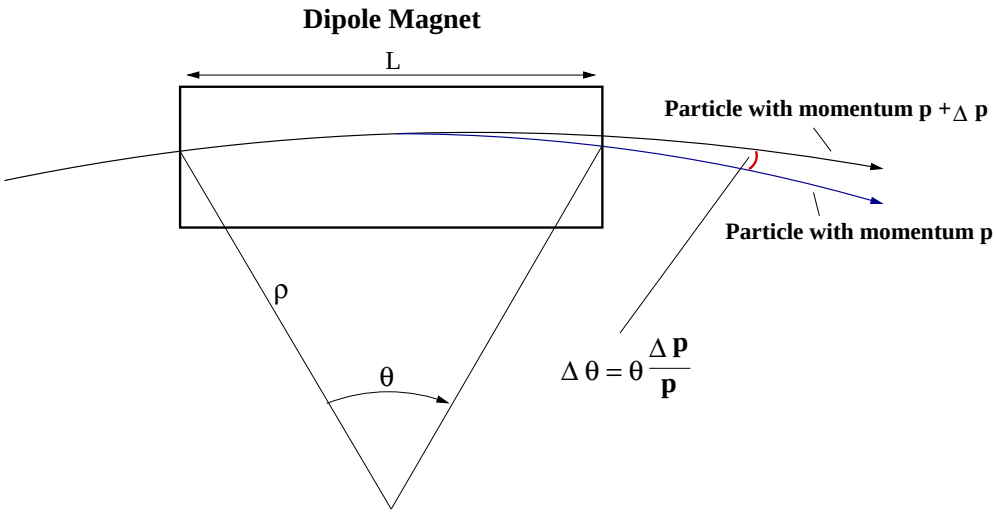

Figure 2.3: Two particles with different momenta undergo different bending angles while passing through a dipole magnet.

where the constant k has been absorbed in the constant A. $\beta(s)$, a periodic function with periodicity C, is called *betatron amplitude* or *betatron function*. The betatron function may be interpreted as the local wavelength of the betatron oscillations divided by 2π. Eq. (2.35) allows the calculation of the phase advance between two points, which is uniquely defined by

$$\Delta\Psi(s_1 \rightarrow s_2) = \int_{s_1}^{s_2} \frac{ds}{\beta(s)}. \tag{2.37}$$

It also allows the computation of the number of betatron oscillations performed by a particle for each turn in a circular machine, the so called *tune* of the accelerator:

$$\nu \equiv \frac{1}{2\pi} \oint \frac{ds}{\beta(s)}. \tag{2.38}$$

Summarizing the obtained results, if the trajectory of the reference particle is the one ideally passing through the center of all the quadrupoles installed in the accelerator, Eq. (2.36) describes the motion of particles whose position and direction differ from it. The particles perform each turn ν betatron oscillations around the reference orbit with local amplitudes proportional to $\sqrt{\beta(s)}$.
In an accelerator structure, the motion can be reconstructed knowing the evolution of the Courant-Snyder parameters and of the phase advance along the coordinate s.

2.2.1 Off-momentum particles motion

So far we have considered only particles travelling with the reference momentum p. In a bending magnet of length L and field B, as illustrated in Fig. 2.3, the deflection θ of a particle with momentum p is governed by

$$p = eB\rho = eB\frac{L}{\theta}. \tag{2.39}$$

It follows that, for a particle with a momentum offset Δp,

$$\Delta\theta = -eBL\frac{\Delta p}{p^2} \quad \Longrightarrow \quad \frac{\Delta\theta}{\theta} = -\frac{\Delta p}{p}. \tag{2.40}$$

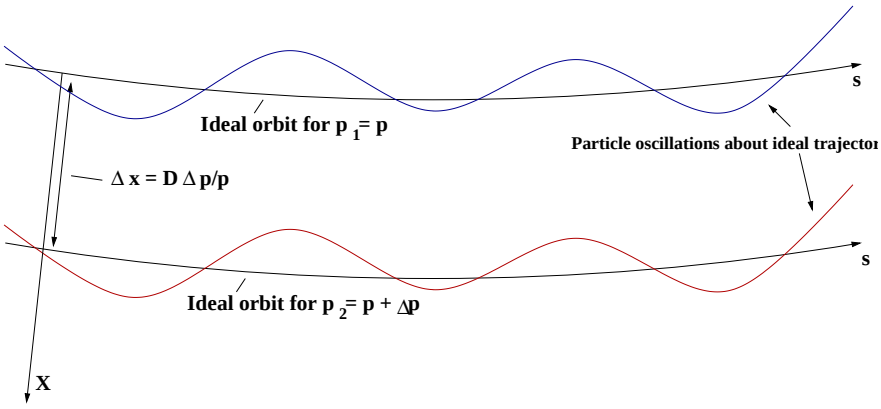

Figure 2.4: Off-momentum particles start to oscillate about new class of orbits.

A particle of higher momentum is less deflected in the magnet. Under these circumstances Eq. (2.6) must be re-written as

$$x'' + \left[\frac{1}{\rho^2(s)} + \frac{1}{(B\rho)}\frac{\partial B_y(s)}{\partial x}\right] x = \frac{1}{\rho(s)}\frac{\Delta p}{p} \tag{2.41}$$

which is an inhomogeneous Hill equation. A particular solution can be expressed as:

$$x(s) = D(s)\frac{\Delta p}{p}. \tag{2.42}$$

in which $D(s)$ is the *dispersion function* which is introduced to characterize the shift of the reference orbit of an off-momentum particle. Therefore the general solution of the complete Hill equation is the sum of a particular solution of this equation and the solution of the homogeneous one. Following these considerations the equations of motion in the two transverse planes can be expressed as:

$$x(s) = A\sqrt{\beta_x(s)}\cos[\Psi_x(s) + \Psi_{x0}] + D_x(s)\frac{dp}{p} = x_\beta + x_D \tag{2.43}$$

$$y(s) = A\sqrt{\beta_y(s)}\cos[\Psi_y(s) + \Psi_{y0}] + D_y(s)\frac{dp}{p} = y_\beta + y_D \tag{2.44}$$

where x_β represents the free oscillations about a closed orbit in the bending plane and x_D the offset of such orbit due to the off-momentum particles.
The off-momentum particles start to oscillate about a new class of orbits (the so called *chromatic closed orbit*) as depicted in Fig. 2.4.
When bending occurs only in the horizontal plane, the dispersion function is small in the vertical plane and comes only from imperfections in the magnetic field and in the magnets alignment. The vertical dispersion is not negligible only in particular cases, such as inclined transverse lines or beam crossing schemes in the collision regions [13].

2.3 Transverse Emittance

This section is dedicated to characterize the distribution of the ensemble of particles in the transverse planes. The particles distribution is generally described by a density function in a six dimension space,

$$\psi = \phi(x, p_x, y, p_y, s, E) \tag{2.45}$$

in which x, y, s again represent the variables that define the coordinate system illustrated in Fig. 2.1. If $p = Ev/c^2$ is the particle momentum, $p_x \approx px'$ and $p_y \approx py'$ are the components of the momentum vector in such coordinates. E is the particle energy, and often the energy deviation from the ideal particle energy $\Delta E = E - E_0$ or the relative energy deviation $\Delta E/E_0$ are taken as sixth degree of freedom in Eq. (2.45). For systems at constant energy, the transverse momenta are generally replaced by the slope of the trajectories x' and y'.
Transverse linear dynamics neglects the coupling between the two transverse planes and between each transverse plane and the longitudinal one. In this case the six dimensional space can be factorized into three independent subspaces (x, x'), (y, y') and (s, E), that are often called *trace spaces*, even if in the following they will be referred as phase spaces. The notions that will be figured out for the horizontal plane (x, x') apply also to the vertical (y, y').

Recalling the general solution of the equation of motion for particles with zero momentum offset (see Eq. (2.36)) together with the definition of the Courant-Snyder parameters and defining $\theta(s) \equiv \Psi(s) + \Psi_0$, we can write:

$$x(s) = A\sqrt{\beta(s)}\cos\theta(s) \tag{2.46}$$

$$\begin{aligned} x'(s) = \frac{dx(s)}{ds} &= -\frac{A}{\sqrt{\beta(s)}}\sin\theta(s) + A\cos\theta(s)\frac{1}{2\sqrt{\beta(s)}}\frac{d\beta(s)}{ds} = \\ &= -\frac{A}{\sqrt{\beta(s)}}[\sin\theta(s) + \alpha(s)\cos\theta(s)]. \end{aligned} \tag{2.47}$$

From these equations, it is interesting to introduce $x(s)$ and $x'(s)$ in the following polynomial expression

$$\begin{aligned} & \gamma x^2 + 2\alpha x x' + \beta x'^2 = \\ = \; & A^2\gamma\beta\cos^2\theta - 2A^2\alpha[\sin\theta\cos\theta + \alpha\cos^2\theta] + \\ & + A^2[\sin^2\theta + \alpha^2\cos^2\theta + 2\alpha\sin\theta\cos\theta] = \\ = \; & A^2[\cos^2\theta(\gamma\beta - \alpha^2) + \sin\theta\cos\theta(2\alpha - 2\alpha) + \sin^2\theta] = \\ = \; & A^2 \end{aligned} \tag{2.48}$$

in which all the variables x, x', α, β, γ and θ are functions of s although not indicated for simplicity. The quantity $\gamma x^2 + 2\alpha x x' + \beta x'^2$ is constant along a particular particle trajectory and is referred to as *Courant-Snyder invariant*.
Considering now a particular location s_0 of a circular accelerator, a particle with initial position $x(s_0)$

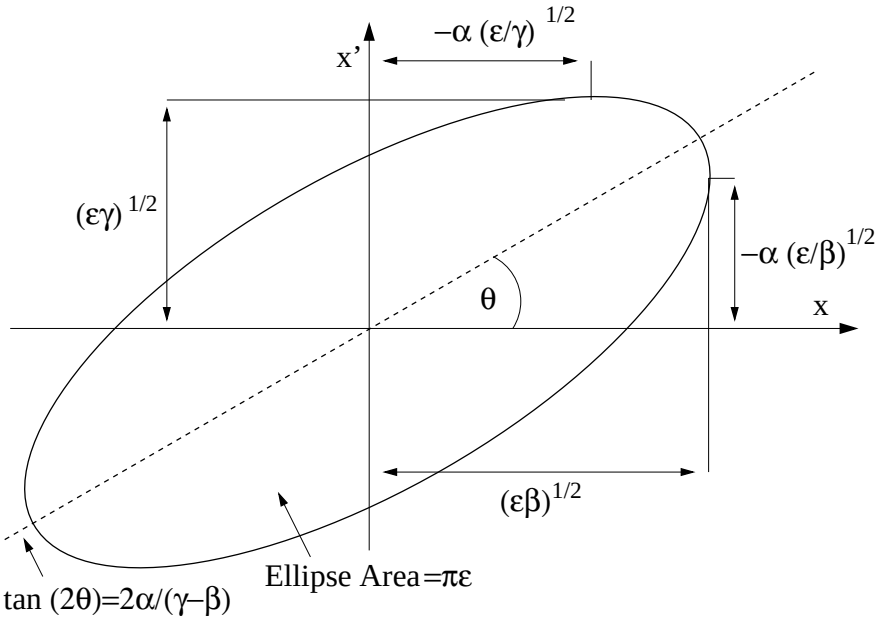

Figure 2.5: The motion of a single particle, at a longitudinal location s, maps an ellipse in the phase space relative to one transverse degree of freedom. The ellipse is characterized by the Courant-Snyder parameters $\alpha(s)$, $\beta(s)$ and $\gamma(s)$.

and $x'(s_0)$, after n turns will be characterized by (using the definition of tune ν given in Eq. (2.38)):

$$\begin{aligned} x_n(s_0) &= x(s_0+nC) = A\sqrt{\beta(s_0)}\cos[\Psi(s_0+nc)+\Psi_0] = \\ &= A\sqrt{\beta(s_0)}\cos[2\pi n\nu+\Psi(s_0)+\Psi_0] = \\ &= A\sqrt{\beta(s_0)}\cos[\Psi(n)] \qquad (2.49) \\ x'_n(s_0) &= x(s_0+nC) = \\ &= -\frac{A}{\sqrt{\beta(s_0)}}\{\alpha(s_0)\cos[\Psi(n)]+\sin[\Psi(n)]\} \qquad (2.50) \\ &\quad \text{with } \Psi(n) = 2\pi n\nu + \text{constant}. \end{aligned}$$

At the location s_0 the Courant-Snyder invariant will be:

$$\gamma(s_0)x_n^2(s_0) + 2\alpha(s_0)x_n(s_0)x'_n(s_0) + \beta(s_0)x'^2_n(s_0) = A^2. \qquad (2.51)$$

The two dimensional space formed by $x_n(s_0)$ and $x'_n(s_0)$ is called *phase space* and the equation expressing the Courant-Snyder invariant is the equation of an ellipse in this phase space. From turn to turn, the phase space points $x_n(s_0), x'_n(s_0)$ map out the ellipse.
A^2 is referred as the *emittance* of a single particle following its individual trajectory,

$$\epsilon = A^2 = \frac{\text{Ellipse area}}{\pi} \qquad (2.52)$$

The parameters of the ellipse are determined by the lattice functions α, β and γ at the location s_0, and by the emittance ϵ, as depicted in Fig. 2.5. The ellipse in phase space may assume different orientations in different locations around the ring, but the ellipse area (i.e. the particle emittance) remains constant.

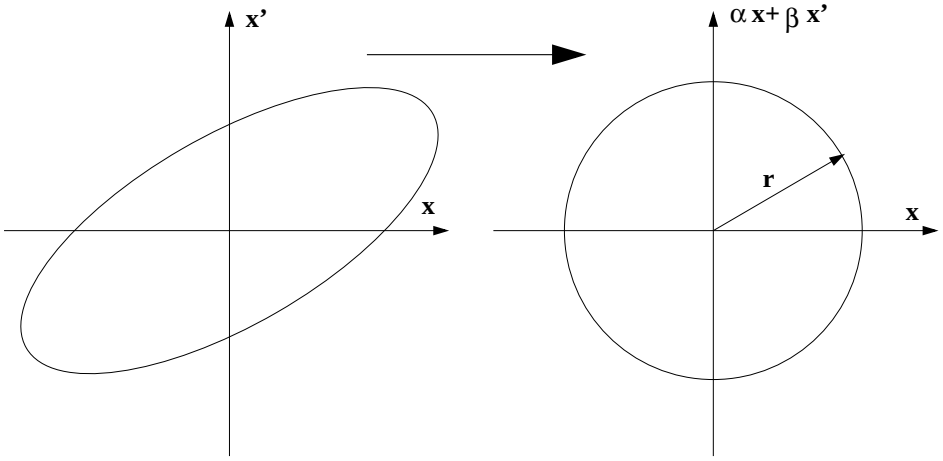

Figure 2.6: Normalized coordinates in phase space: everywhere along the ring the emittance contour becomes a circle of radius $r = \sqrt{\beta}\, A$.

2.3.1 Courant-Snyder invariant in normalized phase space

Sometimes it is useful to apply a change of coordinates in phase space from (x, x') to $(x, \alpha x + \beta x') \equiv (x, z)$, as depicted in Fig. 2.6. In this new coordinate system, which is often named *normalized*, the ellipse in phase space becomes a circle, and in polar coordinates the radial variable is $r^2 = x^2 + z^2 = x^2 + (\alpha x + \beta x')^2$. The Courant-Snyder invariant $\gamma x^2 + 2\alpha x x' + \beta x'^2 = A^2$, becomes (see Appendix A.2)

$$\frac{x^2}{\beta} + \frac{z^2}{\beta} = \frac{r^2}{\beta} = A^2 \tag{2.53}$$

2.3.2 Beam emittance

So far only the motion of single particles has been considered. Now the transverse linear dynamics of the ensemble of particles populating the beam is discussed.
Considering the particles centered around the reference orbit, for any distribution of the particles, it is possible to define a region in phase space occupied by the particles.
It is convenient to change the coordinates system to two axis X, X' centered on the distribution barycenter and orientated in order to minimize the sum of the square distances of each point from each axis. Such coordinate system is showed in Fig. 2.7. If θ is the rotation angle of X with respect to x, the distance of the point $\mathrm{P}(x_i, x_i')$ from the axis X is

$$d_i = |x_i' \cos\theta - x_i \sin\theta| \tag{2.54}$$

Minimizing the distance d defines the rotation angle θ:

$$\frac{d}{d\theta}\left(\frac{1}{N}\sum_{i=1}^{N} d_i^2\right) = \frac{d}{d\theta}\sigma_X^2 = 0. \tag{2.55}$$

This results in

$$tan2\theta = \frac{2\overline{xx'}}{\overline{x^2} - \overline{x'^2}} \tag{2.56}$$

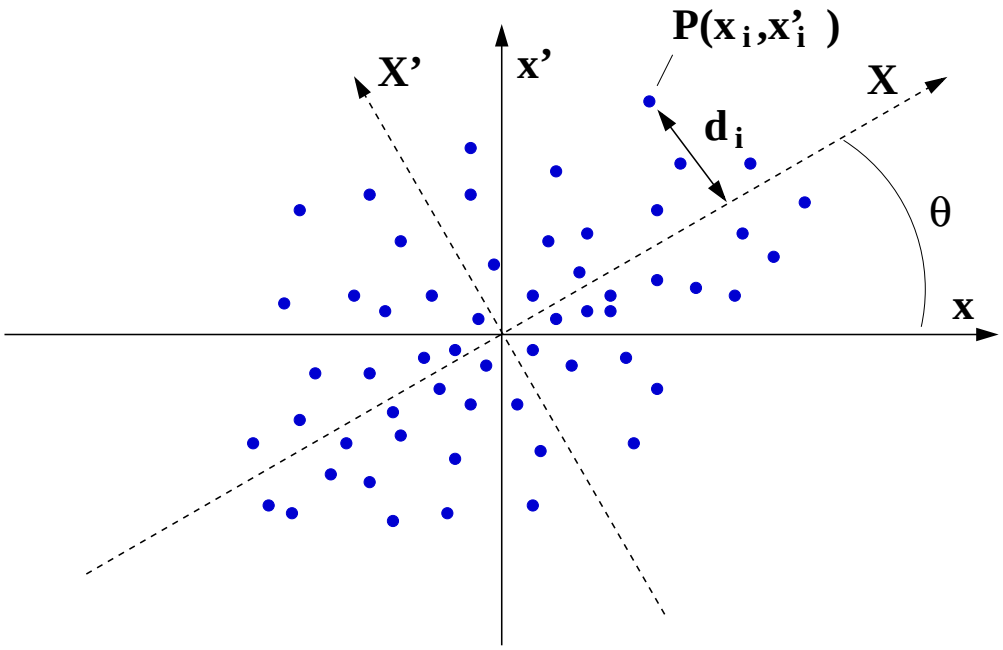

Figure 2.7: Particles distribution in phase space. The Cartesian axes X, X' are chosen in order to minimize the sum of the square distances between the points and the axis X.

where

$$\overline{x^2} = \frac{1}{N}\sum_{i=1}^{N} x_i^2 \tag{2.57}$$

$$\overline{x'^2} = \frac{1}{N}\sum_{i=1}^{N} x_i'^2 \tag{2.58}$$

$$\overline{xx'} = \frac{1}{N}\sum_{i=1}^{N} x_i x_i' \tag{2.59}$$

are the central second-order moments of the distribution, being $\overline{x} = \overline{x'} = 0$. The value of θ also defines the orientation of X' to $\theta + 90°$. Referring to the new artesian system, the variances of the particles distances from X and X' result

$$\sigma_X^2 = \frac{1}{2}\left(\overline{x^2} + \overline{x'^2} + \frac{2\overline{xx'}}{\sin 2\theta}\right) \tag{2.60}$$

$$\sigma_{X'}^2 = \frac{1}{2}\left(\overline{x^2} + \overline{x'^2} - \frac{2\overline{xx'}}{\sin 2\theta}\right). \tag{2.61}$$

The variances of the particles distribution in phase space can be assigned as semi-axes of the *beam envelope ellipse*. The equation of such ellipse is

$$\frac{X^2}{\sigma_X^2} + \frac{X'^2}{\sigma_{X'}^2} = 1 \tag{2.62}$$

and its area results $A = \pi\sigma_X\sigma_X'$. Hence it is possible to define the *beam emittance* or *r.m.s. emittance* as the area of this ellipse divided by π,

$$\epsilon_{rms} = \frac{A}{\pi} = \sigma_X\sigma_{X'}. \tag{2.63}$$

By a rotation of $-\theta$, the ellipse can be expressed with respect to the axes x, x' [14]

$$x^2\sigma_{x'}^2 - 2xx'r\sigma_x\sigma_{x'} + x'^2\sigma_x^2 = \sigma_x^2\sigma_{x'}^2 \tag{2.64}$$

where σ_x and $\sigma_{x'}$ are the standard deviations and $r = \overline{xx'}/\sqrt{\overline{x^2x'^2}}$ is the correlation coefficient. Using the parametrization

$$\sigma_x = \sqrt{\beta\epsilon_{rms}} \tag{2.65}$$
$$\sigma_{x'} = \sqrt{\gamma\epsilon_{rms}} \tag{2.66}$$
$$4r\sigma_x\sigma_{x'} = -\alpha\epsilon_{rms} \tag{2.67}$$

and evoking Eq. (2.63), Eq. (2.64) becomes

$$\gamma x^2 + 2\alpha xx' + \beta x'^2 = \epsilon_{rms} \tag{2.68}$$

which again reproduces the Courant-Snyder invariant. This result explains the concept of beam emittance, as the area of the ellipse with contour defined by the particles' dispersion in phase space. According to this definition, from the variance with respect to x, one can directly calculate the beam emittance

$$\epsilon_{rms} = \frac{\sigma_x^2}{\beta} \tag{2.69}$$

where, as already seen, β is the betatron function at the location s. Along the ring, in order to respect the Courant-Snyder invariant, β and σ_x vary in order to keep the emittance constant.
This remarkable outcome can also be explained by stating that [14]

"in a linear lattice, the envelope ellipse at a position s_1 is mapped into the envelope ellipse of the new particle distribution at another position s_2. Moreover, any ellipse homothetic to the envelope ellipse is mapped into an ellipse homothetic to the new envelope ellipse."

In case of a Gaussian distribution, the standard deviation of the distribution coincides with the Gaussian width σ. Even if the particle distributions inside the bunch can be far from being Gaussian at the particles source, after acceleration to collision energies the normal function is a very good approximation, due to the central limit theorem of probability and the diminished importance of space charge effects[1].
From now on, only Gaussian beams will be considered, with their RMS emittance expressed as

$$\epsilon = \frac{\sigma_x^2}{\beta} \tag{2.70}$$

σ_x is also called *beam size*.
This definition of beam emittance relies on the contour ellipse drawn at one σ_x and one $\sigma_{x'}$ of the distribution in phase space. It can be proven that this corresponds to the ellipse containing $39\,\%$ of the particles populating the distribution. However this definition is not the only one used to represent the particles transverse distribution. Table 2.1 is taken from [12] and resumes the fraction F of a Gaussian beam associated with various definitions of emittance. Note that the first formalization (the one adopted in this thesis) differs from all the others for neglecting the factor π.

[1] Beam dynamics related to space charge effects are not treated in this thesis. The subject can be found for instance in [15]

ϵ	$F(\%)$
σ^2/β	15
$\pi\sigma^2/\beta$	39
$4\pi\sigma^2/\beta$	87
$6\pi\sigma^2/\beta$	95

Table 2.1: Fraction F of particles in a Gaussian beam, associated with different definitions of emittance

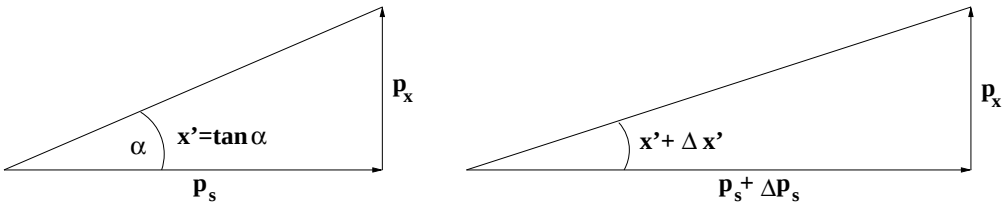

Figure 2.8: Longitudinal momentum increase during acceleration. The transverse momenta remain unchanged.

2.3.3 Beam size for off-momentum particles

So far we have considered only beams without momentum dispersion.
In order to treat also off-momentum particles, keeping the same emittance definition, we have to add a momentum dispersion contribution to the beam size σ.
The beam size results from the sum of the two statistical independent contributions of Eq. (2.43),

$$\sigma^2 = \sigma_\beta^2 + \sigma_D^2 = \beta\epsilon + \left[D\frac{\Delta p}{p}\right]^2. \tag{2.71}$$

The first term is depending on the emittance and the second reflects the beam enlargement due to momentum dispersion.
To recover the beam emittance from the measurement of the beam size with a profile monitor, one has to subtract the momentum dispersion contribution:

$$\epsilon = \frac{1}{\beta}\left[\sigma^2 - \left(D\frac{\Delta p}{p}\right)^2\right] \tag{2.72}$$

2.3.4 Adiabatic damping

This paragraph discusses the emittance variation during acceleration.
The divergence of the particle $x' = p_x/p_s$ is the ratio between the transverse p_x and longitudinal p_s components of the particle momentum. Acceleration is performed with a longitudinal electric field which increases the longitudinal momentum keeping the transverse component unchanged, as indicated in Fig. 2.8. To first order, a momentum increase $\Delta p = \Delta p_s$ leads to a divergence increment given by:

$$x' + \Delta x' = \frac{p_x}{p_s + \Delta p_s} = \frac{p_x}{p_s\left[1 + \frac{\Delta p_s}{p_s}\right]} \approx x'\left[1 - \frac{\Delta p}{p}\right] \tag{2.73}$$

which yields to

$$\Delta x' = -x'\frac{\Delta p}{p}. \tag{2.74}$$

Considering an ensemble of particles, all with the same betatron emittance ϵ, but with random phases, in a location where $\alpha = 0$ (i.e at a relative extremum of the betatron function), the i^{th} particle is characterized by

$$x_i = \sqrt{\epsilon\beta}\cos(\Psi + \Psi_{0i}) \tag{2.75}$$

$$x'_i = -\sqrt{\frac{\epsilon}{\beta}}\sin(\Psi + \Psi_{0i}) \tag{2.76}$$

$$\epsilon = \gamma x_i^2 + \beta x_i'^2 \tag{2.77}$$

and for a change in the particle slope $\Delta x'_i$, the emittance change is

$$\Delta\epsilon = 2\beta x'_i \Delta x'_i = -2\beta x_i'^2 \frac{\Delta p}{p} = -2\epsilon \sin^2(\Psi + \Psi_{0i})\frac{\Delta p}{p} \tag{2.78}$$

Averaging over all the particles to get the beam emittance leads to[2]

$$\langle\Delta\epsilon\rangle = -\epsilon\frac{\Delta p}{p} \text{ or } \frac{d\epsilon}{\epsilon} = -\frac{dp}{p} \tag{2.79}$$

If ϵ_0 is the beam emittance for particles of momentum p_0, after acceleration to momentum p, the emittance becomes:

$$\epsilon(p) = \epsilon_0\frac{p_0}{p} \tag{2.80}$$

The emittance is thus inversely proportional to momentum. This can be generalized for any location where $\alpha \neq 0$. Such process is commonly named *adiabatic damping* (despite the fact that there is no effective damping). It is valid when the momentum variation is small during a betatron oscillation period. In other words the beam emittance reflects the particle source properties and the emittance decrease due to acceleration.
The *normalized emittance* is generally defined as:

$$\epsilon_n = \gamma_L\frac{v}{c}\epsilon = \gamma_L\beta_r\frac{1}{\beta}\left[\sigma^2 - \left(D\frac{dp}{p}\right)^2\right] \tag{2.81}$$

where the Lorentz factor $\gamma_L = E/(m_0c^2)$ is the ration between the particles energy and their rest mass, and the relativistic factor $\beta_r = v/c$ scales their velocity to the speed of light.
The normalized emittance ϵ_n is invariant with momentum, being $p = mv = \gamma_L\beta_r m_0 c$ and consequently

$$\beta_r\gamma_L = \frac{p}{m_0c} = \frac{p}{p_0}. \tag{2.82}$$

Hence the normalized emittance is constant at every location and independent from the particles energy. This provides a great advantage: beam diagnostics, despite its location, can evaluate the beam emittance at collision energy and estimates its impact on the luminosity as described later in this chapter.

[2]This implicitly means that the particles are uniformly distributed with respect to Ψ_{0i}.

2.4 Luminosity

In a collider two particles beams, which circulate in opposite directions, are brought into head-on collisions. With such scheme, the center of mass energy of the colliding particles is much higher than the one achieved with the traditional fix target experiments.
Each collider is designed to have *interaction regions*, where the beams are intercepting each other. At the collision points many different reactions are possible, each characterized by a cross section σ. The interaction event rate $\dot{n}$ is proportional to the cross section according to:

$$\dot{n} = L \cdot \sigma \tag{2.83}$$

The factor of proportionality L is called *Luminosity*. When two bunches containing n_1 and n_2 particles collide, at zero crossing angle, with a repetition frequency f, then the luminosity is given by

$$L = f \frac{n_1 n_2}{4\pi\sigma_x\sigma_y} \tag{2.84}$$

where σ_x and σ_y are the standard deviation of the Gaussian beam profile. Eq. (2.84) is valid for two beams colliding at zero crossing angle and characterized by the same particles transverse distributions at the collision point. It is a pure geometrical quantity depending on the overlap of the two beams. Mutual beam-beam interactions can enhance or lower it. Luminosity is expressed in units of $cm^{-2}s^{-1}$. For instance, the design luminosity of LHC is $10^{34}\,cm^{-2}s^{-1}$ and the total hadronic cross section is $8 \cdot 10^{-26}\ cm^2$. Consequently the event rate will be of $8 \cdot 10^8\ s^{-1}$.
As seen in the previous section, σ_x and σ_y depend on the transverse emittances ϵ_x and ϵ_y and the betatron functions β_x and β_y.
Indicating with β_x^* and β_y^* the betatron functions at the interaction point, Eq. (2.84) becomes:

$$L = f \frac{n_1 n_2}{4\sqrt{\epsilon_x\beta_x^*\epsilon_y\beta_y^*}} \tag{2.85}$$

Therefore, in order to achieve high luminosity collisions, it is necessary to accelerate high population bunches of low transverse emittances and collide them at high frequency, in locations where the beam optics is capable to provide very low betatron functions.

Chapter 3

Beam Transverse Emittance Monitoring

Measuring the beam transverse emittance is of relevant interest in every accelerator complex, in order to allow the characterization of one of the key parameters for high luminosity performance. In a chain of accelerators, like the one conceived to bring the particles in collision at LHC, the emittance has to be measured under different conditions taking into account: 1) the beam parameters, 2) the need for beam studies in the machine set-up periods and 3) the requirement of performing measurments which do not perturb the beam during the physics periods.
In this chapter we will first introduce the emittance measurements requirements for the LHC type beams accelerated in the CERN facilities and then give an overview of various methods developed during the years to monitor the beam transverse emittance. We will then describe in more detail the monitors used in the SPS. Separate sections are dedicated to a method for measuring the betatron function amplitude and to numerical simulations predicting the effects of the monitors limited resolution and dependence on noise.

3.1 Emittance measurement requirements and techniques

For the LHC type beams accelerated in the CERN rings, the requirements concerning emittance monitors can be summarized as follows:

- the accuracy has to be better than $1-2\,\%$ in terms of beam size (on the absolute value as well as on relative variations) for energies up to the LHC injection (450 GeV) and better than $5\,\%$ at the LHC top energy (7 TeV);

- the instruments have to measure beam intensities ranging between $5 \cdot 10^9$ and $5 \cdot 10^{13}$ protons;

- turn-by-turn measurments are required for the optic tuning at the injection of the pre-accelerators as well as of the LHC;

- continuous measurements are required during the acceleration in the SPS and LHC;

- bunch-to-bunch measurements are required while the beam circulates at constant energy in the SPS and LHC.

An overview of the different emittance measurement methods developed during the years can be found in [16]. During the year 2000, at CERN, a workshop [17] has been organized to review the various techniques presently used (or under investigation) worldwide. Here we will outline the most relevant issues discussed in the workshop.
Looking at the activities pursued in the different laboratories, two classes of instruments can be

defined operational as transverse profile monitors: the *Wire Scanner* (WS) and the *Synchrotron Radiation* (SR) monitors.
The principle of operation of the wire scanners will be described in the next section. They are usually considered as a reference for the calibration of other instruments. This technique implies the interaction between a very thin wire and the beam, which potentially perturbs the beam (see Section 5.2) and may cause the wire damage under particular beam conditions. A wire scanner measurement requires hundreds of milliseconds and one instrument provides the beam dimension in only one transverse coordinate.
The synchrotron light monitor profits from the radiation emitted by the accelerated particles for imaging (in two[1] dimensions) the transverse beam distribution. This technique avoids any interceptance with the beam but, depending on the particles mass and energy, may require the installation of additional bending elements to generate enough radiation. Its absolute calibration is rather difficult.
Another technique is represented by the insertion of *Optical Transition Radiation* (OTR) screens [19] on the beam trajectory. Such monitors can be very accurate, however they can cause relevant beam perturbations and are normally only used in transfer lines during beam study periods.
Other classes of instruments are in the development phase, like the *Residual Gas* monitors. The ionization or the excitation of the residual gas encountered by the beam is exploited to image the transverse distribution (see the next section). This technique is also non-interceptive, but requires a cross-calibration with the wire scanners.
Additional methods have been and are under investigation, however they are still in an early development stage. An example is the *pencil beam scanner* [20] which has been tested in the CERN SPS. It consists of a low energy ion probe beam which is transversally sent into the proton beam. The transverse profile is inferred from the probe beam deflection due to the radial electrical field of the proton beam.
The techniques described so far provide a beam image (SR, rest gas monitors and OTR screens) or at least the beam profile in one transverse dimension (WS and pencil beam scanner). Other methods, like the *Quadrupolar Pickup* [21] developed at CERN, allow to calculate the beam emittance without measuring the beam size, but untill now have never been fully operational.
Wire scanners and synchrotron radiation monitors are used in the main hadron accelerator facilities, at Fermilab (Chicago, U.S.A.), Brookhaven National Laboratory (Long Island, U.S.A.), Los Alamos National Laboratory and DESY (Hamburg, Germany). In the Tevatron (at Fermilab, U.S.A.) and RHIC (at Brookhaven, U.S.A.) accelerators, few Ionazation Profile Monitors (IPM) are in the test phase.
At CERN WS monitors are used in the PSB, PS and SPS rings, even though systematic studies, based on measureemnts with different beam types, have never been accomplished. Two IPM are installed in the SPS and can be used in a quasi-operational basis. WS monitors and IPM will be installed at LHC.
This thesis work focusses on the calibration of these two classes of instruments. The synchrotron radiation monitor is not treated here, although it must be reminded that a monitor of this type will be installed at LHC and several pubblications on the subject are available [22, 23].

[1] Information about the three-dimensional distribution can be retrieved if a *streak camera* is used [18].

3.2 Profile monitoring methods used in the SPS

The following paragraphs will describe the two different methods for monitoring the beam transverse profiles used in the SPS, with the aim of defining the principles of operation and outline their advantages and drawbacks. Details of the monitors installed in the CERN accelerator complex will be given in Chapter 4.

3.2.1 Wire Scanners

A wire scanner device consists of a thin wire which crosses the beam. The movement is generally driven by DC motors and, depending on the mechanics and geometry of the system, the displacement is rotational or linear.
For the linear devices the wire movement is orthogonal to the beam trajectory and the wire absolute position is determined very precisely. However the present technology of linear motors and of the mechanical assemblies limit the maximum speed to few meters per second. Hence, for high beam currents, their usage is prevented by the time necessary to complete one scan. For a fixed velocity, above a certain beam intensity they break due to the energy transfer between the beam and the wire material.
Rotational motors provide higher speeds (up to twenty meters per second for the motors used at CERN), but the actual position of the wire needs to be calculated from the reading of the motor shaft position.
There are two methods for acquiring the information about the particle transverse distribution:

- As the wire passes through the beam, particles collide with the wire producing a cascade of secondary particles with an intensity proportional to the number of beam particles present at the position of the wire. The secondary particles are intercepted by a scintillator paddle. A photo multiplier tube coupled to the paddle measures the intensity of the light produced.

- If the wire material is a conductor, the particles hitting the wire create secondary emission electrons generating a current flow on the wire.

For both systems, the acquisition of the wire position and the intensity signal (shower of secondary particles or secondary emission current) are synchronized to the particles revolution frequency (i.e. one acquisition per turn) and are combined to construct the beam profile. A schematic plot of a wire scanner system is shown in Fig. 3.1
The wire position can be monitored using different technologies. Three methods are currently exploited at CERN: one based on a potentiometer tracking the motor position, a second using an optical ruler [24] and another using a resolver [25].
Potentiometers appliance is often limited by high noise levels and low accuracy. Optical rulers are used to detect linear movements and are based on a scanning head (attached to the fork-wire mechanism) and a fixed bar with golden scaling lines coated on it. Their operation is established by the principle of the photo-electrical scanning of very fine gratings. The so-called scanning unit consists of a light source, a condenser lens for collimating the light beam, the scanning reticle with the index gratings, and silicon photovoltaic cells. When the scanning unit is moved relative to the scale, the lines of the scale coincide alternately with the lines or spaces in the index grating. The fluctuation of light intensity, which is periodic if the system is operated at constant speed, is converted by photovoltaic cells into electrical signals. The output signals are two sinusoidal waves that are then interpolated or digitized as necessary and are used to retrieve the relative displacement.
Resolvers are absolute or relative angle transducers and are mounted on the motor shaft in order to

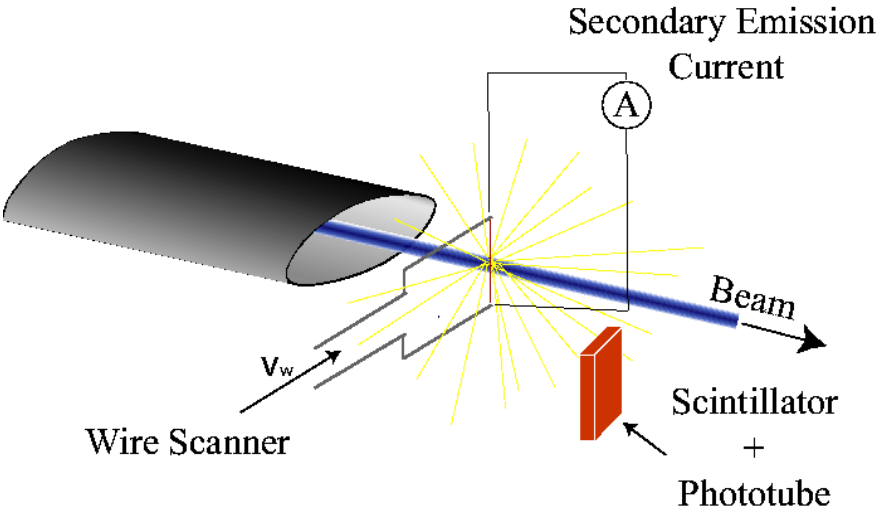

Figure 3.1: Schematic diagram of a wire scanner system.

determine the motor absolute angular position. They are basically rotating transformers and consist of a rotor coil, with N windings and two orthogonal stator coils with usually N or $N/2$ windings. An alternating voltage, the reference signal, is coupled into the rotor winding and provides primary excitation. The two orthogonal stator coils are wound, so that when the rotor shaft turns, the amplitude of the output signals is modulated with the sine and cosine of the mechanical angle, that is therefore deduced from them.
The wire scanners operation is in principle destructive for the beam, but the effect is negligible for most beam conditions if the mode of operation is properly chosen. The perturbations caused to the beam by the passage of the wire through the beam are qualitatively presented in Section 5.2.
The advantages of this kind of monitors are:

- they provide high resolution and accuracy on the wire position detection (down to $1\,\mu m$);
- they are a direct measurement, the accuracy on the transverse coordinate of the beam intensity distribution is given by the calibration of the wire position measurement;
- their statistical and systematic errors are very small compared to other instruments and therefore they are often used as calibration tools for alternative profile monitors.

Wire Scanners also present some drawbacks:

- the ultimate resolution on the beam profile measurement is determined by the wire diameter which is normally between 10 and $30\,\mu m$.
- For high intensity beams the energy deposited by the incident particles on the wire may be sufficient to melt or sublimate the wire; this is particulary true for very small beams, in which case the energy directly transferred from the beam to the wire has very high density and is limiting their employment. With the present setup, the instruments foreseen for LHC are intended to be used up to one tenth of the nominal intensity.
- The wire can melt or sublimate also due to the energy transferred by the beam to the wire by mean of electromagnetic field coupling. This phenomenon depends on the mechanical geometry of the monitor and by the beam longitudinal characteristics (bunch length and bunch

spacing). Electromagnetic coupling at frequencies higher than 100 MHz (Radio Frequencies, RF) was observed in the SPS wire scanners and will be presented in Chapter 6. So far this is not considered as a limitation for the LHC wire scanners, for which the foreseen mechanical design induces low coupling effects.

The accuracy of a wire scanner device depends on many factors. The spatial resolution of the system is determined by the wire speed and the particles revolution frequency, which give the number of acquisitions per profile. Fig. 3.2 shows the position increment recorded during one profile measurement in the SPS. The position is recorded with a potentiometer and its values are given in counts, as read by the analog to digital converter connected to the potentiometer output.
The position increases linearly during the scan. Fig. 3.3 shows the residuals of a linear fit applied to the array of positions of the previous plot. The residuals distribution has a statistical component and some sort of modulation.
Fig. 3.4 shows an histogram of the position increment between two adjacent acquisitions (one revolution of the beam). The mean and RMS values indicated on the plot give the average and standard deviation of the position increment:

$$\Delta x = \langle \Delta x \rangle \pm \sigma_{\Delta x} = 0.63 \pm 0.77 \ [\text{counts}] \tag{3.1}$$

Therefore, despite the positive speed of the wire, the acquisition system can give negative increment values.
For this reason an average position increment is applied to assign a wire position value at each turn. The average of the first ten measurements and of the last ten are taken as initial and final location of the movement, from which the total displacement can be determined. By knowing precisely the time interval between two acquisitions (given by the revolution frequency) and by the number of acquisitions, it is then possible to give the position at every point.
As already mentioned, the determination of the position for the rotational devices is particularly delicate since the read quantity is the angular position while to reconstruct a profile it is necessary to know the position in the transverse plane of interest. This depends on the system geometry and alignment accuracy. A systematic error in the SPS rotative wire scanners has been discovered and corrected in 2003, this subject is treated in Section 8.1.

The hadronic shower produced by the wire-beam interaction is detected by a scintillating material which produces photons. The scintillator is coupled to a photomultiplier tube (PM). A PM has two basic stages: the conversion of photons into electrons and the electron multiplication intended to enhance the signal level in order to improve the signal over noise ratio. PM tubes are well known devices and their properties and design characteristics are nowadays well documented by literature [26]. Here we describe their basic principles.
The incident photons are converted into low energy electrons by a photosensitive layer named *photocathode*. The photon energy must be sufficient to overcome the photocathode material work function, typically few electronvolts, necessary for one electron to escape from the material surface.
Normal conduction electrons within the photocathode material always have some thermal kinetic energy. At room temperature it is on average about 0.025 eV, but it has a large spread. Hence, the electrons at the upper end of the energy distribution can spontaneously escape form the surface, without any incident photon. This effect results in a dark current which represents a noise source, often called *thermionic noise*.
Each photocathode has a characteristic *quantum efficiency* defined as

$$QE = \frac{\text{number of photoelectrons emitted}}{\text{number of incident photons}} \tag{3.2}$$

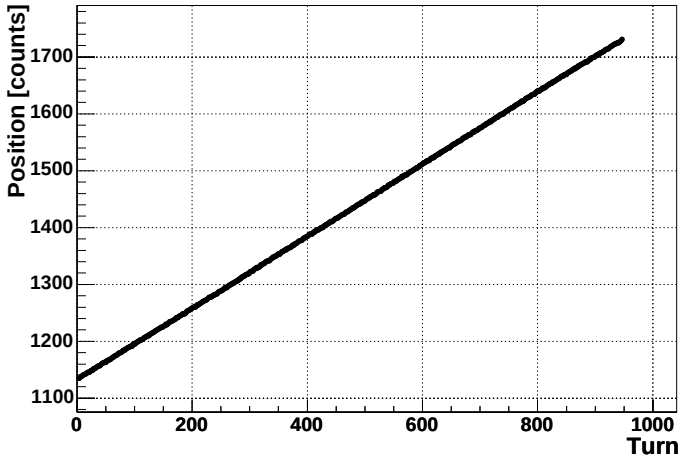

Figure 3.2: Wire position values as function of acquisition number.

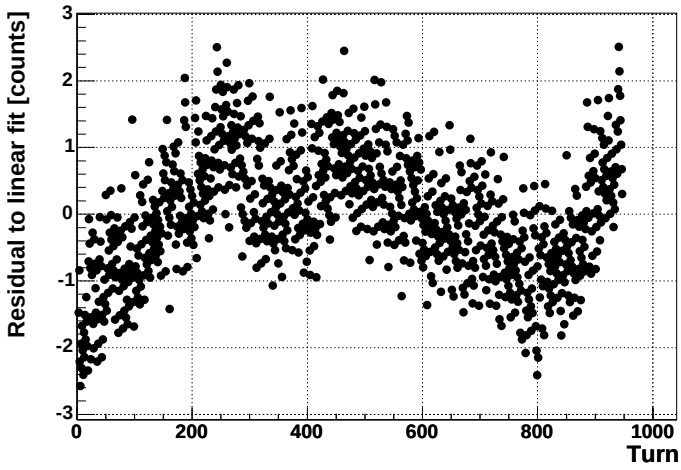

Figure 3.3: Residuals of the linear fit on the position measurement shown in Fig. 3.2

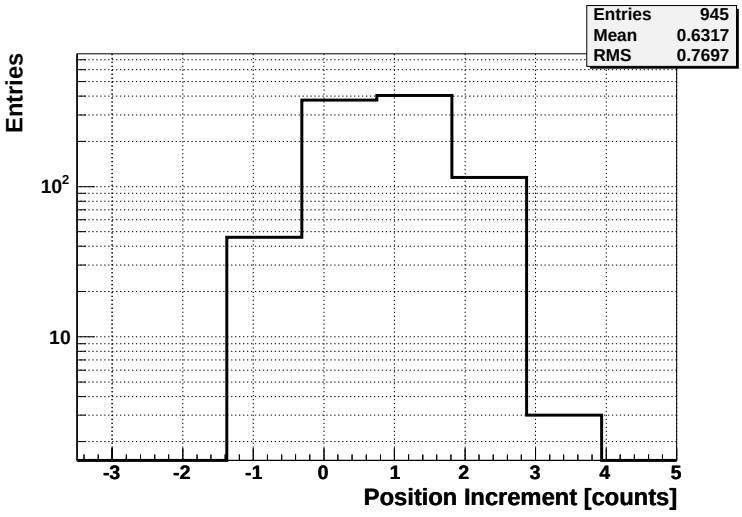

Figure 3.4: Distribution of the wire position increments per aquisition (values recorded during the acquisition of Fig. 3.3.

which depends on the wavelength and can reach $20 - 30\,\%$.
Electrons leaving the photocathode have an energy of 1 eV or less. They are accelerated by a positive voltage and forced to strike the surface of an electrode called *dynode*. Its material is chosen to have a high secondary emission yield: each electron generates δ secondary electrons. For an optimal incident electron energy of about 1 KeV, δ can reach the value of 10, although conventional instruments applying an accelerating potential of few hundreds volts provide $\delta = 4 - 6$. All PM tubes employ multiple stages structures, composed of several dynodes in cascade. With such design one can achieve electron gains larger than 10^6. With N stages, the overall PM gain results

$$G = \alpha\,\delta^N \tag{3.3}$$

where α is the fraction of photoelectrons collected by the structure, accounting for the fact that at each stage not all the electrons leaving one dynode reach the next.
The electrons produced at the last dynode are collected on the last electrode, the *anode*.The anode current is the detected signal.

The uncertainty on the signal intensity detection has two kinds of errors [27]: one related to the noise level, which can be defined as an *absolute (or constant) error*, and one proportional to the signal intensity, referred as *relative (or statistical) error*. The effect of the various error sources on the beam size determination is demonstrated by dedicated numerical simulations in Section 3.6.
Beam position and beam size variations, during the measurement period, can also introduce additional errors.

3.2.2 Residual Gas Monitors

The residual gas pressure inside the beam pipe has to be maintained as low as possible, in order to avoid beam losses and emittance degradation due to the interaction between the beam and the residual gas molecules. The vacuum level in the CERN accelerators is guaranteed by a sophisticated system of pumps which are reducing the pressure in the beam pipe and typical levels are of the order of 10^{-8} torr.
Two processes can take place while the beam is passing through residual gasses: *scintillation* (also called *luminescence*) and *ionization*. Both reactions depend on the beam energy, on the process cross section and on the pressure level. The ionization caused by high energy protons is treated in [28]. The cross-section dependence on the proton energy for Hydrogen and Helium (at normal pressure) is shown in Fig. 3.5.
The scintillation cross section for two gases (nitrogen and xenon) have been measured in the CERN PSB-PS accelerators while injecting protons with momenta from 50 MeV/c to 26 GeV/c [29]. The measurements show that the scintillation cross section is practically independent from the proton energy for momenta above 1 GeV/c.
Scintillation describes the de-excitation of the gas atoms or of electrons which are excited to higher energy levels by the beam passage. If the de-excitation is fast enough, the gas molecule is not drifting in between excitation and de-excitation, and by collecting the light it is possible to reconstruct the beam transverse distribution of particles.
In accelerators beam pipes most of the scintillation light is created by the de-excitation of rest gas ions. The ions drift due to the presence of the electric field characteristic of the charged particles circulating in the ring. In the SPS, the de-excitation time of N_2^+ ions has been measured [30] and is about $60\,ns$. With LHC beam circulating in the SPS, this correspond to the passage of 3 bunches, which (considering their electric field at nominal intensity) causes about $50\,\mu m$ ion drift. This is considered negligible for an accurate beam profile reconstruction. Depending on the wavelength of

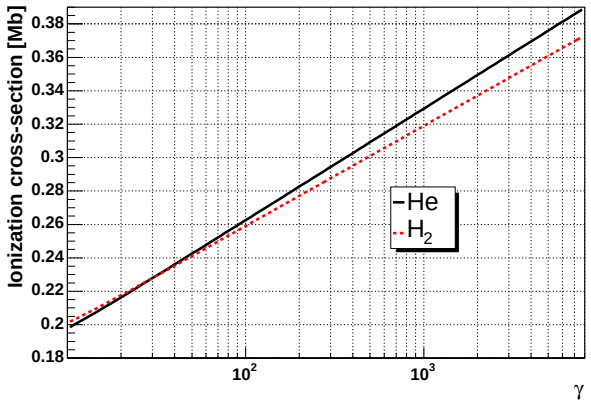

Figure 3.5: Ionization cross section as function of the protons Lorentz factor $\gamma = E/E_0$. In the SPS γ goes from 27 to 480. At collision energy in LHC $\gamma = 7460$

the produced light, the signal can be directly detected by a camera system or by a photo multiplier. The method for constructing the beam profile is similar to the one which will be described below for the gas ionization monitor. The distribution of the light produced by the gas scintillation is the same as the one emitted by the phosphor depicted in Fig. 3.6.

If the combination of the beam energy, cross section and rest gas pressure is favorable, the molecules are ionized. The cations (or the electrons) produced during the rest gas ionization are used to reconstruct the beam transverse distribution. Each cation is in fact accelerated by the proton beam electric field which is radial (i.e. in the transverse planes) for high energy particles, due to Lorentz contraction [28]. The ions collection efficiency and speed is enhanced by applying an external electric field transversal to the beam direction.

Due to their smaller mass, electron drift faster than cations. Mainly for this reason, the monitor configuration with the collection of electrons is the one presently exploited at CERN. Its principle of operation will now be described, referring to the coordinate system x, y, s defined in Chapter 2.1.

The electrons are accelerated transversally to the beam direction s by the high voltage applied to an anode grid which produces an homogeneous electric field along x, as depicted in Fig. 3.6. In proximity of the anode location the electrons encounter a phosphor which converts electrons into photons. A *micro channel plate (MCP)*, installed in front of the phosphor, amplifies the number of electrons. This is done along micro channels with very small diameter and the information about the location of origin of the primary electrons is conserved.

The phosphor (as the MCP plate) lies in a plane $y - s$ parallel to the particles direction s. The distribution of incident electrons along y reproduces the charged particles transverse distribution and the same applies for the photons at the outer side of the phosphor.

At this point an *optical system* is used for imaging on a camera the photons emitted by the phosphor. The optical system parameters, focal length and magnification factor, are designed in order to optimize the monitor resolution and sensitivity. The smaller the magnification, the larger the peak signal on the camera, but the smaller the achieved resolution (the image is distributed over a small number of pixels).

The image is stored and the sum column by column (or row by row depending on the camera orientation) of all the rows (columns) give an averaged beam profile on one transverse plane. The averaging is improving the accuracy by enhancing the signal over noise ratio.

Electrons are also affected by magnetic field produced by the beam, which can drive them away from the electric field lines. For this reason a dipole field may be applied in monitors based on electron collection; such field makes the electrons spin around the electric field lines.

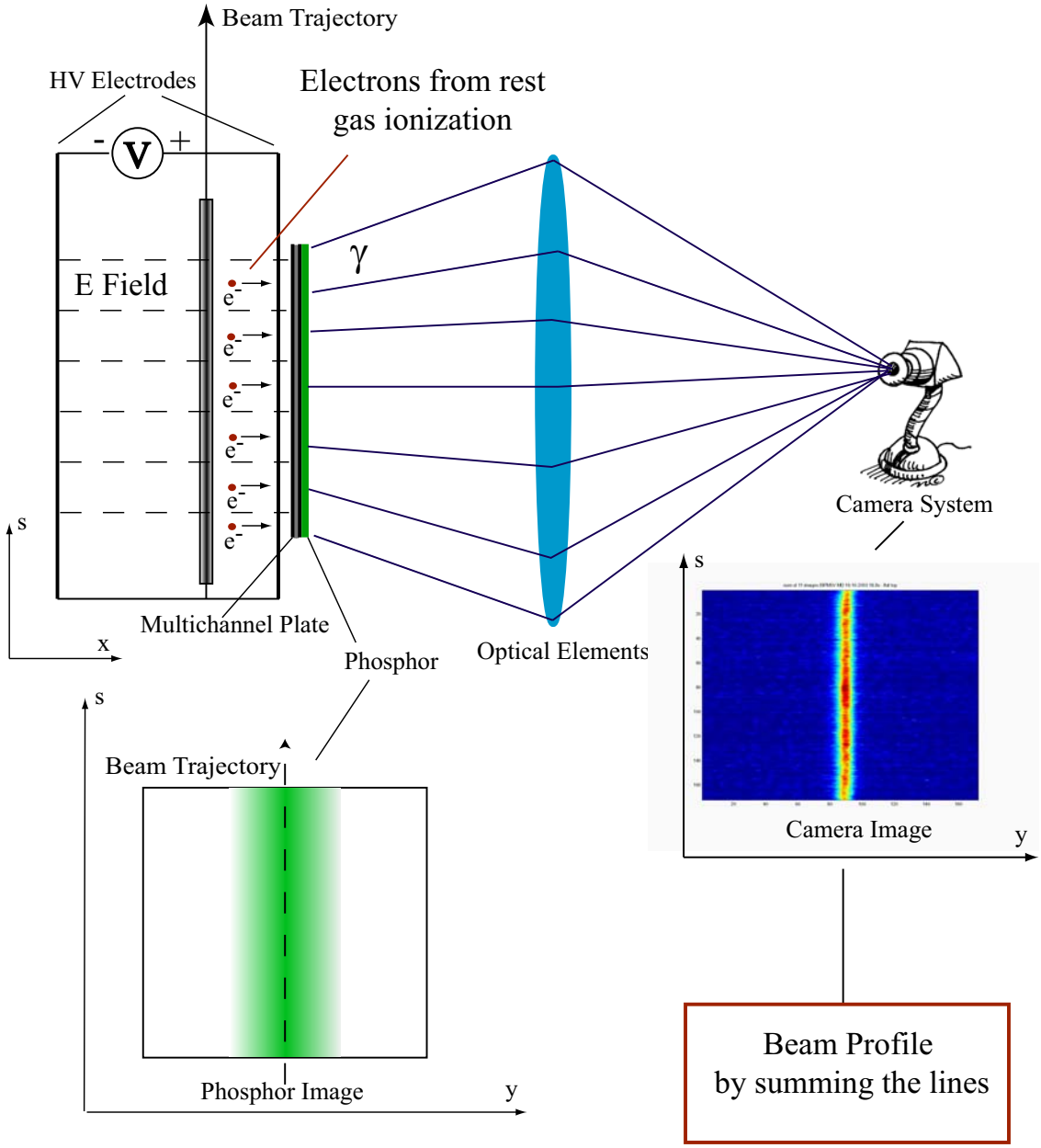

Figure 3.6: Schematic of an Ionization Profile Monitor designed to collect electrons.

3.3 Betatron Function measurement

The emittance defined in Eq. (2.72) is ideally invariant. The invariance at different locations is maintained by the variation of the betatron amplitude function proportionally to the variation of the beam size squared. This section describes one of the methods used to determine experimentally the betatron amplitude function.

3.3.1 K-Modulation

The betatron function around the accelerator is normally inferred from lattice simulation programs such as MAD [31]. The accuracy of the numerical predictions is usually acceptable.
Even if an experimental measurement can be complex and time consuming, it is often desirable to cross check the predicted values with dedicated measurements with the aim of reducing the uncertainties in all the quantities derived from the betatron function.
One method to determine the value of the betatron function is based on its measurement at a quadrupole location, by exciting the quadrupole and detecting the consequent beam tune change. Considering one transverse plane and a quadrupole magnet focusing in such plane, the motion of a particle inside the quadrupole is governed by the equation:

$$\frac{d^2x}{ds^2} = x'' = -kx, \tag{3.4}$$

where k is the quadrupole strength and s the curvilinear coordinate along the beam ideal orbit, as defined in Fig. 2.1. The effect of the quadrupole, integrated over the magnet length l_q, gives the total angle deflection, or "kick", applied to the particle:

$$\Delta x' = -kl_q x = -Kx. \tag{3.5}$$

Introducing, at the quadrupole location, an excitation ΔK, the beam transport matrix for one accelerator turn is the multiplication of the matrix obtained in Eq. (2.34) and of a perturbation matrix which derives from Eq. (3.5):

$$M = \begin{bmatrix} cos2\pi\nu + \alpha sin2\pi\nu & \beta sin2\pi\nu \\ -\gamma sin2\pi\nu & cos2\pi\nu - \alpha sin2\pi\nu \end{bmatrix} \begin{bmatrix} 1 & 0 \\ \Delta K & 1 \end{bmatrix}, \tag{3.6}$$

in which $\nu = \Psi_C/(2\pi)$ is the beam tune as defined in the previous chapter. The trace of the matrix describing one turn in the machine is always equal to $2cos(2\pi\nu)$ and the quadrupole excitation changes the tune from ν to $\nu_q = \nu + \Delta\nu$. Hence the trace of the transport matrix for one turn becomes $tr(M) = 2cos(2\pi\nu_q)$. Explicit calculation of the trace gives an equation which can be solved for β, giving:

$$\beta = \frac{2}{\Delta K}\left[cot(2\pi\nu) - \frac{cos(2\pi\nu_q)}{sin(2\pi\nu)}\right]. \tag{3.7}$$

The equation expresses the average betatron function along the magnet length. It may be demonstrated that for a small tune change and for tune values far from the integer and half integer resonances, an approximate solution can be written as [32]:

$$\beta \approx 4\pi\frac{\Delta\nu}{\Delta K} = 4\pi\frac{\Delta\nu}{l_q\Delta k}. \tag{3.8}$$

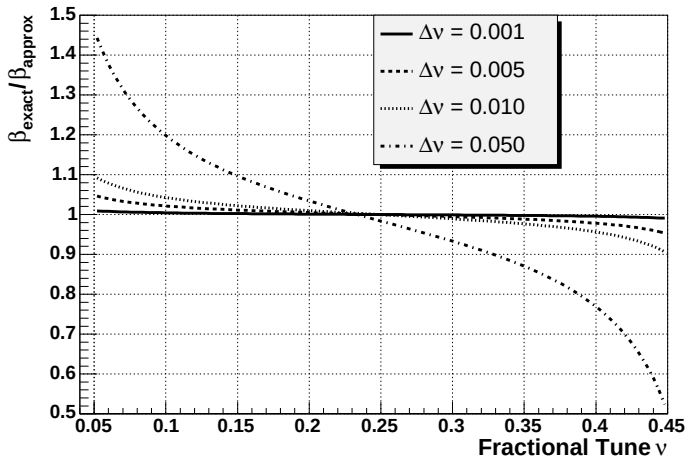

Figure 3.7: Ratio between the rigorous evaluation of the betatron function given in Eq. (3.7) and the approximation of Eq. (3.8), as function of the fractional part of the tune and for different tune changes.

The ratio between the rigorous evaluation of Eq. (3.7) and the approximation of Eq. (3.8) is shown in Fig. 3.7 as function of the tune and for different values of tune changes. The large discrepancies at the tune integers and half integers values are due to the resonance condition which takes place at such values.
Eq. (3.8) asserts that the knowledge of the quadrupole strength variation and of the consequent tune change allows the determination of the betatron function at the quadrupole location.
So far only a static change of the quadrupole strength has been considered, consisting of a step change from k to $k + \Delta k$ at a certain time t_0. In order to induce a detectable tune change at t_0 the required strength variation may be large enough to disturb the beam and cause particle losses. In order to overcome this problem the strength k can be varied periodically with frequency f_0, with a small amplitude. The tune is expected to change at the same frequency and the accuracy on its oscillations amplitude ($\Delta\nu$) improves by the tracking over a certain period. This method is called *k-modulation* and has been used at LEP [33].

3.3.2 Betatron tune measurements

Detecting the betatron tune of an accelerator means counting the number of betatron oscillations performed by the ensemble of particles over one turn in the machine. This is accomplished by monitoring the beam orbit with the Beam Position Monitors (BPMs).
The integer part of the tune can be deduced by exciting the beam with a single orbit corrector magnet and counting (by mean of several BPMs distributed in the ring) the number of oscillations per turn with and without the excitation.
An orbit corrector is a beam line element which uses electric or magnetic forces (or a combination of the two) to transmit a transverse "kick" to the beam. Here the kick can be very fast (lasting less than one revolution period of the particles). After the kick each particle starts a free betatron oscillation, with the same initial phase but with a frequency which is distributed like the tune spread of the particles inside the bunch. When dealing with protons, even if the single particles can keep on oscillating for a long period, the oscillation of the center of mass of the distribution is damped in a short period (see Fig. 3.8).
The determination of the fractional part of the tune is in general needed for the accelerator tuning, in order to ensure the stability of the beam and is relevant in this section in order to compute the

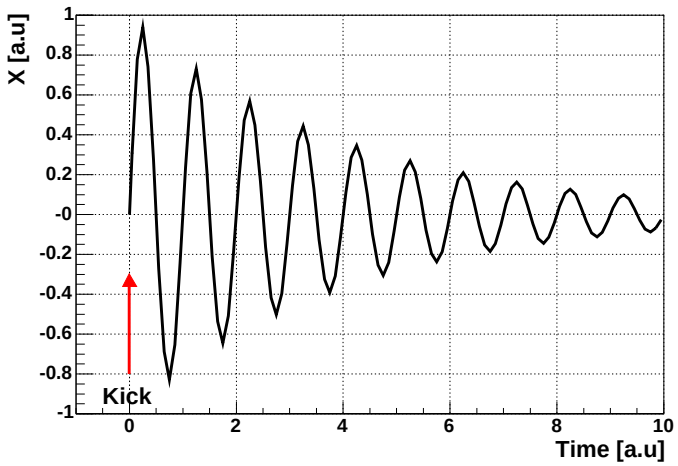

Figure 3.8: At $t = 0$ an orbit corrector kicks the beam and generates coherent oscillations damped over time.

betatron function. It can be determined by analyzing the beam orbit in time domain and in frequency domain [34]; here a method developed in the frequency domain is considered.
The beam is excited with a harmonic modulation of an orbit corrector for a finite period. The frequency of the excitation is linearly varied in time within a certain sweep range. Detecting the amplitude and the phase of the beam oscillations due to the excitation, provides the *beam transfer function* [35, 36]. The tune corresponds to the frequency at which the amplitude of the oscillations is maximum, as explained below.
In the SPS a technique based on the transverse damping system is able to excite the beam for $20\,ms$ with repetition intervals of $30\,ms$. During the $20\,ms$ the frequency is changed in the fractional tune range from 0.55 to 0.7 [37]. Such technique is referred to as "Chirp" excitation, from the fact that listening at the modulation of such frequencies with a loud speaker produces a sound similar to a singing bird. Fig. 3.9 shows an example of the chirp excitation in the SPS, sampled turn-by-turn by one BPM.
When the excitation frequency is equal to the tune value, every particle is kicked in phase at every passage through the kicker magnet. This resonant condition provides the beam oscillations with largest amplitude[2].
The frequency spectrum of these data provides the fractional part of the tune.
The beam position is sampled with a frequency equal to the SPS revolution frequency, $f_{rev} \approx 43.3\,\text{kHz}$. With excitation periods of $20\,ms$, every acquisition consists of a set of $N \approx 870$ data points, that represent a series of beam position measurements $x(k), k = 1 \cdots N$. The frequency spectrum of the signal is inferred by applying the *Discrete Fourier Transform (DFT)*. Every element $x(k)$ can be expanded as a linear combination of N functions:

$$x(k) = \sum_{n=0}^{N-1} X(n) e^{2\pi i k n/N} \tag{3.9}$$

The N functions $X(n)$, called *Fourier coefficients*, are expressed as

$$X(k) = \frac{1}{N} \sum_{n=0}^{N-1} x(n) e^{-2\pi i k n/N} \tag{3.10}$$

[2] In the considered example, before the resonance crossing, the beam oscillates at low frequency due to coupling effects with the longitudinal motion (side band synchrotron oscillations [38]).

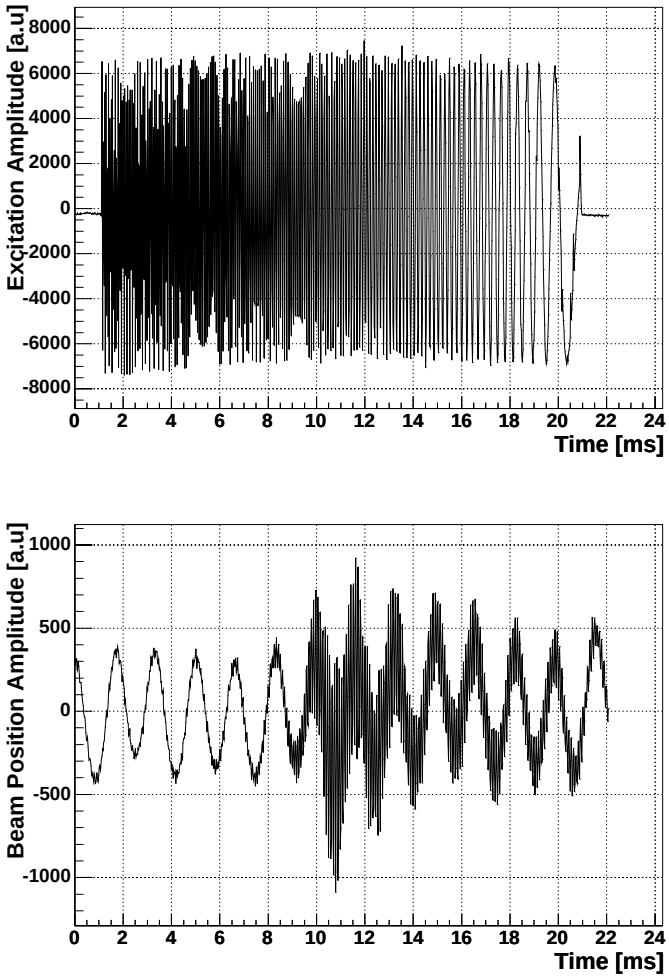

Figure 3.9: "Chirp" excitation of the proton beam in the SPS (top) and vertical beam position during the same period (bottom), as measured by a single beam position monitor. The excitation frequency is linearly decreased during a 20 ms period and can be repeated every 10 ms.

which are in general complex numbers. Their magnitudes $\|X(k)\|$ give the amplitudes of the frequency spectrum lines.
For the data treated in this thesis, the Fourier coefficients have been computed with a Fast Fourier Transform (FFT) algorithm [39].
Fig. 3.10 illustrates the frequency spectrum of the beam position data presented in Fig. 3.9. The spectrum can be determined between a minimum frequency (DC) and a maximum which is given by the Nyquist frequency $f_N = f_{samp}/2 = f_{rev}/2$. The harmonics amplitudes can be calculated only at discrete frequencies which have a constant spacing, determined by the sampling frequency and the number of data points: $\Delta f = f_{rev}/N$. Therefore the frequency spectrum of a signal with N samples in the time domain is composed of $N/2$ harmonics. It follows that, if the harmonic with largest amplitude corresponds to the index i_{peak} (that can vary between 0 and $N/2$), its frequency is

$$f_{peak} = i_{peak}\Delta f = i_{peak}\frac{f_{rev}}{N}. \tag{3.11}$$

When using one BPM, only the fractional part of the betatron tune ν can be estimated. The beam position in one transverse plane, monitored by the BPM can be expressed as

$$x(t) = Asin(2\pi\nu f_{rev}t + \Psi_0), \tag{3.12}$$

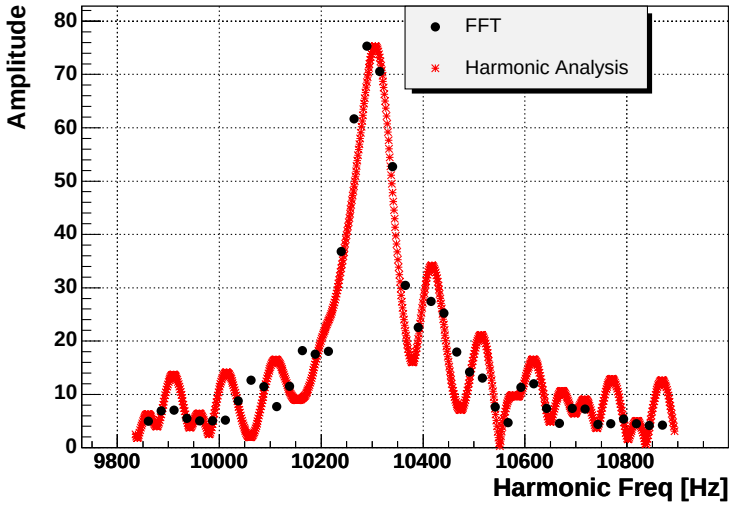

Figure 3.10: Frequency analysis of a the beam oscillations after a chirp excitation. The frequency resolution for the FFT treatment is limited by the number of acquisitions in the time domain, while the harmonic analysis provides a better resolution.

where A and Ψ_0 are constants. νf_{rev} is the ideal beam oscillation frequency over many turns and is often called *Betatron Frequency* f_β. In other words ν is the ratio between the betatron and the revolution frequencies. The betatron frequency corresponds to the maximum harmonic in the frequency spectrum. Hence Eq. (3.11) and Eq. (3.12) lead to:

$$\nu = \frac{f_{beta}}{f_{rev}} = \frac{f_{peak}}{f_{rev}} = \frac{i_{peak}}{N} \tag{3.13}$$

if $\nu < 0.5$ or

$$\nu = 1 - \frac{i_{peak}}{N} \tag{3.14}$$

if $\nu > 0.5$. A priori, there is no way to predict if $\nu > 0.5$ or $\nu < 0.5$ without dedicated beam based measurements which are not treated here.
As aforementioned, the resolution with which the tune can be determined is limited. A larger number of data points would improve such resolution. However, in the SPS, they are limited by the finite duration of the chirp excitation. A number of analysis techniques are available to achieve a better resolution. A method consists in interpolating the shape of the spectrum around the main peak [40]. Another technique which guarantees a high frequency resolution is called *Harmonic Analysis* and is described in [33]. It allows to perform a fine frequency scan around the expected tune value. Fig. 3.10 shows the spectrum resulting from the harmonic analysis (red) on top of the one from the FFT (black). A standard technique to improve the accuracy a Fourier analysis is based on data filtering in the time domain and has been applied to the data which will be presented in the next section. Each term $x(n)$ in the sum of Eq. (3.10) is multiplied by a coefficient $W(n)$ characteristic of the particular filter. The general purpose of the filters is to increase the weight of the maximum harmonic while decreasing the ones of the lateral lobes.

3.3.3 Measurements in the SPS

K-modulation has been tested in the SPS, by equipping six quadrupole magnets with additional back leg windings, powered separately from the main coil cables. The current modulation in the additional

windings induces the variation of the quadrupole strength. The power converters can produce harmonic excitations between 0.72 and 50 Hz, with a maximum peak-to-peak current of $12\,A$. The six magnets are in three consecutive FODO cells in one SPS arc. Three of them can be used to evaluate the vertical betatron function and three for the horizontal.
The variation of the magnetic strength Δk, due to the current in the back-leg windings, can be deduced from the quadrupole field gradient and from the beam energy. For instance for a focusing quadrupole:

$$\Delta k[m^{-2}] = 0.2998 \frac{1}{p[GeV/c]} \Delta \left(\frac{dB}{dx} \right) \left[\frac{T}{m} \right]. \tag{3.15}$$

The additional magnetic field gradient is calculated by the ratio between the effective additional current and the main coil current. If I_{coil}, $I_{back-leg}$ are the two currents and N_{turn_coil}, $N_{turns-back-leg}$ the respective number of windings per quadrupole, the additional gradient is

$$\left. \frac{dB}{dx} \right|_{back-leg} = \left. \frac{dB}{dx} \right|_{coil} \frac{I_{back-leg} N_{turns-back-leg}}{I_{coil} N_{coil}} \tag{3.16}$$

However it was very difficult to retrieve accurate measurements of the magnetic field gradient inside the SPS quadrupoles. Its determination would require dedicated field mappings on the SPS spare magnets available in the laboratory and discussions about this are on-going.
Beam based measurements can also provide the field gradient in the main quadrupoles. MAD calculations yielded the following values for the focusing and de-focusing magnets: $k_{QF} = 0.01464\,m^{-2}$ and $k_{QD} = 0.01462\,m^{-2}$.
With such values the field gradient due to the main coil current is calculated by mean of Eq. (3.15) and provides $dB/dx_{coil} = 1.27\,Tm^{-1}$ for the two focusing planes and an excitation current corresponding to a beam energy of $26\,GeV$.
By mean of the two equations above, one finds: $dB/dx_{back-leg} = 0.079\,Tm^{-1}$ and $\Delta k_{back-leg} = 9.1 \cdot 10^{-4}\,m^{-2}$.
For the measurements in the SPS, introducing this value of Δk in Eq. (3.8), would give betatron functions a factor three different from the ones calculated with the optical functions modeling software. Such discrepancy is not well understood and could be related to systematic errors in the main coil magnetic strength evaluation, or to a systematic uncertainty on the effective additional excitation provided by the back-leg windings.
The acquired SPS data were therefore treated in order to have relative comparisons between the measured betatron functions. One magnet (QF517) has been taken as reference. By imposing the measured betatron function to match the modeled one, and again using Eq. (3.8) (in which the tune variation is the measured one), the focal strength variation due to the back-leg windings becomes: $\Delta k_{back-leg} = 2.79 \cdot 10^{-4}\,m^{-2}$. Such value is used for all the other magnets excited with the same current.
The following figures summarize the results obtained in the SPS, all the measurements were performed with a beam energy of $26\,GeV$.
Fig. 3.11 and Fig. 3.12 show the betatron tune modulation in the horizontal and vertical plane respectively. The tune changes with the same frequency of one of the focusing (de-focusing) magnets strength modulation. In both plot the red curve indicates the fit performed on the tune data with a sinusoidal function at the excitation current frequency.
Fig. 3.13 shows the horizontal tune changes resulting from the excitation of the three focusing magnets. The dots represent the mean values over several measurements, while the error bars indicate the error on the mean. The total number of measurements was 17 for QF51810, 15 for QF52010 and 17 for QF52210. The excitation frequency has been varied from 0.72 to 8 Hz while the current amplitude has been kept constant for each magnet at $12\,A$.

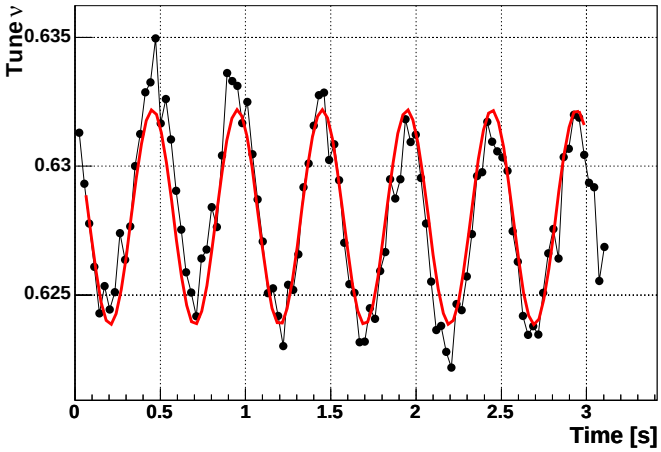

Figure 3.11: Horizontal tune modulation in the SPS, induced by the modulation of the strength of a focusing magnet (Magnet QF52210, $f = 2\,\text{Hz}$).

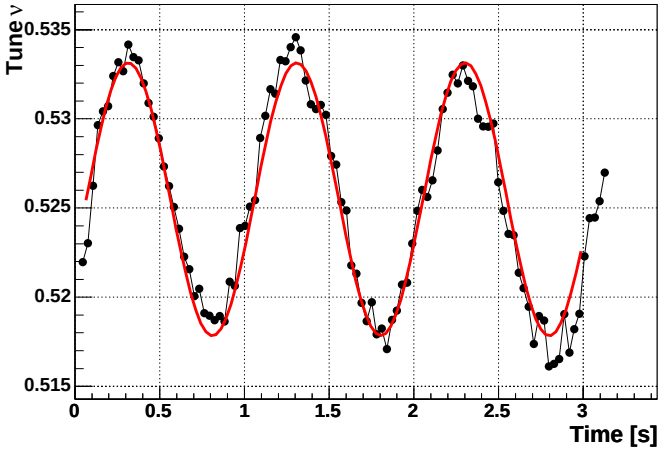

Figure 3.12: Vertical tune modulation in the SPS, induced by the modulation of the strength of a de-focusing magnet (Magnet QD51910, $f = 1\,\text{Hz}$).

Fig. 3.14 shows the tune changes at the different excitation frequencies.
Fig. 3.15 compares the horizontal betatron functions estimated with the k-modulation method with the ones expected from the optical calculation performed with MAD.
A source of error could be related to jitters in the modulation frequency and from the sinusoidal fit.
Fig. 3.16 shows the average differences between the fitting function and the nominal modulation frequencies. The differences have a systematic+statistic values within $\pm 1\,\%$.
Fig. 3.17, Fig. 3.18, Fig. 3.19 and Fig. 3.20 show the same quantities when considering vertical plane (i.e. excitation of the de-focusing magnets). The total number of measurements was 15 for QD51710, 18 for QD51910 and 22 for QD52110.

The tune change induced by the excitation of magnets $QF521$ and $QD522$ is smaller with respect to the other four quadrupoles. This brings to a larger disagreement with the betatron functions computed with MAD and could be related to the fact that such two magnets were winded with smaller diameter additional cables and less windings, due a lack of space between the iron poles and the beam pipe.
The effect could be a different transfer function between the current and the field.

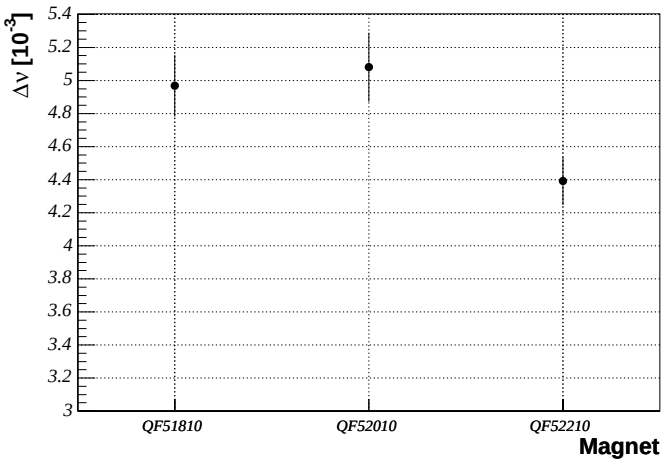

Figure 3.13: Average horizontal zero-to-peak tune changes while powering the three focusing magnets equipped for the k-modulation measurements. The additional excitation current has been kept for each magnet constant at the maximum peak to peak value ($12\ A$).

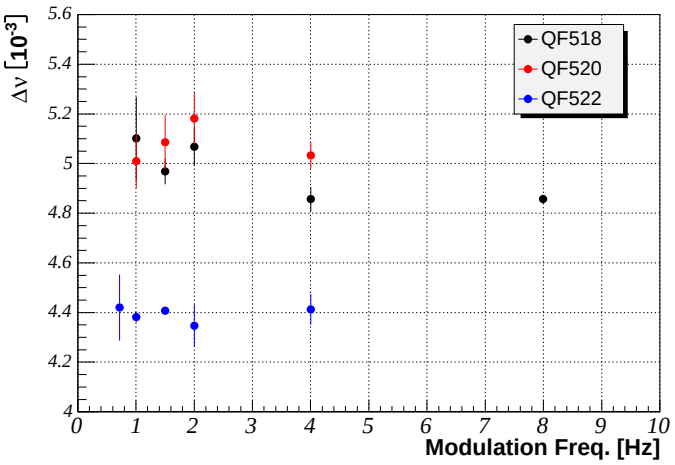

Figure 3.14: Horizontal betatron tune zero-to-peak changes as function of the modulation frequency, for each excited magnet.

The measurements in the SPS proved the feasibility of the k-modulation technique for measuring the betatron functions at a quadrupole location.
The method utilization at several locations could allow the extrapolation of the betatron functions at the profile monitors position, in order to diminish the uncertainties on the transverse emittance.
The experimental results showed that the major source of error comes from the knowledge of the magnetic response of the quadrupoles to the excitation currents, suggesting magnetic measurements to optimize the method.
K-modulation measurements are also foreseen for LHC.

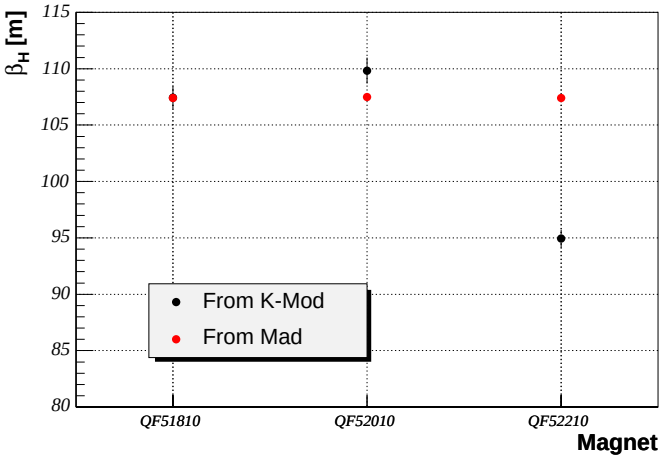

Figure 3.15: Comparison between the theoretical horizontal betatron function (calculated with MadX) and the one estimated with the k-modulation measurements. QF51810 has been set as a reference (see text).

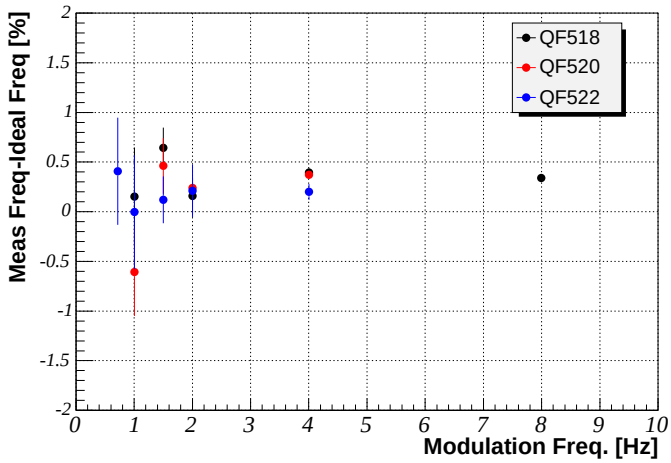

Figure 3.16: Differences between the sinusoidal fit functions and the nominal modulation frequencies (focusing magnets).

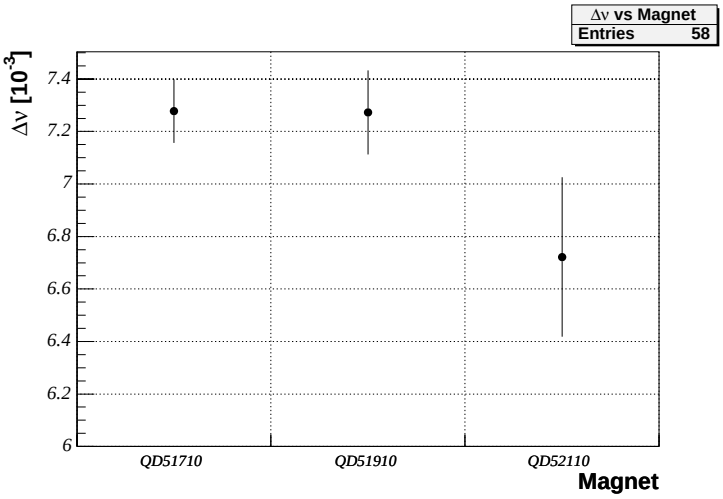

Figure 3.17: Average vertical tune zero-to-peak changes while powering the three de-focusing magnets equipped for the k-modulation measurements. The additional excitation current has been kept constant at the maximum peak to peak value (12 A).

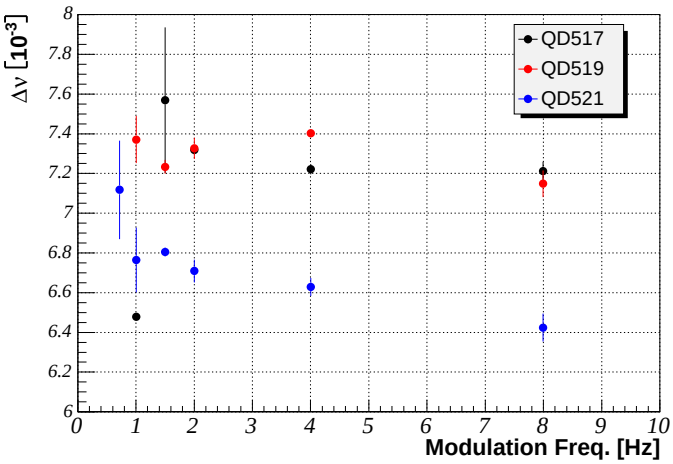

Figure 3.18: Vertical betatron tune zero-to-peak changes as function of the modulation frequency, for each excited magnet.

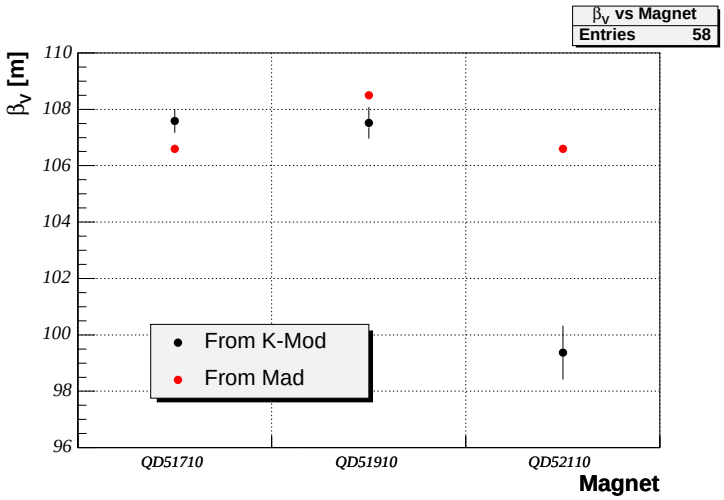

Figure 3.19: Comparison between the theoretical vertical betatron function (calculated with MadX) and the one estimated with the k-modulation measurements.

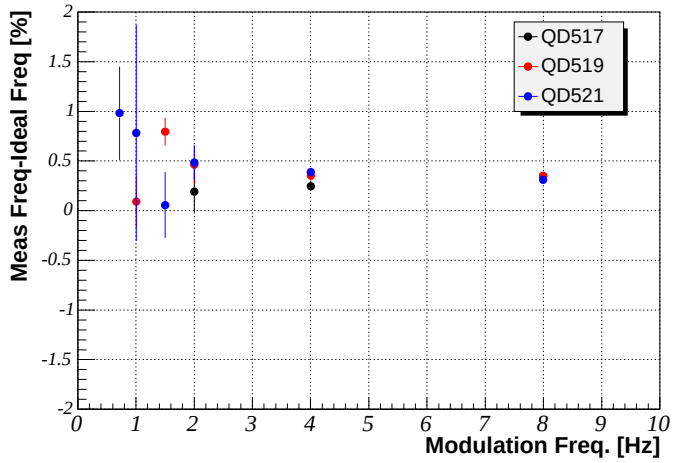

Figure 3.20: Differences between the sinusoidal fit functions and the nominal modulation frequencies (defocusing magnets).

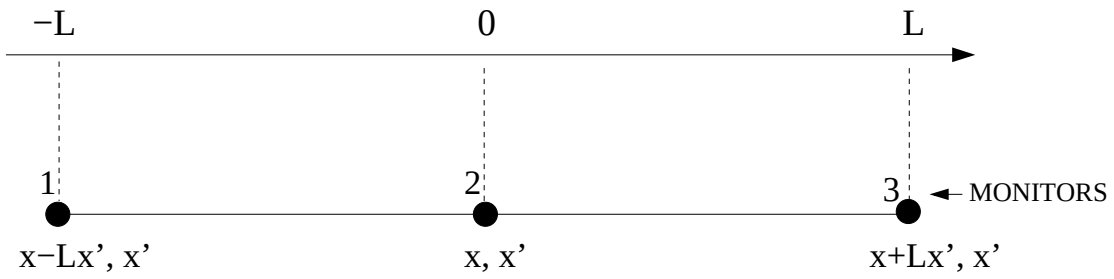

Figure 3.21: Three profile monitors interspaced by two drift spaces of length L. The bottom line indicates the phase space coordinates at the three locations.

3.4 Emittance measurement with the three-profiles method

In the previous chapter, referring to Fig. 2.7 which depicts the particles distribution in phase space, the beam emittance has been defined as

$$\epsilon = \sigma_X \sigma_{X'}. \tag{3.17}$$

σ_X and $\sigma_{X'}$ characterize the particles distribution width in the plane defined by X and X', that have been chosen to minimize the two standard deviations. Inserting Eq. (2.60) and Eq. (2.61) in Eq. (3.17), leads to

$$\epsilon = \sqrt{\overline{x^2}\,\overline{x'^2} - (\overline{xx'})^2}. \tag{3.18}$$

The terms under the square root are the distribution central second-order moments, defined in Eq. (2.57), Eq. (2.58) and Eq. (2.59). This definition of emittance was first introduced by P. Lapostolle [41] and has the property of being valid for any distribution. Furthermore, it does not rely on the definition of a contour ellipse in phase space, but only reckons with the statistical definitions of second-order moments.
Using the definition of Eq. (3.18), the measurement of the beam transverse emittance can be performed having three profile monitors and knowing the beam transport matrix which tracks the particles' trajectory between them. Here the simplest case will be considered, three monitors only separated by two drift spaces. This is depicted in Fig. 3.4, the monitors locations are labelled 1, 2 and 3, and the two drift spaces have length L.
The transport matrix along a drift space of length L is given in Eq. (2.13) and can be used to write:

$$\overline{x_1^2} = \overline{(x_2 - Lx_2')^2} = \overline{x_2^2} - 2L\overline{x_2 x_2'} + L^2\overline{x_2'^2} \tag{3.19}$$
$$\overline{x_3^2} = \overline{(x_2 + Lx_2')^2} = \overline{x_2^2} + 2L\overline{x_2 x_2'} + L^2\overline{x_2'^2}. \tag{3.20}$$

Summing and subtracting the two equations, using the notation $\sigma = \overline{x^2}$ leads to

$$\sigma_1^2 - \sigma_3^2 = -4L\overline{x_2 x_2'} \tag{3.21}$$
$$\sigma_1^2 + \sigma_3^2 = 2\sigma_2^2 + 2L^2\overline{x_2'^2} \tag{3.22}$$

Such equations allow to calculate the quantities $\overline{x^2}\,\overline{x'^2}$ and $\overline{xx'}$ which are needed to compute the beam emittance at the location 2. Inserting Eq. (3.21) and Eq. (3.22) in Eq. (3.18) the transverse emittance is expressed as

$$\epsilon = \sqrt{\sigma_2^2 \frac{1}{2L^2}(\sigma_1^2 - 2\sigma_2^2 + \sigma_3^2) - \left[\frac{1}{4L}(\sigma_3^2 - \sigma_1^2)\right]^2} \tag{3.23}$$

If the location has zero momentum dispersion, this expression is rigorous and the three values σ_1, σ_2, σ_3 are obviously the three beam sizes measured by the profile monitors. In the case of a beam with off-momentum particles and a monitor placed in a dispersion area, the three beam sizes are written as

$$\sigma_i = \sqrt{\sigma^2_{i,measuered} - \left(D_i \frac{dp}{p}\right)^2}, \quad i = 1 \ldots 3 \tag{3.24}$$

This method is currently used in the PSB, where an extraction line is equipped with three monitors interspaced by drift space. Another similar technique is named *three-gradient* or *quad-drift* method. It consists in having a profile monitor downstream of a quadrupole. The emittance can be calculated by evaluating the envelope width $x_{max} = \sqrt{\beta\epsilon}$ while changing the quadrupole strength [42].

3.5 Dispersion Measurements

The horizontal (or vertical) dispersion D_x (D_y) is an accelerator parameter varying along the longitudinal coordinate s. It characterizes the transverse displacement of a particle according to its relative momentum offset $\Delta p/p$ (see Chapter 2). This can be expressed as

$$\Delta x(s) = D_x(s)\frac{\Delta p}{p}. \tag{3.25}$$

The dispersion experimental determination is related to the beam longitudinal dynamics, and can be typically deduced from the orbit change induced by a shift in the RF frequency [32].
This is accomplished by the fact that a frequency shift Δ_{rf} changes the relative momentum offset of the beam centroid according to

$$\frac{\Delta p}{p} = -\frac{1}{\alpha_C - \gamma^{-2}}\frac{\Delta f_{rf}}{f_{rf}}, \tag{3.26}$$

in which $\gamma = E/E_0$ is the Lorentz factor and α_C is named *momentum compaction factor*. For an accelerator of circumference C the momentum compaction factor is

$$\alpha_C = \frac{\Delta C/C}{\Delta p/p} = \frac{1}{C}\int_C \frac{D_x(s)}{\rho(s)} ds \tag{3.27}$$

and therefore depends on the value of the dispersion function around the ring. However different methods are available for determining it independently from the knowledge of D_x, for instance based on the synchrotron tune or on the bunch length measurements [32].
The combination of Eq. (3.25) and Eq. (3.26) leads to the determination of the dispersion value at the location s,

$$D_x(s) = (\gamma^{-2} - \alpha_C)\frac{\Delta x(s) f_{rf}}{\Delta f_{rf}}. \tag{3.28}$$

This method has been for instance used in 2003 in the PSB to determine the dispersion function at the wire scanners' location and provided $D_x = 1.52\,m$ which is $3\,\%$ higher than the value computed with MAD. Such difference is not negligible when calculating the emittance of small size beams, but it is within the error determination of the momentum compaction factor α_c and the beam displacement $\Delta x(s)$.

3.6 Effect of various sources of errors on the beam size determination

LHC will be equipped with few ionization profile monitors and a synchrotron light monitor. Both devices require an imaging system to transport the beam image to the detector location.
Considering the design betatron functions at the instruments' locations and a nominal transverse emittance of $3.5\,\mu m$, the expected beam size will range from about $0.9\,mm$ at injection energy ($450\,GeV$) to about $0.2\,mm$ at collision energy ($7\,TeV$). The beam size is even smaller for the commissioning LHC beams. In determining the transverse beam sizes by means of a profile monitor, both systematic and statistical errors, typical of the instrument and of the measurement conditions, affect the final measurement accuracy.
For imaging systems the total number of events (i.e. the number of photons illuminating the screen) and the spatial resoultion are relevant to establish the measurement precision. A third important aspect is the presence of noise in both the signal amplitude and position measurements. The following sections will first present an analytical estimation of the error systematically introduced by an imaging system with limited resolution. Later, numerical simulations will cross-check the resolution limitations analytically predicted. In addition the simulations allow to evaluate the uncertainties originated by the different noise sources.
We will refer to the relative error on the beam size determination, composed of a systematic and a statistical contribution according to:

$$\frac{\sigma_{measured} - \sigma_{beam}}{\sigma_{beam}} = \delta^{rel} = \mu_\sigma \pm \sigma_\sigma \tag{3.29}$$

3.6.1 Resolution Limitation of Imaging Systems

The resolution of an imaging system depends on the monitor pixel size and on the magnification determined by the optical path. The magnification is defined as the ratio between the size of the image and the size of the object. Hence, for a fixed pixel size, it results in a calibration factor which is usually measured in units of $mm/pixels$.
Considering one pixel coordinate x and assuming that N photons are uniformly distributed along the coordinate, it is possible to calculate the mean value and variance of the photons locations. The normalized uniform distribution along the pixel extension d can be expressed as

$$f(x) = \begin{cases} f(x) = \frac{1}{d} & \text{for } -\frac{d}{2} < x < \frac{d}{2} \\ f(x) = 0 & \text{for } x < -\frac{d}{2} \text{ and } x > \frac{d}{2} \end{cases} \tag{3.30}$$

while the mean and variance are:

$$\langle x \rangle_{pixel} = \mu_{pixel} = \int_{-\infty}^{\infty} x f(x) dx = 0 \tag{3.31}$$

$$\langle x^2 \rangle_{pixel} = \sigma^2_{pixel} = \int_{-\infty}^{\infty} x^2 f(x) dx = \frac{d^2}{12} \tag{3.32}$$

The mean μ_{pixel} defines the pixel center and the standard deviation σ_{pixel} expresses the uncertainty on the location of a photon illuminating the pixel.
When using an image to construct a beam profile, the error on each photon position propagates to the determination of the beam size. The measured beam width has a contribution from the beam particles distribution σ_{beam} (the quantity which has to be detected) and the width σ_{pixel} determined by the finite resolution of the detector. In the approximation of uniform photon distribution within one pixel, the two terms are independent and the beam size resulting from the measurement is

$$\sigma_{measured} = \sqrt{\sigma^2_{beam} + \sigma^2_{pixel}} \tag{3.33}$$

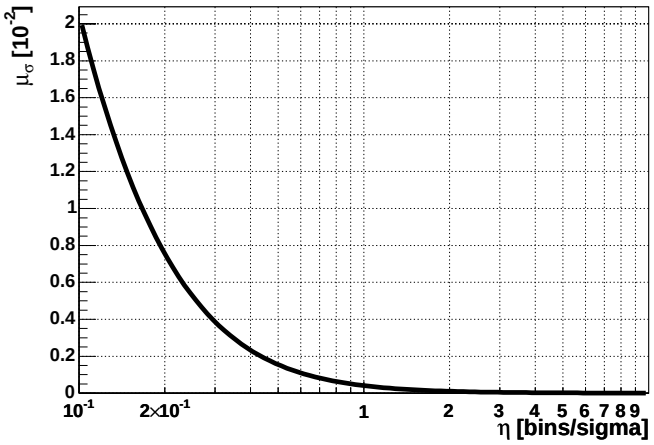

Figure 3.22: Predicted relative error on the measured beam size, as function of the system resolution in terms of bins per sigma, see Eq. (3.35). The beam profile peak has been set to the pixel center.

In the following paragraph this result is compared with the outcome of numerical simulations and the measurement error is expressed as function of the resolution in terms of bins per sigma, defined as

$$\eta = \frac{BeamSize}{PixelSize} = \frac{\sigma_{beam}}{d} \tag{3.34}$$

The error is calculated as the relative difference between the measured beam size and its true value. It represents the systematic contribution to δ^{rel} defined in Eq. (3.29) and results:

$$\begin{aligned} \mu_\sigma &= \left.\frac{\sigma_{measured} - \sigma_{beam}}{\sigma_{beam}}\right|_{systematic} = \frac{\sqrt{\sigma_{beam}^2 + \sigma_{pixel}^2} - \sigma_{beam}}{\sigma_{beam}} = \\ &= \frac{1}{\sigma_{beam}}\sqrt{\left(\sigma_{beam}^2 + \frac{d^2}{12}\right)} - 1 = \sqrt{1 + \frac{1}{12\eta^2}} - 1 \end{aligned} \tag{3.35}$$

The relative error increases to ∞ for $\eta \to 0$ and decreases to 0 for $\eta \to \infty$, as plotted in Fig. 3.22.

3.6.2 Numerical Simulations

In order to evaluate the contribution of different error sources to the final measurement error, we carried out numerical simulations. The simulations are intended to apply to the class of beam profile monitors for which the Gaussian distributed intensities are measured with detectors which integrate the signal over a part of the distribution.
The uncertainties on the amplitude signals depend on the whole amplification chain. For instance, in the case of the IPM (see Section 4.2) the signal originates from a certain number of primary electrons produced by the gas ionization and is then amplified in diffrent stages. The simulations described in this section are investigating the uncertainties at the end of the chain without considering the single contributions.

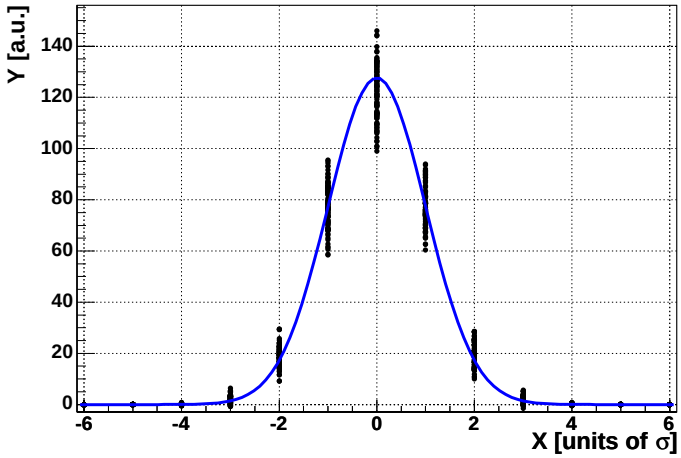

Figure 3.23: For each profile data point, the simulation provides a series of amplitude values following a Gaussian distribution with mean equal to the ideal profile value and deviation equal to the noise at that location (=$\sqrt{Amplitude}$ in this example)

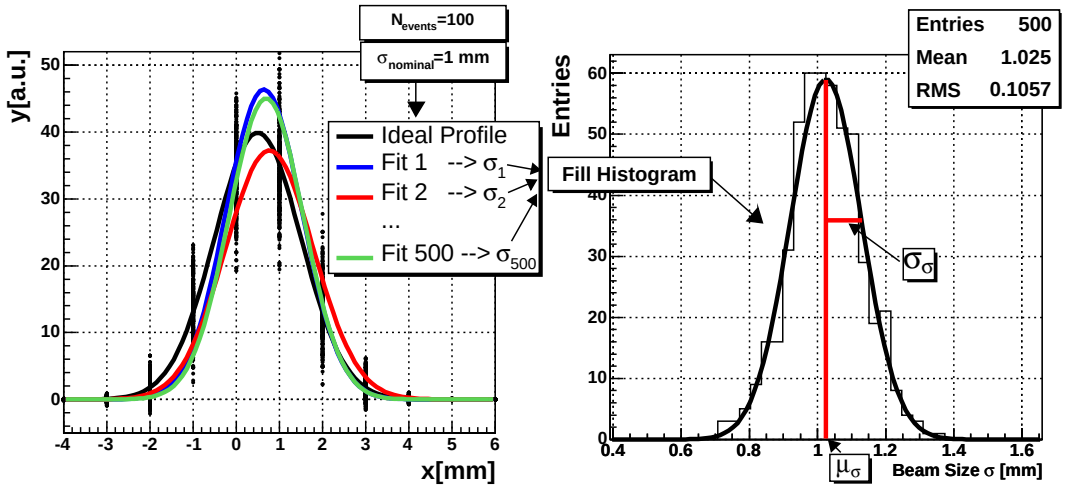

Figure 3.24: The plot on the left shows the ideal profile and three examples of fit on the sets of data randomly chosen from the distributions described in Fig. 3.23. The 500 beam size values thus calculated are fed to an histogram (plot on the right). The Gaussian fit of the histogram gives the statistical (σ_σ) and systematic (μ_σ) error on the beam size determination.

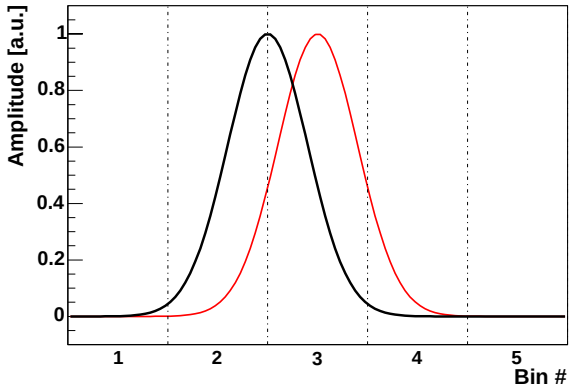

Figure 3.25: Relative position between beam profile and binning.

3.6.3 Influence of resolution and number of events

The first simulations consider the spatial resolution, expressed in terms of *bins per sigma* and the signal amplitude, defined by the *number of events* (= the integral of the profile).
Assuming that the beam profile is parameterized by the Gaussian distribution $f(x)$, each data point is characterized by an error which is typical of the monitor. In these simulations such error has been defined as the square root of the signal intensity. This means that for a given particle distribution, the monitor provides the beam profile composed of k points

$$\overline{y}_i = \int_{\overline{x}_{i-1}}^{\overline{x}_i} f(x)dx, i = 1...k$$

each of them with an error $\epsilon_i = \sqrt{\overline{y_i}}$. Such error estimation corresponds to the assumption of a Poisson distribution of the primary events for each bin. It is important to notice that $\overline{y}_i$ is not evaluated by sampling the Gaussian function at $\overline{x}_i$, but it is calculated as the integral of the function along the bin width, as the real detector does [3].
For a given total number of events and for a given resolution (bins per sigma), the simulation code randomly chooses five hundreds[4] set of *k* points $(\overline{x_i}, y_i)$. The amplitude y_i has mean $\overline{y_i}$ and standard deviation ϵ_i.
Each set of data is fitted with a Gaussian function in order to determine the measured beam size. The fit results are fed to an histogram which, with a sufficiently large number of iterations, also results in a Gaussian distribution. The histogram entries reproduce the measured beam size of five hundreds repeated acquisitions with the profile monitor. The difference between the mean value of the fitted distribution and the nominal beam size (given as input to the simulation) represents the monitor *systematic error* μ_σ for a given number of events and spatial resolution. The standard deviation of the fitted distribution σ_σ provides the *statistical* (or *random*) error. The simulation approach is shown in Fig. 3.23 and Fig. 3.24.
Another aspect to be considered is the relative position between the beam and the binning grid. At first the two extreme cases have been simulated, as illustrated in Fig. 3.25: the one in which the profile peak falls on a bin center (red plot) and the one in which it falls on a bin edge (black plot).

[3] This is true for all the studied detectors, except the WS monitors, being the wire diameter much smaller than the beam size.

[4] Five hundreds iterations were considered appropriate to make the statistical error negligible.

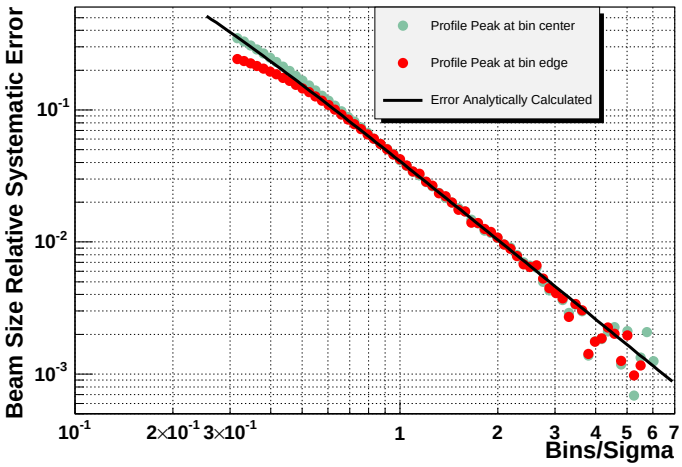

Figure 3.26: Relative systematic error $\frac{\sigma_{meas}-\sigma_{beam}}{\sigma_{beam}}\Big|_{systematic}$ as function of resolution, for a profile with the peak at a bin center and at a bin edge.

3.6.4 Effect of random noise

The signal can be affected by a random noise that is usually defined as *white noise* or *Gaussian noise*. The effect of this kind of disturbance on the profile monitors amplitude signal has been studied with the same method as above, but using $\epsilon_i = const = \epsilon$. More precisely the Signal/Noise ratio has been imposed, taking as signal the beam profile peak and as noise ϵ. In this case (as for the third simulation described below) the number of events has been chosen very high (i.e. the error depending on it is negligible), in order to separate the different error sources.
The third problem investigated is the uncertainty on the WS wire position due to noise on the acquisition system. In order to simulate it, the five hundreds set of *k* data points are of the type $(x_i, \overline{y_i})$ with x_i extracted from a distribution with mean $\overline{x_i}$ and spread ϵ_x. The noise amplitude has been expressed by mean of the ratio $\frac{beamsize}{noise} = \frac{\sigma}{\epsilon_x}$.

3.6.5 Results

The *systematic error* only depends on the detector resolution: Fig. 3.26 shows the measurement accuracy as function of the number of bins per sigma. The figure presents the outcome of the simulations considering the two extreme cases of the relative position between beam and detector channels, superimposed to the analytical prediction of the error introduced in the previous section (see Eq. (3.35)). The three curves overlap for resolutions larger than $1\,bin/sigma$. For resolution values larger than $3\,bins/sigma$, the error drops below $4 \cdot 10^{-3}$. At this error level the numerical simulations spread is larger, due to the small amplitude of the relative difference between the measured and expected beam size statistical fluctuations. When the system resolution is below $1\,bin/sigma$, the simulations disagree with the analytical prediction, because the assumption of a uniform distribution of photons in the pixel is not anymore valid.
Since the accuracy of the systematic error is almost independent from the number of events, only the case with 12000 events is considered[5].
Furthermore, at low resolution, the Gaussian parameters μ_g (expressing the beam position) and σ_g

[5]In this simulation the measurement amplitude errors are taken as the square root of the amplitude, but the results do not change when introducing a random noise on the amplitude or position signals.

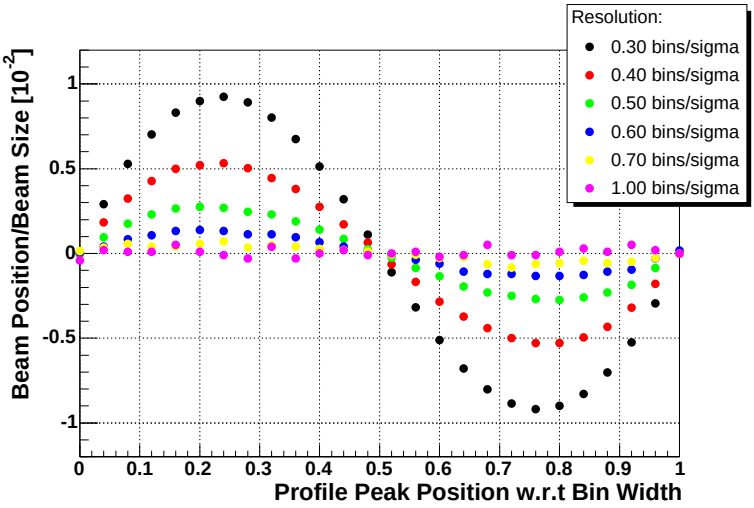

Figure 3.27: Beam position in units of beam size (ideally the beam is at 0) as function of the profile position with respect to the bin center (0 means "beam peak at the lower bin edge", while 0.5 "beam peak at bin center"). Each dot represents the mean over 500 iterations, the error on the mean is here negligible.

(expressing the beam size) depend on the profile peak location with respect to the bin center. Fig. 3.27 shows the beam position deduced from the Gaussian fit (i.e. the mean value of the parameter μ_g after 500 iterations) as function of the relative position between the peak and the bin center, for resolutions ranging from 0.3 to $1\,bin/sigma$. The beam position is correctly evaluated when the profile peak is at the bin edge or at the bin center, while is wrongly determined for the cases in between. The values are very reproducible (the error on the mean is negligible after five hundreds iterations), even when giving random initial values to the fitting parameter μ_g. Hence, for low resolution systems, the measured beam position systematically depends on the profile peak position with respect to the bins.
Fig. 3.28, Fig. 3.29 and Fig. 3.30 show the comparison between the true beam profile and the one fitted using the simulation data, for a resolution of $0.4\,bins/sigma$ and for three different beam positions. For such low resolution the plots evidence the non-uniformity of the intensity distribution along the bin width.
For the three cases, beam at bin center, beam at 0.25 of the bin center and beam at bin edge, the relative systematic error between the measurement and the beam size is $24.5\,\%$, $22.2\,\%$ and $19.5\,\%$ respectively. The relative systematic beam size difference as function of the peak position is shown in Fig. 3.31, for resolutions below $1\,bin/sigma$. At the bin edge and at the bin center the error scales differently with the resolution level.

Fig. 3.32 and Fig. 3.33 present the statistical fluctuation of the measured beam size as function of resolution and for different number of events. Fig. 3.32 refers to the case in which the profile peak is at a bin center, while Fig. 3.33 shows the case of the peak at a bin edge.
In both cases the errors exhibit an unexpected behavior for low resolutions. Such behavior again arises from beam position with respect to the bin edges which biases the Gaussian fit.
Fig. 3.34 shows the statistical error as function of the profile peak position, with 12000 events as input. The largest error (about $2.5 \cdot 10^{-2}$) occurs with a resolution of $0.3\,bins/sigma$ and with the profile peak at the bin edges. With this resolution, the error decreases while shifting the profile peak from the bin edges to the bin center, when it is reduced to about $0.7 \cdot 10^{-2}$. This is expected by the comparison between the 12000 events curves of Fig. 3.32 and Fig. 3.33 at $0.3\,bins/sigma$.
Comparing all the resolutions when the profile peak is at the bin center, the better the resolution the

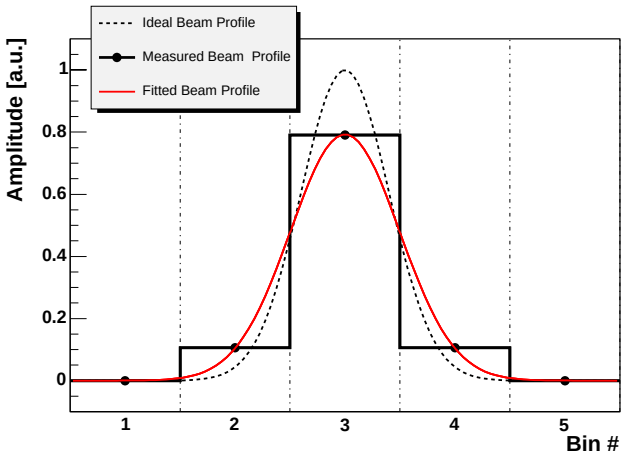

Figure 3.28: Beam profile acquisition in case of $0.4\,bins/sigma$ and the beam peak at the bin center.

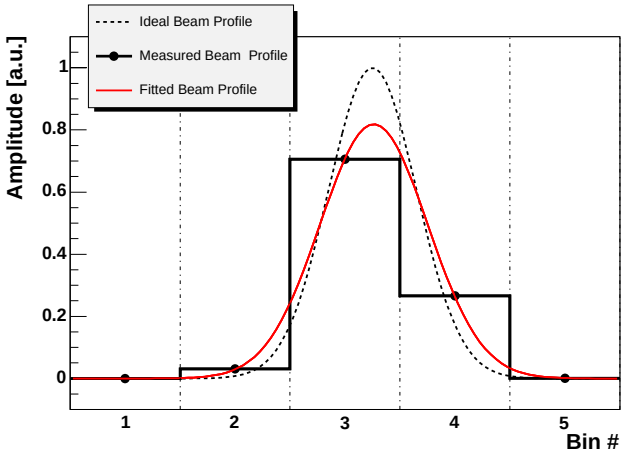

Figure 3.29: Beam profile acquisition in case of $0.4\,bins/sigma$ and the beam peak positioned at 0.25 of the bin width.

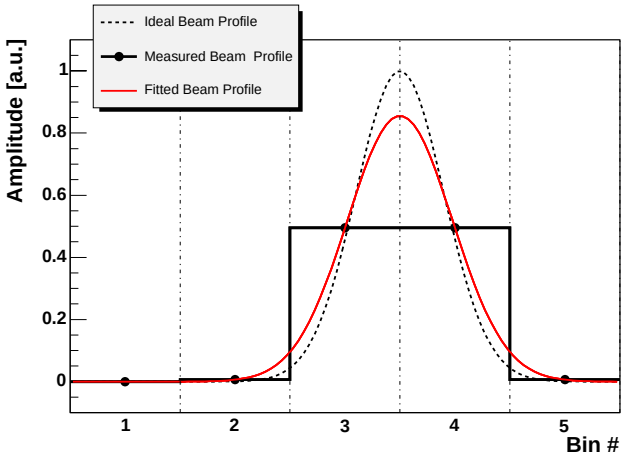

Figure 3.30: Beam profile acquisition in case of $0.4\,bins/sigma$ and the beam peak at the bin edge.

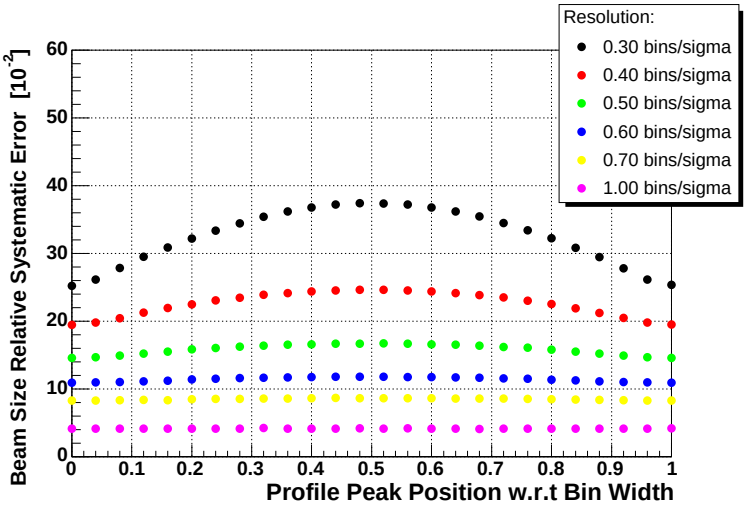

Figure 3.31: Relative systematic error of the measured beam size as function of the profile position with respect to the beam center, for resolutions below $1\,bin/sigma$. The measurements errors are assigned as the square root of their amplitude and N events = 12000

larger the statistical error. This is just a consequence of the worse fit stability. In any case, for such low value of the resolution, the statistical error is always much lower than the systematic, its accurate determination is therefore less important.

The plots presented so far refer to the simulations in which the error on the amplitude signal is determined as the square root of the amplitude itself.
The statistical error in the presence of random noise on the amplitude signal is showed in Fig. 3.35. In this case the beam profile peak has been placed at the bin center, but the plots can not be directly compared to the ones of Fig. 3.33 since the number of events has been set to $N = 1 \cdot 10^8$ and the error on each amplitude signal is not constant but depends on the amplitude itself (see Pag. 48). Fig. 3.36 shows the statistical error as function of the noise level, for different fixed resolutions. Each curve is well parameterized by a function

$$\sigma_\sigma(SNR) = \frac{K}{SNR} \tag{3.36}$$

where SNR is the Signal to Noise Ratio. The quantity K depends on the chosen resolution η and it is well parameterized by the function

$$K(\eta) = \frac{1}{\sqrt{\eta}}, \quad \eta\text{=bins/sigma} \tag{3.37}$$

as shown in Fig. 3.37. The combination of Eq. (3.36) and Eq. (3.37) allows to approximate the statistical error on the beam size determination with

$$\sigma_\sigma(SNR, \eta) \approx \frac{1}{SNR \cdot \sqrt{\eta}} \tag{3.38}$$

where SNR is determined as explained at Pag. 48.

The estimated statistical errors in the presence of random noise on wire scanners wire position determination are presented in Fig. 3.38. The beam profile peak has been placed at the bin center and the results for resolutions below $0.7\,bins/sigma$ are again biased by the fit stability.

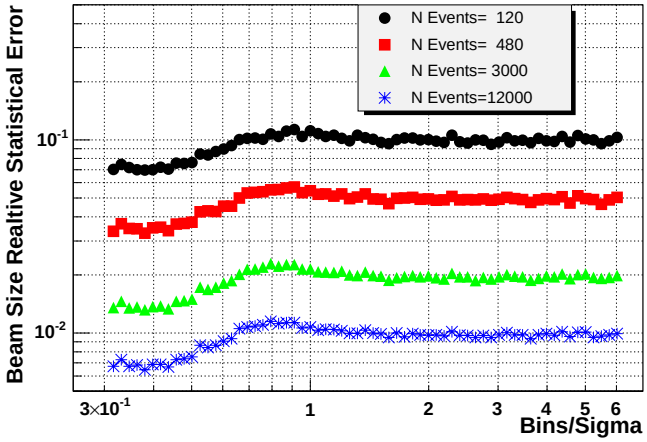

Figure 3.32: Statistical error as function of resolution and number of events (profile peak at bin center)

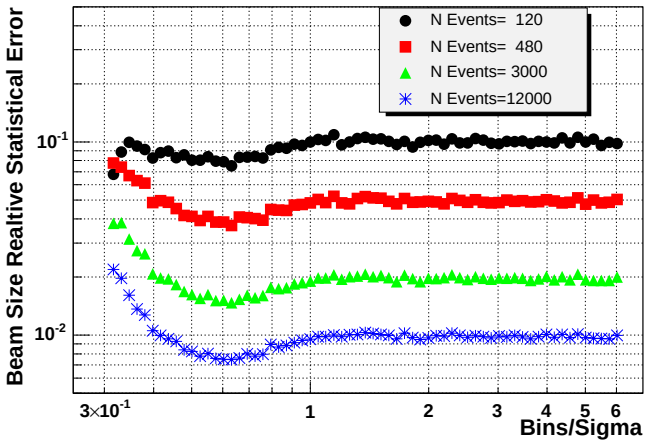

Figure 3.33: Statistical error as function of resolution and number of events (profile peak at bin edge)

3.6.6 Conclusions

The progress in monitors development, reached sofar in the SPS, indicate resolution factors of about $0.17\,mm/pixel$. With such resolution the LHC emittance at collision energy would be monitored with about $1.2\,bins/sigma$, while it would drop below $1\,bin/sigma$ for the commissioning beams.
With $1\,bin/sigma$ the relative systematic error on the beam size (predicted by Eq. (3.35) and confirmed by the numerical simulations) is about $4 \cdot 10^{-2}$. The experimental results have to be corrected for it.
For lower resolutions both the systematic and statistical errors are biased by the limited number of samples, inducing a dependence of the measured beam size on the relative position between beam profile and binning grid. Since such position is not known a priori, a correction is not evident. The numerical simulations confirm what is stated in [43]: an accurate profile monitoring should be performed with more than $1\,bin/sigma$.
In addition the simulations provide a quantitative estimation of the statistical errors introduced by a limited number of events and by the presence of noise, to be considered in designing a monitor, or estimating its accuracy.

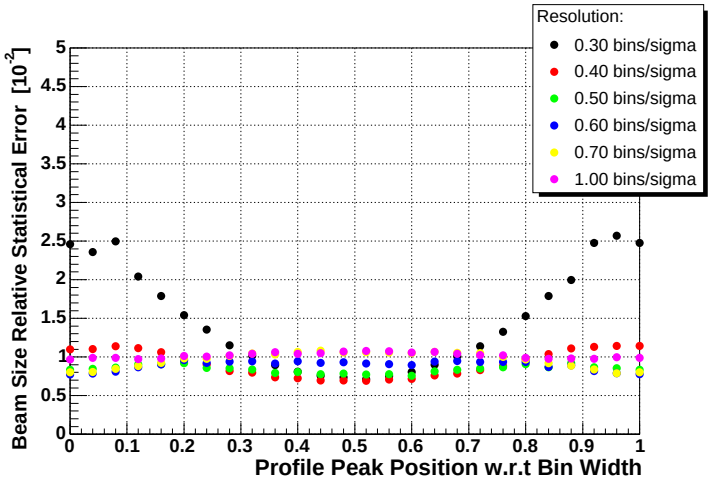

Figure 3.34: Relative statistical error of the measured beam size as function of the profile position with respect to the beam center, for resolutions below $1\,bin/sigma$. The measurements errors are assigned as the square root of their amplitude and N events = 12000.

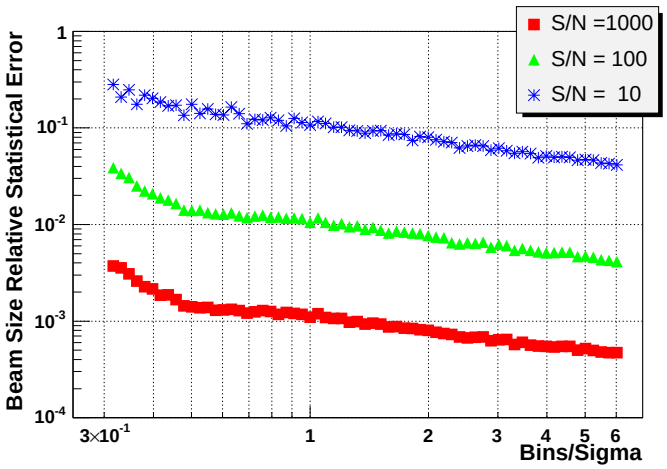

Figure 3.35: Relative statistical error as function of resolution and random noise on the amplitude signal (N events=$1{\cdot}10^8$). The beam profile peak is at the bin center.

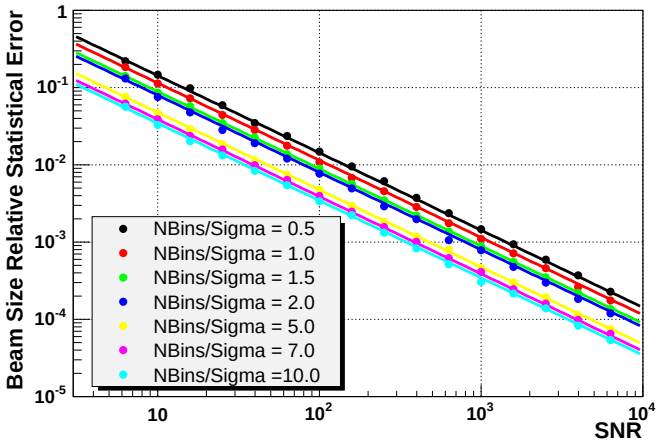

Figure 3.36: Relative statistical error on the beam size as function of noise on the amplitude signal and for different resolutions.

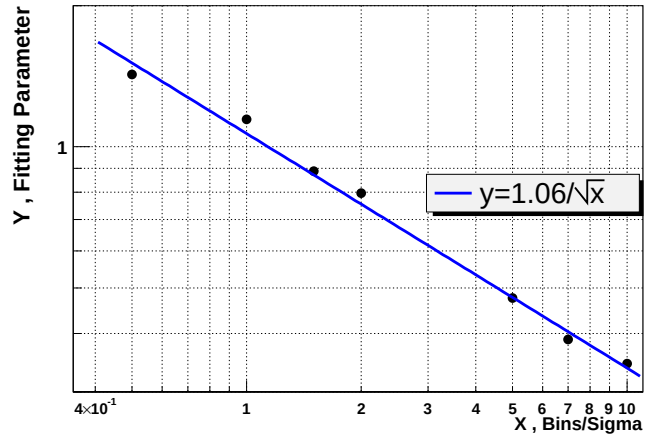

Figure 3.37: Parametrization of the curves drawn in Fig. 3.36

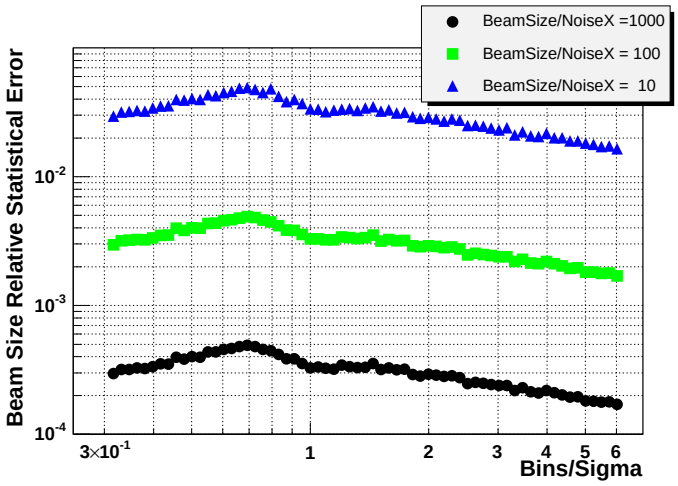

Figure 3.38: Statistical error as function of resolution and random noise on the position (x) signal (N events=$1 \cdot 10^8$)

Chapter 4

Emittance monitors in the CERN Accelerators

This chapter describes the transverse emittance monitors studied during the reported work: the wire scanners and ionization profile monitors.
A general description of the hardware specifications is followed by the details about the monitors modes of operation, in order to facilitate the understanding of the experimental results of the following chapters.

4.1 Wires Scanners

Presently 22 wire scanner monitors are installed in the LHC pre-accelerators. Table 4.1 shows how they are distributed in the PSB, PS and SPS, together with the betatron functions amplitudes at their locations. The horizontal dispersion functions are also indicated.

4.1.1 PSB and PS monitors

The PSB and PS accelerators are equipped with wire scanner devices based on the same mechanical design and the same data acquisition system, both for the wire position and intensity signals. The PSB is equipped with two monitors per ring, one for each plane, while in the PS there are four instruments, two for each plane. The monitors utilize 12 carbon fibers of $7\,\mu m$ diameter twisted together.
A picture and a schematic of the mechanism driving the wire scanners are illustrated in Fig. 4.1. A

Table 4.1: Wire scanner monitors installed in the LHC pre-accelerators

Monitor Label	**Plane**	**Ring**	$\beta_{\mathbf{x}}\,[\mathbf{m}]$	$\beta_{\mathbf{y}}\,[m]$	$\mathbf{D_x}\,[m]$
H1, V1, H2, V2, H3, V3, H4, V4	4H + 4V (2 per ring)	PSB	5.7	4.3	1.5
H54, H64	H	PS	12.6		2.3
V75, V85	V	PS		11.8	
BWS414	H + V	SPS	97.5	22.4	3.3
BWS416	H + V	SPS	37.1	64.5	-0.2
BWS517	H + V	SPS	21.5	100.3	-0.3
BWS519	H + V	SPS	83.4	27.4	0.0
BWS521	H + V	SPS	48.5	49.8	2.2

$400\,W$ DC motor allows a fast acceleration and deceleration of the fork on which the wire is fixed. The motor rotation is converted into a linear displacement of a rod transmitting the movement to the shaft holding the wire fork. This rod passes through the air-vacuum border which is established by bellows.
The motor angular position is detected by a resolver (see Section 3.2) mounted on the motor axis, and its signal is treated by an embedded CPU which provides the correspondent wire position. The wire speed is selectable among three values: 10, 15 and $20\,m/s$. To overcome errors due to mechanical imperfections, the uncertainties are characterized in a laboratory calibration setup. A calibration curve between measured and real wire position is determined for all the selectable wire speeds.
The amplitude signal is measured by detecting the shower of secondary particles created by the wire-beam interaction (by mean of a scintillator-photomultiplier setup) or by measuring the secondary emission currents on the wire. The second method is particularly useful at the PSB proton injection energy ($50\,MeV$), which is below the threshold of the production of pions that populate the showers of secondary particles. In addition to this, for reduced interaction rates and large angular distributions, it is difficult to detect the shower of secondary particles.
The wire position is sampled in synchronization with the amplitude signal at a constant sampling period of $2\,\mu s$.
More information about the hardware and software chosen for these instruments can be found in [25].

4.1.2 SPS monitors

In the SPS, two different mechanism are used for the wire scanner monitors. The first provides a linear movement of the wire along a direction orthogonal to the beam reference trajectory, while the second a rotational one. All of them use DC motors and are equipped with carbon fibers of $30\,\mu m$ diameter[1].
The linear devices are limited to a maximum speed of $1\,m/s$ and their safe operation is limited to proton intensities below about $5 \cdot 10^{12}$. Above this intensity the protons energy transfer to the wire causes its sublimation[2].
The speed of the rotational wire scanners can be selected from 1 to $6\,m/s$ and the wire integrity is preserved for all the beam intensities currently injected in the SPS.
For both systems the motor shaft rotation angle can be measured by a potentiometer. In addition, the linear monitors are equipped with an optical ruler (see Section 3.2) which guarantees a better signal over noise ratio.
The rotational monitors require an algorithm that transforms the wire angular position into the linear coordinate along the transverse plane of interest, see Section 8.1.
The wire-beam interaction rate is detected by a scintillator-photomultiplier setup that acquires the secondary particles shower intensity.
At every revolution period of the particles in the ring, which is about $23\,\mu s$, the wire position is recorded once[3] while the intensity signal can be acquired in correspondence of the passage of only a portion of the beam (see pag. 59).
Fig. 4.2 shows one of the SPS linear wire scanners in the initial parking position. As visible from the picture, the wire has a copper coating on each side, extending for about $2\,cm$. This is done in order to protect the very thin carbon wire while clamping it to the fork. The coating is done in an electrolytic bath, after depositing a thin layer of chromium to ensure the copper adherence.

[1] Other materials have been tested, as exposed in Chapter 6.

[2] In calculating the beam intensity damage threshold, a beam size of $1\,mm$ has been considered. With smaller beams the energy transfer density is higher and potentially also lower intensities can cause the wire damage.

[3] At each revolution period the wire can be considered at rest with respect to the particles.

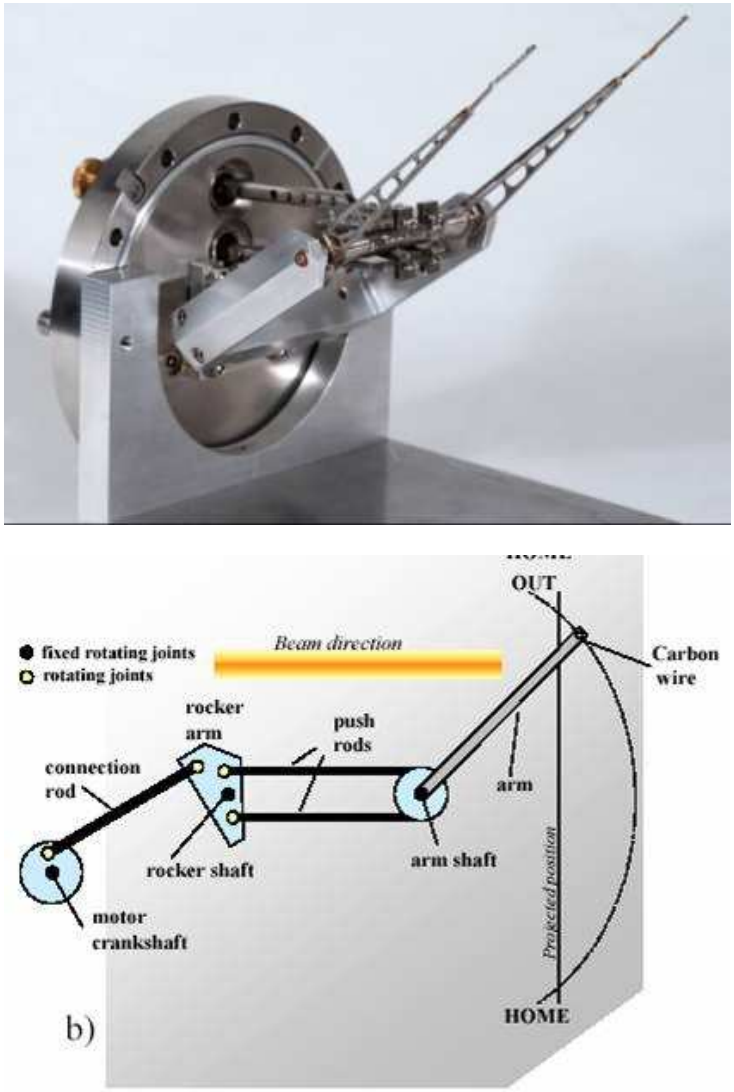

Figure 4.1: Picture and schematic drawing of the PS/PSB flying wire mechanism.

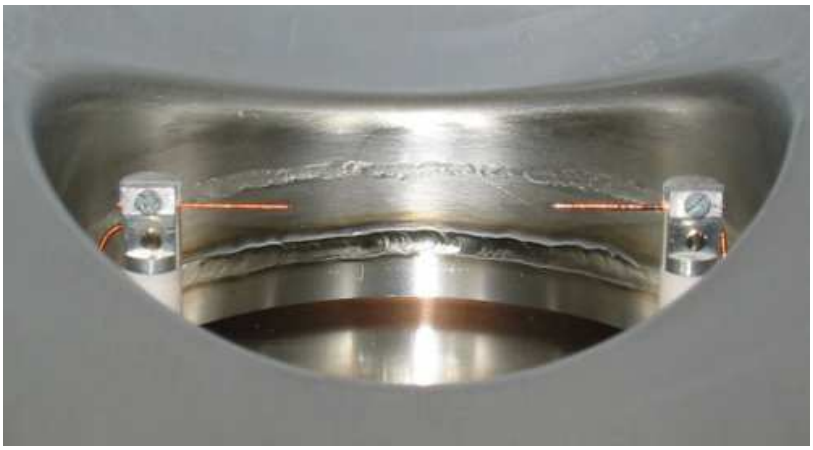

Figure 4.2: A SPS linear wire scanner in its initial parking position.

A picture of a SPS rotational wire scanner device is presented in Fig. 4.3.

Figure 4.3: SPS rotational wire scanner mechanism.

Intensity signal acquisition modes

Fig. 4.4 shows the intensity signal detected during one wire scan when four PS batches are circulating in the SPS. As the wire encounters the tails of the particles distribution, the photomultiplier signal starts to increase[4] (after $50\,\mu s$ on the plot). At each turn in the SPS, the time interval between the beginning of the first PS batch and the end of the fourth is about $8\,\mu s$, which corresponds to about $35\,\%$ of the particles revolution period. Therefore $65\,\%$ of the ring is empty, as can be seen in the plot: the signal is repeated every $23\,\mu s$ and has maximum amplitude when the wire crosses the core of the transverse distribution.
The data acquisition system of the SPS wire scanner monitors has been designed to gate, turn by turn, individual portions of the particles distribution along the ring. Therefore, for each revolution, the wire position can be correlated to different longitudinal sections of the beam, providing more than one transverse profile per scan.
The particles bunching and distribution along the SPS ring is described in Chapter 1. For instance, during one nominal beam transfer from the SPS to LHC, the SPS is filled with 4 PS batches of 72 bunches of protons each. The acquisition gates must respect a minimum duration ($225\,ns$) and a minimum spacing ($675\,ns$), imposed by the time needed to detect the intensity signals and store them. Hence, with the present instrumentation, it is not possible to distinguish individual bunches, which are spaced of $25\,ns$. The electronics in preparation for LHC profits of a $40\,MHz$ sampling frequency, suitable for such purpose.
The intensity signal and the acquisition gates, over one turn of the particles in the SPS, are plotted in Fig. 4.5(a) and Fig. 4.5(b). They show two gating examples , one selecting single batches and one detecting two portions of a batch and the beginning of the following. Such signals give also information about the batch populations, which are fairly constant in the second case (Fig. 4.5(b)), while are increasing in the case of Fig. 4.5(a). Such variation of the batch intensities is normally observed when the accelerator parameters are not properly set at injection energy. In fact this signal has been acquired just after the fourth batch injection; the other three batches already circulated in the machine for several seconds and suffered particles losses.
The intensity signal within the gate width can be acquired with two alternative modes: i) with a peak detector which discriminates the maximum amplitude in the considered interval, or ii) with a integrator detecting the signal rise from the beginning to the end of the gate.

[4]The signal is negative because the electrons collected on the photomultiplier anode result in a negative current.

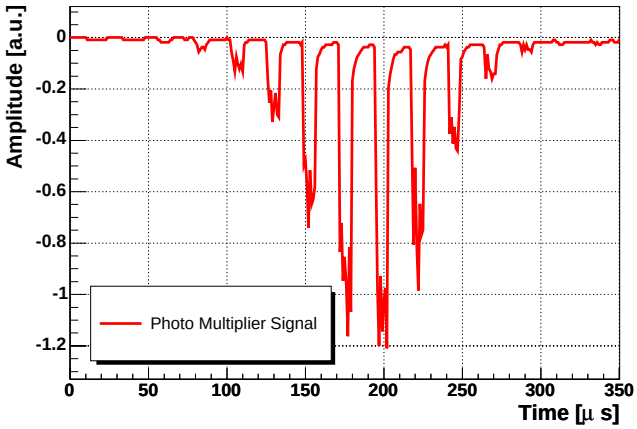

Figure 4.4: Photomultiplier current detected during one SPS wire scan.

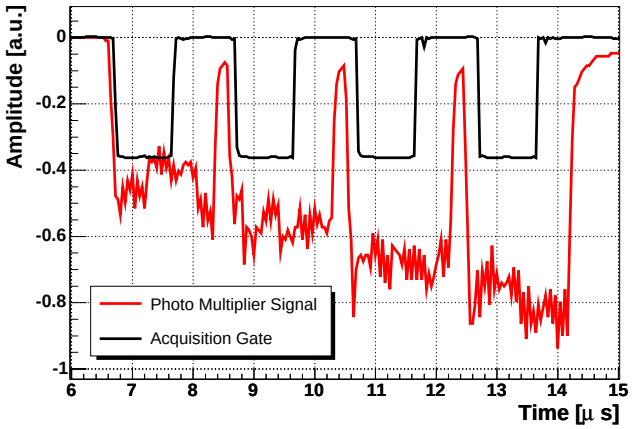

(a)

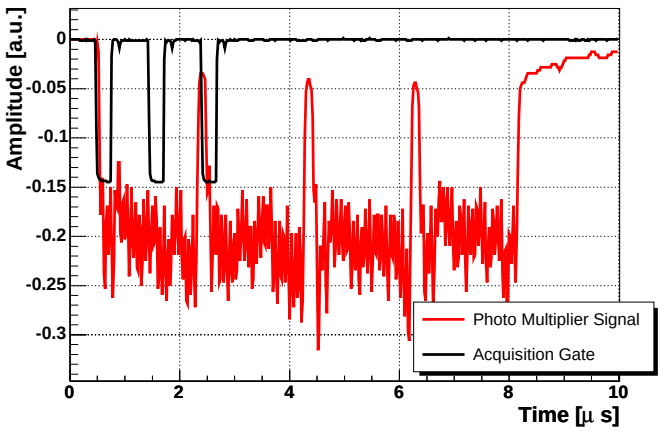

(b)

Figure 4.5: Photomultiplier signal and acquisition gate signal during the passage of the 4 PS batches in the SPS: (a) signal gating on the first part of each batch and (b) on the beginning of the first two batches and on the middle of the first.

4.2 Ionization Profile Monitor

The principle of operation of a Ionization Profile Monitor (IPM) is described in Chapter 3.
Two IPMs are currently installed in the SPS ring, monitoring the horizontal and vertical particles distribution. Their label and the optical functions at their location are listed in Table 4.2. In the following we will give an overview of the most recent device, the one measuring the vertical beam size.

Table 4.2: Optical functions of the two ionization profile monitors installed in the SPS

Monitor Label	**Measuring Plane**	$\beta_{\mathbf{x}}\,[\mathbf{m}]$	$\beta_{\mathbf{y}}\,[m]$	$\mathbf{D_x}\,[m]$
IPMP41696	H	26.2	86.5	-0.3
BPV51708	V	20.9	102.7	-0.3

The electrons produced by the rest gas ionization are attracted perpendicularly to the beam direction by mean of high voltage electrodes. Referring to Fig. 4.6(a), the beam is passing between the two metal plates, the anode and the cathode. A rectangular frame placed on the anode is hosting a Micro Channel Plate (MCP), which collects the electrons. A schematic drawing of the MCP is shown in Fig. 4.6(b).
The electrons are multiplied along the MCP, by applying a voltage between its input and output, which can vary from few tens of volt to several hundreds. The basic parameters of the currently used MCP are [44]:

- Dimensions $(H \times V)$: $5 \times 5\,cm$;
- Pitch spacing (center to center): $32\,\mu m$;
- Maximum voltage: $1000\,V$;
- Gain : $> 4 \cdot 10^3$.

At the MCP output a phosphor converts the electrons into photons in the visible wavelenght range. The phosphor material in 2003 was $CdS : In$. It was chosen for its very fast decay time (less than $1\,ns$ to decrease to $10\,\%$ of the maximum intensity). However such material has a low efficiency[5]. In 2004 it was substituted with $Y3Al5O12 : Ce$ [45] (commercially named *P46*), which, despite its slower decay time (about $300\,ns$ to go down to $10\,\%$), provides a better efficiency. This choice, together with other adjustments, lead to the monitor accuracy improvements exposed in Chapter 8.
The phosphor emits photons in the visible range (for the P46 phosphor the spectrum is between 490 and $620\,nm$, with a maximum intensity at $530\,nm$). The photons are then focused on a *Charged Coupled Device* (CCD camera), which is imaging the signal as described in Chapter 3. The CCD has a matrix of 576×288 pixels [46], with a pixel size of $20 \times 30\,\mu m$.
The camera produces an image every $20\,ms$ and needs other $20\,ms$ to transfer the data to the storage server. Hence the monitor provides an image every $40\,ms$ which corresponds to about 1700 particles revolutions in the SPS.
A fast acquisition mode, intended to provide a turn-by-turn profile tracking is under development. It substitutes the CCD camera with a multi anode photo multiplier tube [47]. This detector is capable of sampling the output current at $40\,MHz$ (sampling frequency required to select single LHC bunches). With this acquisition mode the resolution is limited to $1\,mm$ and the signal over noise ratio is quite poor due to the very short integration period.
Fig. 4.7 shows an image acquired with the IPM (in CCD camera mode) and the correspondent projection on the vertical plane, which results in the beam profile.

[5]The efficiency depends on the phosphor material together with other parameters like grain size and layer thickness

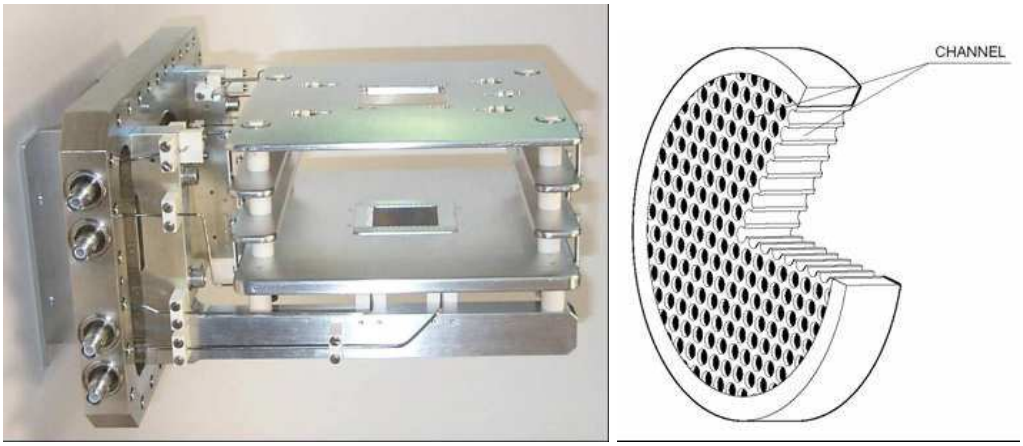

(a) (b)

Figure 4.6: (a) Picture of the IPM high voltage electrodes with the rectangular hole hosting the MCP. (b) Schematic drawing of a MCP. Each channel provides electron multiplication keeping track of the location of the incoming primary electrons.

The high voltage electrodes, the MCP and the phosphor are in vacuum. A window with very high transmission for visible light wavelenghts, acts as interface between vacuum and the normal pressure environment, in which are installed the other components.
The so called *electron cloud* has been observed in the SPS during the last few years [48]. This phenomenon concerns the electron multiplication at the surface of the beam pipe after the production of a primary electron which, radially accelerated by the beam passage, hits the surrounding materials. A number of secondary electrons is produced, depending on the secondary emission yield (SEY) of the material. Two main processes lead to the generation of the primary electrons: rest gas ionization and synchrotron radiation hitting the beam pipe walls. The first is dominant in the SPS and the second will be dominant in the LHC.
If an electron cloud is generated at the IPM location, the monitor primary signal is degraded: the secondary electrons are collected on the MCP together with the ionization electrons and the beam image results corrupted.
Such effect is identifiable while changing the beam intensity and above all the bunch spacing. The presence of electron cloud was observed in 2002 in the SPS IPM. For this reason the electrodes surface has been coated with a special material called NEG (a $TiZrV$ compound) with the aim of reducing the secondary emission of electrons from the surface material [49].

The tank hosting the core part of the device is surrounded by a dipole magnet which is necessary to avoid the electrons divergence from the direction orthogonal to the beam trajectory. The electrons drift toward the high voltage electrode spiraling about the magnetic field lines. The magnet dimensions

Table 4.3: IPM dipole magnet parameters

Magnet Dimensions	$681 \times 646 \times 680\, mm^3$
Gap Width	$200 \times 200\, mm^2$
Maximum Current	$55\, A$
Maximum Dipole Field	$0.240\, T$
Strength at nominal field	$0.14\, Tm$

and parameters are listed in Table 4.3.
A schematic drawing of the magnet is illustrated in Fig. 4.8. The figure also evidences the hole which

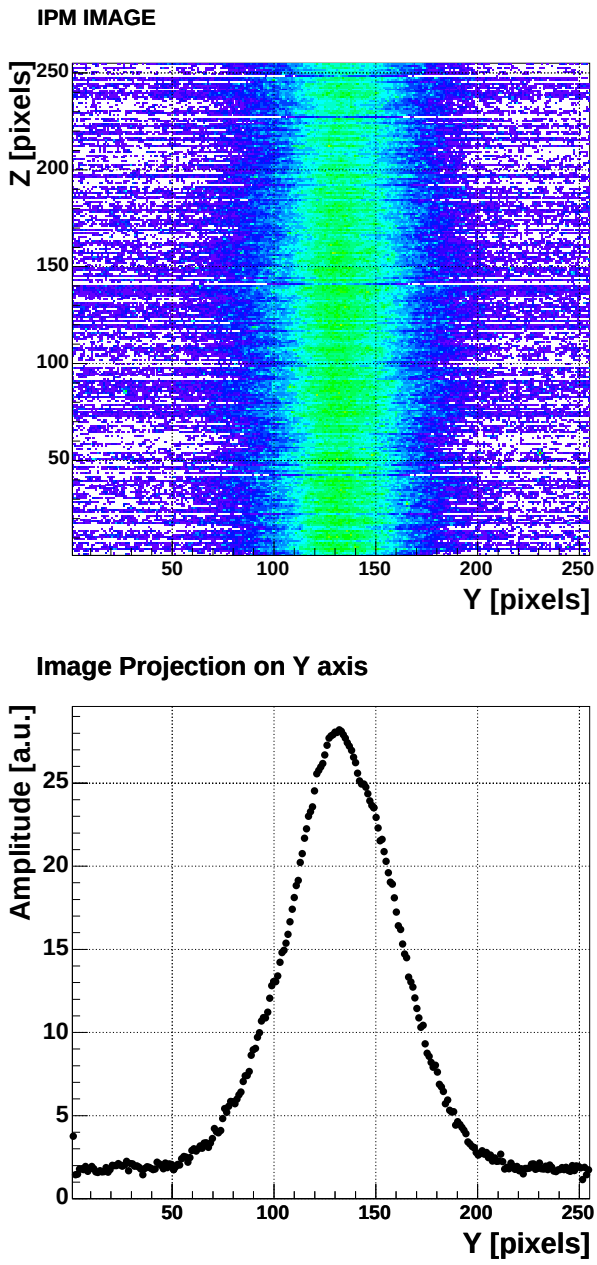

Figure 4.7: Image acquired with the SPS IPM and its projection on the vertical plane. The beam is moving along z axis.

is machined on the magnet top in order to extract the light signal.
The dipole magnet obviously bends the beam orbit. Two other dipoles are placed upstream and downstream the IPM, in order to compensate the orbit bending. The IPM and the two corrector magnets are shown in Fig. 4.9, a side view of the SPS tunnel location where the monitor is installed.

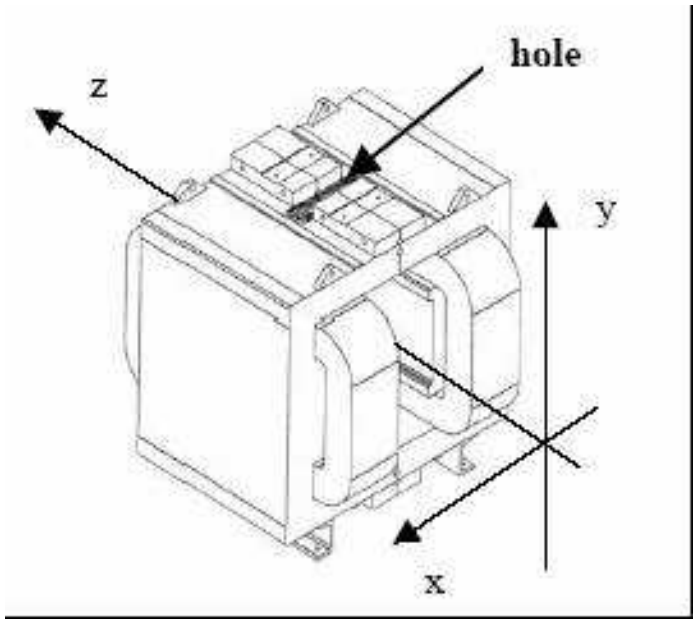

Figure 4.8: Schematic drawing of the IPM dipole magnet.

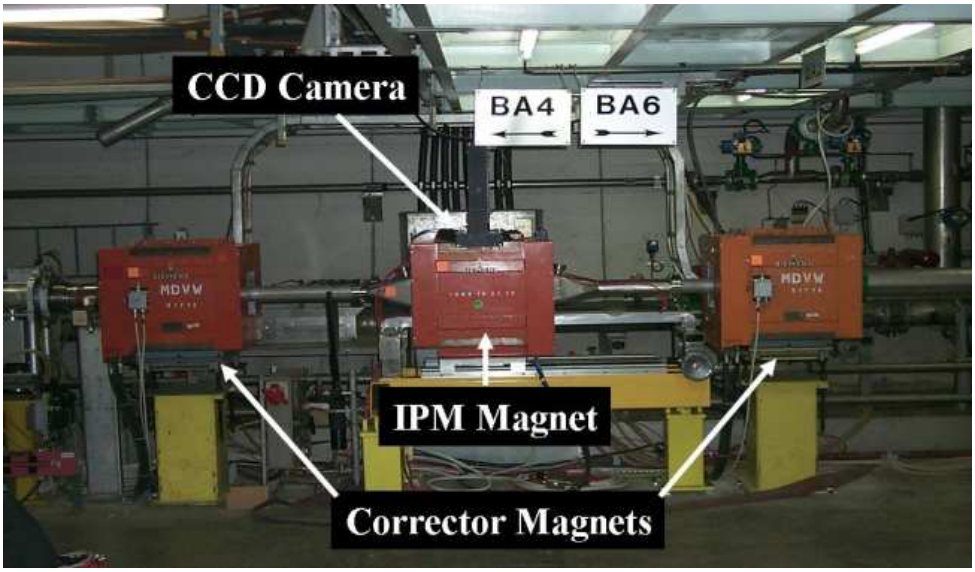

Figure 4.9: The IPM and the two corrector magnets as installed in the SPS tunnel.

Chapter 5

Emittance Increase due to the Operation of the Wire Scanner Monitors

Despite the invariant definition of the normalized emittance, during the real operation of the machine there are a variety of processes which lead to an emittance growth. In some cases a single abrupt change of the particles distribution in phase space results in a larger phase space area demanded by the beam. Other phenomena can continuously afflict the particles oscillations in the transverse plane. The following sections will discuss the effect of Coulomb scattering on the beam transverse distribution. Analytical predictions of the emittance increase during a wire scanner measurement will be compared with experimental measurements carried out in the SPS.

5.1 Coulomb Scattering

Charged particles traversing a material are elastically[1] scattered by the time-averaged potential created by the atomic nucleus of the material and its associated electrons. This process is well described by the Coulomb scattering theory. In the following we will assume to be in the *Multiple Coulomb Scattering* regime. Under this assumption the incoming charged particles undergo many small-angle deflections and emerge from the material at a small angle which is the cumulative statistical superimposition of a large number of deflections. With a much lower probability a collision of the particles with the material can result in a large deflection angle and the process falls in the *Single Scattering* regime. For a detailed treatment of this second case the reader can refer to J.D. Jackson's *"Classical Electrodynamics"* [50].
Fig. 5.1 shows a particle with charge e approaching a target nucleus with total charge Ze. The particle has speed v and impact parameter b. The Coulomb repulsion (or attraction) induces a change of the particle direction by an angle θ.
Such process is described by the *Rutherford scattering* cross section formula, which for small angles reads:

$$\frac{d\sigma}{d\Omega} = 4\left(\frac{Ze^2}{4\pi\epsilon_0 pv}\right)^2 \frac{1}{\theta^4}. \tag{5.1}$$

where the differential cross section $d\sigma/d\Omega$ represents the area $d\sigma$ provided by a target particle for scattering an incident particle into the solid angle $d\Omega$.

Coulomb scattering allows to study the case of a thin layer of material through which a particle passes, interacting with many atoms on its way.

[1] In the cases analyzed in this work, we will neglect the energy loss of the high energy incident protons.

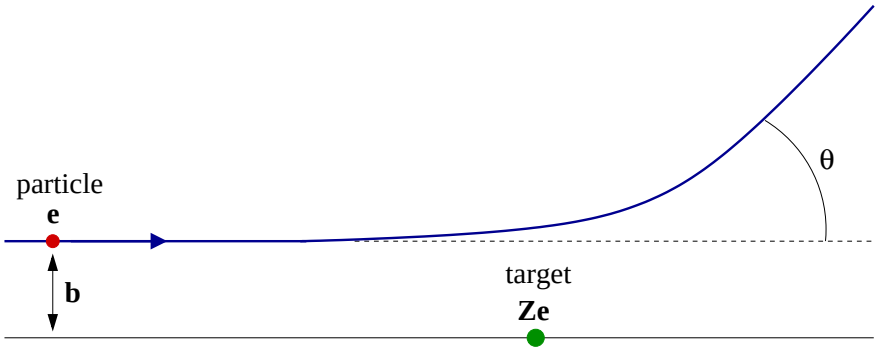

Figure 5.1: Coulomb scattering of a particle with charge e approaching a nucleus with total charge Ze. b is the impact parameter and θ the scattering angle.

For each interaction the particle transverse position changes very little, while its direction varies according to Eq. (5.1). When considering one scattering center, the variance of the particle's scattering angle is given by:

$$\langle\theta^2\rangle_1 = \frac{\int_{\theta_{min}}^{\theta_{max}} \theta^2 (d\sigma/d\Omega) d\Omega}{\int_{\theta_{min}}^{\theta_{max}} (d\sigma/d\Omega) d\Omega} \tag{5.2}$$

The limits of integration correspond to

$$\theta_{min} \approx \frac{Ze^2}{2\pi\epsilon_0 pva} \tag{5.3}$$

$$\theta_{max} \approx \frac{Ze^2}{2\pi\epsilon_0 pvR} \tag{5.4}$$

where a is the radius of the target atom and R is the radius of the target nucleus. Recovering $d\sigma/d\Omega$ from Eq. (5.1), noticing that $d\Omega = 2\pi d\theta$ and $\theta_{max} \gg \theta_{min}$,

$$\langle\theta^2\rangle_1 = 2\theta_{min}^2 ln(\theta_{max}/\theta_{min}) = \tag{5.5}$$

$$= 8Z^2 r_e^2 \left(\frac{m_e c^2}{pv}\right)^2 \frac{ln(a/R)}{a^2} \tag{5.6}$$

where $r_e = e^2/(4\pi\epsilon_0 m_e c^2)$ is the classical radius of the electron. Considering now the contributions of scattering with centers within the radius a and through a material with thickness d, the variance of the scattering angle distribution becomes

$$\langle\theta^2\rangle = \frac{N_A}{A}\rho(d\pi a^2)\langle\theta^2\rangle_1 \tag{5.7}$$

ρ and A being the density and the atomic weight of the material. N_A is the *Avogadro's number*.
When dealing with radiation processes, lengths are often expressed in units of the *radiation length* L_{rad} defined as the mean distance over which a high energy electron looses all but $1/e$ of its energy by bremsstrahlung. It is generally measured in g/cm^2 and is tabulated for various materials.
It is rigorously expressed as:

$$\frac{1}{L_{rad}} \equiv 2\alpha\frac{N_A}{A}\rho Z^2 r_e^2 ln\frac{a}{R}, \tag{5.8}$$

where $\alpha \approx 1/137$ is the fine structure constant. With this definition the variance of the scattering angle distribution becomes

$$\langle\theta^2\rangle = \frac{4\pi}{\alpha}\left(\frac{m_e c^2}{pv}\right)^2 \frac{d}{L_{rad}} = \left(\frac{E_s}{pv}\right)^2 \frac{d}{L_{rad}} \tag{5.9}$$

in which $E_s = m_e c^2 \sqrt{4\pi/\alpha} = 21.2\,MeV$. This formula was obtained in 1941 by Rossi and Greisen [51]. Later, experimental data showed that this approximation has an error of more than $30\,\%$ for many values of Z and does not consider the particles path length during the scattering process. Highland proposed in 1975 another model which includes a correction for the number of radiation lengths [52],

$$\langle\theta^2\rangle = \left(\frac{E_s}{pv}\right)^2 \frac{d}{L_{rad}} \left[1 + \delta\, ln\left(\frac{d}{L_{rad}}\right)\right]^2 \tag{5.10}$$

The value of the logarithm coefficient δ was precisely calculated by Lynch and Dahl in 1990 [53], using Montecarlo simulations. Their work provided $\delta = 0.038$, with an error smaller than $11\,\%$ for every value of Z, and for $10^{-3} < d/L_{rad} < 100$. They also provided an estimation of the quantity $E_s = 19.2\,MeV$, based on the form factor α evaluation at 1 radiation length rather than 0.1 radiation lengths. These values are also the ones cited in the most recent *Review of Particle Physics* [54] and are the ones we will adopt.
So far scattering has been considered through solid angles. Applying a projection on the transverse plane, leads to the decomposition

$$\langle\theta^2\rangle = \langle\theta_x^2\rangle + \langle\theta_y^2\rangle = 2\langle\theta_x^2\rangle \tag{5.11}$$

It follows that the variance of the scattering angle in one transverse direction is

$$\langle\theta_x^2\rangle = \left(\frac{13.6\,MeV}{pv}\right)^2 \frac{d}{L_{rad}} \left[1 + 0.038\, ln\left(\frac{d}{L_{rad}}\right)\right]^2 \tag{5.12}$$

It must be remarked that the logarithmic correction term diverges to $-\infty$ when the ratio $d/L_{rad} \ll 1$. Its accuracy is therefore arguable for small material thicknesses.
In the same publication, Lynch and Dahl also formulated an estimation which is not directly dependent on the material radiation length. Such estimation has been later implemented in the Monte Carlo program named GEANT. Even if this program has not been used for any result presented in this work, we introduce here the analytical relations adopted in the scattered particles distribution generator:

$$\chi_{cc}^2 = (0.3961 \cdot 10^{-3})^2\, Z \frac{\rho}{A}\, [GeV^2 cm^{-1}] \tag{5.13}$$

$$\langle\theta_x^2\rangle = 6.538\, \chi_{cc}^2 \frac{d}{(pc\beta^2)^2} \tag{5.14}$$

where ρ, A and Z are the material density, atomic weight and charge number.
In the next sections we will use Eq. (5.12) and Eq. (5.14) to predict the emittance increase induced by the operation of the SPS wire scanner monitors and compare the prediction with experimental measurements.

5.2 Prediction of the emittance increase during a wire scanner measurement

During a wire scanner measurement, when the beam particles hit the wire, they experience collisions with its atoms provoking Coulomb and nuclear scattering. This may deflect a particle strongly enough to make it leave the nominal beam orbit. Scattering at smaller angles results in a widening of the particles distribution and to the consequent emittance growth. Therefore, the passage of the wire through the particles beam may cause two effects: 1) beam losses with a consequent beam intensity reduction with a possible emittance reduction and 2) transverse emittance increase.
Losses greater than 10^{-3} of the beam intensity can be detected by the beam current diagnostics. No losses were observed during the wire scanners operation.
Emittance growth is determined by the process which is predominant in the beam-wire interaction: *Multiple Coulomb Scattering*, discussed above. This results in a change of direction of the incident particle, leaving unchanged its energy and its position.
The effect of Coulomb scattering is described in [55] for a beam passing through a vacuum window and is here adapted and applied to the wire scanners case.
Recalling the emittance definition in phase space explained in Section 2.3, the effect of Coulomb multiple scattering can be depicted as a change of a particle's phase space angle. This results in a jump to another ellipse in phase space and the change is governed by the statistics of the scattering process. The effect of the process is illustrated in Fig. 5.2 in which the phase space is converted from the coordinates (x, x') to the normalized coordinates $(x, \beta x' + \alpha x)$; in the new coordinate system the ellipse in phase space becomes a circle. Referring to the figure and initially considering the beam before the wire-beam interaction, the i^{th} particle follows a trajectory on the circle with a radius ρ_i and a transverse size:

$$\sigma_0(x) = \sqrt{\langle x^2 \rangle} = \sqrt{\frac{\rho^2}{2}}. \tag{5.15}$$

After one passage of the beam through the wire, the particle's trajectory amplitude changes from ρ_i to a_i, with (see Appendix A.3):

$$a_i^2 = \rho_i^2 + (\beta_x \Delta\theta_i)^2 + 2\rho_i \beta_x \Delta\theta_i sin\phi \tag{5.16}$$

in which β is the betatron function at the monitor location and $\Delta\theta_i$ is the deflection angle due to Coulomb multiple scattering. ϕ_i is the particle's phase angle describing its phase space rotations and is uniformly distributed among all the particles; it is therefore uncorrelated with ρ_i and $\Delta\theta_i$. Averaging over all the particles leads to:

$$\begin{aligned} \langle a^2 \rangle &= \langle \rho^2 \rangle + \beta_x^2 \langle \theta_x^2 \rangle + 2\beta_x \langle \rho \rangle \langle \theta_x \rangle \langle sin\phi \rangle \\ &= \langle \rho^2 \rangle + \beta_x^2 \langle \theta_x^2 \rangle \end{aligned} \tag{5.17}$$

where the scattering angle θ_x and $\sin\phi$ average to zero as there is not preferred angle.
This process brings each particle to oscillate in phase space with different amplitudes. The new equilibrium in phase space is described by another circle in a new normalized coordinate system. The consequent transverse amplitude is

$$\sigma_f^2(x) = \langle x^2 \rangle_f = \langle \frac{\rho^2}{2} \rangle + \frac{1}{2}\beta_x^2 \langle \theta_x^2 \rangle \tag{5.18}$$

$$= \sigma_0^2(x) + \frac{1}{2}\beta_x^2 \theta_{rms}^2 \tag{5.19}$$

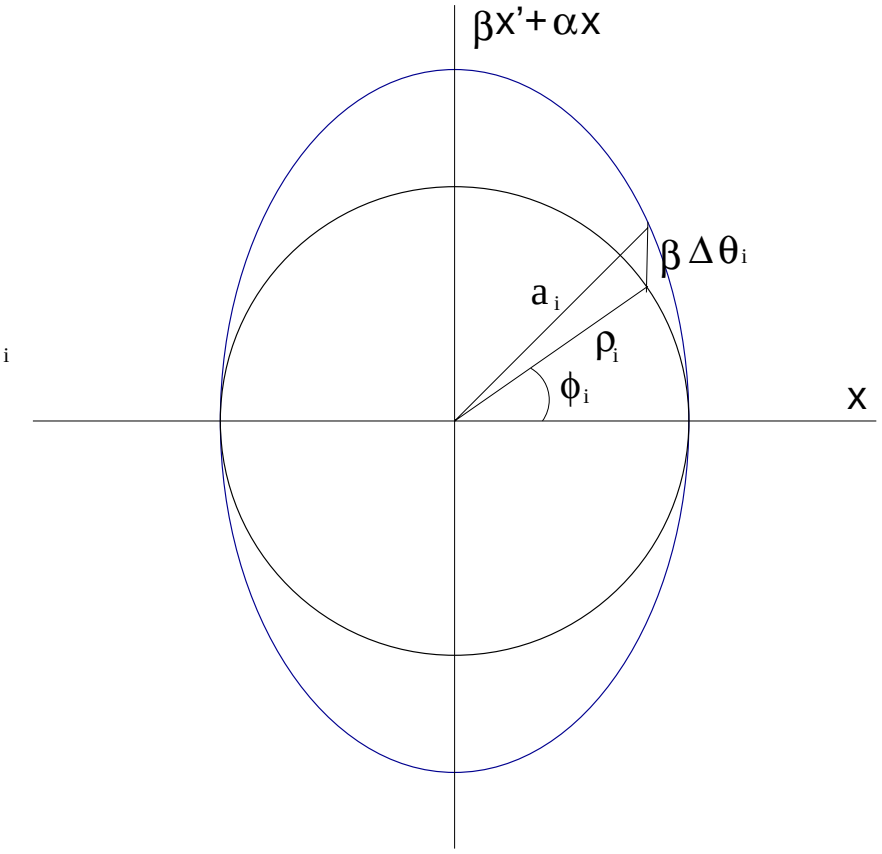

Figure 5.2: Effect of Coulomb scattering seen in a normalized phase space diagram. The two curves can be seen as the beam envelopes before and after (at equilibrium) the interaction with the wire.

where $\langle\theta_x^2\rangle \equiv \theta_{rms}^2$ is the RMS scattering angle due to Coulomb multiple interactions. From the normalized emittance defined as $\epsilon_n = \sigma^2/\beta_x \cdot (\beta\gamma)$, the emittance growth results to be:

$$\Delta\epsilon_n = \frac{\Delta\sigma^2}{\beta_x}(\beta\gamma) = \frac{1}{2}\beta_x\theta_{rms}^2(\beta\gamma) \tag{5.20}$$

Such emittance change is induced by one passage of the beam particles through the wire material. However, during one measurement with a wire scanner device the wire and each particle may interact many times. The number of passages of the beam particles through the wire depends on the revolution frequency f_r, the wire speed v and the wire diameter d, and precisely is $n = d \cdot f_r/v$. In order to estimate the emittance growth this factor has to be introduced in Eq. (5.20).
The parameter n also expresses the probability of a single particle to encounter the wire during one scan [56]. If the beam is populated by N particles, $N_{hit} = n \cdot N$ represent the number of particles hitting the wire in one scan; with the assumption of initial phases uniformly distributed, N_{hit} does not depend on the betatron tune.
In addition, to take into account that the beam particles traverse a different thickness every turn, we introduce an equivalent diameter d_e, which provides the average crossed thickness. Formulating the wire half circumference as $f(x) = \sqrt{r^2 - x^2}$ with $-r < x < r$, where r is the cross section radius, the equivalent diameter is found averaging over the cross section,

$$d_e = \frac{2\int_{-r}^{r} f(x)dx}{\int_{-r}^{r} dx} = \frac{2\pi r^2/2}{2r} = \frac{\pi d}{4}. \tag{5.21}$$

In conclusion, for a single scan, the normalized emittance growth can be expressed as:

$$\Delta\epsilon_n^{x,y} = n\,\frac{1}{2}\beta_{x,y}\,\langle\theta_{rms}^2\rangle\,(\beta\gamma) \tag{5.22}$$

$$= \frac{\pi\,d\,f_r}{4\,v}\,\frac{1}{2}\beta_{x,y}\,\langle\theta_{rms}^2\rangle\,(\beta\gamma) \tag{5.23}$$

The subscripts *x,y* specify the two transverse planes. The quantity θ_{rms}^2 in Eq. (5.20) is calculated from the r.h.s of Eq. (5.12) or Eq. (5.14).
A series of particles tracking simulations have been implemented in order to verify the analytical prediction provided by Eq. (5.22). The RMS scattering angle is an input of the simulations and the agreement between the simulations and the analytical prediction is better than $1\,\%$ when using Eq. (5.12) or Eq. (5.14) for the two approaches [57].

5.2.1 Experimental results

The emittance increase due to the operation of the wire scanner monitors has been observed in the SPS. At first it has been measured with a small emittance beam with momentum $p = 26GeV/c$. For a number of times, two scans have been performed with a $4.5\,s$ interval. After the second scan the beam has been damped and new particles injected. The results are plotted in Fig. 5.3. The measurements have been performed with the monitor BWS517V which scans in the vertical plane, where the betatron function β_y is equal to $100\,m$.
This instrument is equipped with a $d = 30\,\mu m$ wire that moves at $1\,m/s$. Since the radiation length of Carbon is $L_{rad} = 18.9\,cm$, the ratio d/L_{rad} results only about $1.5 \cdot 10^{-4}$ and the logarithmic term in Eq. (5.12) tends to diverge.
The emittance increase due to a single scan can be calculated using three analytical predictions differing for the RMS scattering angle approximation:

1) using Eq. (5.12) *with* the logarithmic term correction;

2) using Eq. (5.12) *without* the logarithmic term correction;

3) using Eq. (5.14).

The three correspondent values (following from from Eq. (5.22)) result 1) $21\,nm$, 2) $49\,nm$ and 3) $40\,nm$.
The measurements show an emittance growth of $43.5 \pm 11.8\,nm$ per scan, which is best approximated by prediction 3).
A second set of measurements aiming to characterize the effect of multiple Coulomb scattering were executed in the SPS during long periods with *coasting beam* (i.e. with the particles circulating in the ring for periods varying from few minutes to few hours[2]).
The same monitor as for the previous case (BWS517V) has been used on the circulating beam during such periods. One example of the vertical emittance evolution is illustrated in Fig. 5.4. The two plots demonstrate that the emittance increase depends on the number of scans. The top figure, in fact, shows how the growth is not linearly increasing with time, the slope is instead proportional to the frequency with which the scanner is used. The red dots result from the measured values corrected for the theoretical increase for scan. In the bottom plot the predicted evolution is superimposed to the experimental data. The emittance increase consequent to the wire scanner operation explains almost

[2]According to other name conventions, the attribute "coasting" is given to the beam when the accelerator RF system, that guarantees the longitudinal bunched structure of the particles distribution, is switched off.

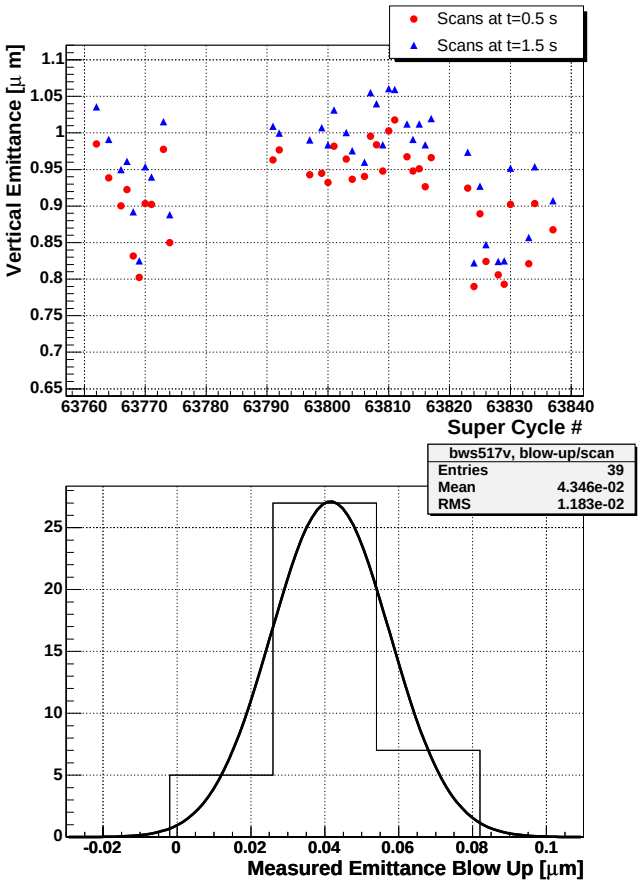

Figure 5.3: Top: vertical emittance increase due to a single scan with BWS517V as function of SPS cycle number, at each cycle new particles have been injected. Bottom: histogram filled with the emittance growths (bottom).

.

entirely the growth. The remanent emittance increase (difference between the black and the red line in the plot) can be attributed to a natural degradation of the vertical distribution during such a long period (about 1.4 hours).

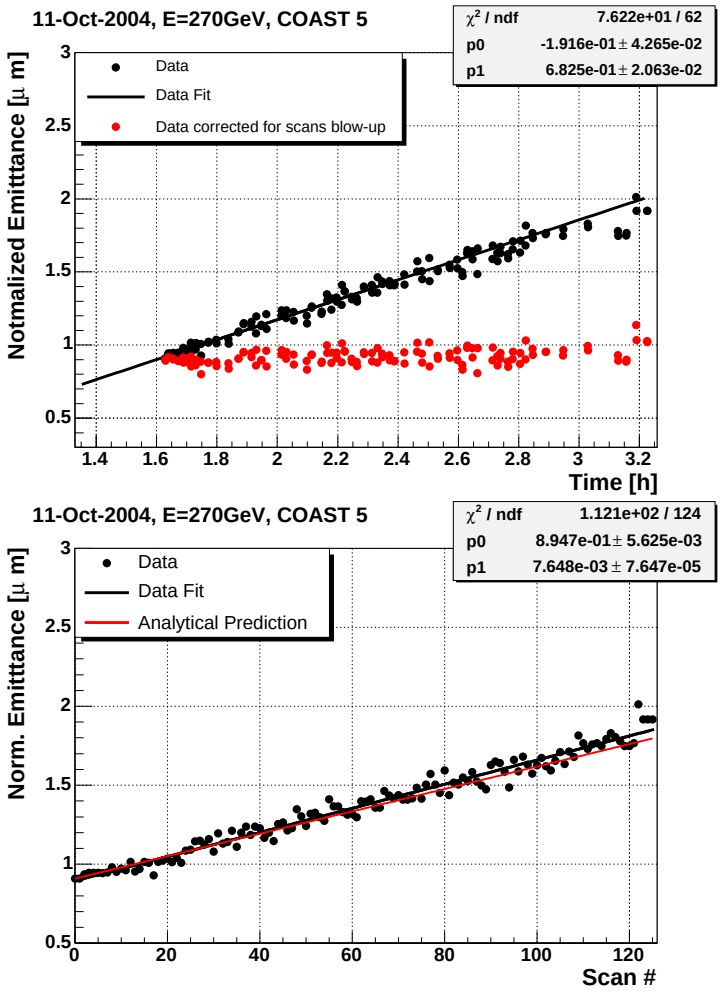

Figure 5.4: Emittance blow up due to wire scans while keeping the beam coasting in the SPS, as function of time (top) and as function of the number of scans (bottom)

5.2.2 Emittance increase predictions for the CERN rings

The prediction named "3)", described above, has been applied, for Carbon wires of $30\,\mu m$ diameter, to the PSB, PS and SPS WS, for each of them considering the nominal LHC beam normalized emittance at the injection and extraction energies. The results are displayed in Table 5.1. The two values of relative emittance growth for each plane correspond to two values of wire speed. The chosen speeds are the minimum and maximum wire velocity which can be selected in the PSB and PS, and the default velocities of the linear and rotational wire scanners in the SPS. The revolution period for each ring is indicated as t_r. The betatron amplitude functions are the actual values for the PSB and PS monitor locations[3]. For the SPS the larger betatron functions, among all the wire scanners locations, are considered.

As outlined by the values in bold in the table, there are some conditions in which operating the wire scanners may induce an emittance increase larger than $3\,\%$. The more critical cases regard the PSB wire scanner operation at injection energy and low speed, for which the emittance increase exceeds $10\,\%$.

The relative emittance change is of course larger for smaller emittance beams (i.e. pilot bunch and TOTEM beam), as will be shown later in Chapter 8.

[3] In the PSB all the monitors locations have the same betatron functions. The same applies to the PS.

	p $[GeV]$	β	t_r $[\mu s]$	d $[\mu m]$	β_x $[m]$	β_y $[m]$	$\epsilon_{x,y}$ $[\mu m]$	v $[m/s]$	$\delta\epsilon_x/\epsilon_x$ %	$\delta\epsilon_y/\epsilon_y$ %
PSB	0.3	0.914	1.67	25	5.7	4.3	2.5	10|*20*	**13.8**|***6.9***	**10.3**|***5.2***
PSB	2.1	0.915	0.57	25	5.7	4.3	2.5	10|*20*	**5.9**|*2.9*	**4.4**|*2.2*
PS	2.1	0.915	2.29	25	12.7	11.7	3.0	10|*20*	2.7|*1.4*	2.5|*1.3*
PS	26.9	0.999	2.10	25	12.7	11.7	3.0	10|*20*	0.2|*0.1*	0.2|*0.1*
SPS	26.9	0.999	23.07	30	100	100	3.5	.4|*6*	**3.0**|*0.2*	**3.0**|*0.2*
SPS	450.9	1.000	23.05	30	100	100	3.5	.4|*6*	0.2|*0.0*	0.2|*0.0*

Table 5.1: Beam emittance growth in the two transverse planes, due to the Carbon wire passage through the beam. The nominal LHC beam emittance is considered, for injection and extraction energies of the three LHC pre-accelerators and different wire velocities.

The LHC ring will be equipped with wire scanners moving at $1\,m/s$ at locations where the maximum betatron function will be about $370\,m$. The predicted emittance increase caused by one scan is about $2\,nm$ at injection energy (450 GeV), only 0.1 % of the nominal emittance. At LHC one should only worry about multiple scans on the circulating beam.

Chapter 6

Electromagnetic coupling between the proton beam and the SPS Wire Scanners

During the SPS high intensity run with the LHC beam in summer 2002 the breaking of several of the carbon wires in the wire scanners has been observed, even while resting in their parking position.
The direct energy transfer between the beam and the wire is dominated by inelastic scattering and ionization. The amount of energy lost by the protons depends on the particles energy, on the wire material properties and on the wire speed.
Estimations of the wire heating for different scanner devices can be found in [43, 58]. The beam intensity allowing the usage of the linear wire scanners is limited to $5 \cdot 10^{12}$ protons, while the calculations did not predict any wire breaking for the rotational SPS WS, even at the maximum LHC beam intensity. Indeed the monitors had been continuously operated for several years without any damage.
The breaking happened in coincidence with the injection and acceleration of the LHC type beam with nominal longitudinal parameters. This suggested first to detect the amount of wire heating during the particles passage, and then to organize dedicated laboratory measurements to understand and cure the phenomenon.
The following sections describe such studies, which went in the direction of investigating the electromagnetic coupling between the charged particles and the wires.

6.1 Observations of the rotational wire scanners wire heating

The electronic circuit shown in Fig. 6.1 has been designed to monitor the SPS wire scanners wire heating. The carbon wire is represented in the diagram by the resistor R_W which is inserted on the feedback loop of the inverting circuit using the operational amplifier A. The inverting input of the amplifier is a common ground and the amplifier input current can be considered null. Hence voltage source V_s and the resistor R_1 provide a costant current I_{in} to the feedback loop. Information about the wire heating is inferred by measuring two signals:

- the voltage V_{out}: any change of the wire resistance R_W due to temperature induces a change in V_{out} such that the voltage difference between the inputs of the operational amplifier A remains null;

- the current difference $I_{out} - I_{in}$, as measured by the voltage drops V_{R2} and V_{R3}, which can be different from zero only if the carbon wire heating is enough to generate thermionic emission of electrons.

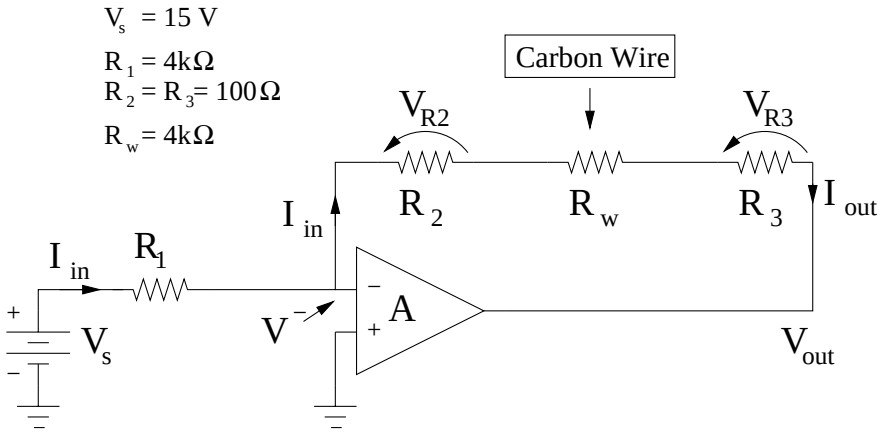

Figure 6.1: Simplified diagram of the electronic circuit detecting the wire scanners wire heating (V_{out} varies only due to the variation of the wire resistance R_W) and thermionic emission current ($I_{out} - I_{in}$).

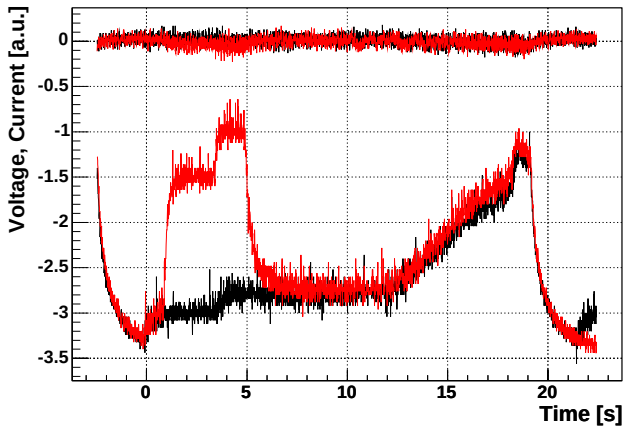

(a) Two PS batches injected in the SPS. Black curves refer to a cycle with the wire in the initial parking position, red curves to a cycle with two scans (at t=1 s and t=5 s).

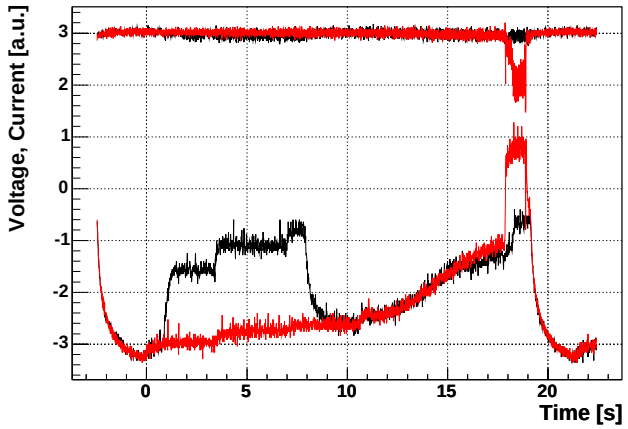

(b) Four PS batches injected in the SPS. Black curves refer to a cycle with scans at t=1 s and t=8 s, red curves to a cycle with scans at t=18 s and t=19 s.

Figure 6.2: Diagnostic signals detected on one SPS wire scanner. Bottom of each figure: Voltage (proportional to the wire heating). Top of each figure: Differential current (proportional to thermionic emission current).

Fig. 6.2(a) and Fig. 6.2(b) show the voltage (bottom lines for each plot) and differential current (top lines) evolution during the LHC cycle in the SPS. Two scans (with "forward" and "backward" directions) can be performed with each instrument during a filling cycle. One to four PS batch injections take place at $t = 0, 3.6, 7.2$ and $10.8\,s$ and the acceleration from 26 to $450\,GeV$ takes place from $t = 10.9\,s$ to $t = 18.5\,s$. During the two cycles showed in Fig. 6.2(a) two PS batches are injected and four during the two cycles of Fig. 6.2(b). The black lines of Fig. 6.2(a) refer to the voltage and differential current detected in a cycle with no WS measurements. The voltage evolution illustrates that the wire heating is noticeable even when leaving the wire in the parking position. It is thus evident that the wire heating does not depend on the wire-beam interaction, but on other beam parameters evolving during the cycle.
In particular it is possible to relate the wire heating to the beam intensity and to the bunch length which is decreasing along the beam energy ramp to 450 GeV. The width of the Gaussian distribution in the longitudinal direction varies from $\approx 1\,ns$ at low energy to $\approx 0.38\,ns$ after the particles acceleration.
At the end of the beam energy ramp a radio-frequency cavity at $800\,MHz$ is switched on in order to further decrease the bunch length. The plots show that the wire heating is very sensible to this event.
The red lines in Fig. 6.2(a) and all the curves in Fig. 6.2(b) refer to SPS cycles during which two scans were performed. In between the two scans the wire remains in a second parking position and the beam is passing through a loop formed by the wire and the fork supporting it. The voltage indicating the wire heating strongly increases during this period.
The red curves in Fig. 6.2(b) refer to a cycle with scans at $t = 18\,s$ and $t = 19\,s$ and the top curve shows that the differential current increases during the period between the two scans, indicating the generation of thermionic emission current. This case is the worst in terms of wire heating since the two factors enhance the electromagnetic coupling: the beam passage through the wire-fork loop while the wire is in the second parking position and the short bunch length at top energy.

6.2 Laboratory investigations of the wire braking causes

The measurements described in the previous section revealed that the beam bunch length variation during the beam energy increase causes a larger wire heating than the beam intensity variation. After such observation it was decided to study the electromagnetic coupling effects between the wire scanner wires and the proton beam travelling inside the wire scanner tank, which acts as a resonant cavity.
The proton beam circulating in the accelerator structure generates electromagnetic fields, with a frequency spectrum which mainly depends on the bunching structure (bunch length, bunch spacing) and is normally in the Radio Frequency (RF) range. The wire scanner tank, due to its geometry and the structure materials, allows the presence of resonating standing waves. If one or more of these modes matches a beam spectrum line, the RF power can be transmitted from the beam to the wire. The amount of transmitted power also depends on the wire material dielectric constant.
These hypothesis have been investigated through dedicated laboratory measurements which are reported in the next two paragraphs. At first a spare SPS wire scanner tank has been equipped with two probe antennas powered by a Vector Network Analyzer (VNA) in order to simulate the RF modes in the beam frequency spectrum. The following studies and measurements regarded the characterization of the wire materials dielectric constant.

6.2.1 Beam-Wire electromagnetic coupling studies

When an RF signal is applied to a network (the wire scanner tank in this case), that signal is altered in magnitude and phase. If the magnitude and phase of the signal can be compared to a known reference

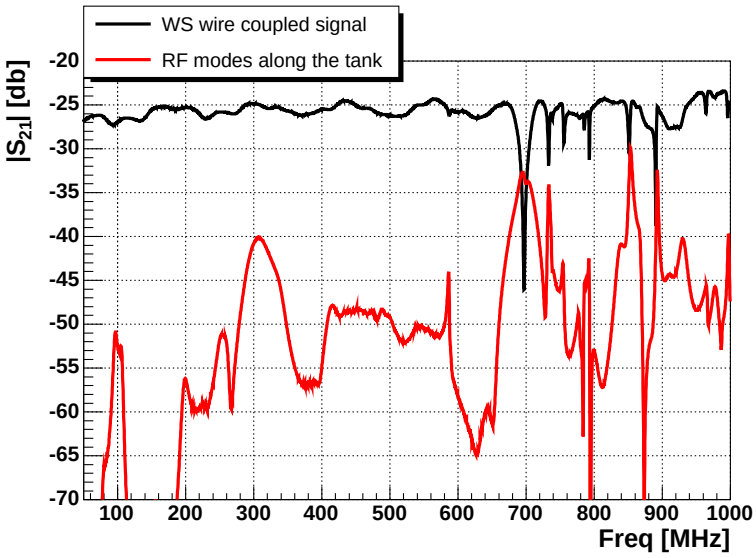

Figure 6.3: Vector Network Analyzer measurements of the SPS rotational wire scanner tank: magnitude of the transmission signal along the tank (red line) and of the differential signal at the wire ends (black line).

signal of magnitude and phase, the characteristics of that network can be evaluated. A VNA create its own signal which is used for both the reference and the network stimulus. The stimulus represents the RF power source. The measurements presented here are performed at constant source power while varying the frequency (*swept-frequency* measurement). The VNA has two ports (labelled 1 and 2, acting as transmitter and receiver) and allows to measure the so called *S-parameters*. Such parameters are complex and are defined in terms of voltage traveling waves; a two-ports device has four parameters (S_{11}, S_{12}, S_{21} and S_{22}). The magnitude of the transmission parameter S_{21} is expressed in dB, as

$$|S_{21}| = 20Log\left|\frac{V_1}{V_2}\right| \tag{6.1}$$

and is a measure of the signal coming out port 2 relative to the RF stimulus entering port 1. When the indexes are the same (e.g., S11), it indicates a reflection measurement, as the input and output ports are the same. A detailed describtion of this measuring technique can be found in [59].
With the wire scanner tank as passive network connected to the VNA, two types of configurations have been applied, both used for swept-frequency measurements. The first consisted in connecting two antenna probes to the VNA ports. The two antennas have been inserted in the tank from the longitudinally opposite extremities. The magnitude of the transmitted signal $|S_{21}|$ has been analyzed for frequencies varying between $50\,MHz$ and $1\,GHz$. This evidences the modes which resonate in the tank (i.e. the relative maxima of the signal).
The second configuration consisted in powering one antenna and connecting to the second port, as receiver, the differential signal at the WS wire ends, in vicinity of the wire fixations on the fork. The differential signal is obtained with a passive $0-180^o$ RF signal combiner. The second antenna has been matched with a $50\,\Omega$ resistor. In this case, the relative minima of the magnitude of the S_{21} signal evidence the electromagnetic coupling between the wire and the RF power source.
Fig. 6.3 shows the signals analyzed with the two configurations as function of frequency. Where the frequency of the transmitted signal matches a peak of the differential signal, the power loaded in the cavity can be absorbed by the wire. A classical way to overcome RF coupling effects in accelerators consists in damping the resonant modes with the insertion of materials, which, due to their electromagnetic properties absorb the RF power delivered by the beam. Ferrite tiles were inserted in the SPS

wire scanner spare tank and their effect investigated by measuring the transmission signal S_{21} with the first of the two measurement configurations described above. In order to understand the results it is necessary to give an overview of a resonance *quality factor* measurement. The method and the following definitions are treated in [60].
The quality factor Q is the figure of merit for characterizing a resonator at a defined frequency. It is a measure of the energy dissipation per cycle, compared to the energy stored in the fields inside the resonator, and its definition reads:

$$Q = \frac{2\pi f_0 \cdot \text{max stored energy}}{\text{loss power}} \tag{6.2}$$

where f_0 is the resonant frequency. Depending on the measurements conditions, one can distinguish between two quality factors:

- the *unloaded Q factor (Q_0)*: the value of Q obtained when only the incidental dissipation of the system elements is present;

- the *loaded Q factor (Q_L)*: the value of Q when the system is coupled to an external device that dissipates energy.

The two factors are related to each other according to

$$\frac{1}{Q_L} = \frac{1}{Q_0} + \frac{1}{Q_{ext}} \tag{6.3}$$

where Q_{ext} accounts for the power dissipated in the external device, which is in this case the VNA. At each resonant frequency the loaded Q factor is calculated by measuring the resonance central frequency (f_0) and bandwidth:

$$Q_L = \frac{f_0}{f_2 - f_1} \tag{6.4}$$

The frequencies f_1 and f_2 determine the level at which the signal amplitude decreases to $\sqrt{2}$ of its maximum.
The ratio of the power dissipated in the external circuit to the power dissipated in the resonator is called *coupling coefficient* κ and it can be written as:

$$\kappa = \frac{Q_0}{Q_{ext}} \tag{6.5}$$

When $\kappa << 1$ more power is dissipated in the network under test than in the external devices and the measurements respects a *weak coupling* condition. In this case, according to Eq. (6.3), the mesured Q_L approximates the unloaded Q factor. In practice, during the measurements in the wire scanner tank, at each resonance the antenna-probes position has been adjusted in order to reach the condition of weak coupling (S_{11} and S_{22} signals minimized to $< .5$ dB) thus allowing the calculation of the unloaded Q factor.
Different measurement configurations have been setup, some of them including the mounting of a copper wire in order to have a conductive loop and detect its influence:

- No wires mounted on the forks, no ferrite tiles inserted

- One copper and one carbon wires mounted and kept in the initial parking position, no ferrite tiles

- Two carbon wires mounted and kept in the initial parking position, no ferrite tiles

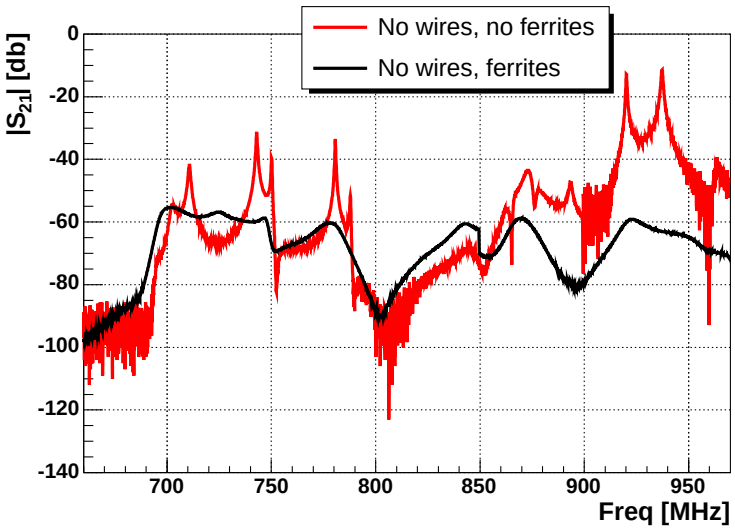

Figure 6.4: Vector Network Analyzer measurements of the SPS rotational wire scanner tank: transmission signal along the tank, before and after inserting the ferrite tiles in the tank.

- Two carbon wires mounted, the horizontal wire kept in the initial parking position and the vertical wire in proximity of the beam orbit position, no ferrite tiles
- Two carbon wires mounted, the horizontal wire kept in the proximity of the beam orbit position and the vertical wire in the initial parking position, no ferrite tiles
- No wires mounted, nine ferrite tiles inserted in the tank
- One carbon wire mounted, nine ferrite tiles inserted in the tank
- Two carbon wire mounted, nine ferrite tiles inserted in the tank

Fig. 6.4 shows two of the recorded signals, one with no wires mounted and no ferrite tiles inserted and one with no wires installed and nine ferrite tiles inserted. Fig. 6.5 summarizes the quality factors measured for all different configurations at the wire scanner tank resonance frequencies. The RF modes damping by inserting the ferrite tiles is evident[1]. After these studies all the SPS rotational wire scanner tanks have been filled with ferrite tiles in order to reduce the power absorbed by the wire scanners wires. The ferrite properties can be found in [61].

[1]The figure also shows a frequency shift of the resonances when the ferrite tiles are inserted. This is expected, as the dielectric constant of the materials and the geometry of the cavity change.

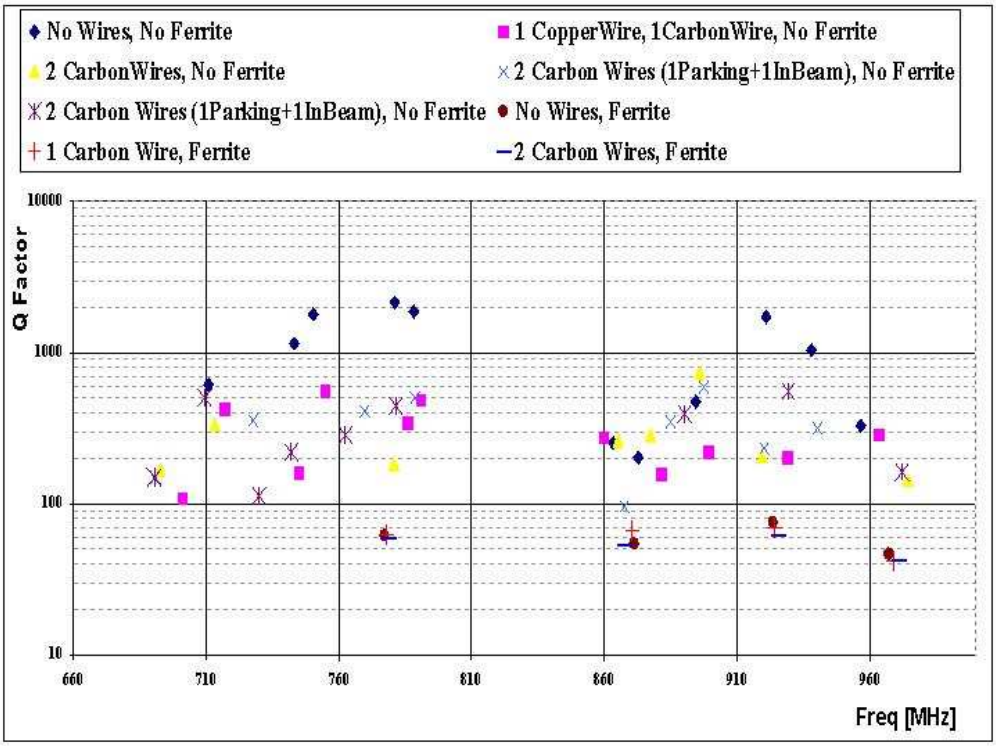

Figure 6.5: Unloaded Q factors for all the measurements setups as function of frequency

6.2.2 Material Studies

The purpose of the studies described in this paragraph is to determine the dielectric constant and the loss factor of different wire materials.
The classical cavity mode technique has been used for the determination of the complex permittivity of different wires in the range from 2-4 GHz. A VNA has been again used as RF power source and signal analyzer. As a resonator a rectangular transverse electric (TE) type device is utilized, as depicted in the drawing of Fig. 6.6. For an empty rectangular cavity the resonant frequencies can be analytically calculated according to [62]:

$$f_{mnl} = \frac{c}{2\pi\sqrt{\mu_r \epsilon_r}} \sqrt{\left(\frac{m\pi}{a}\right)^2 + \left(\frac{n\pi}{b}\right)^2 + \left(\frac{l\pi}{d}\right)^2} \tag{6.6}$$

where $b < a < d$ are the cavity dimensions, c is the speed of light, while μ_r and ϵ_r are the dielectric permeability and permittivity. The integers m, n, l are not negative and define the resonant modes. Given the cavity dimensions ($a = 72\,mm$, $b = 34\,mm$, $d = 373\,mm$) and using $\mu_r = \epsilon_r = 1$, the first two modes are $f_{110} = 2.12\,GHz$ and $f_{210} = 2.23\,GHz$.
If z is the coordinate along the shortest cavity dimension (b), the simulated transverse electric and magnetic fields of the first two modes on the surface at $z = b/2$ are illustrated in Fig. 6.2.2. The color codes (red=maximum, blue=zero) indicate that, at a given resonant frequency, where the electric field is maximum the magnetic field is zero and viceversa. In particular, at the cavity center, for every second resonant frequency the electric field is maximum and the magnetic field zero.
The complex permittivity of a material can be expressed as

$$\bar{\epsilon} = \epsilon_0 \bar{\epsilon_r} = \epsilon_0 \left(\epsilon_r^{'} - j\epsilon_r^{''}\right) \tag{6.7}$$

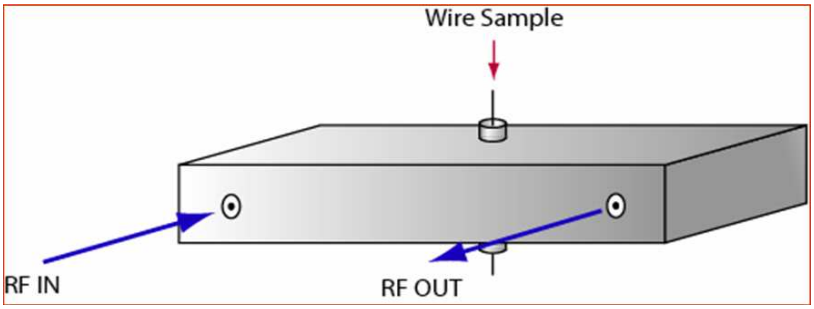

Figure 6.6: Schematic drawing of a rectangular transverse electric (TE) resonator. The RF IN and RF OUT connectors have been connected to the two VNA ports.

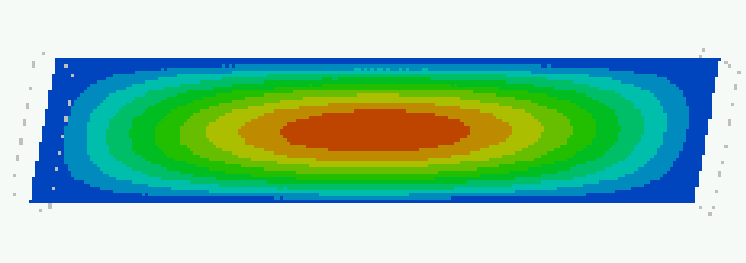

(a) Electric field at $f_{110} = 2.12\,GHz$

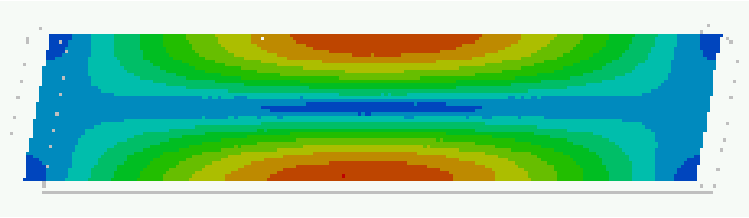

(b) Magnetic field at $f_{110} = 2.12\,GHz$

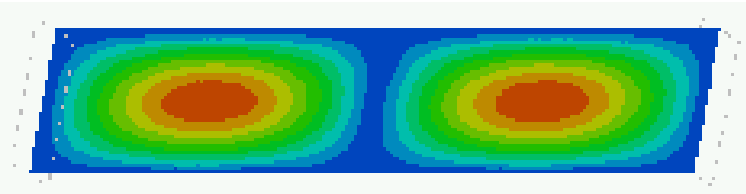

(c) Electric field at $f_{210} = 2.23\,GHz$

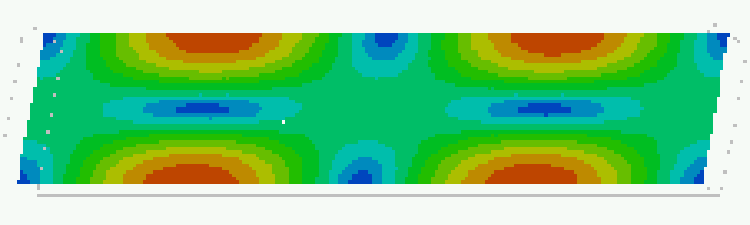

(d) Magnetic field at $f_{210} = 2.23\,GHz$

Figure 6.7: Simulated transverse electric and magnetic fields inside the rectangular cavity of Fig. 6.6, at the first two resonant modes, on a surface cut at half of the cavity height (Courtesy of J.Prochnow, 2003).

from where the loss factor can be defined:

$$\tan\delta_\epsilon = \frac{\epsilon_r^{''}}{\epsilon_r^{'}} \tag{6.8}$$

The loss factor (or loss tangent) corresponds to the inverse of the quality factor Q of the dielectric resonator. The higher the loss factor, the lower the quality factor and the larger the amount of RF power absorbed by the dielectric.
As mentioned above, in the test cavity there are locations, in which either the electric or the magnetic field vanishes. If one puts a sufficiently small sample, which does not disturb the field, in these locations only the magnetic or electric properties of the cavity are influenced by the sample. In both cases the resonance frequency f_r and the quality factor *Q* change. In the following we derive $\epsilon_r^{''}$, $\epsilon_r^{'}$ and $\tan\delta_\epsilon$ from such changes.
The relative variation of the resonant frequency f_r follows from the relative variation of the energy W stored in the resonator [63]:

$$\frac{\Delta\bar{f}_r}{\bar{f}_r} = -\frac{\Delta\bar{W}}{\bar{W}} \tag{6.9}$$

The variables in this equation are complex. If the sample is non-magnetic and positioned in a zero-magnetic-field region, which is our case, then $\bar{W}$ and $\Delta\bar{W}$ in Eq. (6.9) are only calculated from the electric fields:

$$\frac{\Delta\bar{f}_r}{\bar{f}_r} = \frac{\bar{f_{r_s}} - \bar{f_{r_e}}}{\bar{f_{r_e}}} = \frac{-\epsilon_0 \int_{V_s}(\bar{\epsilon_r}-1)\vec{E}_e(x,y,z)\vec{E}_s(x,y,z) * \mathrm{dV}}{2\epsilon_0 \int_{V_r} E_e^2\,\mathrm{dV}} \tag{6.10}$$

The subscripts "e" and "s" indicate the empty cavity and the cavity with sample, whilst V_s and V_r are the volumes of the sample and of the resonator. When the electric field is tangential to the surface of the sample and the sample ends on the resonator walls, then the internal field equals the external field:

$$E_e = E_s \tag{6.11}$$

Given a small volume of the sample:

$$\vec{E_e}(x,y,z) = \vec{E}_{e0} \tag{6.12}$$

and it can be pulled out from the integrals of Eq. (6.10). The imaginary part of the resonant frequency shift is related to the change in the loaded quality factor:

$$\mathrm{Im}(\Delta\bar{f_r}) = \Delta f_r^{''} = \frac{f_r}{2}\left[\frac{1}{Q_{L_s}} - \frac{1}{Q_{L_e}}\right] \tag{6.13}$$

Eq. (6.10) to Eq. (6.13) lead to the evaluation of the real and imaginary part of the dielectric constant:

$$\epsilon_r^{'} = 1 - \frac{f_{r_s} - f_{r_e}}{f_{r_e}}\frac{V_r}{2V_s} \tag{6.14}$$

$$\epsilon_r^{''} = \left[\frac{Q_{L_e}}{Q_{L_s}} - 1\right]\frac{1}{Q_{L_e}}\frac{V_r}{4V_s} \tag{6.15}$$

and therefore to the characteristic loss factor as defined in Eq. (6.8). $\epsilon_r^{''}$ can also be deduced from the material conductivity σ and the resonant frequency f_r according to:

$$\sigma = \omega\epsilon^{''} = 2\pi f_r \epsilon^{''} = 2\pi f_r \epsilon_0 \epsilon_r^{''} \tag{6.16}$$

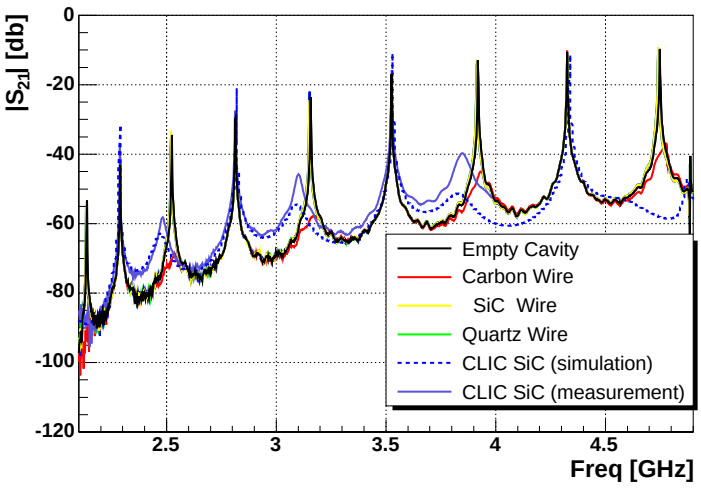

Figure 6.8: Modes resonating in the test cavity while inserting different materials. At frequencies where the electric field is maximum and the magnetic field null, the presence of the dielectric induces a resonance frequency shift and a quality factor reduction.

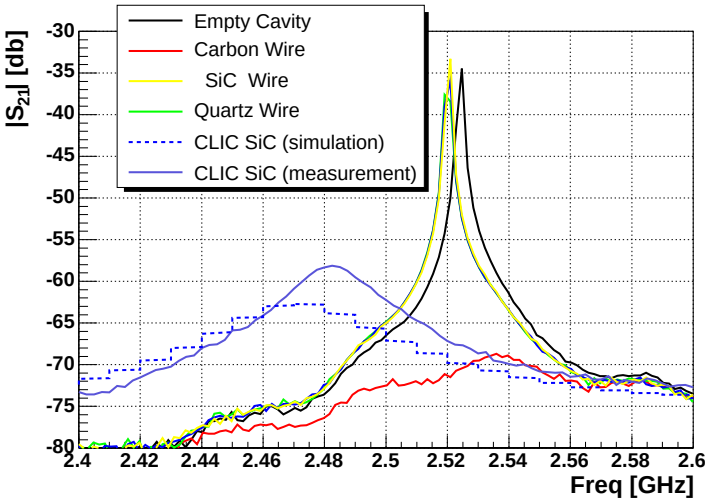

Figure 6.9: Enlargement of the plot of Fig. 6.8 around the resonance at $2.5\,GHz$ (TE mode f_{310}).

These relations have been used to characterize the experimental results described below. The VNA has been used to anlyze the transmission signal S_{21} characterizing the cavity resonant frequencies.
Fibers of three different materials were inserted in the cavity using a small hole (see Fig. 6.6): Carbon, Silicon Carbide and Quartz. Different materials such as silicon carbide (SiC), carbon and quartz fibers were examined. SiC fibers are an interesting alternative to carbon fibers and their properties had to be investigated, since SiC bulk material is often used as a microwave absorber.
Fig. 6.8 shows the measurements results as the magnitude of the transmission signal S_{21} versus frequency. Fig. 6.9 is an enlargement around one of the resonating modes with maximum electric field at the sample location. The plot qualitatively proves the RF power absorption of Carbon, and the non-absorption of Silicon Carbide and Quartz. The plots also includes the results of a numeric simulation and measurement concerning the SiC material which is presently considered as a suitable

RF absorber for the Compact Linear Collider (CLIC). A pyramid shaped piece of such material was inserted in the resonator at the same location where the wire scanner wires were placed. The fact that this material is absorbing RF power as shown by the simulation and by the measurements, proved that this is a SiC compound different from the one used for the wire scanners wires.
The insertion of one carbon fiber ($d = 36\,\mu m$) is reducing the signal amplitude to a level where the mode frequency is not well defined since the resonance curve is strongly asymmetric. Therefore, for this material, Eq. (6.14) cannot be applied. The imaginary part of the dielectric constant was evaluated both from Eq. (6.15) and Eq. (6.16). The insertion of 500 SiC fibers (d=15 μm) allowed the evaluation of both the real and imaginary part of the dielectric constant by mean of Eq. (6.14) and Eq. (6.15). The results for the resonance at $f_{310} \approx 2.50\,GHz$ are summarized in Table 6.2.2, together with the available data for the CLIC SiC bulk material [64]. Quartz is a weakly absorbing material and, in

	ϵ_r'	ϵ_r''
C		$2.30 \pm 0.05 \cdot 10^5$
SiC	10.790 ± 0.016	2.158 ± 0.005
SiC (CLIC)	14.4	6.6

Table 6.1: Real and imaginary part of the dielectric constant for the TE mode, at $f_{310} \approx 2.5\,GHz$.

order to evaluate ϵ' and ϵ'', one should insert a large number of fibers as it has been done for SiC. However not enough Quartz material was available.

6.2.3 Ferrite Effects

During the 2002-2003 SPS shut-down period, the rotative wire scanners tanks have been equipped with ferrite tiles. Fig. 6.10 show their effectiveness as absorber material. All the curves refer to cycles during which the wire has been kept in the initial parking position. The ferrites have been added in three stages, by filling larger regions on the bottom and on the internal sides of the tank. The temperature increase indicated by the voltage is almost independent from the quantity of ferrite tiles, while the thermionic emission current peak is strongly reduced only by the insertion of the maximum number of tiles.

6.2.4 SiC wires breaking

As a consequence of the laboratory investigations on the materials dielectric properties, during the 2003 SPS run three wire scanners have been equipped with SiC wires. They proved to stand the electromagnetic coupling with the beam, but two of them broke during a scan. Fig. 6.11 shows the measured beam profile before SiC wire breaking. The wire traversed the beam and broke just after encountering the particles distribution peak. This measurement has been taken during a setup period, and the photomultiplier signal saturated.
Hence SiC wires are not usable due to the direct energy transfer from the beam and have been abandoned.

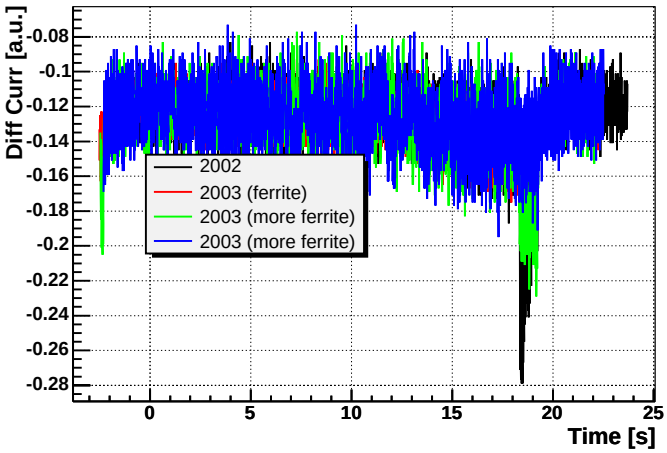

(a) Thermionic emission current

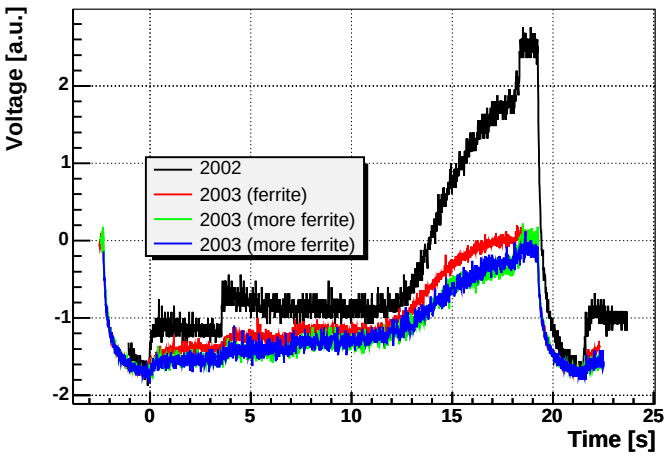

(b) Voltage proportional to the wire temperature

Figure 6.10: Effect of the insertion of ferrite tiles in the wire scanner tank. In all cases no scans have been carried out during the cycle (i.e. the wire have been kept in the initial parking position).

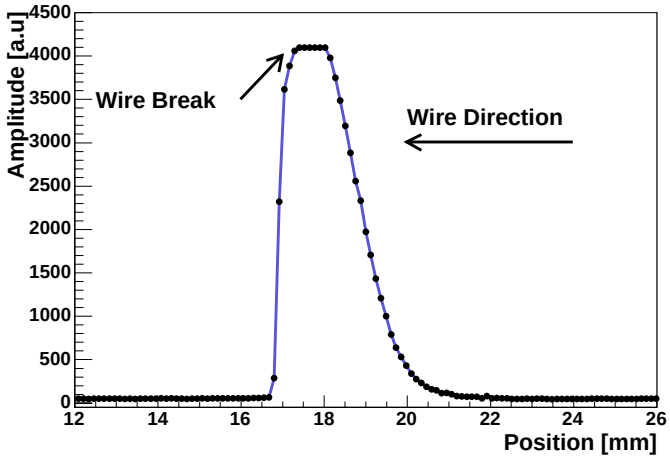

Figure 6.11: Measured profile when a SiC wire broke during the scan.

6.3 Summary

The SPS WS wire breaking in 2002 forced a series of dedicated studies to investigate the origin of the phenomenon. Laboratory measurements demonstrated that the SPS rotative wire scanner tanks act as a resonant cavity, whose modes can couple to the instruments wires. As a cure, a number of ferrite tiles have been inserted in the tank, in order to absorb the RF power present in the cavity. The wire heating during the beam circulation and during the profile measurements has been strongly reduced. Carbon provided evidence of RF power absorbtion properties, unlike silicon carbide and Quartz. However the silicon carbide utilization was not successful, due to its low resistance to the direct energy transfer during the scan through the beam. Quartz was not considered as a candidate after recovering information about its utilization in previous accelerators. We assume that its very high resistivity (of the order of $10^3\,\Omega\,cm$ compared to $10^{-3}\,\Omega\,cm$ for Carbon) caused break downs due to collection of static charges. It must be remarked that the thermal conductivity at normal temperature is comparable for the two fiber materials [65]: about $14\,W\,cm^{-1}\,^oK^{-1}$ for Carbon and about $12\,W\,cm^{-1}\,^oK^{-1}$ for SiC. The melting (sublimation) temperature is about $3600\,^oC$ for Carbon and about $3000\,^oC$ for SiC. From the second half of the year 2003, the SPS wire scanners have been operated with carbon wires and their tanks filled with ferrite tiles.

Chapter 7

Processing strategies for the transverse profile data

This chapter describes the elaboration of an offline data treatment common for all the emittance monitors. Each instrument provides the same kind data structure: an amplitude signal as function of position, that characterizes the particles distribution in the transverse planes.
As mentioned in Chapter 2, in high energy particle beams, the Gaussian function describes well the particles transverse distribution. In order to determine the beam size it is therefore necessary to find the Gaussian fit which best approximates the measured profile. The fitting procedure has to be flexible enough to correct for some instrumental systematic errors, like background in the photomultiplier tube. Statistical uncertainties, due to electronic noise or random background noise, must be also considered and compensated while evaluating the beam size.
In the case of non-Gaussian distributions, the transverse beam size has to be deduced from other parameters which characterize the distribution, typically the Full Width at Half Maximum (FWHM) and the Root Mean Squared (RMS) values. A series of algorithms was therefore implemented with the aim of accurately determine the best fit. The code has been written in the C++, linking to the ROOT [66] package libraries which are particular suitable for such kind of analysis.

7.1 Gaussian (or Normal) Distribution

The Gaussian distribution is commonly used in statistics as the limit distribution of data affected by the sum of small statistical errors and by negligible systematic errors. The general form of a Gaussian function is:

$$f(x) = \frac{1}{\sigma\sqrt{2\pi}} e^{-\frac{1}{2}\left(\frac{x-\mu}{\sigma}\right)^2} \tag{7.1}$$

The parameters μ and σ are defined as the mean and the standard deviation of the distribution. The integral of the beam profile represents the total number of events generating the signal, which depends on the number of particles composing the beam and on the detection system which usually amplifies the primary signal. The function has therefore a third parameter N_e accounting for the number of events, and:

$$f(x) = \frac{N_e}{\sigma\sqrt{2\pi}} e^{-\frac{1}{2}\left(\frac{x-\mu}{\sigma}\right)^2} \tag{7.2}$$

Fig. 7.1 shows a Gaussian function and evidences the relation between the parameter σ and the quantity Full Width at Half Maximum (FWHM).

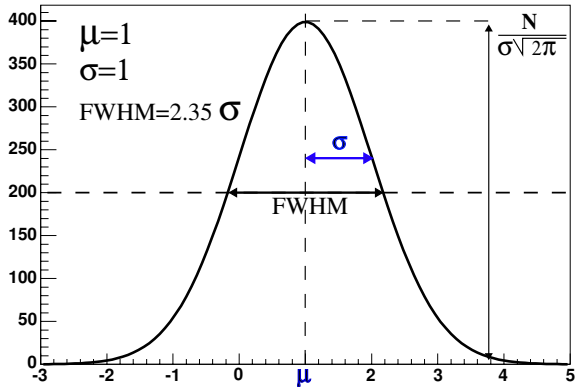

Figure 7.1: Gaussian function with mean $\mu = 1[a.u]$, standard deviation $\sigma = 1[a.u.]$ and number of events $N_e = 1000$.

7.2 χ^2 Goodness of Fit Test

Let us consider a set of N data points y_i , $i = 0, ...N$ approximated by the general function f. For each value y_i the value predicted by the function is $f(x_i)$. Hence $\overline{y_i} = f(x_i)$ is the measurement *expected* value if the function is well approximating the data point. The standard deviation of a large enough (infinite in the ideal case) number of measurements of each y_i will be here indicated as e_i and indicates the *error* on the determination of y_i. This quantity has a very important role in the beam profile analysis, as it will reminded at the end of this section after introducing other concepts necessary to understand such importance (see p. 91).
To characterize the data approximation with the function f, one can consider the ratio:

$$\frac{y_i - \overline{y_i}}{e_i} \tag{7.3}$$

This quantity is positive for some points and negative for others. However, if the fit is appropriate, it averages to 1. It is then useful to square it and to make the sum over all the measurement points. This results in the definition of χ^2 :

$$\chi^2 = \sum_{i=1}^{N} \frac{(y_i - \overline{y_i})^2}{e_i^2} \tag{7.4}$$

In the case of χ^2 =0 the fit would be perfect ($y_i = \overline{y_i}$ for each point) but this is very unlikely the case when dealing with real measurements. In general each term should give a contribution of about 1 and therefore: $\chi^2 \approx N$. If $\chi^2 \leq N$ the parametrization describes well the data, while $\chi^2 \gg N$ indicates a disagreements.
A more refined method consists in comparing the χ^2 with the *Degrees of Freedom (d)* rather than the number of points. The number of degrees of freedom is defined as the difference between the number of acquired data and the number of parameters used in the calculations to describe the data distribution,

$$d = N - C \tag{7.5}$$

where C defines the number of *constraints*. The minimum number of constraints is 1, since N is a parameter depending on the measurements. Normally the other constraints are the number of parameters P characterizing the fitting function. It can be demonstrated that the expected value of χ^2 is equal to the number of degrees of freedom:

$$< \chi^2 >= d = N - C = N - 1 - P \tag{7.6}$$

We can now define the *Normalized (or reduced)* χ^2 as

$$\overline{\chi^2} = \frac{\chi^2}{d} = \frac{1}{N-1-P}\sum_{i=1}^{N}\frac{(y_i - \overline{y_i})^2}{e_i^2} \tag{7.7}$$

and expect

$$< \overline{\chi^2} >= 1 \tag{7.8}$$

This does not mean that for a single fit to the samples populating the distribution the normalized χ^2 has to be equal to 1, but only that in the ideal case of infinite repetitions of the measurements, with a fit to the results for every repetition, the average value of $\overline{\chi^2}$ will be 1. For pure statistical fluctuations in fact, the value of $\overline{\chi^2}$ has a certain probability of being larger than a value $\overline{\chi^2}_0$. This probability is described by the χ^2 probability function:

$$P_d(\overline{\chi^2} \leq \overline{\chi^2}_0) = \frac{2}{2^{d/2}\Gamma(d/2)}\int_{\overline{\chi^2}_0}^{\infty} x^{d-1}e^{-x^2/2}dx \tag{7.9}$$

where

$$\Gamma(d/2) = \int_0^{\infty} e^{-t}t^{(d/2-1)}dt$$

is called *Gamma Function*. After fitting the data and calculating the $\overline{\chi^2} = \overline{\chi^2}_0$, one can therefore evaluate which is the probability of getting a $\overline{\chi^2} \leq \overline{\chi^2}_0$ for a given number of degrees of freedom.
The probability expressed by Eq. (7.9) is also called *confidence (or significance)* level.
For example let us assume to have a set of fitted data with 15 degrees of freedom and the calculated $\overline{\chi^2}$ is 1.5. With 15 degrees of freedom the probability of having a $\overline{\chi^2}$ larger than 1.5 is 10 %,

$$P_{15}(\overline{\chi^2} \geq 1.5) = 10\,\% \tag{7.10}$$

Only in 10 % of the cases the $\overline{\chi^2}$ is expected to be equal or larger than 1.5. In this case one could conclude that the fit is not appropriate. Once decided which confidence level is acceptable, such quantity indicates if the chosen parametrization represents well the data and this can happen also for a $\overline{\chi^2} > 1$. If the obtained confidence level is not acceptable the fitting function and the data disagree and in the case of particle beam profiles fitted with a Gaussian distribution, this is typically due to the non-Gaussian shape of the beam or to bunch oscillations in the batch.

7.2.1 Importance of the data errors assignment

The errors e_i defined at the beginning of this section play and important role in the whole analysis. By definition each e_i is the standard deviation of infinite measurements of the quantity y_i, but it is of course not known a priori. When measuring once the set of points y_i, the N e_i represent the errors to be assigned to every point before performing the fit. They determine the value of the variable χ^2 (see Eq. (7.4) and Eq. (7.7)) and therefore of the fit confidence level. In other words they define the *weight* with which the fitting routine considers each point y_i in order to converge with an acceptable confidence level.
In many classes of mesurements the errors e_i are estimated as the standard deviation of a Poisson distribution with mean y_i (i.e. $e_i = \sqrt{e_i}$). We tested this option and observed an overestimation of the errors at the profile peak and an underestimation in the tail regions. The resulting fit does not properly approximate the core of the measured distribution.
The best evaluation of every e_i could be inferred by an error estimation of the measurement devices and procedures used to detect y_i. It is normally difficult accurately determine such value and an

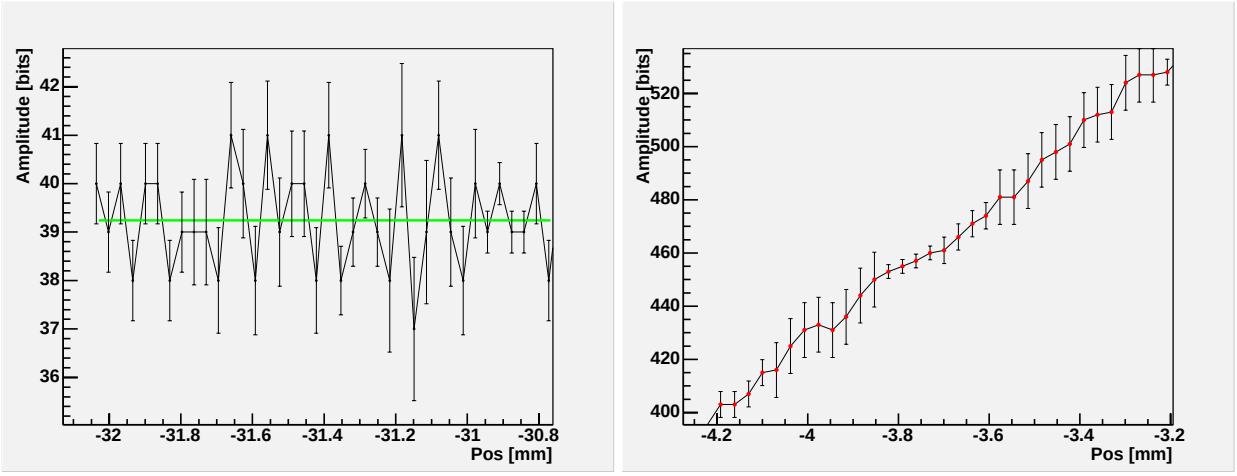

(a) Detail of the tail region

(b) Detail of the region with $dy/dx > 0$

Figure 7.2: Error assigned to the data of a beam profile, each consecutive N=4 points have the same error bar, calculated as the standard deviation of the N values.

empirical estimation of the data points errors will be proposed in the next section.
It must be also noticed that, in the analysis tools presented here, we will not account for any error on the position determination of each beam profile data point (horizontal axis on the profile plots). They are in most cases negligible (as it can be seen from the simulations of Section 3.6) and would imply a more complicated definition of χ^2 and confidence level.

7.3 Algorithm description

The first part of the data processing is taking preliminary actions depending on the accelerator where the measurement was performed and on the instrument type. For instance the data coming from the SPS wire scanners undergo a correction of the angular position when necessary (Section 8.1).
The core part of the analysis concerns the data fitting and the emittance calculation. At first each profile data point is characterized by an error e_i, which is considered by the fitting routine in order to converge. The routine looks for a function passing through all the error bars associated with the measurements and is based on the χ^2 minimization [67].
The errors e_i have been in this work defined as the spread of N measurements, following each other in the transverse coordinate. The N measurements are expected to detect about the same quantity. Such assumption is legitimate in the tails and in the profile peak regions, while overestimates the error bars where the gradient dy/dx is different from zero. Several tests showed that this drawback does not compromise the analysis accuracy. The error assignment strategy is depicted in Fig. 7.2.
The value of N depends on the number of samples along the profile. Therefore it is established according to the expected beam size and the to wire speed. For instance $N = 4$ for the SPS rotational wire scanners monitoring the LHC beam at $26\,GeV$ and $N = 18$ for the SPS linear wire scanners during the same beam conditions.
The algorithm then passes to the fit with a Gaussian function, plus a constant which accounts for the signal offset:

$$f(x) = A + \frac{B}{\sigma\sqrt{2\pi}} e^{-\frac{1}{2}\left(\frac{x-\mu}{\sigma}\right)^2}. \tag{7.11}$$

In order to increase the fitting efficiency, it is necessary to provide initial values to the following quantities:

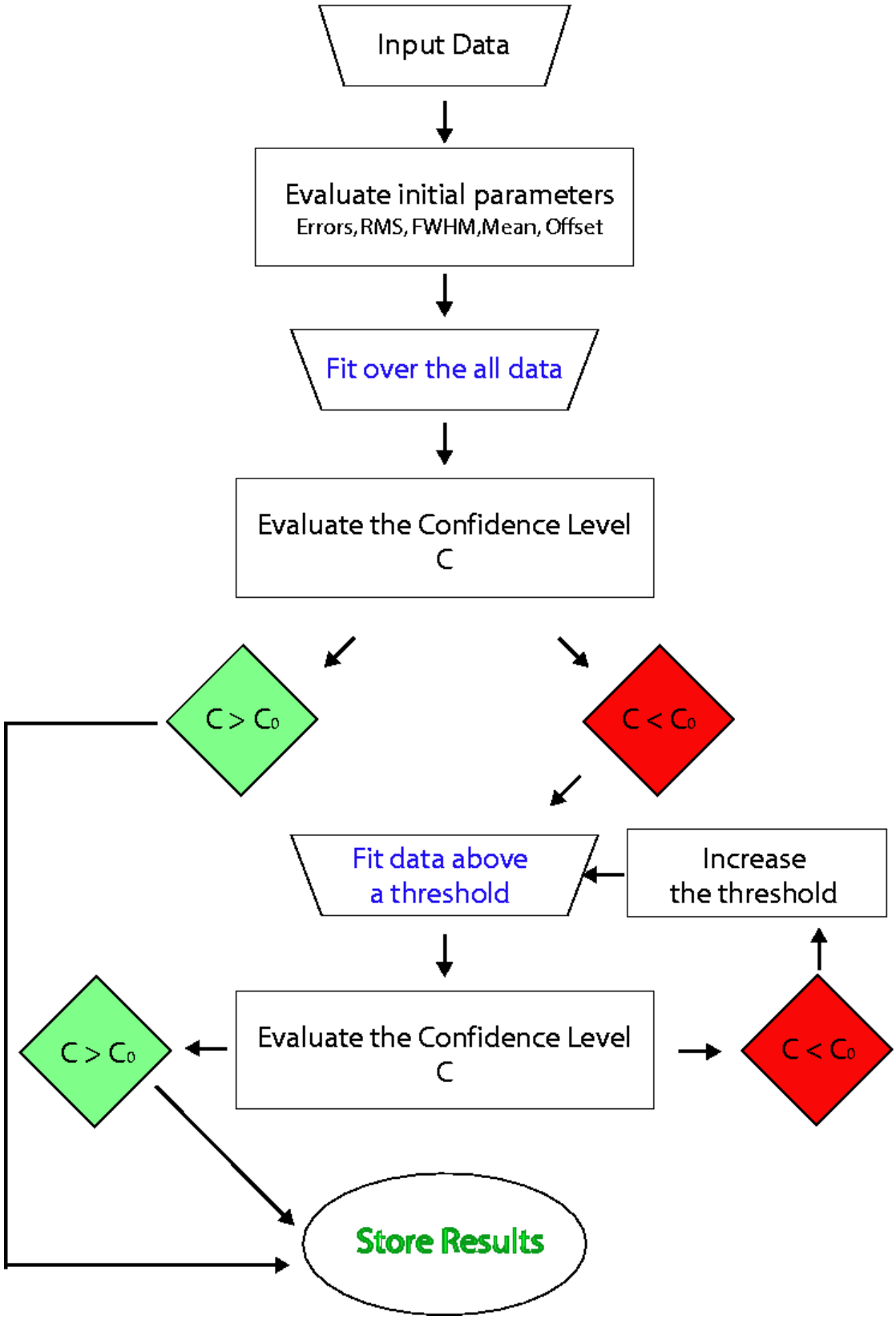

Figure 7.3: Flow chart describing the data analysis treatment

- beam position μ_0
- beam size σ_0
- profile offset A_0
- profile amplitude B_0

μ_0 and σ_0 are estimated by filling an histogram with the measurements and evaluating the Mean and RMS values. A_0 is calculated as the average of the measurements in the tail regions while B_0 is given by the maximum value of the acquired data. The parameters resulting from the fit convergence (μ, σ, A, B) are saved, together with the *number of degrees of freedom*, the *normalized* $\overline{\chi^2}$ and the *confidence level* as defined in Section 7.2.
If the confidence level is not accepted, a second fit is performed taking into account only the measurements with an amplitude above a fixed threshold. The threshold is defined as a percentage of the profile amplitude and is initially set to 1%. Such action corresponds to a parametrization of a limited percentage of the particles populating the distribution, excluding the particles laying outside the beam core.
The confidence level of the new fit is again taken as the indicator of the parametrization quality. If the confidence level is not yet acceptable, the amplitude threshold is increased and the fit performed again on a smaller number of measurements. When the confidence level is accepted, the iterations during which the amplitude threshold is increased are interrupted. A last fit is performed, only considering the data points below the threshold. This is often useful to characterize the distribution tails.
The normalized transverse emittance is calculated according to Eq. (2.81), using the Gaussian width σ as a measure of the beam size.
The data treatment scheme is resumed in the flow chart presented in Fig. 7.3.

7.4 Beam profile analysis example

The following plots refer to a measurement taken by a SPS WS in the horizontal plane, with a pilot bunch (very low emittance beam) at $26\,GeV$. The distribution has large tails (the horizontal tune was deliberately changed to study beam instabilities). This example was chosen in order to demonstrate the results sensitivity to the analysis strategies.
Fig. 7.4 shows the acquired data with the three fitting curves: one fitting all the data (blue), one fitting only the data above a threshold level in order to have an acceptable confidence level (green) and one fitting the data below the threshold (red).
Fig. 7.5 shows the errors given to each measurement before the fitting as explained in Section 7.3 and the residuals between each measurements and the fitting function sampled at the measurement location.
Fig. 7.6 and Fig. 7.7 shows the $\overline{\chi^2}$ and the beam size σ respectively, as function of the varying threshold. Both quantities decrease while excluding a larger number of measurements in the tails. The $\overline{\chi^2}$ decreases due to the fact that the parametrization represents better the fitted measurements. At the threshold equal to $25\,\%$ of the profile peak, the confidence level is accepted and Fig. 7.6 shows that the further increase of the threshold does not improve the $\overline{\chi^2}$. As expected, also the beam size does not vary anymore when the threshold changes from 25 to $28\,\%$.
Many output parameters are stored in order to properly compare different emittance measurements and the more significant are:

- the beam size and the normalized emittance when using the FWHM as estimate of the beam size.
- the beam size, the normalized emittance and the normalized χ^2 when fitting all the data.

	σ [mm]	$\epsilon[\mu m]$	$\overline{\chi^2}$
FWHM	0.561	0.262	
Fitting All Points	0.634	0.374	14.9
Fitting Points Above Thresh.	0.533	0.223	0.9
Confidence Level:	70 %		
Residual Integral:	5.2 % of Total		
Fit Threshold:	25 % of Profile Maximum		

Table 7.1: Summary of the results for the considered example.

- the beam size, the normalized emittance and the normalized χ^2 when fitting only the data above the threshold.
- The value of the introduced threshold, after the iterations to reach an acceptable confidence level.
- The confidence level of the parametrization when fitting only the data above the threshold.
- The ratio between the residuals (between the data and the fit using the threshold) integral and the total profile integral.

The results of the considered example are summarized in Table 7.1. The relative difference between the normalized emittance calculated after fitting all the points and the one obtained after fitting only the data above the threshold is:

$$\delta_\epsilon = 2\frac{\epsilon_{all} - \epsilon_{thresh}}{\epsilon_{all} + \epsilon_{thresh}} = 50.6 \cdot 10^{-2}. \tag{7.12}$$

The normalized χ^2 decreases from 14.9 to 0.9. Even though the normalized χ^2 arising from the fit over all the acquisitions looks reasonably low, the confidence level is less than $1\,\%$: if the parametrization is well representing the data, with the correspondent number of degrees of freedom, the probability of finding such a high $\overline{\chi^2}$ is less than $1\,\%$.

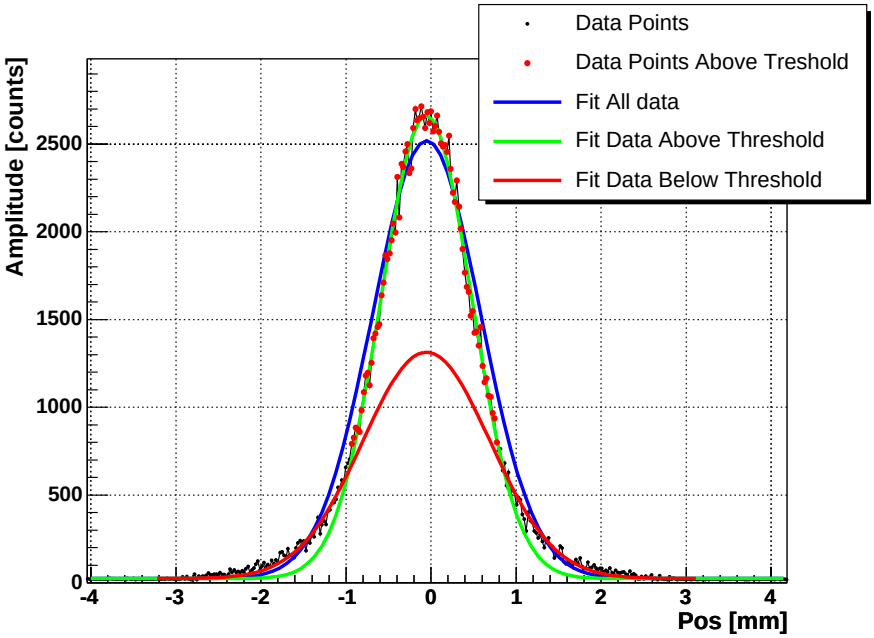

Figure 7.4: Beam profile from an SPS wire scanner monitor, with three different fitting functions.

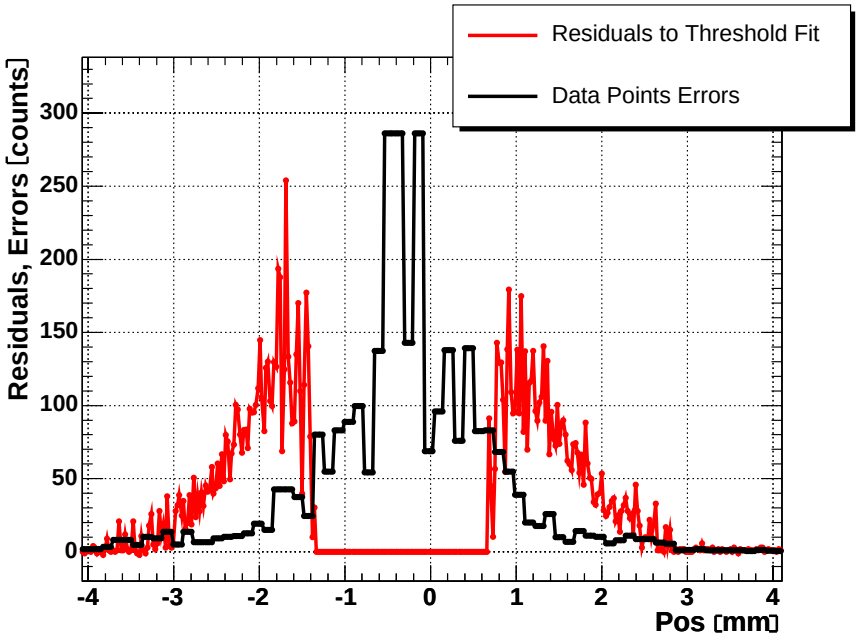

Figure 7.5: Graph of the errors assigned to the acquisitions of the profile in Fig. 7.4 (Black) and graph of the residuals between the data and the fitting curve which considers only the measurements above a threshold (red).

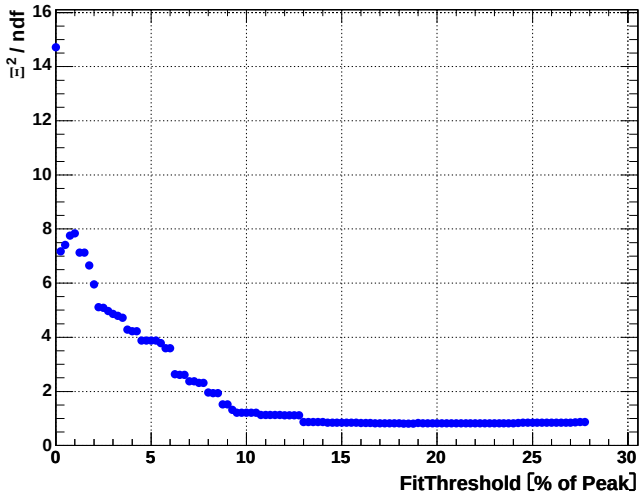

Figure 7.6: Variation of the normalized χ^2 while changing the fit threshold.

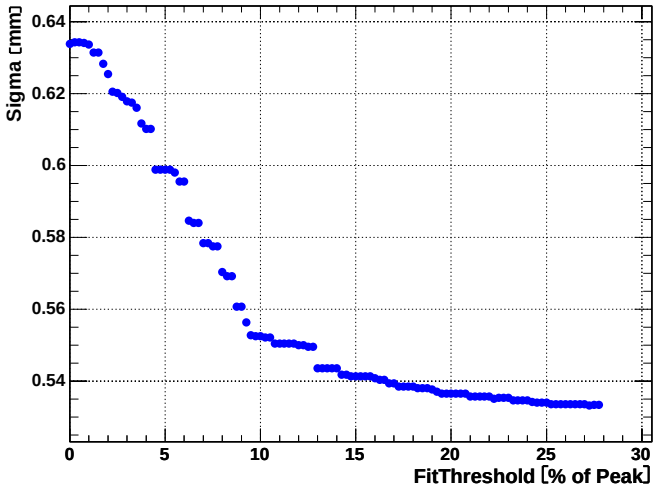

Figure 7.7: Variation of the evaluated beam size while changing the fit threshold.

Chapter 8

Monitors accuracy determination

This chapter is devoted to the beam based experiments carried out in the SPS in order to determine the precision of the WS and IPM monitors. Throughout the chapter we will address concepts as accuracy, reproducibility, repeatability and resolution; in order to avoid ambiguities about these definitions, the reader is invited to refer to the glossary written at the beginning of this report.
Calibrating one or more instruments with an absolute reference is not possible, since a beam with a perfectly known emittance is not available.
We approached the precision determination in different stages:

1. the preparation of data analysis tools (see Chapter 7) which should allow a non biased treatment of single instruments with different beams and the consistent comparison of different monitors;

2. the studies of single monitor dependencies, like the dependence of the measured beam width on the monitor mechanics and on their operation setups (like the wire scanners wire movement direction and the gating on the particles bunches);

3. the relative comparisons among different instruments in order to individuate systematic differences and statistical fluctuations of the measured emittances. This was done at first among the wire scanners and later between the wire scanners and the ionization profile monitor in the SPS.

For the WS monitors two measurement sessions are presented. The first (Section 8.1) concerns the study of a systematic error discovered in the rotational devices wire position determination and the methods to overcome it.
The second part (Section 8.2) discusses comparative measurements among the SPS wire scanners. At first, the measurements have been carried out with low intensity beams, the TOTEM beam and the pilot bunch. This allowed to operate all the WS monitors, including the linear devices, which can be used without any wire damage only at a beam intensity below $5 \cdot 10^{12}$ protons. The systematic differences among two rotational wire scanners have been later studied also with the nominal LHC beam.
The following part of the chapter (Section 8.3) is dedicated to the cross-calibration between the SPS IPM and WS monitors.
Section 8.4 gives an overview of the emittance measurements carried out with the wire scanner monitors in the PSB, PS and SPS during the year 2003, in order to determine the emittance preservation of different beam types during the acceleration from 50 MeV to 450 GeV.

Throughout the chapter we will indicate as *beam size* or *beam width* the width σ of the Gaussian fit applied to the beam transverse profiles and *beam emittance* the normalized emittance ϵ_n defined in Eq. (2.81).

8.1 Dependence of SPS rotational wire scanners on the wire position determination

The rotational SPS wire scanners measurement procedure consists of two passages through the particles beam during the same cycle[1]. During the *IN* scan the wire moves from the inner (or lower) part of the ring to the outer (or upper), while during the *OUT* scan it moves backward. Throughout the measurement, the advance of the motor shaft is monitored by a potentiometer and digitalized every revolution period of the particles. An algorithm calculates the wire position on the transverse plane.
The geometry of the system is shown in Fig. 8.1. The definition of all the angles and distances necessary to project the angular wire position on the transverse plane are given in Table 8.1.
The angle α_{max} indicates the full stroke that extends between the two wire parking positions. α_0 relies on the mechanical alignment and is determined by the fork length L and the distance between the rotation axis and the beam reference orbit. The acquisition system is enabled only when the wire position is near the beam location, where the wire moves at constant speed and α_{first} is the angle of the first acquisition point. The angles α^* and α_1 are introduced to have the nominal transverse position equal to zero at the reference beam orbit.
For each revolution period the system reads the potentiometer value which is a direct measure of the running angle α_i. The wire position projection onto the transverse plane (horizontal or vertical) is resolved according to:

$$x_i = L \cdot [sin(\alpha_1 + \alpha_i) - sin(\alpha_0)] \tag{8.1}$$

In the following we present a series of measurements dedicated to investigate the dependency of the measured beam size on the wire movement direction. Three hundred fifty scans have been performed, employing five instruments out of the six available.
The IN and OUT scans were executed assuming that the emittance was preserved in the period between the two measurements. The scans have been carried out at constant beam energy $E = 26\,GeV$.
The measurements exhibit a systematic difference between the beam size detected in the two measurements, as shown in Fig. 8.2. The absolute values are shown in the top plot as function of the beam size. The discrepancy is roughly proportional to the beam width. The bottom plot refers to the relative differences which result to have a mean of about $8\,\%$ with an RMS of about $1.7\,\%$.
The beam position measured with the WS is plotted in Fig. 8.3, for the same set of scans of Fig. 8.2. The position is given by the mean value of the Gaussian parametrization. The beam orbit monitor system was used to verify that the beam position difference between IN and OUT scan is smaller than $0.5\,mm$. Hence there is a discrepancy in the WS beam position measurement, between the two scans, which exceeds $20\,mm$.
Such instrumental effect is due to a low pass filter included in the wire position read-out system. The filter is needed to reduce the fluctuations caused by the electronic signal noise. With the chosen filter time constant, the position value given by the instrument is delayed compared to the real wire position.
On the absolute angle scale, the delay in the time domain introduces opposite effects: a negative offset if the angle increases during the scan and a positive offset if it decreases.
This suggested to introduce a correction on the absolute angle $(\alpha_1 + \alpha_i)$ expressed in Eq. (8.1). Hence Eq. (8.1) becomes

$$x_i = L \cdot [sin(\alpha_1 + \alpha_i \pm \Delta\alpha) - sin(\alpha_0)] \tag{8.2}$$

The correction $\Delta\alpha$ is determined by imposing the two profiles to have the same mean value (i.e. by imposing the beam to be in the same position). As a first approximation such value is chosen as the average between the initial IN and OUT mean values. A more accurate method requires the use of the

[1] See Section 1.3 for the definition of SPS cycle

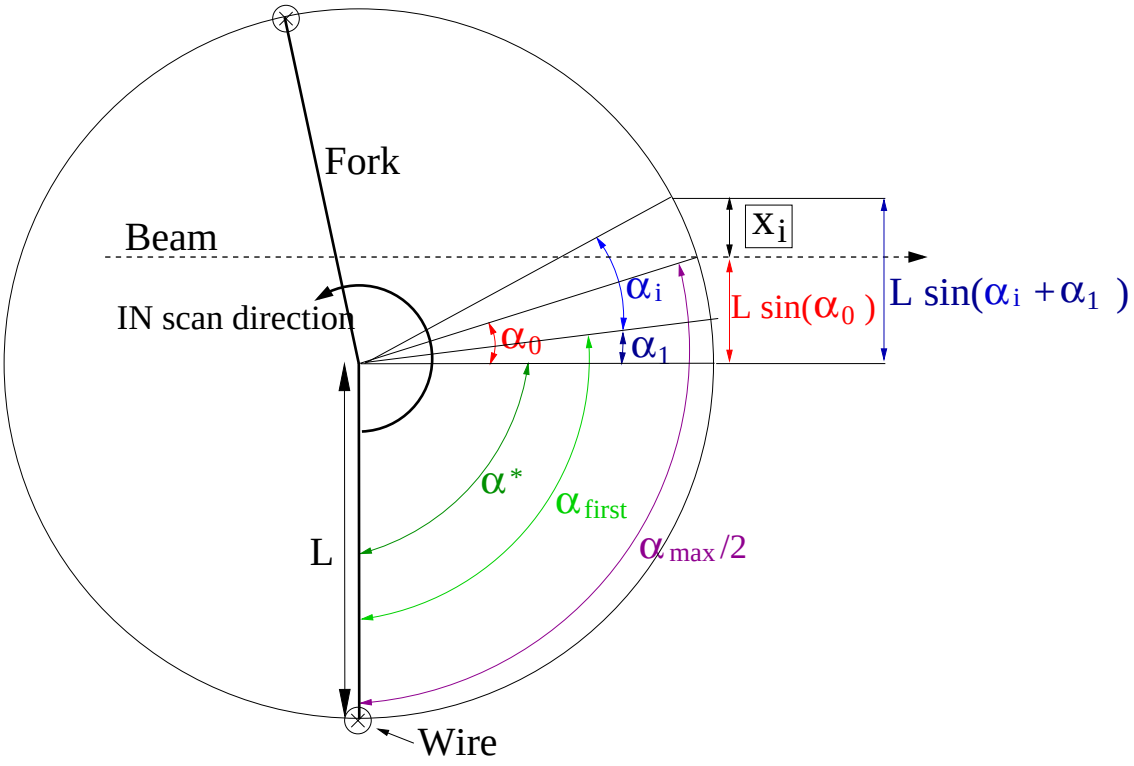

Figure 8.1: Schematic diagram of the SPS rotational wire scanners geometry.

Table 8.1: Definition and values of the quantities shown in Fig. 8.1

Name	Meaning	Value
L	Fork Length	$200\,[mm]$
α_{fs}	Full scale potentiometer	$2866\,[bit]$
α_{max}	Maximum rotational stroke	186^o (BWS414&BWS519) 120^o (BWS416)
α_0	Angle determined by the distance between the rotation axis and the beam reference orbit	24.8^o
α_i	Angle running during the scan	Variable
α_{first}	Angle of the first acquisition point	Variable
α^*	$\alpha_{max}/2 - \alpha_0$	68.2^o (BWS414&BWS519) 35.2^o (BWS416)
α_1	$\alpha_{first} - \alpha^*$	Variable
x_i	Wire position projected on the transverse plane	Variable

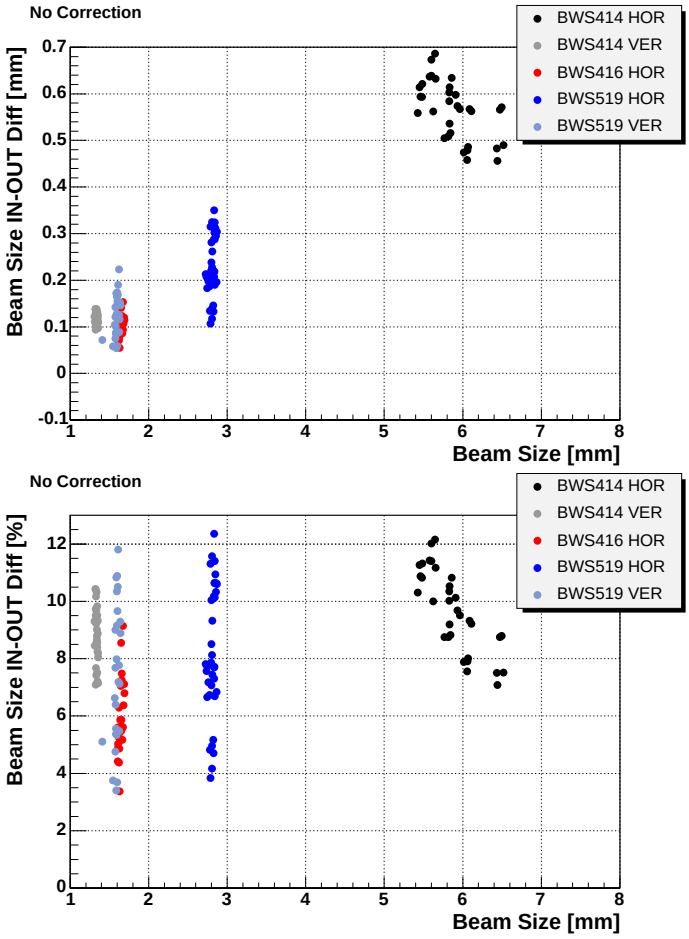

Figure 8.2: Absolute (top) and relative (bottom) difference between the beam size measured by the SPS rotational wire scanners as function of the absolute beam size, when scanning with opposite wire movement direction.

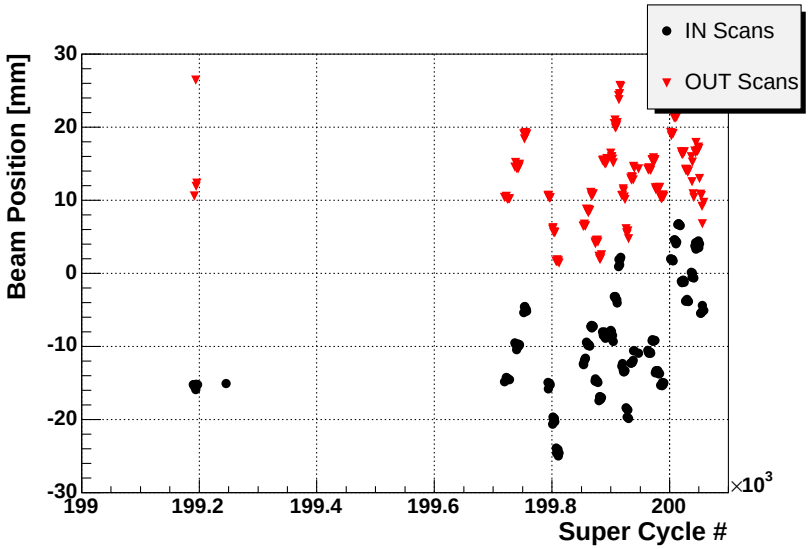

Figure 8.3: Beam position during the IN and OUT scans, measured for the same set of data of Fig. 8.2.

beam orbit monitor system to measure the beam position. With this second method, the uncertainty on the alignment angle α_0 is also discarded.
During the measurements considered here, the beam orbit monitor system was used to check relative beam displacements between two wire scans, but not to measure the absolute beam position. Consequently only the first correction is applied.
The effectiveness of the correction is shown in Fig. 8.4, where the average differences after the correction are plotted on top of the original discrepancies, as function of the absolute beam size.
After the correction the average relative difference is below $2.5\,\%$. The values for the single instruments are resumed in Table 8.2.
The correction angle $\Delta\alpha$ varies for every wire scanner and depends on the scan direction, as summarized in table Table 8.3. The table also includes the RMS of the correction angle, that varies from 0.7 to $1.8\,mrad$ and never exceeds $3\,\%$ of the absolute angle.
The nominal speed of the SPS rotational wire scanners is $v = 6\,m/s$. Given the fork length $L = 200\,mm$, the angular speed can be expressed as

$$\omega = \frac{v}{L} = 30 \left[\frac{rad}{s}\right] \tag{8.3}$$

Therefore an angle offset of $50\,mrad$ corresponds to a time delay of $1.67\,ms$, which gives the order of magnitude of the effect introduced by the low pass filter on the wire position read-out system.

It can be concluded that, thanks to the off-line correction, the effect of the potentiometer low-pass filter on the measured beam size is strongly reduced but not eliminated. An alternative read-out system, without the filter, is therefore recommended.
The validity of the correction is confirmed by the concordance of the normalized emittance among different instruments is improved after the angle variation. This is demonstrated in the next section, where the emittances measured by the rotational devices are compared with the ones measured by the linear monitors.

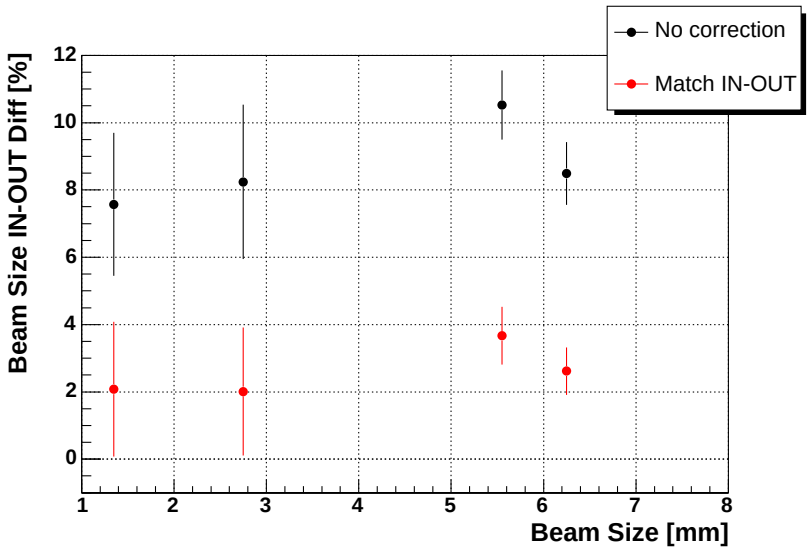

Figure 8.4: Average beam size relative differences between each IN/OUT scan on the same cycle, as function of the absolute beam size, with and without the angle correction. The error bars represent the RMS of the measurements.

Table 8.2: Beam size relative differences between IN/OUT scans on the same cycle.

Monitor	**Relative Beam Size Difference** [%]			
	No Correction		**Match IN-OUT**	
	Mean	RMS	Mean	RMS
BWS414H	9.662	1.409	3.221	0.951
BWS414V	8.859	0.953	2.338	0.920
BWS416H	5.896	1.247	0.666	1.412
BWS519H	8.241	2.290	2.010	1.900
BWS519V	7.678	2.648	3.184	2.574
ALL	**8.067**	1.709	**2.284**	1.551

Table 8.3: Correction angles computed to correct the measurements of Fig. 8.2

Monitor	**Correction Angle** $\Delta\alpha$			
	Match IN-OUT			
	Mean [mrad]		**RMS [mrad]**	
	IN	OUT	IN	OUT
BWS414H	65.4	-67.5	1.7	1.8
BWS414V	68.3	-70.5	0.7	0.8
BWS416H	48.5	-49.8	0.7	0.7
BWS519H	67.8	-69.9	1.7	1.6
BWS519V	50.5	-51.7	1.1	1.1

8.2 SPS wire scanners comparative measurements

The measurement sessions reported below were only possible after the optimization of the monitors setup and of the measurement procedures, including the analysis tools described in Chapter 7. During the setup preparation, the synchronization between the acquisition system and the bunch trains structure (see Section 4.1.2) as been studied and adjusted, as well as the synchronization among different instruments.
The time at which the wire has to intercept the beam is selectable. The motor control is then activated with an advance period which is calculated from the initial parking wire position and the nominal speed. In addition, the wire movement start time is read by the accelerator timing system. On average the difference between the demanded and measured times is negligible and its statistical fluctuation is about $1\,ms$. This can be considered as the asynchronism between two wire scanners operated with the same demanded time.
The beam size σ varied from about $0.8\,mm$ to about $2\,mm$ depending on the beam type and the monitors locations. Considering the wire speed ($0.4\,m/s$ for the linear scanners and $6\,m/s$ for the rotational) it takes from about 1.33 to $50\,ms$ to pass through $\pm 5\,\sigma$. Hence, a wire scan launched simultaneously to another can pass through the beam core when the first one already left the distribution tails. However, the synchronization is considered sufficient, since only very small variations of the beam size are expected over few milliseconds.
The monitors comparison is made by considering one wire scanner per plane as reference, BWS517H and BWS517V. These two instruments are driven by a linear mechanism. The uncertainty on the wire position determination only depends on the optical ruler resolution and accuracy, that are $4\,\mu m$ and $1\,\mu m$ respectively [68].

8.2.1 Measurements in the vertical plane with TOTEM beam

The total number of protons populating the TOTEM beam (see Table 1.1), is below the damage threshold of the wires of the linear scanners. Therefore 5 monitors (3 rotational and 2 linear) could be utilized. To be as independent as possible from the beam instabilities, the intensity signal acquisition has been adjusted to detect the signal of only the first bunch.
The systematic errors of the rotational wire scanners position determination (discussed in the previous section) have been corrected. This is done by imposing the measured bunch posiiton to be the same during the two scans with the same instrument. The beam position stability between the IN and OUT scan is also confirmed by the beam orbit monitoring system, used during other periods with the same beam type.
At first we will analyze the occurrence of the emittance increase due to multiple Coulomb scattering between the wires and the proton beam and later compare absolute emittance as measured by the five monitors.

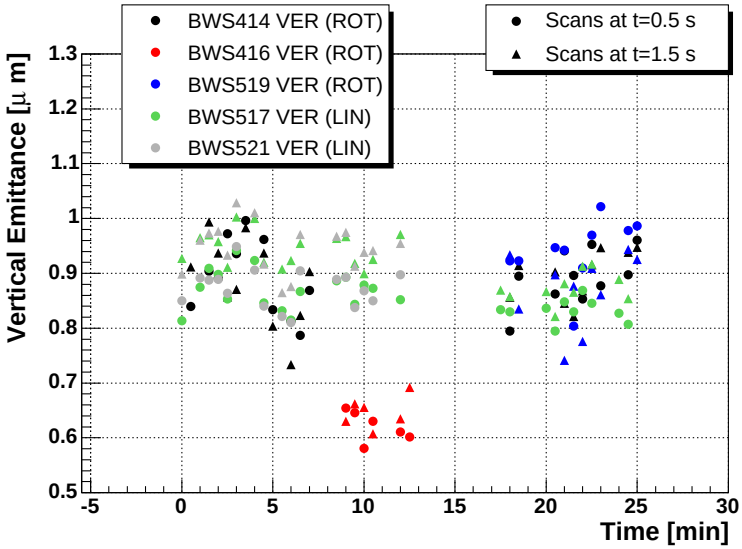

Figure 8.5: Vertical emittance of the TOTEM beam at $26\,GeV$, monitored with the SPS wire scanners. For each period two or three monitors simultaneously used.

Emittance increase due to multiple Coulomb scattering.

The vertical normalized emittance, as measured at a beam energy of $26\,GeV$, is shown in Fig. 8.5. During the SPS cycle, each monitor was operated twice, at $t = 0.5\,s$ (IN scan) and $t = 1.5\,s$ (OUT scan) after the beginning of the cycle. The emittance measured during the OUT scan is often larger than the one measured during the IN scan. This is particularly evident for the two linear scanners, BWS517V and BWS521V.
The emittance increase is caused by multiple Coulomb scattering between the wire and the accelerated protons (see Section 5.2). The increase generated by the IN scan is detected by the OUT scan.
The emittance growth is proportional to the value of the betatron function at the monitor location and inversely proportional to the wire speed. For the linear wire scanners, the effect of BWS517V is amplified by the value of the vertical betatron function at its location, which is $100\,m$ (two times the vertical betatron function at the location of BWS521V), approximately the largest around the SPS ring, while the effect of BWS521V is enhanced by its lower speed (=0.58 m/s for these measurements, compared to 1 m/s of BWS517V). Table 8.4 summarizes the emittance increase expected by a single scan of the five SPS monitors at a beam energy of 26 GeV, calculated according to Eq. (5.22).
The rotational wire scanners are operated at $6\,m/s$ and the maximum value of the betatron function at their location is $64\,m$. The emittance increase induced by their passage through the beam has a maximum of $5\,nm$ for BWS416V.

Table 8.4: Normalized emittance increase due to multiple Coulomb scattering between the wire scanners wire and the proton beam, for a beam energy of 26 GeV

Monitor	$\beta_v[m]$	$v[m/s]$	$\Delta\epsilon_{mc}[nm]$
BWS414V (ROT)	22.45	6.0	2
BWS416V (ROT)	64.56	6.0	4
BWS517V (LIN)	100.29	1.0	40
BWS519V (ROT)	27.36	6.0	4
BWS521V (LIN)	49.84	0.6	34

The occurrence of such emittance growth can be used to study the SPS linear wire scanners precision. The measured emittance change is

1. predictable by an analytical model ;
2. very small and therefore suitable for studying the monitors resolution;
3. measured with the two linear wire scanners which can be compared while monitoring the variation of the normalized emittance, independently from their absolute offset errors.

In the following we will compare the emittance increase measured by the two linear wire scanners with the predictions of Table 8.4. The comparisons will be done over three measurement periods:

- *Period 1* includes the measurements of Fig. 8.5 when both BWS517V and BWS521V are operated. During this period the emittance increase caused by the two instruments adds up.
- *Period 2* includes the measurements of Fig. 8.5 when only BWS517V is operated.
- *Period 3* includes a series of measurements using BWS517V and BWS521V not simultaneously. These measurements have been carried out many weeks before the ones of Period 1 and Period 2 .

The plot in Fig. 8.6(a) shows the emittance increase as measured by the two monitors during Period 1 and Period 2, as function of the cycle number. To the set of measurements of Fig. 8.5 three measurements are added (cycle number larger than 68500 in the figure) in order to reduce the statistical error on the differences evaluation. Fig. 8.6(b) and Fig. 8.6(c) show the emittance increase distributions measured by the two instruments during the two periods, calculated as:

$$\Delta\epsilon_{BWS517V} = \epsilon^{OUT}_{BWS517V} - \epsilon^{IN}_{BWS517V} \quad (8.4)$$

$$\Delta\epsilon_{BWS521V} = \epsilon^{OUT}_{BWS521V} - \epsilon^{IN}_{BWS521V} \quad (8.5)$$

The equivalent plots for the measurements of Period 3 are displayed in Fig. 8.7. It must be noticed that, even though the beam type is the same (TOTEM), the absolute emittance is on average more than $20\,\%$ smaller than the one of Period 1 and Period 2. Since the emittance increase due to multiple Coulomb scattering does not depend on the absolute emittance, the relative increase is larger.
A summary of the results achieved in the three periods is presented in Table 8.5. The significance of the results is assessed by the error on the mean of the distributions. If μ is the distribution mean value and σ the standard deviation, the error associated to the mean is $\sigma_\mu = \frac{\sigma}{\sqrt{N}}$ where N is the number of samples populating the distribution.[2] During Period 1, when the two monitors are used at the same time, the average discrepancy between the emittance increase measurements is $6\,nm$. In terms of beam size (after denormalizing for the betatron functions and the beam energy) this corresponds to only $6\,\mu m$ for BWS517V and $4\,\mu m$ for BWS521V. From Table 8.5, we deduce that BWS517V exhibits the largest error on the mean, which is $4\,nm$ during the first period. It corresponds to less than $1\,\%$ of the absolute emittance and determines the level of accuracy of these set of measurements (i.e. not of the monitors).
In addition, the standard deviations of the differences distributions, divided by $\sqrt{2}$ [3], allows to address

[2]Only evaluating σ_μ it is possible to characterize a systematic emittance increase which overcomes the statistical fluctuations of the measurements because a single measurement has a statistical error of the same order of the effect we want to measure.

[3]The standard deviation is divided by $\sqrt{2}$ because each value of the emittance increase results from two measurements with the same instrument. The assumption is rigourously correct if the IN and OUT scans exhibit the same statistical fluctuations.

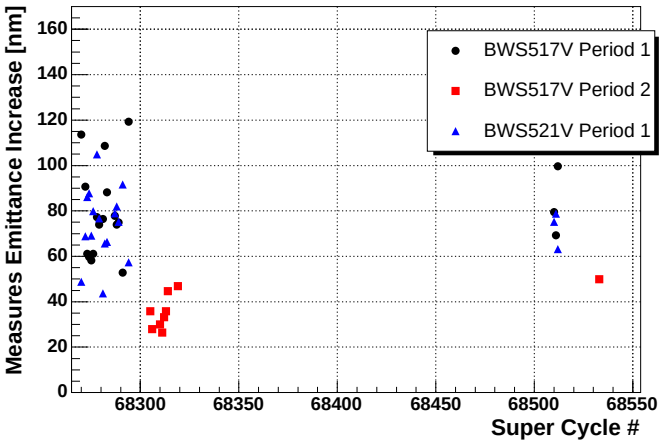

(a) Emittance increase $\epsilon_{OUT} - \epsilon_{IN}$ due to Multiple Coulomb scattering, measured by BWS517V and BWS521V, as function of the cycle number.

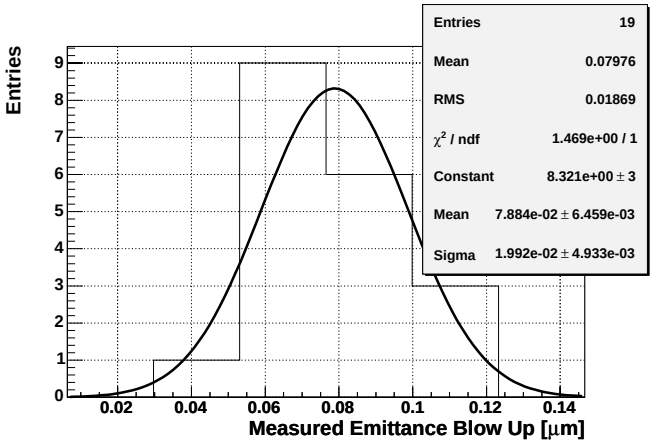

(b) $\epsilon^{OUT}_{BWS517V} - \epsilon^{IN}_{BWS517V}$ with scans of BWS517V and BWS521V at the same time (Period 1)

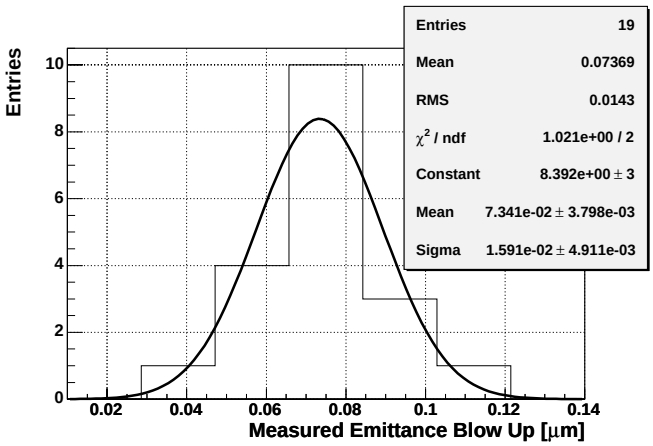

(c) $\epsilon^{OUT}_{BWS521V} - \epsilon^{IN}_{BWS521V}$ with scans of BWS517V and BWS521V at the same time (Period 1)

Figure 8.6: Normalized emittance increase due to multiple Coulomb scattering when scanning with BWS517V and BWS521. In the histograms legends *Mean* (second line) and *RMS* are calculated form the data distribution, while *Mean* (sixth line) and *Sigma* come from the Gaussian fit.

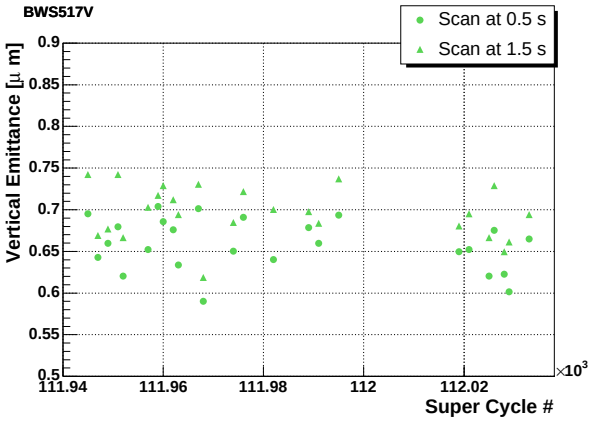

(a) Emittance measured by BWS517V (scans IN and OUT), as function of the cycle number (Period 3).

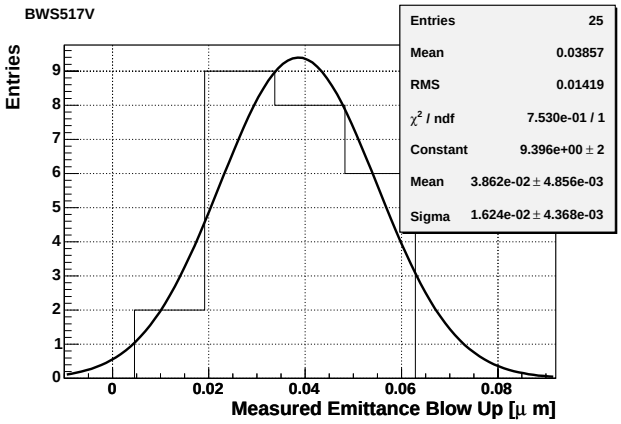

(b) $\epsilon^{OUT}_{BWS517V} - \epsilon^{IN}_{BWS517V}$ (Period 3)

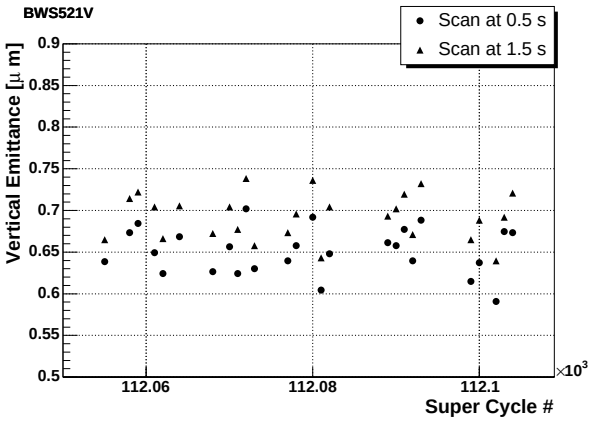

(c) Emittance measured by BWS521V (scans IN and OUT), as function of the cycle number (Period 3).

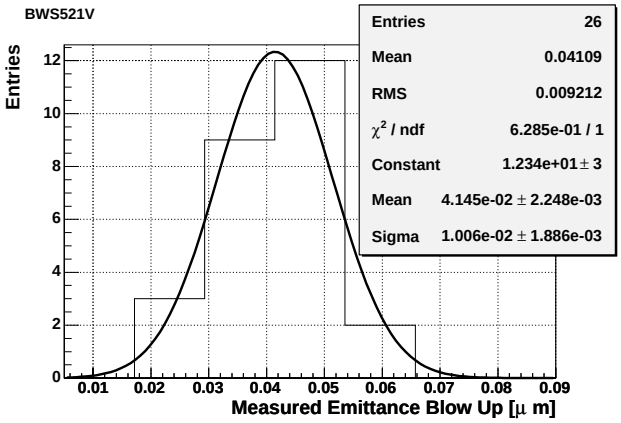

(d) $\epsilon^{OUT}_{BWS521V} - \epsilon^{IN}_{BWS521V}$ (Period 3)

Figure 8.7: Normalized emittance as function of cycle number and distributions of the emittance increase when running BWS517V and BWS521 with TOTEM beam during non simultaneous measurements. These measurements have been carried out many weeks before the measurements shown Fig. 8.6. In the histograms legends *Mean* (second line) and *RMS* are calculated form the data distribution, while *Mean* (sixth line) and *Sigma* come from the Gaussian fit.

Table 8.5: Normalized emittance increase during the operation of two linear wire scanners. "Period 1" is with both BWS517V and BWS521V scanning, "Period 2" with BWS517V only. $\Delta\epsilon_{mc}$ stands for the emittance increase predicted by the multiple Coulomb scattering theory.

	Period 1				
		$\Delta\epsilon_m\,[nm]$			$\Delta\epsilon_m - \Delta\epsilon_{mc}\,[nm]$
MONITOR	Entries	μ	$\sigma/\sqrt{N}$	$\sigma/\sqrt{2}$	
BWS517V	19	79	4	14	5
BWS521V	19	73	3	11	-1
	Period 2				
BWS517V	9	37	3	6	-3
	Period 3				
BWS517V	25	39	3	11	-1
BWS521V	26	41	2	7	- 7

the monitors *repeatability*. In terms of normalized emittance, averaging over the three periods, the repeatability results $10\,nm$ for BWS517V and $9\,nm$ for BWS521V. Both values are below 1.5 % of the (small) absolute emittance of the TOTEM beam.
After denormalizing for the betatron functions and the beam energy, the repeatability in terms of beam size reads:

$$\begin{aligned} 10\ \mu m \quad & \text{for BWS517V} \\ 6\ \mu m \quad & \text{for BWS521V} \end{aligned}$$

Such values indicates the random (or statistical) error characterizing a single profile measurements with the SPS linear wire scanners.

The last column of Table 8.5 lists the difference between the emittance increase measured by the wire scanners and the prediction of the multiple scattering theory. Assuming that the theory is exact, such values would indicate the instruments *systematic* errors. The largest error arises from BWS521V during Period 3 and is equal to $7\,nm$ in terms of emittance, corresponding to only $5\,\mu m$ in terms of beam size. Condidering the the five available errors in terms of emittance, it results:

$$\text{Systematic error (SPS linear WS)} = \Delta\epsilon_m - \Delta\epsilon_{mc} = -1 \pm 4\ nm \tag{8.6}$$

This set of measurements allow also to consider the linear wire scanners *resolution*. As verified by the results of Period 2 and Period 3, the monitors are able to resolve an emittance variation of about $40\,nm$ with a repeatability which is better than $10\,nm$. This indicates a resolution R which is (in terms of beam size)

$$\begin{aligned} R_{517V} &= 40 \pm 10\,\mu m \\ R_{521V} &= 28 \pm 7\,\mu m \end{aligned}$$

For both instruments the mean value is four time larger than the standard deviation. It follows that in 99.9 % of the cases a single measurement is sufficient to discriminate the given beam size variation. This is based on the *smallest known emittance variation* that was available.

Sofar, nothing can be stated for the rotational wire scanners, except that, due to the residual error on the wire position read-out, depending on the wire movement direction[4], they can not resolve the emittance increase generated by the linear monitors. However, their resolution is not necessary worse than the linear scanners, it should be evaluated by scanning with the same movement direction during a known emittance increase, but this has not been done yet.

[4]This will be for instance shown in Fig. 8.8

Comparison of different monitors

The data acquired during Period 1 are now used to calculate the differences between the emittance measurements of couple of instruments operated simultaneously, see Fig. 8.8.
For every couple of instruments (BWS517V with the others) four values can be calculated: the difference between the IN scans (at t=0.5 s) before and after the IN/OUT correction of the rotational wire scanners and the difference between the OUT scans (at t=1.5 s) before and after the correction. Table 8.6 presents the differences values averaging, for each couple of instruments, the IN and OUT scans. Table 8.7 lists the relative differences after the angle corrections, separating the IN and OUT scans. The relative difference between the two linear devices (BWS517V and BWS521V) is below $0.5\,\%$ when averaging the IN and the OUT scans. The residual dependence of the rotational wire scanners on the wire direction movement prevents any consideration about the monitors agreement to better than $5\,\%$ of the TOTEM beam vertical normalized emittance. The average values μ showed in Table 8.7 can be used to evaluate the systematic differences, which vary from -38 to $10\,\%$.
As an example of the transverse distributions analyzed in these synchronized measurements, three profiles from three different monitors are shown in Fig. 8.9. These measurements belong to the period in which BWS414V, BWS517V and BWS519V were used simultaneously (after t=15 m in Fig. 8.5) and only the IN scans are shown. The fit takes into account only the points which are above the threshold (see Chapter 7) determined by the fit 70 % confidence level. This results in an approximation where the non Gaussian tails are excluded from the fit (see Fig. 8.9, left). The general shape of the residuals between the fit and the measurements, as function of the wire position, is identical for the three monitors (see Fig. 8.9, right).
Table 8.8 summarizes the outputs of the three profiles parametrization. The fit threshold is expressed as a percentage of the maximum profile amplitude, while the "Tails" are the ratio between the integrals of the residuals and of whole profile. This example allows to draw some noticeable conclusions:

i) the emittance difference between the monitors, when considering BWS517V as a reference, is $4\,\%$ for BWS414V and $15\,\%$ for BWS519V. The correspondent errors on the beam sizes are

Table 8.6: Summary of the vertical normalized emittance comparisons (average of the IN and OUT scan on the same cycle) with TOTEM beam, before and after the off-line correction of the rotational wire scanners.

		Relative Emittance Difference [%]			
		Before Correction		**After Correction**	
Monitors	Entries	$\mu[\%]$	$\sigma_\mu[\%]$	$\mu[\%]$	$\sigma_\mu[\%]$
BWS414 (ROT)-BWS517 (LIN)	28	-0.6	2.6	0.2	1.7
BWS416 (ROT)-BWS517 (LIN)	10	-35.4	2.3	-35.3	1.7
BWS519 (ROT)-BWS517 (LIN)	14	4.3	3.8	4.3	2.9
BWS521 (LIN)-BWS517 (LIN)	34	0.2	0.4	\	\

Table 8.7: Summary of the vertical normalized emittance comparisons after the rotational wire scanners correction, separating the IN and OUT scans.

		Relative Emittance Difference [%]					
		Scan IN			**Scan OUT**		
Monitors	Entries	μ	σ_μ	σ	μ	σ_μ	σ
BWS414V (ROT)-BWS517V (LIN)	14	4.0	1.9	7.1	-3.7	2.3	8.7
BWS416V (ROT)-BWS517V (LIN)	5	-32.7	2.1	4.7	-37.9	2.2	4.9
BWS519V (ROT)-BWS517V (LIN)	7	10.4	2.7	7.1	-0.8	4.1	10.8
BWS521V (LIN)-BWS517V (LIN)	17	0.3	0.6	2.3	0.1	0.6	2.5

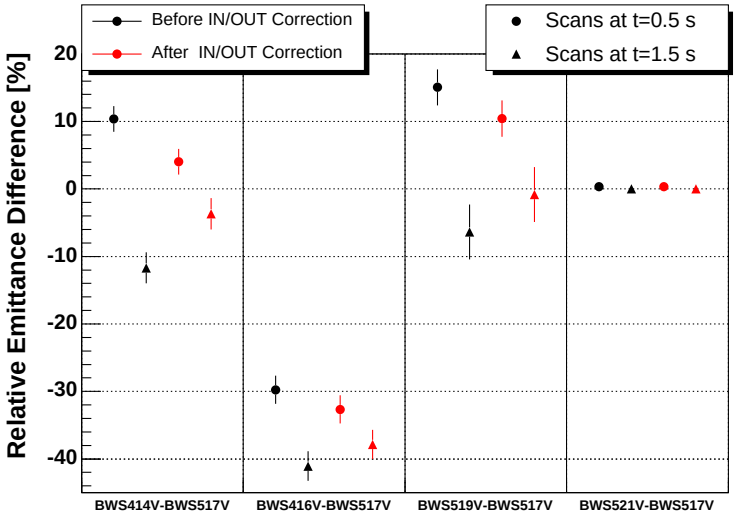

Figure 8.8: Relative normalized emittance differences from the measurements presented in Fig. 8.5.

$19\,\mu m$ and $52\,\mu m$ respectively;

ii) both rotational wire scanners measure a higher emittance than the linear device. This is consistent with the residual error of the IN/OUT correction: the IN scan overestimates the beam profile size;

iii) a systematic error of the betatron function would explain the emittance discrepancy. For instance, it would mean an error of $1.8\,m$ on the betatron function at the location of BWS414V. This is very unlikely the case.

Reconsidering now the comparisons summary of Table 8.7, the error on the mean σ_μ, expression of the accuracy of this set of measurements, has a maximum value of $4\,\%$ for BWS519V (OUT scans). The *repeatability* of the differences follows from the repeatability of the compared instruments. With the assumption that all the monitors are characterized by the same statistical fluctuations in measuring the beam size, the repeatability would be the standard deviation of the differences divided by the square root of 2. However it is not known a priori if the repeatability of the rotational wire scanners is equal to the one of the linear devices.
Profiting of the considerations of the previous paragraph, we can take $r_{517V} = 10\,\mu m$ as the repeatability of the reference wire scanner in terms of beam size (see Pag. 110). This corresponds to a variation of $10\,nm$ of the absolute emittance which is about $0.9\mu m$. In terms of relative emittance the repeatability of BWS517V is $r_{\epsilon 517v} = 1.1\,\%$. This value, together with the statistical fluctuations of the differences between couples of instruments can be used to calculate the repeatability of the other monitors according to:

$$r_{dif,i} = r_{i-517V} = \sqrt{r^2_{\epsilon 517V} + r^2_{\epsilon i}} \tag{8.7}$$

$$\Rightarrow \quad r_{\epsilon i} = \sqrt{r^2_{dif,i} - r^2_{\epsilon 517V}} \quad \text{with i=414V, 519V, 521V} \tag{8.8}$$

where the values $r_{dif,i}$ are the standard deviations σ of the differences (see Table 8.7) in terms of relative emittance. From each value $r_{\epsilon i}$ the repeatability in terms of absolute beam size can be calculated, as summarized in Table 8.9, where the average and RMS values are calculated from the IN and OUT scans. It can be concluded that the repeatability in terms of beam size varies from 10 and $14\,\mu m$ for the linear wire scanners and from 33 to $42\,\mu m$ for the rotational.

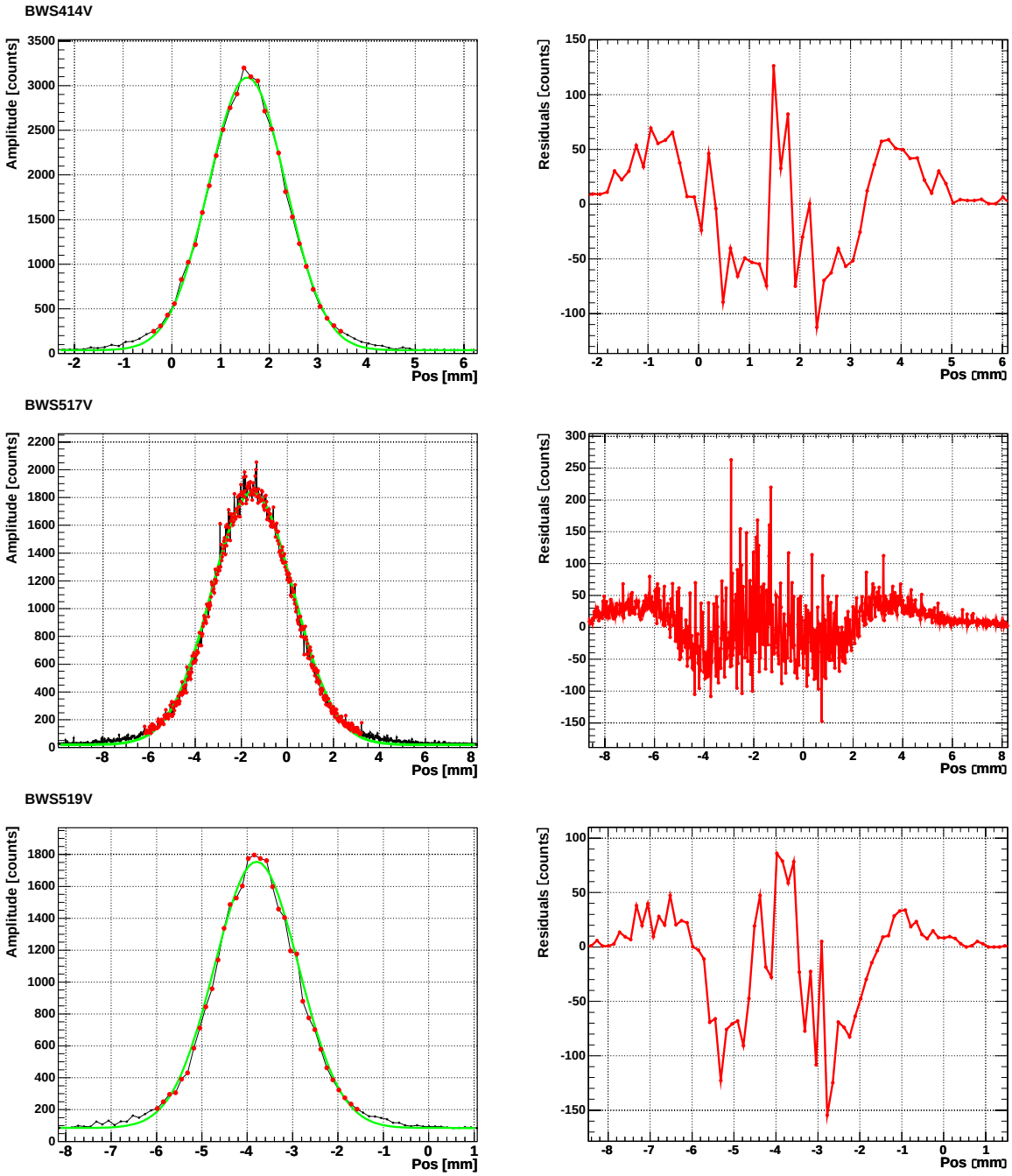

Figure 8.9: Beam profiles measured by three SPS wire scanners at the same instant on the same cycle. The fit (green line) is applied only to the amplitudes above the threshold which brings to the acceptable confidence level. The numerical values (beam sizes and normalized emittances) for this example are presented in Table 8.8.

Table 8.8: Comparison between three SPS wire scanners during synchronized acquisitions on the same cycle (profiles of Fig. 8.9). The emittance differences are calculated considering BWS517V as a reference.

Monitor	β_y $[m]$	σ $[mm]$	Tails [% of tot.]	Thres [% of Peak]	χ^2/ndf	ϵ $[\mu m]$	$\Delta\epsilon/\epsilon$ [%]
BWS414V	22.5	0.829	3.0	5	0.6	0.845	4
BWS517V	100.3	1.717	2.9	7	0.7	0.812	\
BWS519V	27.3	0.963	1.1	5	0.6	0.940	15

Table 8.9: Repeatability in terms of beam size of the five SPS wire scanners monitoring the vertical plane.

Monitor	**Repeatability** $[\mu m]$			
	Scan IN	Scan OUT	Average	RMS
BWS414V (ROT)	29.9	36.8	33.4	4.9
BWS416V (ROT)	32.6	36.8	33.4	1.0
BWS519V (ROT)	33.1	50.6	41.8	12.4
BWS517V (LIN)	10			
BWS521V (LIN)	12.8	14.3	13.6	1.0

8.2.2 Measurements in the horizontal plane

Horizontal emittance comparisons with Pilot bunch

As for the TOTEM beam, the LHC pilot bunch intensity is below the damage threshold of the linear wire scanners, hence the five installed monitors could be operated. The measurements have been taken at a beam energy of $26\,GeV$. As for the previous measurements, two scans with opposite wire movement direction (IN and OUT) have been performed for each instrument during every considered SPS cycle. A maximum of three scanners could be operated at the same time.
The pilot bunch horizontal normalized emittance evolution over about 16 hours is displayed by the top plot of Fig. 8.10, as measured by the five wire scanners. BWS416H, BWS517H and BWS519H are located in low dispersion regions ($D_x < 0.5\,m$), while BWS414H and BWS521H are in locations where $D_x = 3.84\,m$ and $D_x = 2.21\,m$ respectively.
For such a small beam, the emittance is very much depending on the product $D_x \cdot dp/p$, as assessed by the definition of emittance given in Chapter 2 which is here rewritten for convenience:

$$\epsilon_x = \frac{\beta\gamma}{\beta_x}\left[\sigma_x^2 - \left(D_x\frac{dp}{p}\right)^2\right]. \tag{8.9}$$

Fig. 8.11 shows the emittance changes as function of the momentum spread, for three beam size values at the location of BWS521H. A $5\,\%$ decrease of the momentum spread causes an emittance growth of $200\,\%$. This explains the large spread of the emittance values measured by the two monitors at high dispersion regions. The figure also shows the variation of the emittance calculated at the location of BWS517H, where $D_x = 0.35\,m$.
The momentum spread can be calculated by measuring the RF cavities frequency and the bunch longitudinal width. The dispersion is generally determined by knowing the characteristics of the accelerator magnets. A method for experimentally measure the dispersion function is described in Section 3.5. In order to accurately measure the horizontal emittance of small beams (i.e. $\epsilon_h < 1\,\mu m$), one should continuously track the momentum spread variations. This is not the case in the SPS yet.
As can be deduced from Fig. 8.11, also the emittance at the location of BWS517H has a dependence on the momentum spread, about $3\,\%$ variation over a $5\,\%$ change of the momentum spread. Here the momentum spread has been calculated by mean of Eq. (8.9), imposing the emittance measured by the monitors at high dispersion locations to be on average equal to the emittance measured by BWS517H. The estimated value is $dp/p = 0.95 \cdot 10^{-3}$.
The above considerations apply for the dispersion function D_x too. In addition, the fact that the dispersion depends on the horizontal tune must also be considered. Fig. 8.12 shows the dispersion variation at the location of BWS517H , for a change of the SPS horizontal tune from 26 to 27 [5], as

[5] Both the horizontal and vertical tune in the SPS are in this range

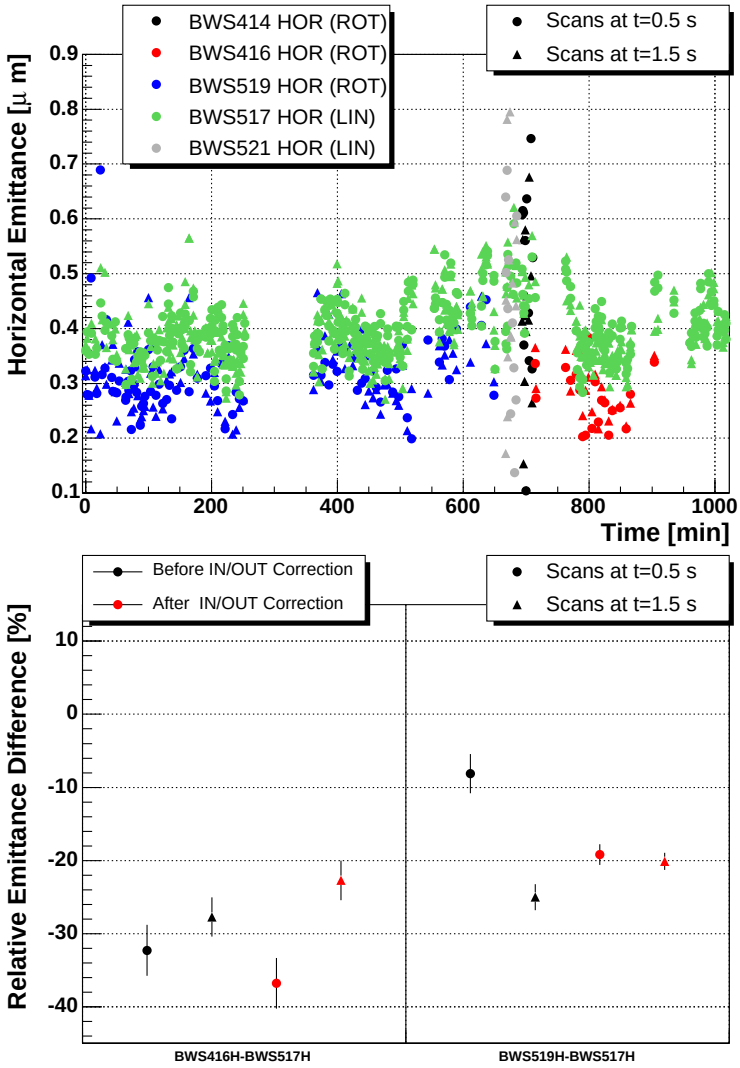

Figure 8.10: Pilot bunch normalized horizontal emittance as measured by the five SPS wire scanners, after the correction for the rotational wire scanners wire position determination (top) and emittance comparisons between the instruments located at low dispersion regions before and after the rotational wire scanners correction (bottom). Measurements at 26 GeV.

Table 8.10: Comparison among the SPS wire scanners located at low dispersion regions, with pilot bunch.

Monitors	Entries	Relative Emittance Difference [%]					
		Scan IN			Scan OUT		
		μ	σ_μ	σ	μ	σ_μ	σ
BWS416H (ROT)-BWS517H (LIN)	16	-36.8	3.5	13.8	-22.7	2.7	10.8
BWS519H (ROT)-BWS517H (LIN)	58	-19.2	1.4	10.7	-20.1	1.2	9.0

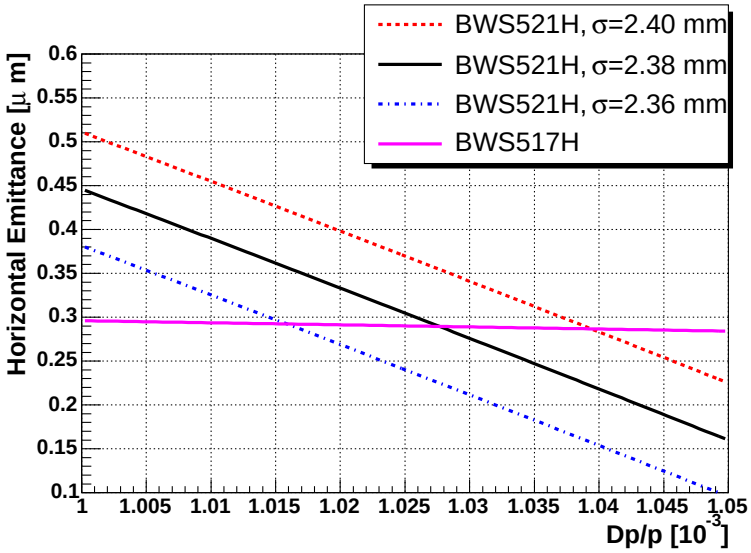

Figure 8.11: Dependence of the pilot bunch normalized horizontal emittance on the momentum spread.

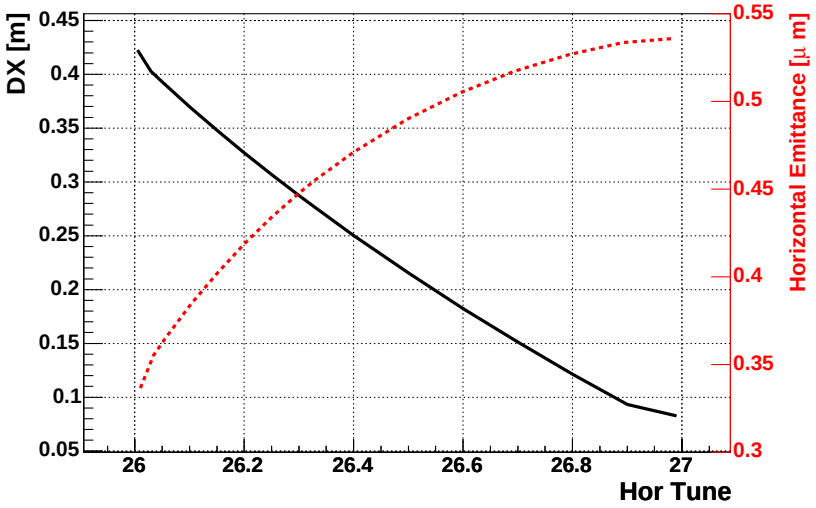

Figure 8.12: Dispersion function (solid black line) and normalized horizontal emittance (dotted red line) at the location of BWS517H. The normalized emittance is calculated with a fixed beam size $\sigma = 0.65\,mm$ (typical of the pilot bunch at this location) and momentum spread $dp/p = 0.95 \cdot 10^{-3}$.

simulated by MADX [31]. The operational SPS horizontal tune for all the LHC type beams was changed from 26.22 in 2003 to 26.18 in 2004, causing the dispersion function to increase from 0.33 to 0.35 m. As also shown in Fig. 8.12, the pilot bunch normalized horizontal emittance at 26 GeV, for a fixed momentum spread and beam size, changes from 0.422 to $0.409\ \mu m$. The relative variation is about $3.1\,\%$.

The relative differences between BWS517H and the other two instruments installed at low dispersion locations are shown in the bottom plot of Fig. 8.10, before and after the correction for the rotational wire scanners systematic error. The average values, after the rotational wire scanner correction, are listed in Table 8.10, separating the IN and OUT scans together with the errors on the mean and the standard deviations.

BWS416H systematically measures a normalized emittance which is more than $25\,\%$ lower than the one of BWS517H, while the relative difference between BWS519H and BWS517H is about $20\,\%$.

The uncertainty of these set of measurements is assessed by the errors on the mean σ_μ, below $3.5\,\%$ for the four considered differences.
The IN/OUT correction applied to BWS416H has a contradictory effect. After the correction the relative emittance difference between scans with opposite direction increases. This will be confirmed by the results of the next paragraph and is not understood yet.
As already mentioned for the measurements in the vertical plane (see Eq. (8.8)), the standard deviation of their difference expresses the monitors *repeatability*. Here we assume that the reference monitor (BWS517H) has the same repeatability as the linear wire scanner BWS517V studied in the previous section. The two instruments share the same tank and are driven by the same mechanism and electronics, therefore there is no reason for which they should exhibit different precisions. Hence the repeatability of the reference monitor is $10\,\mu m$ in terms of beam size. Such value represents an variation of $15\,nm$ of the average value which is about $350\,nm$. Consequently the repeatability of BWS517H in terms of relative emittance is $r_{\epsilon 517h} = 4.3\,\%$. This value can be introduced in Eq. (8.8) together with the standard deviations of Table 8.10 in order to calculate the repeatability of BWS416H and BWS519H. The results are shown in Table 8.12 and will be discussed at the end of the next paragraph.

Horizontal emittance comparisons with TOTEM beam

The SPS wire scanners has been also used while measuring TOTEM beam horizontal emittance, at the beam energy of $26\,GeV$. The same consideration made for the measurements in the vertical plane with TOTEM beam apply: to avoid averaging over different bunches, the signal intensity gate has been adjusted on only one bunch.
Also in this case, due to the small normalized emittance ($\epsilon_h \approx 0.9\,\mu m$) the contribution of the product $D_x \cdot dp/p$ to the emittance magnitude is considerable. As for the measurements with the pilot bunch, the momentum spread has been calculated imposing the average emittances measured the two wire scanners located at high dispersion regions to be equal to the one measured by BWS517H. The estimated value is $dp/p = 1.5 \cdot 10^{-3}$.
The horizonal emittance, as tracked by the five SPS wire scanners, and the comparisons between BWS517H and the two rotational monitors located at low dispersion regions are shown in Fig. 8.13. Table 8.11 summarizes the comparisons. The second column of the table indicates the number of comparisons for each couple of monitors, which were considerably less than the measurements with pilot beam.
The average discrepancies between the three wire scanners agree within $6\,\%$ with the quantities deduced from the previous measurements with pilot bunch. This is a remarkable result, because underlines the hypothesis of large systematic errors of BWS416H and BWS519H.
Despite the few number of acquisitions, the error on the mean σ_μ also agrees (within $1\,\%$) with the previous set of measurements and is below $3.2\,\%$.
The standard deviations of the differences (i.e. the differences repeatability) exhibit the largest values for the OUT scans, $7.9\,\%$ for BWS416H and $8.9\,\%$ for BWS519H. In terms of relative differences, they result about half the values obtained with pilot bunch, but here the absolute emittance is almost doubled.
As for the previous cases, assuming the repeatability of the reference monitor to be $10\,\mu m$ in terms of beam size, the repeatability of the rotational wire scanners can be determined. In Table 8.12 the calculated values are compared with the ones obtained with the pilot bunch. The *average* and *RMS* shown in the last two columns are determined considering the four available values for each instrument (IN/OUT for pilot bunch and IN/OUT for TOTEM beam).
The repeatability of BWS519H results the largest among all the studied monitors (see also Table 8.9).

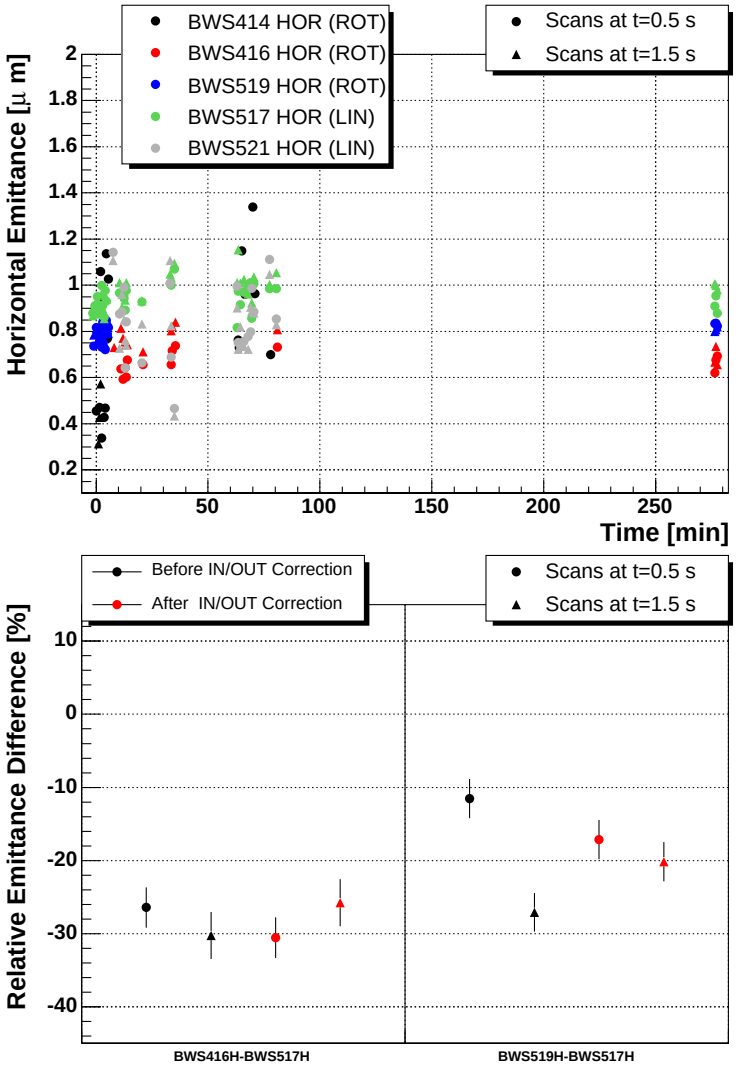

Figure 8.13: TOTEM beam normalized horizontal emittance as measured by the five SPS wire scanners, after the correction for the rotational wire scanners wire position determination (top) and emittance comparisons between the instruments located at low dispersion regions before and after the rotational wire scanners correction (bottom).

Table 8.11: Comparison among the SPS wire scanners located at low dispersion regions, with TOTEM beam.

Monitors	Entries	Relative Emittance Difference [%]					
		Scan IN			Scan OUT		
		μ	σ_μ	σ	μ	σ_μ	σ
BWS416H (ROT)-BWS517H (LIN)	6	-30.5	2.8.0	6.8	-25.8	3.2	7.9
BWS519H (ROT)-BWS517H (LIN)	11	-17.1	2.7	8.9	-20.2	2.7	8.9

This is attributed to the statistical fluctuations of the momentum spread, which contribute to the emittance measurements repeatability.

Table 8.12: Repeatability in terms of beam size of the SPS wire scanners monitoring the horizontal plane.

Monitor	**Repeatability** $[\mu m]$					
	Pilot Bunch		**Totem Beam**		**Average**	**RMS**
	Scan IN	Scan OUT	Scan IN	Scan OUT		
BWS416H (ROT)	45.5	34.4	35.2	41.7	39.2	5.3
BWS517H (LIN)	10					/
BWS519H (ROT)	50.3	40.6	70.3	70.3	57.8	14.9

8.2.3 Comparisons between two vertical wire scanners with five different beams.

In this section we compare two rotational wire scanners (BWS414V and BWS519V) when used to measure the vertical emittance of five different beams:

1. Pilot bunch at 26 GeV;
2. Totem beam at 26 GeV;
3. 75 ns bunch spacing beam at 26 GeV;
4. LHC nominal beam at 26 GeV;
5. LHC nominal beam at 450 GeV;

With the exception of the scans with the TOTEM beam, the measurements have been carried out during periods dedicated to optimize the beam, rather than studying the instruments. Therefore the following features should be considered:

1. the beam transverse emittances were not necessarily stable;
2. the scanners were not operated at the same time;
3. the beam profiles have been acquired adjusting the gating in order to average over all the bunch trains circulating in the SPS.

However it was considered interesting to compare the exhibited systematic discrepancies over a wide range of absolute emittances.
For each beam type, the difference has been computed between the average emittance values measured during the IN and OUT scans. For instance, the vertical emittances of the LHC nominal beam, as measured by the two monitors, are shown in Fig. 8.14 as function of the time in the SPS cycle (the energy ramp from 26 to 450 GeV starts at $t = 10.8\,s$ and ends at $t = 18.5\,s$).
The LHC design normalized emittance at 26 GeV is $3.5\,\mu m$ in both planes, about 10 times larger than the pilot bunch and about 3.5 times than the TOTEM beam.
The histograms in Fig. 8.15 show the distributions of the emittances measured with the pilot bunch, the 75 ns bunch spacing beam and the LHC nominal beam (at two different energies in the second case).

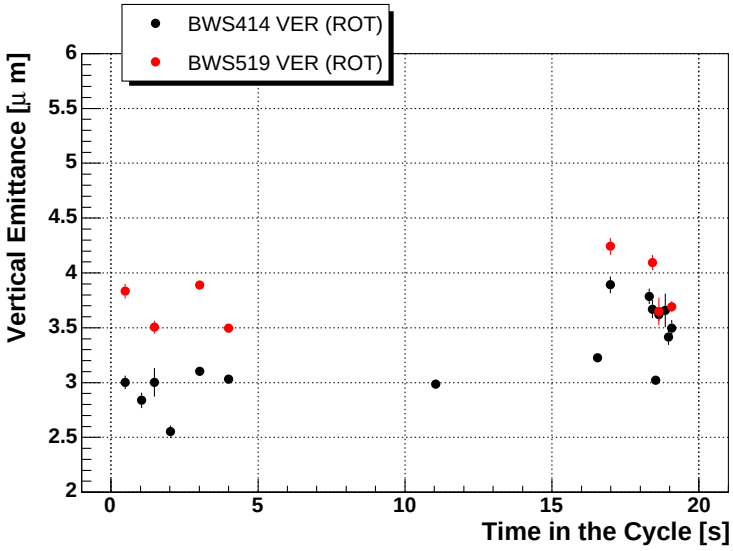

Figure 8.14: Vertical normalized emittance as measured by two rotational wire scanners with the LHC beam accelerated in the SPS.

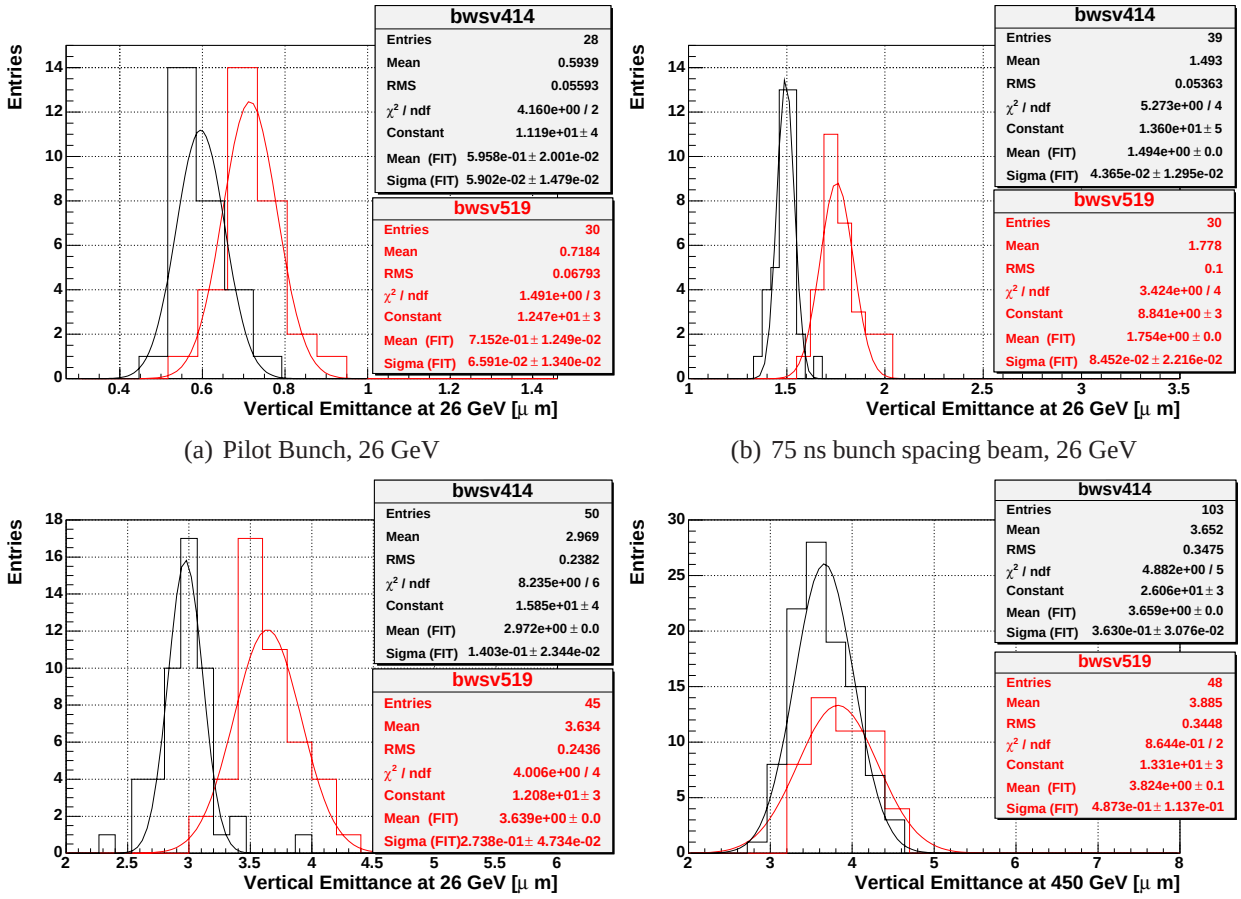

(a) Pilot Bunch, 26 GeV

(b) 75 ns bunch spacing beam, 26 GeV

(c) LHC nominal beam, 26 GeV

(d) LHC nominal beam, 450 GeV

Figure 8.15: Normalized vertical emittance measured by BWS414V and BWS519V with four different beam conditions. The acquisition have not been carried out simultaneously with the two monitors, but over different periods.

From the mean values of the differences we can estimate the systematic disagreement between the two monitors. The statistical fluctuations of the differences (RMS values and standard deviations of the fit in the histogram plots) would indicate that the monitors repeatability is worse than the one determined in the previous paragraphs. Given the measurements conditions discussed above, this is attributed to the contribution of the beam size statistical fluctuations to the measurements repeatability.
The comparison between the two monitors used with TOTEM beam follows from the measurements of Section 8.2.1 (see Table 8.7).
Fig. 8.16(a) shows the normalized vertical emittance as measured by the two instruments for the different beams. Fig. 8.16(b) displays the difference $(\sigma_{v519}^{meas} - \sigma_{v519}^{expect})$ between the beam size measured by BWS519V and the one calculated from the emittance measured by BWS414V and transported to the location of BWS519V by mean of the betatron functions, according to

$$\epsilon_{v414}^{meas} = \frac{(\sigma_{v414}^{meas})^2}{\beta_{v414}} \cdot (\beta\gamma) \tag{8.10}$$

$$\sigma_{v414}^{meas} = \sqrt{\frac{\epsilon_{v414}^{meas} \cdot \beta_{v414}}{(\beta\gamma)}} \tag{8.11}$$

$$\sigma_{v519}^{expect} = \sqrt{\frac{\epsilon_{v414}^{meas} \cdot \beta_{v519}}{(\beta\gamma)}} = \sigma_{v414}^{meas} \cdot \sqrt{\frac{\beta_{v519}}{\beta_{v414}}} \tag{8.12}$$

Since there are only two monitors, the same results (with a factor of opposite sign) would have been obtained plotting the same quantity for BWS414V. The difference is plotted as function of the beam size at BWS519V in order to visualize how it increases with increasing beam size. Only the comparison with TOTEM beam (beam size about $0.9\,mm$ in the plot) exhibits a value in disagreement with the observation of a quasi quadratic increase as function of beam size.
The relative difference $(\sigma_{v519}^{meas} - \sigma_{v519}^{expect})/\sigma_{v519}^{meas}$ is shown in Fig. 8.16(c) and exhibits a linear increase. The disagreement between the two monitors may be interpreted as a *scaling error* of one of the two instruments, the larger the beam size, the larger the difference.
The discrepancy can not be explained with the residual error depending on the wire movement direction, since the comparison is done, after the error correction, between the IN/OUT averages for each instrument. Further investigations about a scaling error of the SPS rotational wire scanners are recommended.

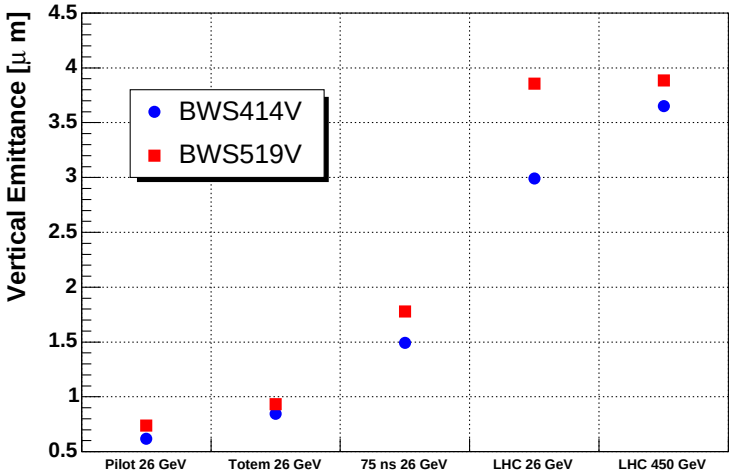

(a) Normalized vertical emittance as measured by the two monitors.

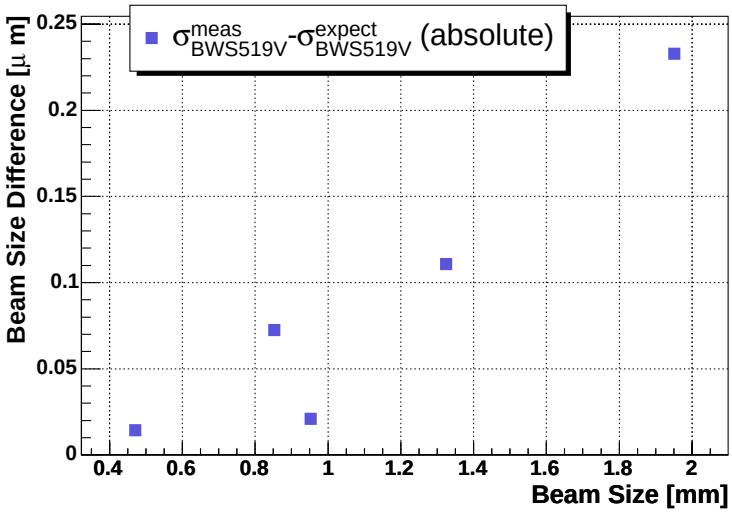

(b) Difference between the beam size measured by BWS519V and the one calculated from the measurement of BWS414V.

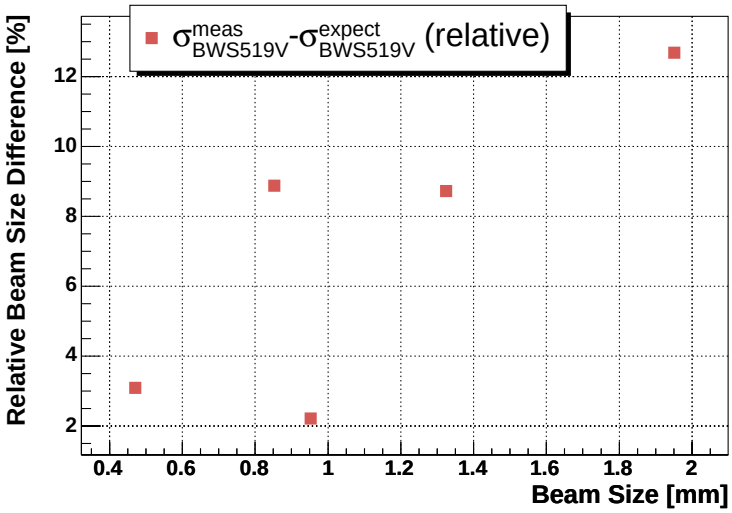

(c) Relative difference between the beam size measured by BWS519V and the one calculated from the measurement of BWS414V.

Figure 8.16: Comparison between BWS414V and BWS419V with five different beam conditions.

8.3 Ionization Profile Monitor calibration and comparison with the SPS wire scanners

This section regards the studies carried out with the Ionization Profile Monitor (IPM), with the aim of cross-calibrating it with the SPS wire scanners under different beam conditions.
Unlike the previous measurements with the SPS wire scanners, where the different monitors have been compared simultaneously on the same beam, the comparison between IPM and wire scanners has been carried out over long periods. In such a way it was possible to assess the IPM repeatability with different gain settings and its reproducibility with different beam conditions.
During the considered periods the beam emittance measured by the IPM is determined by averaging a number of IPM beam profiles. In the following subsections the averages, presented in the plots and tables, are computed from 1) all the profiles acquired during an SPS cycle at constant energy or 2) all the profiles at a fixed time in the cycle for several cycles (i.e. several beam injection in the SPS).
The IPM measured emittance is compared with the average measurements performed by the wire scanners during the same periods. For both instruments the error bars indicated on the plots represent the error on the mean. For an adequate setting of the gain, the statistical fluctuations of the IPM measurements are negligible compared with the systematic differences between IPM and wire scanners. For this reason the errors on the mean, which also reflect the beam instabilities during long periods, are not included in the tables summarizing the results.

8.3.1 Comparison between IPM and WS with beam in coast.

The LHC beam is normally injected and accelerated in the SPS during dedicated machine studies according to the SPS-LHC beam transfer, as described in Section 1.3. When operating with this scheme, the beam remains in the SPS for approximately $21\ s$ and then is sent to a beam dump.
During special periods the injected particles have been set to a *coast mode*: the beam is kept circulating in the accelerator for a longer period, in order to study the beam stability and life time[6], reproducing the same conditions which will appear in LHC before and during the collision periods.
A coast period is abandoned after a time extent variable from few minutes to few hours, depending on the particle losses and on the interest on continuing the studies, rather than injecting new particles.
Some of the results are used here to illustrate how the vertical emittance is tracked by the IPM and the WS while the particles are circulating in the SPS.
We will also address the beam intensity evolution during the costing periods. The beam intensity is monitored in the SPS with Beam Current Transformers (BCT) (see the Glossary at the beginning of the report).
The beam intensity can also be estimated with the IPM by calculating the profile integral, which is proportional to the number of particles populating the beam. One can cross-calibrate the IPM with the BCT at a fixed beam intensity and consequently follow the intensity evolution by observing the profile integral variations.
The measurements presented below refer to the injection and coast of one PS batch in the SPS at a constant energy equal to $26\,GeV$. The wire scanners measurements have been set up in order to monitor the vertical emittance of the very first and very last part of the batch. This has been indicated with "Gate 1" and "Gate 2" on the plots.
The beam intensity is varying with time due to particles losses. In order to quickly follow the emittance evolution, it was not possible to change the monitors gain during a single coast period. The

[6]The beam lifetime describes the decrease of the beam intensity due to particles losses. In most cases a constant fractional loss occurs, causing an exponential intensity decay and the life time τ represents the exponential time constant.

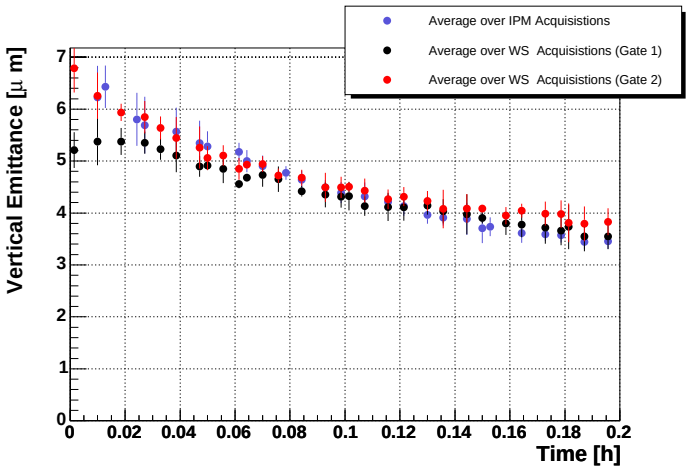

(a) Emittance from IPM (20 profiles for each time slot) and WS (2 profiles for wach time slot) monitors.

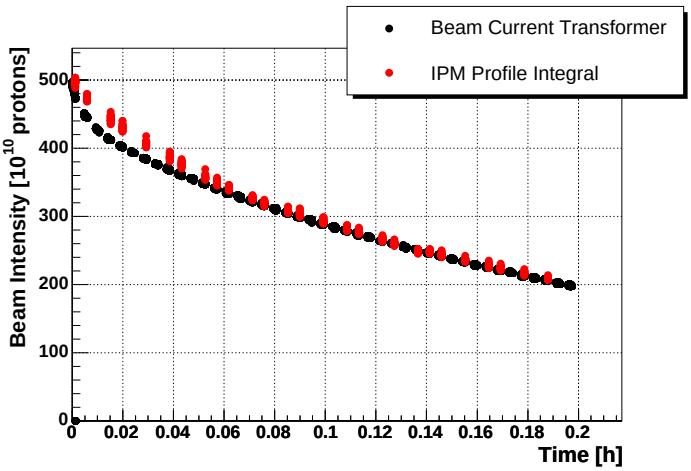

(b) IPM beam intensity comparison with the BCT monitor.

Figure 8.17: Beam emittance and beam intensity measurements as function of time after injection. Coast period with 1 PS Batch in the SPS, during which the IPM gain was optimal for the whole beam intensity range.

beam intensity variation did not affect the wire scanners accuracy, while caused uncertainties in the IPM measurements.

The top plot of Fig. 8.17 shows the beam emittance evolution as measured by the wire scanners and the IPM as function of time after injection. The bottom plot shows the beam intensity variation during the coast.

The beam intensity, as seen by the beam current monitor and by the IPM integral of the profile, decreases of a factor 2.4. Due to the intensity variation, the vertical emittance also decreases of a factor 1.6. The largest emittance difference between WS and IPM (about $16\,\%$) is at the beginning of the period, but only when comparing the first part of the batch, monitored by the WS, with the IPM. Comparing the last part of the batch the difference is only $1\,\%$. This is not contradictory since the residual gas monitor averages over the whole batch and is not able to discriminate the emittance increase along the batch.

During the rest of the period the agreement between WS and IPM is within $1\,\%$.

The top plot of Fig. 8.18 refers to a coasting beam period in which the initial beam intensity was to high for the IPM settings and the monitor likely reached saturation and the measured IPM beam size is larger than the one measured with the wire scanners. When the intensity drops, the agreement

between IPM and WS is within the error bars.
The bottom plot shows the beam current evolution during the same period. The IPM overestimates the beam intensity in the first part of the period, where also the emittance detected by the IPM is in disagreement with the WS monitors. This confirms the not appropriate IPM settings for the initial beam intensity.

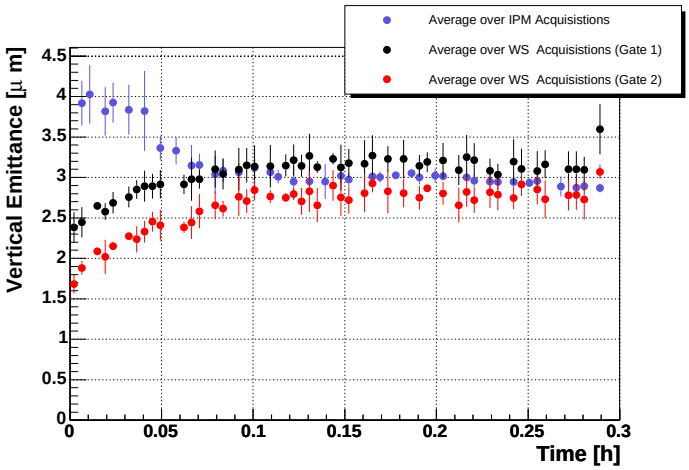

(a) Emittance from IPM (20 profiles for each time slot) and WS (2 profiles for each time slot) monitors.

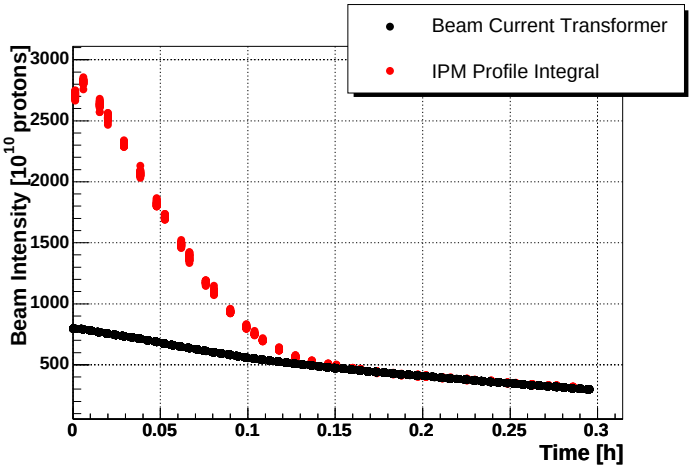

(b) Beam intensity comparison with the BCT monitor.

Figure 8.18: Beam emittance and beam intensity measurements as function of time after injection. Coast period in which the IPM gain was too high for the initial beam intensity.

8.3.2 Comparison between IPM and WS during beam acceleration

Here the beam emittance measurements with the IPM are compared with the WS at injection energy and and during acceleration from 26 to 450 GeV.
The monitors have been compared with three beam types: LHC nominal beam, the LHC beam with $75\,ns$ bunch spacing and the LHC Pilot beam. All the available WS monitors have been utilized.
The comparison has been for the first time systematically performed in the SPS 2003 run. The results were used to understand the IPM limitations and lead to some hardware modifications during the SPS closure period between 2003 and 2004. The measurements have been then repeated during the 2004 run.
The three dimensional plot in Fig. 8.19(a) shows the vertical normalized emittance measured by the IPM as function of time in the SPS cycle (described in Section 1.3) and for different cycles, during the 2003 run with LHC nominal beam. For the first few cycles the emittance is larger at low energy ($E = 26\,GeV$ for $t < 10.8\,s$) than at high energy. It is very unlikely that the beam follows such evolution, unless the beam losses during acceleration are so high to result in an emittance decrease.
In order to search for dependencies, the beam position is plotted, for the same period, in Fig. 8.19(b). The beam position is changing during acceleration. This means that the IPM image is acquired on a different portion of the MCP plate.
After the first SPS cycles, the beam was voluntarily displaced on another orbit. After such action, the IPM measurements show a smaller emittance at low energy and an emittance increase during acceleration. It can be concluded that, during the first period, the beam image fell on a damaged portion of the MCP plate, where the electron multiplication factor was not homogeneous[7]. This lead to the image broadening.
The normalized emittance evolution as detected by the IPM with the $75\,ns$ bunch spacing beam and pilot beam is presented in Fig. 8.20(a) and Fig. 8.20(b) respectively. The figures allow to asses the beam width stability over the measurement periods and the IPM repeatability. For instance the acquisitions with pilot beam refer to 60 SPS cycles (i.e. about 20 minutes) and the measurements repeatability at 26 GeV results about $0.1\,\mu m$ in terms of normalized emittance, which correpsonds to about $100\,\mu m$ in terms of beam size.
The average vertical emittance measured by the IPM, with the LHC nominal beam during the year 2003 (after the beam displacement described above) is plotted in Fig. 8.21(a) and compared with the WS data acquired in the same period.
The error bars indicate a large statistical fluctuation of the IPM measurements acquired at 26 GeV. This can be again referred to the low gain settings applied in order to avoid saturation at high beam energy[8]; the signal over noise ratio is consequently lower at low energy.
The average emittance oscillations at $t \approx 13\,s$ and $t \approx 17\,s$ are caused by the interferences between the IPM and the electromagnetic field carried by the beam. In particular, at the end of the energy ramp, the bunches longitudinal distribution is voluntarily shrank by manipulating the radio frequency cavities (see Chapter 6). During such manipulations light disturbances on the IPM CCD sensor have been frequently observed. They are caused by the lightening of the IPM high voltage electrodes due the high RF power stored in the IPM tank. Such disturbances may last several hundreds milliseconds and enlarge the beam image.
The comparison between IPM and wire scanners, in terms of average normalized emittance as function of time in the cycle, are shown in Fig. 8.22(a) and Fig. 8.23(a) for the $75\,ns$ bunch spacing beam and pilot bunch respectively.

[7] The measurements took place several months after the hardware installation and the MCP aging is not surprising.
[8] With a constant gain during the energy ramp, saturation may occur due to the beam size reduction due to adiabatic damping.

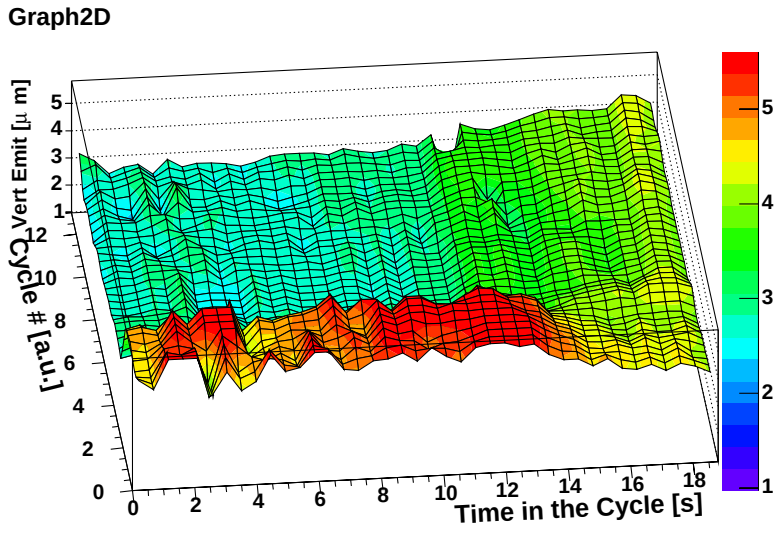

(a)

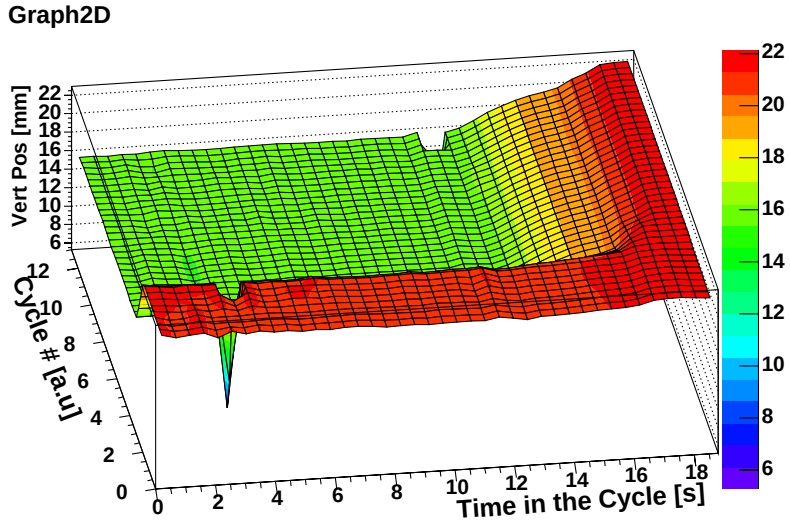

(b)

Figure 8.19: IPM measurements with LHC nominal beam: (a) normalized beam emittance and (b) beam position, as function of time in the cycle and anc cycle number.

Table 8.13 summarizes the IPM comparison with the WS for the year 2003. The following conclusions can be drawn:

- the average differences between WS and IPM are smaller than $5\,\%$ at $26\,GeV$ for varying beam intensity, bunch spacing and beam emittance; with LHC nominal beam. The average IPM measured normalized emittance is smaller than the one measured by the wire scanners, however the agreement remains within the measurements error bars, as shown in Fig. 8.21(a);

- the differences are larger at $450\,GeV$, when the beam size shrinks. The smaller the beam size, the larger the discrepancy. This points out the IPM spatial resolution is a limiting parameter;

- the IPM beam size overestimation is not only related to the monitor intrinsic resolution in terms of pixels per sigma, as can be deduced by the fifth column of Table 8.13 and the simulations described in Section 3.6.

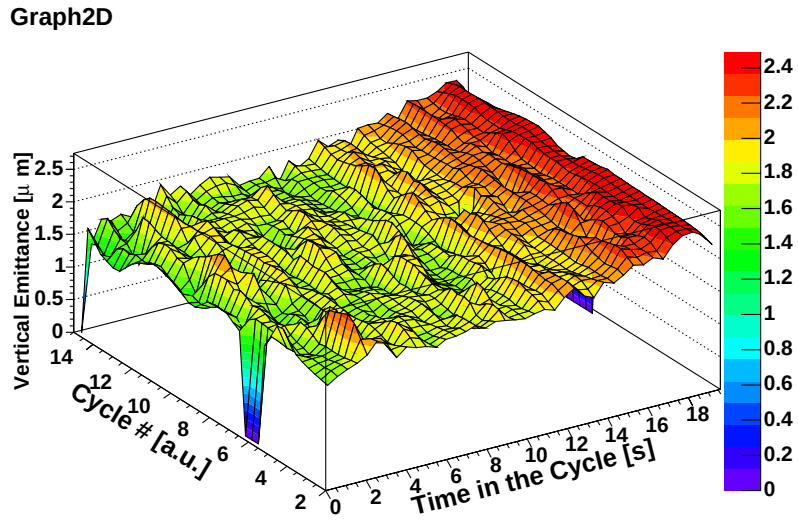

(a)

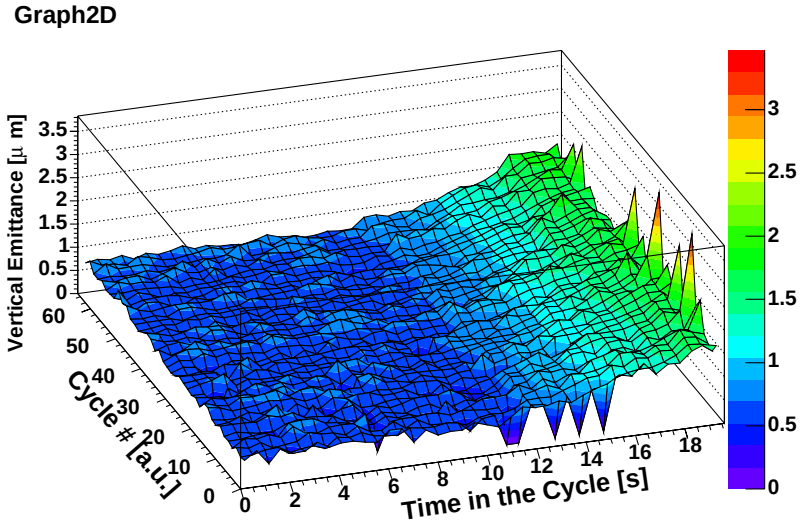

(b)

Figure 8.20: Vertical normalized emittance, as function of time in the cycle and cycle number, measured by the IPM, with (a) $75\,ns$ bunch spacing beam and (b) pilot beam .

Before the 2004 run it was possible to improve the IPM hardware. In particular a new optical imaging system was designed and installed in order to minimize the imaging errors between the phosphor layer and the CCD sensor. This improved the spatial resolution. The phosphor glued at the MCP output has been exchanged for a more sensitive one, with the drawback of having a slower time response. The resolution on the CCD camera was characterized by a conversion factor of $0.247\,mm/pixel$ in 2003, the improved optic lead to $0.161\,mm/pixel$ in 2004. Of course a smaller conversion factor, for the same total amount of incoming photons, means a smaller number of photons per pixel.
It must be remarked that the conversion factor is precisely measured in the laboratory by mean of light sources with a known spot size, thus independently from the comparisons with the wire scanners.
The cross calibration with the WS were repeated in 2004 and the results are plotted in Fig. 8.21(b), Fig. 8.22(b) and Fig. 8.23(b) for the different beams. The beam optimization, in visage of high LHC luminosity, lead to vertical emittances smaller than 2003, for the LHC nominal beam and for the pilot

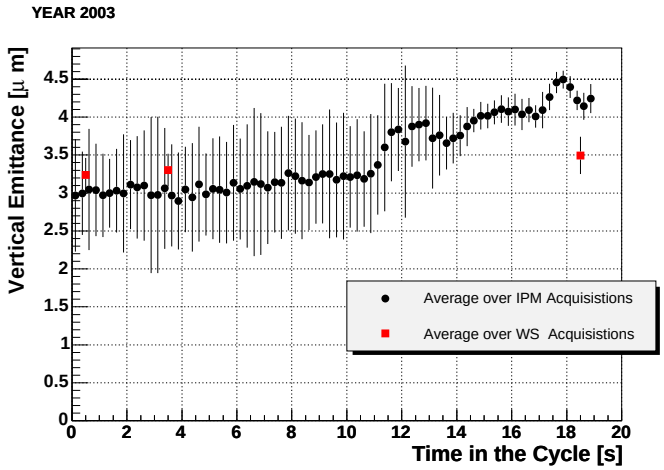

(a) Emittance from IPM (14 cycles) and WS (10 cycles)

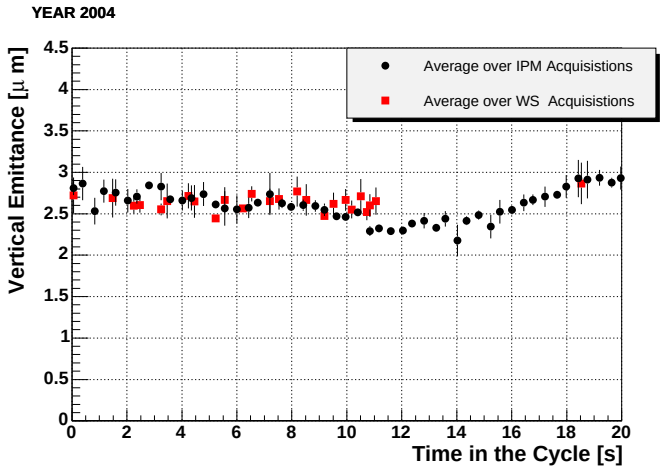

(b) Emittance from IPM (26 cycles) and WS (10 cycles)

Figure 8.21: Vertical normalized emittance with LHC nominal beam as measured in 2003 and 2004.

beam.
With the $75\,ns$ bunch spacing beam it was possible to compare IPM and WS at a reduced beam intensity, Fig. 8.22(c). Only one out of four PS batches was injected, equivalent to about $2.6 \cdot 10^{12}$ protons. The agreement between IPM and WS is better than $1\,\%$ along the whole acceleration. When measuring the beam with total intensity, Fig. 8.22(b), the IPM shows resolution limitations at high energy and overestimates the beam emittance in the first part of the cycle where only one batch is present and the monitor gain is not adequate.
Similarly, during the acquisitions with pilot beam the monitor overall gain[9] was set in order to optimize the beam size detection at high energy. As a consequence the signal over noise ratio was quite poor at low energy, as seen by the increased error bars (see Fig. 8.23(b)). Like for the emittance tracking of a coasting beam with variable intensity, an automatic variable gain throughout the MCP is desirable to follow the emittance evolution during acceleration. Such feature has been in fact implemented but has not been tested yet.
Table 8.14 summarizes the IPM results for the year 2004. The agreement between IPM and wire scanners clearly improved after the hardware modifications carried out before the SPS 2004 run. The

[9]The gain can be adjusted by changing the voltage settings on the high voltage electrodes and at the MCP input and output.

comparisons between the instruments, during the years 2003 and 2004, are presented in Fig. 8.24. The top plot shows the absolute difference between the beam size measured by the IPM and the expected value at the IPM location, derived from the WS measurements[10]. The difference is plotted as function of the expected size for the various measured beams. The bottom plot exhibits the relative normalized emittance differences as function of the absolute normalized emittance.
Defining as the IPM *beam size error* and *emittance overestimation* the two plotted quantities, we can conclude the following:

- the largest discrepancy between IPM and wire scanners remains with the smallest beam, the pilot bunch at 450 GeV. However the IPM beam size error which was about $240\,\mu m$ in 2003, decreased to $140\,\mu m$ in 2004. These two values are very close to the $\mu m/pixel$ factors achieved in the two years with the different optical imaging systems;

- by mean of a linear interpolation of the data shown in Fig. 8.24(a), it is possible to assess that an IPM beam size error of $100\,\mu m$ could be attributed to the measurement of an absolute beam size of about $600\,\mu m$ in 2003 and about $250\mu m$ in 2004; furthermore, using the linear interpolation, the beam size error in measuring a beam size of about $400\,\mu m$ decreases from about $240\,\mu m$ to about $90\,\mu m$;

- the IPM relative emittance overestimation, for the pilot bunch at 450 GeV, decreased from $175\,\%$ to $160\,\%$. For the same beam, but at 26 GeV, the emittance overestimation was lower in 2003 than 2004; however in 2004 the emittance was sensibly smaller and the IPM signal very noisy as already discussed commenting Fig. 8.23(b);

- the IPM emittance overestimation in 2004 is below $5\,\%$ for beam sizes larger than $0.6\,mm$, with the exception of the 75 ns bunch spacing beam at 450 GeV. The fact that this discrepancy is within $1\,\%$ for the same beam at reduced intensity (see Fig. 8.22(c)) gives the indication of possible saturation effects for the high intensity case;

Table 8.13: IPM resolution with different beam conditions and comparison with parallel wire scanner measurements. Measurements taken during the SPS 2003 run. $\sigma_{IPMexpected}$ is the beam size expected at the IPM location, derived by the wire scanners measurements.

Beam	**Energy** $[GeV]$	$\sigma_{\mathbf{IPMmeas}}$ $[mm]$	$\sigma_{\mathbf{IPMexpected}}$ $[mm]$	**Pix/**σ	$\epsilon_{\mathbf{IPM}}$ $[\mu m]$	$\epsilon_{\mathbf{WS}}$ $[\mu m]$	$\frac{\epsilon_{\mathbf{IPM}}-\epsilon_{\mathbf{WS}}}{\epsilon_{\mathbf{WS}}}$ $[\%]$
LHC Nominal	26	3.276	3.328	13.5	3.100	3.200	-3.1
	450	0.906	0.837	3.4	4.100	3.500	17.1
75 ns	26	2.201	2.121	8.6	1.400	1.300	7.7
	450	0.648	0.533	2.2	2.100	1.420	47.9
Pilot	26	1.512	1.506	6.1	0.660	0.655	0.8
	450	0.598	0.361	1.5	1.790	0.650	175.4

[10]The expected beam size is calculated denormalizing the emittance measured by the wire scanners for the betatron function at the IPM location

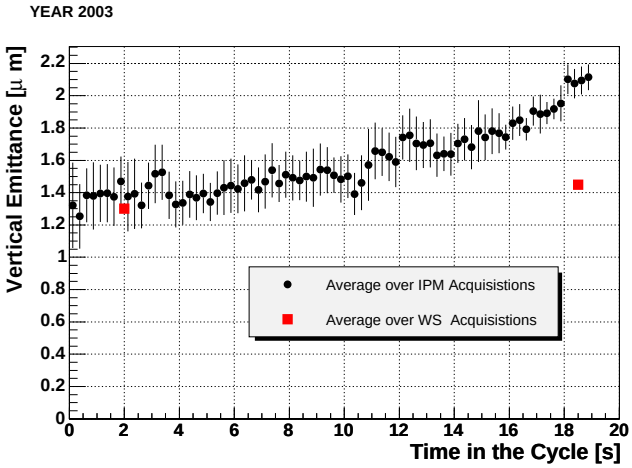

(a) Emittance from IPM (38 cycles) and WS (10 cycles)

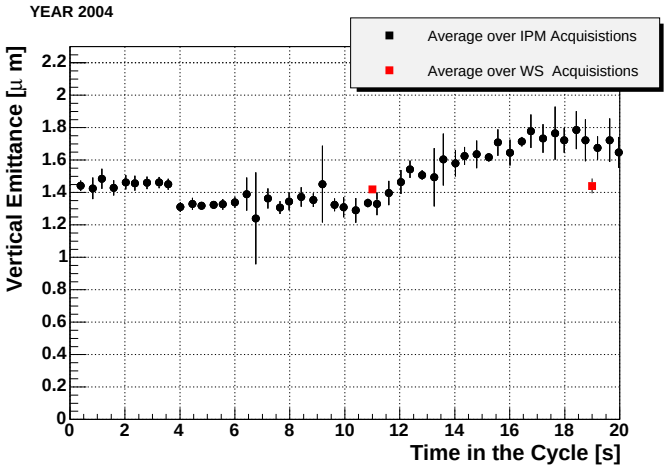

(b) Emittance from IPM (32 cycles) and WS (10 cycles)

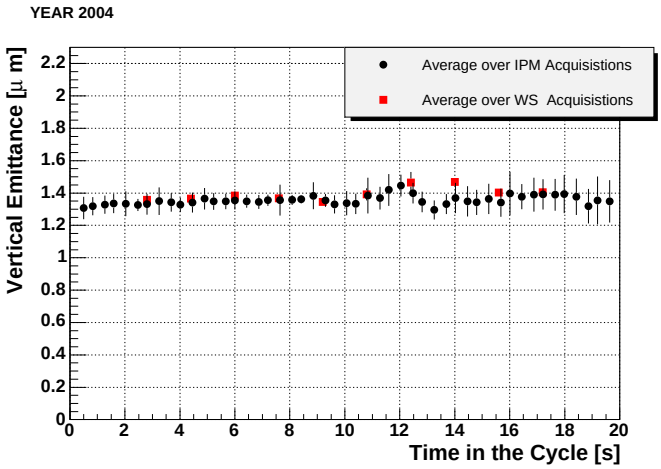

(c) Emittance from IPM (56 cycles) and WS (10 cycles)

Figure 8.22: Vertical normalized emittance with $75\,ns$ bunch spacing beam: as measured in: (a) 2003, (b) 2004, (c) 2004 reduced beam intensity.

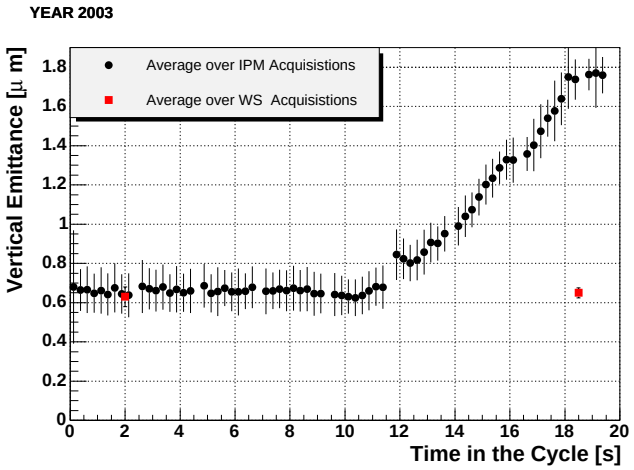

(a) Emittance from IPM (68 cycles) and WS (10 cycles)

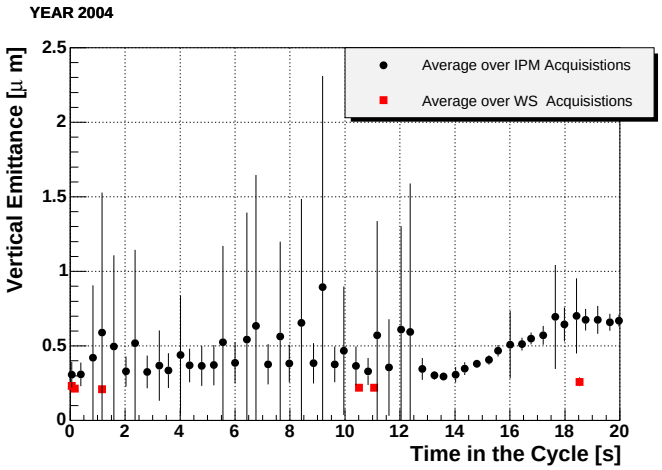

(b) Emittance from IPM (40 cycles) and WS (10 cycles)

Figure 8.23: Vertical normalized emittance with LHC pilot bunch as measured in 2003 and 2004.

Table 8.14: IPM resolution with different beam conditions and comparison with parallel wire scanner measurements. Measurements taken during the SPS 2004 run.

Beam	**Energy** $[GeV]$	$\sigma_{\mathrm{IPMmeas}}$ $[mm]$	$\sigma_{\mathrm{IPMexpected}}$ $[mm]$	**Pix/σ**	ϵ_{IPM} $[\mu m]$	ϵ_{WS} $[\mu m]$	$\frac{\epsilon_{\mathrm{IPM}}-\epsilon_{\mathrm{WS}}}{\epsilon_{\mathrm{WS}}}$ $[\%]$
LHC Nominal	26	3.097	3.085	19.2	2.770	2.750	0.7
	450	0.762	0.755	4.7	2.900	2.850	1.8
75 ns	26	2.209	2.201	13.7	1.410	1.400	0.7
	450	0.583	0.535	3.3	1.700	1.430	18.9
Pilot	26	0.985	0.911	5.7	0.280	0.240	16.7
	450	0.361	0.224	1.4	0.650	0.250	160.0

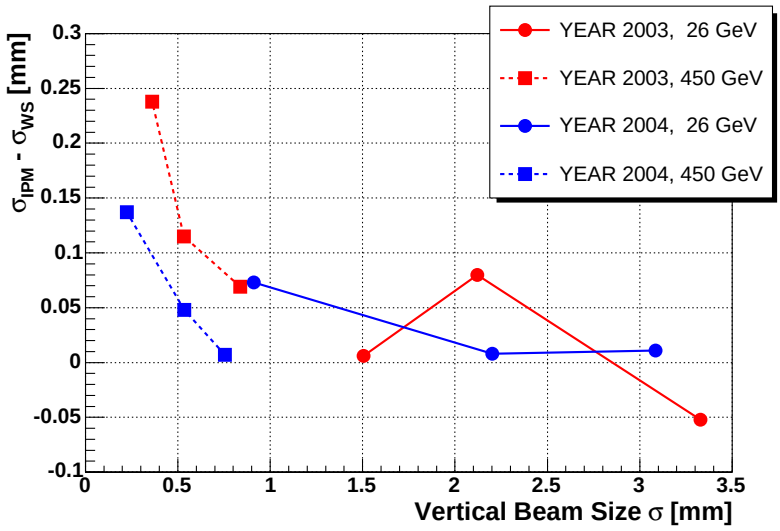

(a)

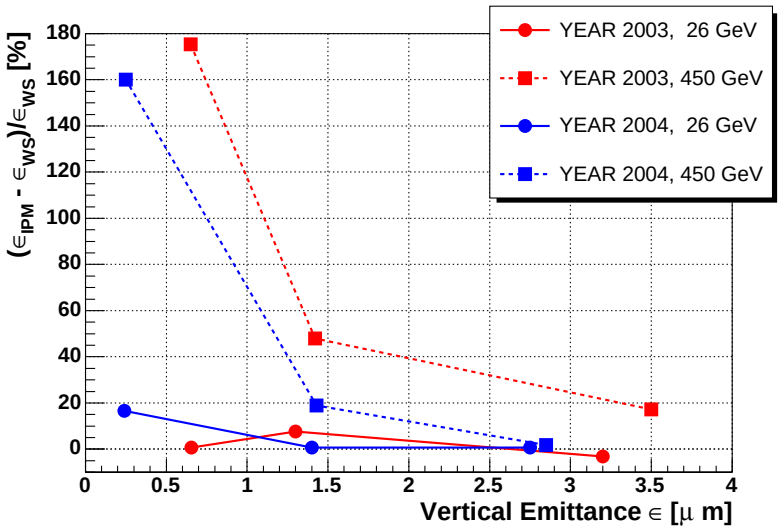

(b)

Figure 8.24: Comparison between IPM and WS derived from all the available measurements, in terms of (a) beam size differences and (b) normalized emittance difference .

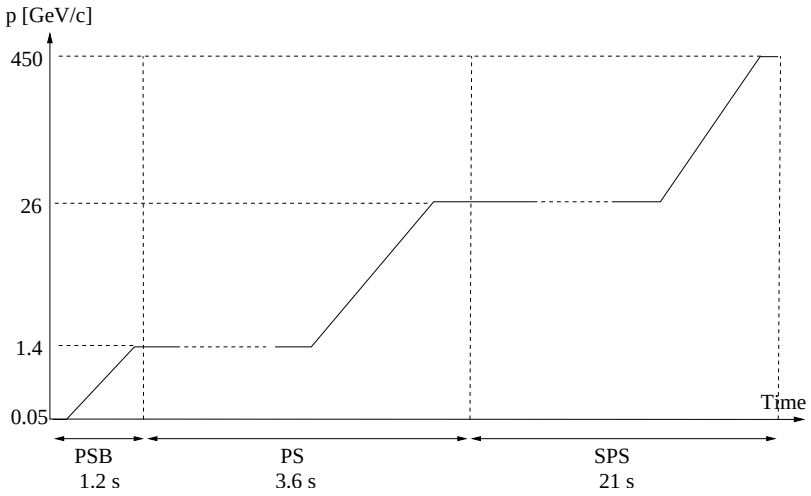

Figure 8.25: Proton momentum evolution during the acceleration from $p = 50\,MeV/c$ to $p = 450\,GeV/c$.

8.4 Emittance tracking from the PSB to the SPS

During the SPS run in the year 2003 the wire scanner monitors installed in the PSB, PS and SPS have been used to track, for the first time systematically, the transverse emittance during the acceleration from 1.4 to $26\,GeV/c$.
Three beams were considered: the LHC nominal beam, the $75\,ns$ bunch spacing beam and the pilot beam. The acquisitions were performed during periods dedicated to the beams optimization and characterization. The measurements were taken during consecutive filling cycles of the SPS. The same analysis tools have been applied to all the data (see Chapter 7) in order to consistently compare the results. The particles momentum evolution is illustrated in Fig. 8.25.
In all the following plots the dots indicate mean values of the emittances, while the error bars express the error on the mean. The number of scans for the different beams in the three accelerators are listed

Table 8.15: Number of scans performed with the different beams.

Beam type	**Plane**	**PSB**	**PS**		**SPS**	
		Extr.	Inj.	Extr.	Inj.	Extr.
LHC nominal	H	38	24	27	36	28
	V	46	42	29	34	32
75 ns bunch spacing	H	6	30	11	30	24
	V	4	37	13	29	36
Pilot bunch	H	0	♣	7	37	24
	V	19	♣	♣	44	18

♣ Values provided by PS operators.

in Table 8.15.
The horizontal and vertical emittance of the LHC nominal beam (4 PS batches injected in the SPS) are presented in Fig. 8.26.
Each PS batch (72 bunches) in the SPS is obtained by the consecutive injection from the PSB to the PS of 6 PSB bunches (one bunch for each of the 4 rings at first and two bunches few seconds later). Each PSB bunch is split in three at $1.4\,GeV$ by mean of three groups of RF cavities [10]. After the acceleration, in the PS, to $26\,GeV$ each bunch is then again split twice. Hence the final bunch train passes from 6 to 72 bunches.
The PSB measurements refer to averages in the four rings, over consecutive measurements, while

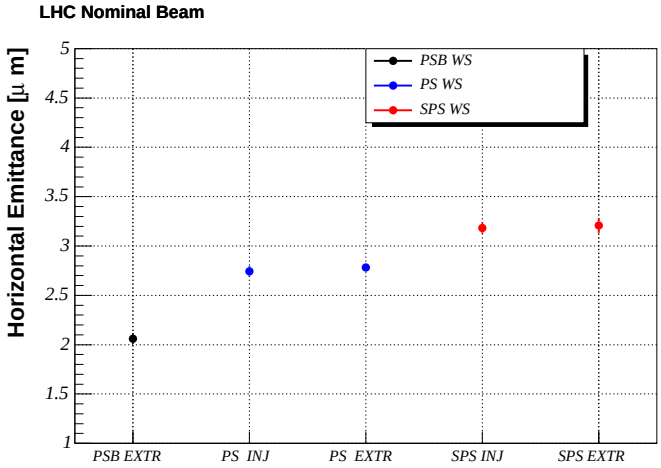

(a) Horizontal Plane.

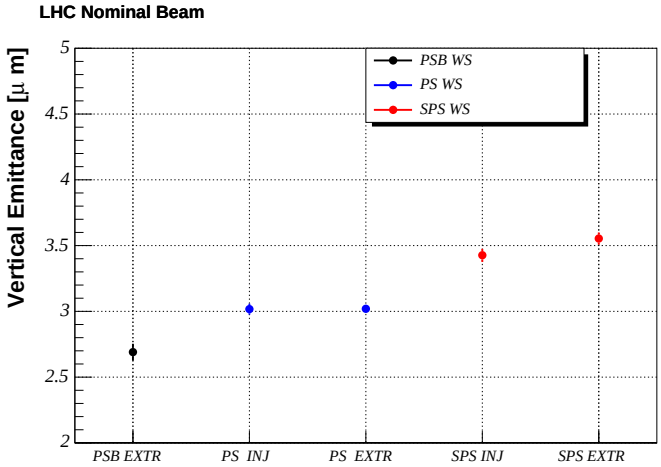

(b) Vertical Plane

Figure 8.26: Normalized emittance evolution of the LHC nominal beam at the different CERN accelerators, during the acceleration from $p = 1.4\,GeV/c$ to $p = 450\,GeV/c$.

in the PS the data were taken during one PS batch transfer from the PS to the SPS. The software presently used in the PS does not allow to select a particular batch[11]. Over many acquisitions the results characterize an average of the four batches.
Consequently, both for the PSB and the PS the WS intensity signal is taken on all the bunches each time circulating in the rings.
In the SPS, instead, the WS intensity signal has been acquired using the gating mode which selects the central part of each PS batch, the first 20 and the last 20 bunches of each batch have been disregarded[12].
Fig. 8.27 and Fig. 8.28 show the horizontal and vertical emittances for the $75\,ns$ bunch spacing and the pilot beams respectively.
For the pilot beam the PSB emittances have been also evaluated by extracting the beam on a measurement line ending with a beam dump. This line is equipped with some profiles monitors named *Secondary Emission Monitors (SEM)*. They consist in grid of wires which can be inserted in the beam

[11] In other words, the operator does not know to which of the four batches the profile measurement refers
[12] As explained in Section 4.1.2, this is imposed by the minimum distance between two acquisition gates.

line. The current generated on the wires by the beam passage allows the reconstruction of the beam profile at the monitor location. With three of them on a transfer line, one can retrieve the normalized emittance according to the method described in Section 3.4.
These measurements can be compared with the PSB wire scanners only in the vertical plane, since during the measurement session it was not possible to utilize the PSB and PS scanners in the horizontal plane.
The average normalized vertical emittance measured by the SEM results $\approx 4\,\%$ higher then the one measured with the PSB wire scanners. The discrepancy can give an indication of systematic errors in the two kind of instruments, but could also be related to the beam degradation during its extraction in the measurement line hosting the SEM.
The emittance differences measured from the extraction of an accelerator (PSB or PS) to the injection of the following in the chain (PS or SPS) can be addressed to the monitors systematic errors or to an increase of the true emittance. The measured relative emittance increase from the PS extraction to the SPS injection is $\approx 14\,\%$ in both planes, for the LHC nominal beam. The emittance growth is even higher for the two other beam types.
Throughout this thesis dissertation we only studied the accuracy of the SPS wire scanners. The monitors used here to determine the LHC nominal beam emittance are BWS519H in the horizontal plane and BWS519V in the vertical. From Table 8.7, Table 8.10 and Table 8.11 it can be deduced that, with respect to the reference monitors BWS517H and BWS517V, BWS519H underestimates the horizontal emittance, while BW519V overestimates the vertical. Therefore only the vertical emittance difference between PS extraction and SPS injection could be attributed to the monitor error. However no qualitative conclusions can be assessed since the calibration has been performed with a smaller emittance beam.
One reason for an increase of the beam emittance during the transfer from one accelerator to the other can be the so called "optics mismatch". Since the particles distribution in phase space depends on the accelerator optics parameters. If they are not matched between the two accelerators, the distribution undergoes an abrupt variation with a consequent emittance growth.

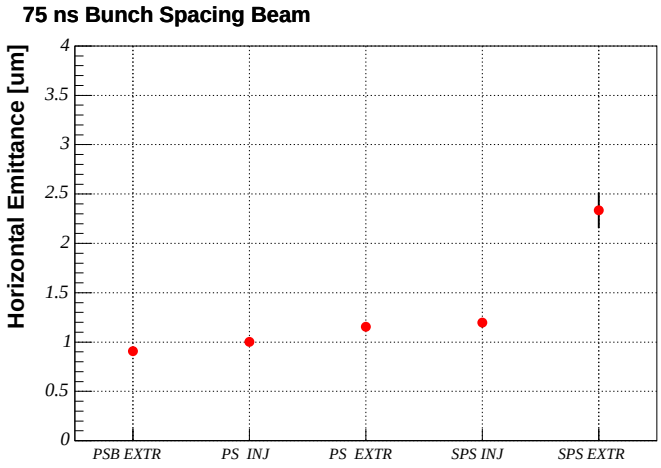

(a) Horizontal Plane

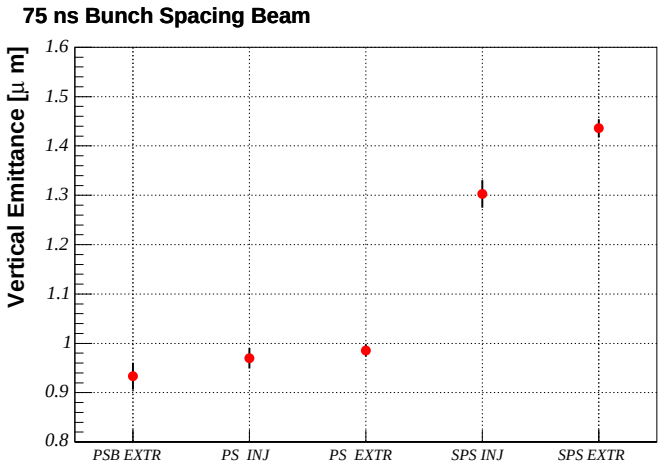

(b) Vertical Plane

Figure 8.27: Normalized emittance evolution of the LHC beam with $75\,ns$ bunch spacing, during the acceleration from $p = 1.4\,GeV/c$ to $p = 450\,GeV/c$.

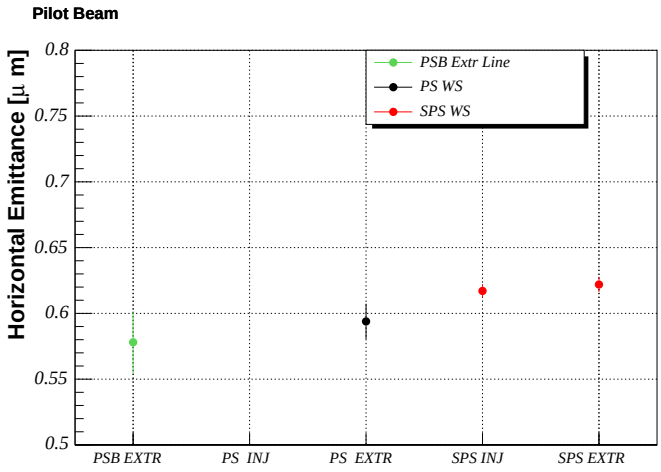

(a) Horizontal Plane

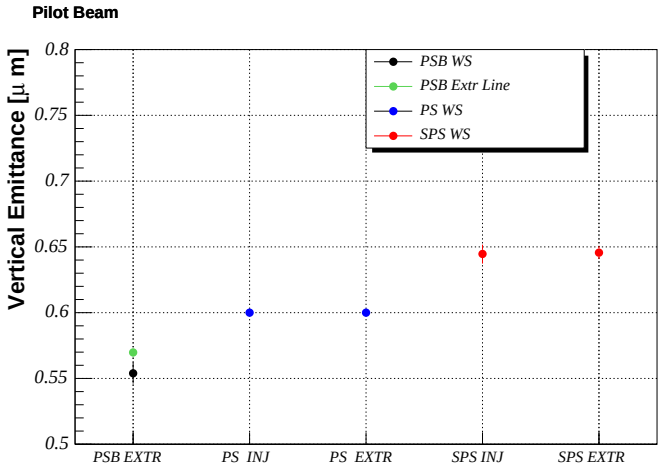

(b) Vertical Plane

Figure 8.28: Normalized emittance evolution of the LHC pilot bunch, during the acceleration from $p = 1.4\,GeV/c$ to $p = 450\,GeV/c$. In addition to the wire scanner monitors, the emittance could be measured in an extraction line devoted to beam diagnostics at the PSB extraction, equipped with Secondary Emission Monitors.

Summary and Conclusions

The main purpose of this thesis was to study and optimize the SPS Wire Scanner and Residual Gas monitors and to provide solutions for the discovered limitations. The choice of these two classes of instruments was driven by their existence in the SPS and by the fact that their installation is foreseen in the LHC.

The breaking of all the SPS rotational wire scanners during the year 2002 suggested to investigate the electromagnetic coupling between the wires and the beam. Measurements during the SPS operation demonstrated the the dependence of the wires temperature increase on the beam intensity and on the bunch length. The insertion of ferrite tiles in the wire scanner tanks, with the aim of absorbing the electromagnetic power, was proposed after dedicated laboratory measurements. Such solution avoided any further wire damage.

The wire scanner devices have been studied in order to discover dependencies on beam parameters (like beam intensity, bunch spacing and bunch length) and operational setups (like the wire movement direction).
A systematic error of the beam size determination with the SPS rotational wire scanners was identified. The error was caused by a delay between the wire position and the intensity measurements. This delay, induced by a filter designed to reduce noise in the wire position determination, lead to a scaling error on the measured beam size. The relative error was about $9\,\%$. A correction is now implemented and the relative error is below $3\,\%$ when measuring the LHC nominal beam. For beams with normalized emittance lower than $1\,\mu m$ the residual difference between scans carried out with opposite direction can reach $5\,\%$.
A new wire position read-out system for the SPS and LHC wire scanners is in the design phase; for such system we recommend to avoid the utilization of any filter introducing a time delay.
Since the SPS rotational wire scanners have been operated for many years, any accelerator study (for instance dynamic aperture studies), based on their utilization before the correction, is biased by the error. Therefore, an off-line correction is needed.

Multiple Coulomb scattering, between the accelerated particles and the wire scanners wire, induces an emittance growth. The effect is inversely proportional to the square of the particles energy and to the wire speed. The operation of the PSB monitors (low energy) and of SPS linear wire scanners (low wire speed) can introduce a significant relative emittance increase, especially for low emittance beams. The phenomenon has been studied and the predicted emittance increase agrees with experimental measurements within $7\,nm$ in terms of normalized emittance and $5\,\mu m$ in terms of beam size.

In parallel with the SPS normal operation, or during dedicated measurements sessions, the SPS emittance monitors have been cross-calibrated with each other.
During the acceleration in the SPS of low intensity, low emittance beams (namely the TOTEM beam

and the LHC pilot bunch) the wire scanner monitors were operated simultaneously. The linear wire scanners, regarded as the most accurate, have been considered as a reference and the rotational compared to them. The systematic discrepancy (averaged over the number of measurements) among the emittance measured by different wire scanners assesses the monitors accuracy.
The difference between the rotational and linear monitors in terms of relative normalized emittance ranges between 3 and $38\,\%$. In particular, two rotational wire scanners (BWS416H/V) installed in the same location exhibit a systematic underestimate of the emittance larger than $30\,\%$ with respect to the other wire scanners. A calibration in the laboratory is recommended for these instruments.
The systematic difference between two linear wire scanners is below $0.5\,\%$ of the measured emittance (which is below $1\,\mu m$). In terms of beam size this discrepancy results lower than $10\,\mu m$, assuming that the two linear wire scanners have the same relative error. This estimation is confirmed by the multiple Coulomb scattering studies mentioned above, after which the disagreement between the measurements and the theoretical model is below $10\,\mu m$.
Therefore, this value is considered as the accuracy of the SPS linear wire scanner monitors and fulfills the accuracy requirements for the emittance measurements in the SPS and LHC. However, these monitors can be used without any wire damage only for beam intensities below $5 \cdot 10^{12}$ protons.

The wire scanners precision is assessed by their repeatability. During the measurements with the pilot bunch and the TOTEM beam, the repeatability in terms of beam size resulted on average $11\,\mu m$ for the linear devices. The rotational wire scanners exhibit an average repeatability of $39\,\mu m$ in the vertical plane and $58\,\mu m$ in the horizontal. Since the particles momentum spread variations contribute to the statistical fluctuations of the emittance measurements in the horizontal plane, the wire scanners repeatability in the vertical plane is considered more indicative of the monitors precision.

The SPS Ionization Profile Monitor has been optimized and tested under several beam conditions and the measured normalized vertical emittance has been compared with the one measured with the wire scanners.
With the LHC nominal beam, the relative discrepancy between the two classes of instruments is below $1\,\%$ during the whole acceleration period from $26\,GeV$ to $450\,GeV$.
The IPM overestimates the width of low intensity, low emittance beams. Such effect is attributed to the limited resolution of the imaging system. Improvements were observed in the year 2004 with respect to the year 2003, but the relative disagreement between IPM and WS remains above $20\,\%$ when the beam size at the IPM location is below $500\,\mu m$.

The gained experience and the analysis tools were also applied to the PSB and PS wire scanner monitors. For the first time it was possible to characterize, with a systematic and consistent method, the LHC type beams along the whole acceleration up tho the SPS top energy.

The knowledge of the betatron function at the monitor locations is needed to accurately determine the beam emittance. This is normally accomplished with computational models of the accelerator, that have an estimated accuray of 1-2 %. We tested an experimental method for measuring the betatron function amplitude at the location of six quadrupoles in the SPS. The results exhibit a good relative agreement, but a large absolute systematic error has not been explained yet. An hypotesis for explaining that error could refer to uncertainties in the knowledge of the quadrupoles current-magnetic field transfer function.
In conclusion, this work allowed to assess the status of the wire scanner and ionization profile monitors used in the SPS. The accuracy of the linear wire scanners is sufficient to guarantee the correct monitoring of LHC type beams (with a limited intensity). In fact, the LHC will be equipped

with linear scanners having the same design as the SPS monitors. For the rotational devices, the main uncertainty remains the wire position determination. For future installations, their calibration in the laboratory must be always followed by a beam based cross calibration with the linear devices.
Furthermore, the mechanical design of new monitors should consider as a primary issue the minimization of electromagnetic coupling effects (unlike it was done at the time of the SPS wire scanners design). This is not only important for the wires integrity, but also for the transverse impedance limitations which are imposed to achieve a successful operation of an accelerator, in terms of beam stability and luminosity [69].
The recent development of the SPS ionization profile monitor allowed to improve its accuracy and its successful utilization in the LHC can be expected. However, the imaging resolution of the system must be further improved and the saturation levels of the different monitor components better understood.
We demonstrated that the precision of a set of monitors can be determined in a systematic way by cross calibrating different instruments and applying to the measurements results the same analysis tools. The same methods could be easily utilized for other monitors, such as scintillating screens used in transfer lines and synchrotron radiation monitors installed in rings.

Appendix A

Appendix

A.1 Calculations used in Chapter 2

A.1.1 Equation of motion

By deriving two times Eq. (2.21) with respect to s (see pag.11),

$$x'(s) = Aw'(s)cos(\Psi(s)+\Psi_0) + Aw(s)[-sin(\Psi(s)+\Psi_0)]\Psi'(s) \tag{A.1}$$

and consequently

$$\begin{aligned} x"(s) &= Aw"(s)cos(\Psi(s)+\Psi_0) + Aw'(s)[-sin(\Psi(s)+\Psi_0)]\Psi'(s) + \\ &+ Aw'(s)[-sin(\Psi(s)+\Psi_0)]\Psi'(s) + \\ &+ Aw(s)[-cos(\Psi(s)+\Psi_0)]\Psi'^2(s) + \\ &+ Aw(s)[-sin(\Psi(s)+\Psi_0)]\Psi"(s) + \\ &= A\{cos(\Psi(s)+\Psi_0)[w"(s) - w(s)\Psi'^2(s)] + \\ &\quad -sin(\Psi(s)+\Psi_0)[2w'(s)\Psi'(s) + w(s)\Psi"(s)]\} \end{aligned} \tag{A.2}$$

Inserting $x"(s)$ and $x(s)$ in Eq. (2.11) gives

$$cos(\Psi(s)+\Psi_0)[w"(s) - w(s)\Psi'^2(s) + K(s)] - sin(\Psi(s)+\Psi_0)[2w'(s)\Psi'(s) + w(s)\Psi"(s)] = 0 \tag{A.3}$$

A.1.2 Error propagation from the transverse emittance to the luminosity

The luminosity is defined as

$$L = f\frac{n_1 n_2}{4\sqrt{\epsilon_x \beta_x^* \epsilon_y \beta_y^*}} \tag{A.4}$$

and from Eq. (**??**):

$$\delta L = \sqrt{\left(\frac{\partial L}{\partial \epsilon_x}\delta\epsilon_x\right)^2 + \left(\frac{\partial L}{\partial \epsilon_y}\delta\epsilon_y\right)^2} \tag{A.5}$$

The contribute due to the horizontal emittance results to be:

$$\begin{aligned} \frac{\partial L}{\partial \epsilon_x}\delta\epsilon_x &= -\frac{1}{2}f\frac{n_1 n_2}{4}(\epsilon_x \beta_x^* \epsilon_y \beta_y^*)^{-\frac{3}{2}}(\beta_x^* \epsilon_y \beta_y^*)\delta\epsilon_x \\ &= -\frac{1}{2}f\frac{n_1 n_2}{4\sqrt{\epsilon_x \beta_x^* \epsilon_y \beta_y^*}}\frac{\delta\epsilon_x}{\epsilon_x} \\ &= -\frac{1}{2}L\frac{\delta\epsilon_x}{\epsilon_x} \end{aligned} \tag{A.6}$$

and an analog term can be calculated for the vertical emittance.
Eq. (A.5) becomes:

$$\delta L = \frac{L}{2}\sqrt{\left(\frac{\delta\epsilon_x}{\epsilon_x}\right)^2 + \left(\frac{\delta\epsilon_y}{\epsilon_y}\right)^2}, \tag{A.7}$$

from which

$$\frac{\delta L}{L} = \frac{1}{2}\sqrt{\left(\frac{\delta\epsilon_x}{\epsilon_x}\right)^2 + \left(\frac{\delta\epsilon_y}{\epsilon_y}\right)^2} \tag{A.8}$$

A.2 Courant-Snyder invariant in normalized coordinates

In the phase space coordinates x, x' the Courant-Snyder invariant is

$$\gamma x^2 + 2\alpha x x' + \beta x'^2 = A^2 \tag{A.9}$$

When changing the coordinate system to $(x, \alpha x + \beta x') \equiv (x, p_x)$, it follows $x' = (p_x - \alpha x)/\beta$ and the invariant becomes:

$$\begin{aligned}
& \gamma x^2 + 2\alpha x\left(\frac{p_x - \alpha x}{\beta}\right) + \beta\left(\frac{p_x - \alpha x}{\beta}\right)^2 = \\
= \;& \gamma x^2 + 2\alpha\frac{p_x x}{\beta} - \frac{2\alpha^2 x^2}{\beta} + \frac{p_x^2}{\beta} + \frac{\alpha^2 x^2}{\beta} - \frac{2p_x\alpha x}{\beta} = \\
= \;& \left(\gamma - \frac{\alpha^2}{\beta}\right)x^2 + \left(\frac{2\alpha}{\beta} - \frac{2\alpha}{\beta}\right)p_x + \frac{p_x^2}{\beta} = \\
= \;& \frac{1}{\beta}x^2 + \frac{1}{\beta}p_x^2
\end{aligned} \tag{A.10}$$

in which the identity $\gamma \equiv (1 + \alpha^2)/\beta$ has been used.

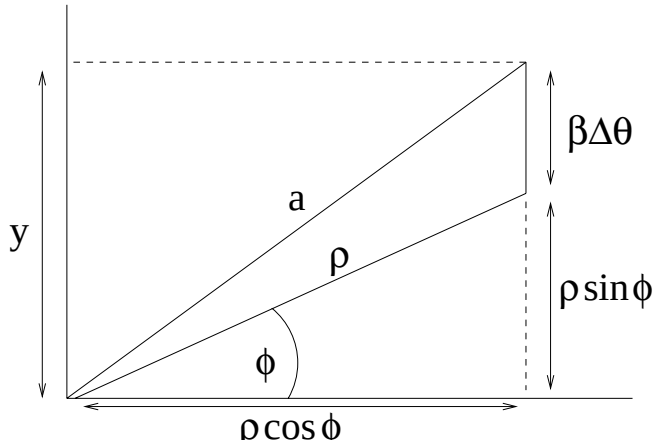

Figure A.1: Enlargement of Fig. 5.2

A.3 Calculations used for the results of Chapter 3

Trigonometric relations leading to Eq. (5.16). Referring to Fig. A.1:

$$a^2 = y^2 + \rho^2 cos^2\phi \quad \text{(A.11)}$$

$$y^2 = [\beta\Delta\theta + \rho sin\phi]^2 \quad \text{(A.12)}$$

$$\begin{aligned} a^2 &= (\beta\Delta\theta)^2 + \rho^2 sin^2\phi + 2\rho\beta\Delta\theta sin\phi + \rho^2 cos^2\phi \\ &= \rho^2 + (\beta\Delta\theta)^2 + 2\rho\beta\Delta\theta sin\phi \end{aligned} \quad \text{(A.13)}$$

Bibliography

[1] ISO. *International vocabulary of basic and general terms in metrology*. ISBN 92-67-01075-1, 1993.

[2] ISO. *Guide to the expression of uncertainty in measurement*. ISBN 92-67-10188-9, 1995.

[3] J.J. Gras, J.P. Koutchouk. *Concepts and glossary for the specification of the beam instrumentation. Specification Team Note 001*, CERN, 2000.

[4] *ATLAS, A Toroidal Lhc ApparatuS*, URL:http://atlas.web.cern.ch/atlas/welcome.html.

[5] *CMS, The Compact Muon Solenoid*, URL: http://cmsinfo.cern.ch/welcome.html/.

[6] *ALICE, A Large Ion Collider Experiment*, URL: http://alice.web.cern.ch/alice/.

[7] *LHCb, The Large Hadron Collider Beauty experiment*, URL: http://lhcb.web.cern.ch/lhcb/.

[8] *TOTEM, Total Cross Section, Elastic Scattering and Diffraction Dissociation at the LHC* , URL: http://totem.web.cern.ch/totem/.

[9] *LHC Design Report Volume I*. CERN-2004-003-V-1, 2004.

[10] *LHC Design Report Volume III*. CERN-2004-003-V-3, 2004.

[11] J.B. Jeanneret et al. *Quench levels and transient beam losses in LHC magnets*. *CERN-LHC-Project-Report-44*, 1996.

[12] D.A. Edwards, M.J. Syphers. *An Introduction to the Physics of High Energy Accelerators*. Wiley, 1993.

[13] F. Meot. *Correction of Vertical Crossing Induced Dispersion in LHC. CERN-LHC-Project-Note-122*, 1997.

[14] *CAS - CERN Accelerator School: 5th General Accelerator Physics Course*, Editor: S. Turner, CERN-94-01, 1994.

[15] H. Wiedemann. *Particle Accelerator Physics I (Second edition)*. Springer, 1998.

[16] C. Bovet et al. *Comparison of Different Methods for Transverse Emittance Measurement and Recent Results from LEP*. *CERN-SL-97-67(BI)*, 1997.

[17] *LHC Emittance Workshop*, cern, 2000,
URL: http://emittanceworkshop.web.cern.ch/emittanceworkshop/prog.work.htm.

[18] S. I. Kurokawa (Editor) et al. *Beam Measurement: Proceedings of the Joint Us-Cern-Japan-Russian School on Particle Accelerators*. World Scientific, 1999.

[19] J. Camas et al. *The OTR screen betatron matching monitor of the CERN SPS. CERN-OPEN-2000-238*, 2000.

[20] J. Bosser et al. *Transverse Profile Monitor using Ion Probe Beams. Nucl. Instrum. Methods Phys. Res., A 484*, 2002.

[21] A. Jansson. *Noninvasive single-bunch matching and emittance monitor. Phys. Rev. Spec. Top. Accel. Beams 5 072803*, 2002.

[22] J. Bosser et al. *Characteristics of the radiation emitted by protons and antiprotons in an undulator. J. Phys. Lett.: 45 pp.L343-L351*, 1984.

[23] L. Ponce. *LHC proton beam diagnostics using synchrotron radiation. CERN-2004-007*, 2004.

[24] B. Bouchet et al. *Wire scanners at LEP. Proceedings of the 1991 IEEE Acc. Conference, San Francisco*, 1991.

[25] S. Burger et al. *The PS Booster Fast Wire Scanner. Proceedings of DIPAC2003, Mainz,Germany*, 2003.

[26] G.F. Knoll. *Radiation Detection and Measurement.* John Wiley & Sons, 1988.

[27] M. Plum et al. *SNS Linac Wire Scanner System: Signal Levels and Accuracy. Proceedings of LINAC 2002, Gyeongju, South Korea*, 2002.

[28] A. Arauzo et al. *A Proposal for a Gas Ionization BSM for LHC. LHC Project Note 198, CERN, Geneva*, 1999.

[29] J. Bosser et al. *N_2 and Xe Gas Scintillation Cross-Section, Spectrum and Lifetime Measurements from 50 MeV to 26 GeV at the CERN PS and Booster. CERN-PS-2001-065(BD)*, 2001.

[30] G. Burtin et al. *The Luminescence Profile Monitor of the CERN SPS. CERN-SL-2000-031-BI*, 2000.

[31] MAD, Methodical Accelerator Design, URL: http://frs.home.cern.ch/frs/xdoc/mad-x.html.

[32] M.G. Minty and F. Zimmermann. *Measurement and Control of Charged Particle Beams.* Springer, 2003.

[33] F. Tecker. *Methods of Improving the Orbit Determination and Stability at LEP.* Ph.D. Thesis,RWTH Aachen, 1998.

[34] *CAS - CERN Accelerator School: 4th General Accelerator Physics Course,* Editor: S. Turner, CERN-91-04, 1991.

[35] D. Boussard. *Schottky noise and beam transfer function diagnostics. CERN-SPS-Div-Rep-86-11-ARF*, 1986.

[36] P.J. Chou et al. *Beam transfer function and transverse impedance measurements in the FERMILAB main ring. Proceedings of the 1995 Particle Accelerator Conference, Dallas, Texas*, 1995.

[37] C. Boccard et al. *Tune Measurements in the SPS as a Multicyling Machine. Proceedings of the 1996 European Particle Accelerator Conference, Sitges, Spain*, 1996.

[38] J. Wenninger, CERN-AB-OP. *Private Communication*.

[39] M. Frigo, S.G. Johnson. *FFTW: An adaptive software architecture for the FFT*. In Proc. 1998 IEEE Intl. Conf. Acoustics Speech and Signal Processing, volume 3, pages 1381–1384. IEEE, 1998.

[40] R. Bartolini et al. *Algorithms for a Precise Determination of the Betatron Tune*. *CERN-SL-96-48*, 1996.

[41] P.M. Lapostolle. *Possible emittance increase through filamentation due to space charge in continuous beams*. *IEEE Trans. Nucl. Sci. 18*, 1971.

[42] J.A. Nolen et al. *Transverse Emittance systematics Measured for Heavy-Ion Beams*. *Joint Accelerator Conferences Proceedings*, 1999.

[43] C. Bovet et al. *Wire Scanners For LHC*. *LHC-Project-Note-108*, 1997.

[44] BURLE Long Life^{TM} Micro Channel Plates, URL: http://www.burle.com.

[45] PROXITRONIC Phosphor Screens, URL: http://www.proxitronic.de.

[46] E2V Technologies, URL: http://e2vtechnologies.com.

[47] C. Fisher et al. *Beam studies made with the SPS Ionization Profile Monitor*. *Proceedings of DIPAC 2003, Meinz, Germany*, 2003.

[48] G. Rumolo et al. *Electron cloud effects on beam evolution in a circular accelerator*. *Phys. Rev. ST Accel. Beams 6, 081002*, 2003.

[49] B. Henrist et al. *The secondary electron yield of TiZr and TiZrV non-evaporable getter thin film coatings*. *Applied Surface Science, Volume 172, Pages 95-102*, 2001.

[50] J. D. Jackson. *Classical Electrodynamics (Third Edition)*. John Wiley & Sons, 1999.

[51] B. Rossi and K. Greisen. Rev. Mod. Phys. *Vol.13, p.240*, 1941.

[52] V.L. Highland. Nucl. instr. and meth. *Vol.129, p.497*, 1975.

[53] G.R. Lynch and O.I. Dahl. Nucl. instr. and meth. *Vol.B58, p.6*, 1990.

[54] Number 1-4 Phys.Rev.C, Vol.3. Review of particle physics, 1998.

[55] C. Johnstone et al. *Analysis and Measurements of Emittance Dilution from Vacuum Windows in the Fermilab Recylcler Transfer Lines*. *Proceedings of the 2003 Particle Accelerator Conference, Portland, Oregon*, 2003.

[56] M. Syphers et al. *Emittance Growth Due to Tevatron Flying Wires*. *Fermilab National Laboratory, Chicago (IL), Beams-doc-1199-v2*, 2004.

[57] F. Roncarolo, B. Dehning. *Transverse emittance blow-up due to the operation of Wire Scanners, analytical prediction and measurements*. *Proceedings of PAC 2005, Knoxville, Tennessee*, 2005.

[58] P.R. Cameron et al. *Carbon Wire heating due to scattering in the SNS*. *Proceedings of the 2001 Particle Accelerator Conference, Chicago, U.S.*, 2001.

[59] *Network Analyzer Basics*, ©Agilent Technologies,
URL: http://cpliterature.product.agilent.com/litweb/pdf/5965-7917e.pdf.

[60] D. Kajfez, E.J. Hwan. *Q factor measurements with network analyzer*. *IEEE Trans. Microwave Theory Tech., vol MTT-32*, 1984.

[61] E. Campisi et al. Proceedings of the Workshop on Microwave-Absorbing Materials for Accelerators (p.169). Newport News, Virginia, US (1993).

[62] D.M. Pozar. *Microwave Engineering*. Addison-Wesley, 1990.

[63] E. Nyfors et al. *Industrial microwave sensors*, artech house. 1989.

[64] Luong M., *private communication*, cea-cen-saclay, gif sur yvette, france.

[65] Goodfellow Corporation, devon, pa, u.s., URL: http://www.goodfellow.com.

[66] ROOT, An Object Oriented Data Anylisis Framework., URL: http://root.cern.ch/.

[67] John R. Taylor. *An introduction to error analysis : the study of uncertainties in physical measurements*. Univ. Science Books, 1982.

[68] Dipak I Weaver, James M.; Patel. Interactive multiaxis encoder positioning system, 1988.

[69] A.W. Chao. *Physics of collective beam instabilities in high energy accelerators*. Wiley, 1993.